Constraints on the formation of ultramafic and mafic pseudotachylytes in the Schistes Lustre Complex, Corsica.

By

Natalie Deseta

A thesis submitted to the Faculty of Science, University of the Witwatersrand, in fulfillment of the requirements for the degree of

Doctor of Philosophy

School of Geosciences

University of the Witwatersrand, 2014

Plagiarism declaration

I have read and understood the rules on plagiarism set out by the University of the Witwatersrand. I hereby declare that this thesis is the result of my own scholarly work, and that in all cases material from the work of others (books, articles etc) has been acknowledged. This written work has not previously been used as material for examination by this or any other university or institution.

Signed,

Natalie Deseta (0506491 H)

(Candidate)

At the University of the Witwatersrand, July 2014

ACKNOWLEDGMENTS

The geosciences are becoming an increasingly interdisciplinary field, combining physics, chemistry, geology and the life sciences in tackling various research problems. The interactions among these fields and how they can be used to solve scientific problems are of great interest to me. Through the course of this project I have become particularly fascinated by the formation of high-pressure, high-temperature microstructures in minerals and how these processes are explained by the interaction of physical and chemical processes at different scales. The spectroscopy facilities at the University of the Witwatersrand, the University of Johannesburg and Oslo University enabled me to gain invaluable experience in using electron microprobe analysis in imaging pseudotachylyte-related microstructures. Major and trace element analysis using X-Ray Flourescence spectroscopy, Raman and Inductively-Coupled Plasma Mass Spectrometry combined with the observed microstructures allowed me to link theoretical, experimental and natural systems, providing a more holistic perspective of geological processes.

I would like to thank the University of the Witwatersrand, The Mellon Foundation, The National Research Foundation and Physics of Geological Processes (Oslo, Norway), without whose funding this project would not have been possible. I would also like to acknowledge the support and kindness of Alasdair Walton, the Walton family and of course friends and peers who withstood the rants and blurts of a scattered mind at work. There have been times I am sure when my complaints and moodiness regarding this work have been unbearable. The skills learned and experiences gained throughout the course of this project are invaluable and have changed me profoundly.

Thanks to both Profs. Lew Ashwal and Torgeir Andersen, for giving me the independence to teach myself and to learn organically how to tackle a large scientific project from start to finish. I was given the opportunity to come to my own conclusions and lend their ears for discussion, no matter how ridiculous the idea.

I am grateful to my supervisor abroad, Torgeir for his hospitality, his unfailing patience in tolerating my stubbornness and for discussing and explaining concepts to me over and over and over again. My local supervisor, Lew is owed appreciation for conversation on and off topic. His guidance, support, cynicism and friendship, whatever the issue or the time show his unfailing commitment to his students. Thanks also to Denny Crane and Alan Shore.

Just as important and perhaps paramount in this experience has been the mutual enjoyment of geological curiosities and the fostering of a passion for science and problem solving, which are now deeply ingrained within me.

Natalie Deseta

"There are more things in Heaven and Earth,

Horatio, Than are dreamt of in your

philosopy." Hamlet, Act 1, Scene V,

Shakespeare.

Abstract

Intermediate-depth earthquakes occur at depths of 60 – 300 km at these depths high confining pressure inhibits brittle failure from generating earthquakes. Fault-related pseudotachylytes from Corsica are exhumed paleofaults from a high pressure, low temperature subduction zone environment, and are considered analogues of intermediate-depth earthquakes. Hence, it is important to analyse the physico-chemical processes by which these pseudotachylytes form in order to gain primary insight into the controls of their formation and how this seemingly paradoxical process takes place. Up until the recent discovery of high pressure pseudotachylytes there was no known direct method of evaluating the formation mechanisms of intermediate-depth earthquakes. High pressure pseudotachylytes found in subduction complexes are regarded as relict paleo-earthquakes. Previous research aimed at understanding the generation of these phenomena and the role of fluids on their origin has been based on seismic, experimental and numerical modelling. The principal aims of this project were to carry out detailed geochemical, petrographic and microtextural analyses of such pseudotachylytes located in the Eocene Schistes Lustres Complex, Corsica, and to determine whether the data from natural samples corroborate current models. The pseudotachylytes in this study reside in peridotitic and metagabbroic lozenges enclosed within serpentinites. Pseudotachylytes are notoriously complex and messy, with compositions that vary widely over small distances (< 1 mm). For this reason the pseudotachylytes in this study were systematically analysed from the outcrop-scale to the micron-scale according to their wallrock type. From these data it was observed that greenschist and blueschist facies hydrous minerals present in the peridotite and metagabbro wallrocks were entrained into pseudotachylyte fault veins. Back scatter electron (BSE) imaging shows that these hydrous minerals underwent wholesale fusion in the melt. No evidence for prograde dehydration reactions was observed in the wallrocks or in association with the pseudotachylytes. Electron microprobe analyses (EPMA) of the bulk matrix of the pseudotachylytes revealed variable H_2O content, 0 – 14 wt % in peridotite-pseudotachylytes and 0 – 4 wt % in metagabbro-hosted pseudotachylytes. The principal minerals that underwent fusion are: clinopyroxene, plagioclase, glaucophane, Mg-hornblende and actinolite (metagabbro- hosted) pseudotachylyte), and olivine, orthopyroxene clinopryroxene, chlorite, serpentine and tremolite (peridotite-hosted pseudotachylyte). The bulk of H_2O entering the melt remained in solution until it reached supersaturation, upon which it exsolved to form fluid-rich, vesicular veins. Cuspate and lobate rims of microlites (omphacite, clinopyroxene, olivine and orthopyroxene) along the boundaries of hydrous veins indicate that the melt was still molten when the fluids exsolved. The presence of

hydrous fluids in the melt appears to have enhanced the fracturing process. Fault veins hosted by peridotite that have the greatest H_2O content are the thickest, have more chaotic injection networks and exhibit more cataclastic deformation features than the anhydrous fault veins observed. With regard to the mechanism of pseudotachylyte generation, it is clear that water present in hydrous minerals or entrapped in the crystal lattices of anhydrous minerals plays a fundamental role in facilitating intermediate-depth earthquakes through hydrolytic weakening. A melt richer in hydrous fluid also has a lower viscosity, facilitating fault slip. Dissolved H_2O is also a flux and may enhance further melting of the wallrock, relative to an anhydrous pseudotachylyte vein.

Sheared, kinked and twinned wallrock minerals and survivor clasts associated with the pseudotachylyte fault veins indicate crystal-plastic deformation. No significant grain size reduction was observed in proximity to fault veins. The grain size of wallrock minerals at fault vein boundaries ranges from 5 – 20 mm. From this it was inferred that the mechanism of deformation is controlled by power law creep, temperature and high strain rate.

The presence of metastable high temperature crystallisation products in the pseudotachylyte such as hoppers and dendrites of olivine, orthopyroxene and diopside (in peridotite) and Al-rich omphacite and Fe-rich anorthite (in metagabbro), are suggestive of a short-lived high temperature event resulting from thermal instability. These high temperature mineral assemblages are overprinted by ones indicating a return to ambient conditions (lower temperatures, but still high pressures), namely, glaucophane, albite and epidote (in metagabbro) and clinochore, fine-grained granoblastic olivine, enstatite and diopside (in peridotite). The observations from this detailed study of natural samples suggest that intermediate-depth seismicity may be generated by a thermal runaway process.

Contents

ACKNOWLEDGEMENTS

Abstract

1. Introduction.....1

2. Geological Setting.....3

2.1 Formation of the Schistes Lustres Nappes.....3
2.2 Study area.....8

Figures

Fig. 2.1.....5
Fig. 2.2.....6
Fig. 2.3.....7
Fig. 2.4.....9

3. Previous work.....10

3.1 Pseudotachylyte.....11
3.2 High pressure pseudotachylytes.....13
3.3 Rheological controls of deformation along the fault plane.....14
3.3.1 The brittle-ductile transition.....14
3.3.2 Comminution and cataclasite.....17
3.3.3 Fracture toughness.....*21*
3.3.4 Intracrystalline deformation: creep.....25
3.3.5 Transition from comminution to frictional melting.....28

3.4 Current models of high pressure pseudotachylyte formation...... 30

3.5 Seismicity and pseudotachylytes.....*34*

3.5.1. Present day seismicity: current perspectives on intermediate-depth seismicity.....*34*
3.5.2 Paleoseismicity.....*36*

3.6 Water in the subducting slab.....*37*
3.6.1 Fluids and dehydration.....*41*

3.7 Previous work on Corsican pseudotachylytes.....*44*

Fig. 3.1.....10
Fig. 3.2.....12
Fig. 3.3.....13
Fig. 3.4.....16
Fig. 3.5.....17
Fig. 3.6.....19

Fig. 3.7.....20
Fig. 3.8.....23
Fig. 3.9.....27
Fig. 3.10.....28
Fig. 3.11.....32
Fig. 3.12.....34
Fig. 3.13.....40
Fig. 3.14.....42
Fig. 3.15.....43
Fig. 3.16.....45

4. Aims of study.....46

5. Methodology.....47

5.1 Unsucessful analyses.....*47*

6. Summary of scientific contributions.....49

Manuscript summaries:

6.1 A weakening mechanism for intermediate-depth seismicity? Detailed petrographic and microtextural observations from blueschist facies pseudotachylytes, Cape Corse, Corsica.....50

Individual contribution.....50
Article summary.....51

6.2 Initiating intermediate-depth earthquakes: insights from a HP-LT ophiolite from Corsica.....52

Individual contribution.....52
Article summary.....56

6.3 Large subduction earthquakes along the fossil MOHO in Alpine Corsica.....58

Individual contribution.....58
Article summary.....59

Articles

7. A weakening mechanism for intermediate-depth seismicity? Detailed petrographic and microtextural observations from blueschist facies pseudotachylytes, Cape Corse, Corsica.

Published online: Tectonophysics, December, 2013.

Abstract.....60

7.1. Introduction.....61

7.2. Geological Setting.....62

7.2.1 Field observations.....64

7.3 Materials and methods.....66

7.4. Petrographic and microtextural observations.....66

7.4.1 Metagabbro host rock.....66
7.4.2 Peridotite host rock.....69
7.4.3 Fault vein characteristics......69
7.4.4 Injection vein characteristics.....73
7.4.5 Microtextures of ultracataclasite.....75
7.4.6 Microtextures of the pseudotachylyte matrix.....75
7.4.7 Microtextures of survivor clasts.....76
7.4.8.1 Metagabbro: Pseudotachylyte.....77
7.4.8.1.1 Microlite assemblage in the metagabbro pseudotachlytes.....78
7.4.8.1.2 Metagabbro: Devitrification and recrystallization of pseudotachylytes.....79
7.4.9.1 Peridotite: Pseudotachylyte.....80
7.4.9.1.1 Microlite assemblage in peridotite-hosted pseudotachylytes.....80
7.4.9.1.2 Peridotite: Devitrification and recrystallization of pseudotachylytes.....83

7.5. Discussion

7.5.1 Precursors to pseudotachylyte formation.....83
7.5.2 Possible influence of grain size on pseudotachylyte formation.....84
7.5.3 Present model compared to previous mechanisms.....89

7.6. Conclusions.....90

Figures

Fig. 7.1.....63
Fig. 7.2.....64
Fig. 7.3.....68
Fig. 7.4.....69
Fig. 7.5.....71
Fig. 7.6.....71
Fig. 7.7.....72
Fig. 7.8.....74
Fig. 7.9.....74
Fig.7.10.....77
Fig. 7.11.....79
Fig. 7.12.....81
Fig. 7.13.....82
Fig. 7.14.....83

8. Initiating intermediate-depth earthquakes: insights from a HP-LT ophiolite from Corsica

Re-submitted to Lithos 10th July, 2014

Abstract……92

8.1. Introduction……94

8.1.1. Pseudotachylyte formation and flash melting……95
8.1.2. Current models of high pressure pseudotachylyte formation……95

8.2. Geological setting……98

8.2.1 Field observations and sampling……101

8.3. Materials and methods……102

8.4. Results……103

8.4.1 Petrographic analysis……103
8.4.1.1 Metagabbro: host rock……103
8.4.1.2 Peridotite: host rock……106
8.4.2 Presence of hydrous minerals in the wallrock:……108
8.4.3 Pseudotachylyte……109
8.4.3.1 Fine-grained wallrock derived pseudotachylyte……114
8.4.4 Bulk rock and mineral compositions……119
8.4.4.1 Metagabbro – pseudotachylyte microlites……124
8.4.4.2 Peridotite – pseudotachylyte microlites……124

8.5. Discussion……126
8.5.1 Style of melting and principal components involved:……126
8.5.2 2 Influence of grain size on pseudotachylyte formation: a fine-grained peridotite vs coarse-grained peridotite case study……126
8.5.3 H_2O content of the melt……131
8.5.4 High-Al omphacite……132
8.5.5 Implications……134
8.5.6 Summary of conclusions……138

Figures

Fig. 8.1.....99
Fig. 8.2.....101
Fig. 8.3.....105
Fig. 8.4.....107
Fig. 8.5.....110
Fig. 8.6.....111
Fig. 8.7.....113
Fig. 8.8.....116
Fig. 8.9.....118
Fig. 8.10.....120
Fig. 8.11.....121
Fig. 8.12.....122
Fig. 8.13.....123
Fig. 8.14.....125
Fig. 8.15.....128

Tables

Table 8.1.....141
Table 8.2.....142
Table 8.3.....143
Table 8.4.....144

9. Large subduction earthquakes along the fossil MOHO in Alpine Corsica

Published in Geology, June, 2014

Abstract.....145

9.1 Introduction.....146

9.2 Field observations.....147

9.3 Melt volumes, energy budget and earthquake magnitude.....151

9.4 Discussion.....153

9.5 Conclusion.....154

Figures

Fig. 9.1.....148
Fig. 9.2.....149
Fig. 9.3.....150
Fig. 9.4.....151

Figures

Fig. 9.1.....148
Fig. 9.2.....149
Fig. 9.3.....150
Fig. 9.4.....151

10. Discussion and conclusions.....156

10.1. Style of fusion.....156
10.2 Role of water in seismic failure: decoupling dehydration from shear heating.....158
10.3 Character of pseudotachylyte generating mechanism.....165

Figures

Fig. 10.1.....157
Fig. 10.2.....161
Fig, 10.3.....162
Fig. 10.4.....163
Fig. 10.5.....164
Fig. 10.6.....166
Fig. 10.7.....169
Fig. 10.8.....170
Fig. 10.9.....171
Fig. 10.10.....173

11. Future outlooks.....174

References.....175

Appendix

Laue patterns..... A1
EBSD examples.....A6
Interlayered PST.....A10
Hostrock XRF results.....A11
Metagabbro PST matrix data.....A12
Metagabbro wallrock mineral data.....A15
Metagabbro Glass data.....A20
Metagabbro microlite data.....A24
Peridotite PST matrix data.....A27
Peridotite wallrock mineral data.....A32
Peridotite glass data.....A37
Peridotite microlite data.....A38
Geology supplementary data.....A39
Tectonophysics article.....A46
Geology article.....A58

1. Introduction

Pseudotachylytes are considered the only known direct evidence of paleoseismicity, and by studying them we can attempt to gain insight into the nature and mechanism of faulting (Di Toro et al., 2005; Spray, 1992; Swanson, 1992). Of particular interest are ultramafic and mafic pseudotachylytes, which have been interpreted by previous workers as having been derived from remnant subducted lithosphere in ophiolite complexes (Austrheim & Andersen, 2004; Fabbri et al., 2000; Jin et al., 1998; Lund & Austrheim, 2003). These melts record faulting that would have taken place in the subducting slab of a convergent margin setting, the upper section of the Wadati-Benioff Zone, which is where most of today's deep earthquakes appear to originate (Hacker, 2003; Nakajima et al., 2009a; Reynard et al., 2010). Shallow pseudotachylytes are typically those that form at depths < 15 km, and are the result of frictional fusion, forming in faults under a brittle to brittle-ductile regime (Magloughlin & Spray, 1992). This is supported by field, petrographic, theoretical, chemical and experimental evidence (Del Gaudio et al., 2009; Fabbri et al., 2000; Lin, 1994a, 1994b; Moecher & Sharp, 2004; O'Hara & Sharp, 2001). However, in the case of subduction-related earthquakes, the distinction between a shallow versus intermediate-depth earthquake is not clear-cut. Hence for the purposes of this study I consider intermediate-depth earthquakes as subduction-related earthquakes that take place at depths between 60 and 300 km (Hacker et al., 2004; Kirby et al., 1995). At these depths, high confining pressure should inhibit the formation of coseismic brittle friction melts (Del Gaudio et al., 2009; John et al., 2009; Ogawa, 1987) and, therefore, the fusion mechanism of these pseudotachylytes warrants exploration.

The ultramafic and mafic pseudotachylytes (PST) that are the focus of this study are located in the blueschists of the Schistes Lustres Complex in Cape Corse Region, Corsica (Figs. 2.1 – 2.4) (Austrheim and Andersen, 2004). These blueschist to lawsonite-eclogite facies rocks are part of

an Eocene, Alpine subduction complex (Fig. 2.1) and have been interpreted as exhumed oceanic lithosphere (Agard et al., 2002; Caron & Péquignot, 1986; Molli & Malavieille, 2011). By studying these PST in detail (petrographically, structurally and geochemically) we can assess the percent melting that occurred, which materials underwent melting and whether the melt was locally derived or was injected into the rock (O'Hara, 1992, Obata & Karato, 1995, Austrheim and Andersen, 2006). Furthermore, it is possible also to analyse the relationship between frictional heating and metamorphic (dehydration/hydration) reactions, which take place in, and which allow such pseudotachylyte veins to form (Di Toro et al, 2005; Green and Houston 1995; Jung et al. 2004).

2. Geological Setting

2.1 Formation of the Schistes Lustres Nappes

The early Alpine evolution of the Schistes Lustres Complex started in the Late Cretaceous and was concluded by the Early Oligocene (Agard et al., 2002; Caron & Péquignot, 1986). During the Late Cretaceous, the continental margin of Europe was thrust beneath Apulian ocean crust, closing the Ligurian Sea and starting to form the Ligurian Accretionary Complex (Fig. 2.1). Subduction continued until the Eocene, during which it appears that the eclogitised slab detached and initiated exhumation (~ 80 – 60 Ma). Exhumation appears to have paused at this stage, under blueschist facies conditions (~ 45 Ma), at which point subduction polarity reversed and the Apulian Plate began to subduct beneath continental Europe. At ~ 33 Ma the slab recommenced exhumation and was incorporated into the accretionary complex. Extensional deformation continued during and after exhumation, marked by the formation of the Liguro-Provençal back-arc basin, causing further deformation of the accretionary complex and the isolation of Corsica from the European continent (Fournier et al., 1991; Ravna et al., 2010). The Schistes Lustres Complex dominates the northeastern section of Corsica, recording high pressure, low temperature (HPLT) glaucophane-lawsonite facies metamorphism that took place at ~ 45 Ma (Figs. 2.1 and 2.3). It lies within an orogenic wedge in the Schistes Lustres Suture Zone, delineating the contact between the high pressure Brianconnais Domain and the ultra-high pressure Dora Massif (Fig. 1) (Agard et al., 2002; Martin et al., 2011; Molli & Malavieille, 2011). The Complex comprises several thrust sheets that were folded and faulted into the Cap Corse-Castagniccia antiform during slab exhumation (Caron & Péquignot, 1986; Molli & Malavieille, 2011; Ravna et al., 2010). The thrust sheets constitute Ligurian-Tethys ocean crust, upper mantle ultramafics, gabbro and basaltic pillow lavas and associated Jurassic-Cretaceous metasediments, interleaved with relicts of the previous ocean-continental domain. Kinematic indicators synchronous with the high pressure episode recorded by the rocks indicate a top-to-the-west shear sense congruent with under-

thrusting of the European basement beneath the oceanic nappes (Fig. 2.1) (Molli & Malavieille, 2011; Ravna et al., 2010). The Schistes Lustres Complex shows a prograde development of HP-LT metamorphism from 100 – 60 Ma and records two exhumation episodes with opposing vergences, reflecting two subduction episodes with opposite polarities (Agard et al., 2002; Ravna et al., 2010). The age of the latest HP-LT event recorded is uncertain but has been estimated using $^{40}Ar/^{39}Ar$ from phengite, giving an approximate age of ~ 65 Ma for the eclogite phase and ~ 45 – 35 Ma for the blueschist phase, under pressures ranging from 1.5 – 2.6 GPa and ambient mantle slab temperatures of 335 – 420 ˚C (Agard et al., 2002; Caron & Péquignot, 1986; Ravna et al., 2010).

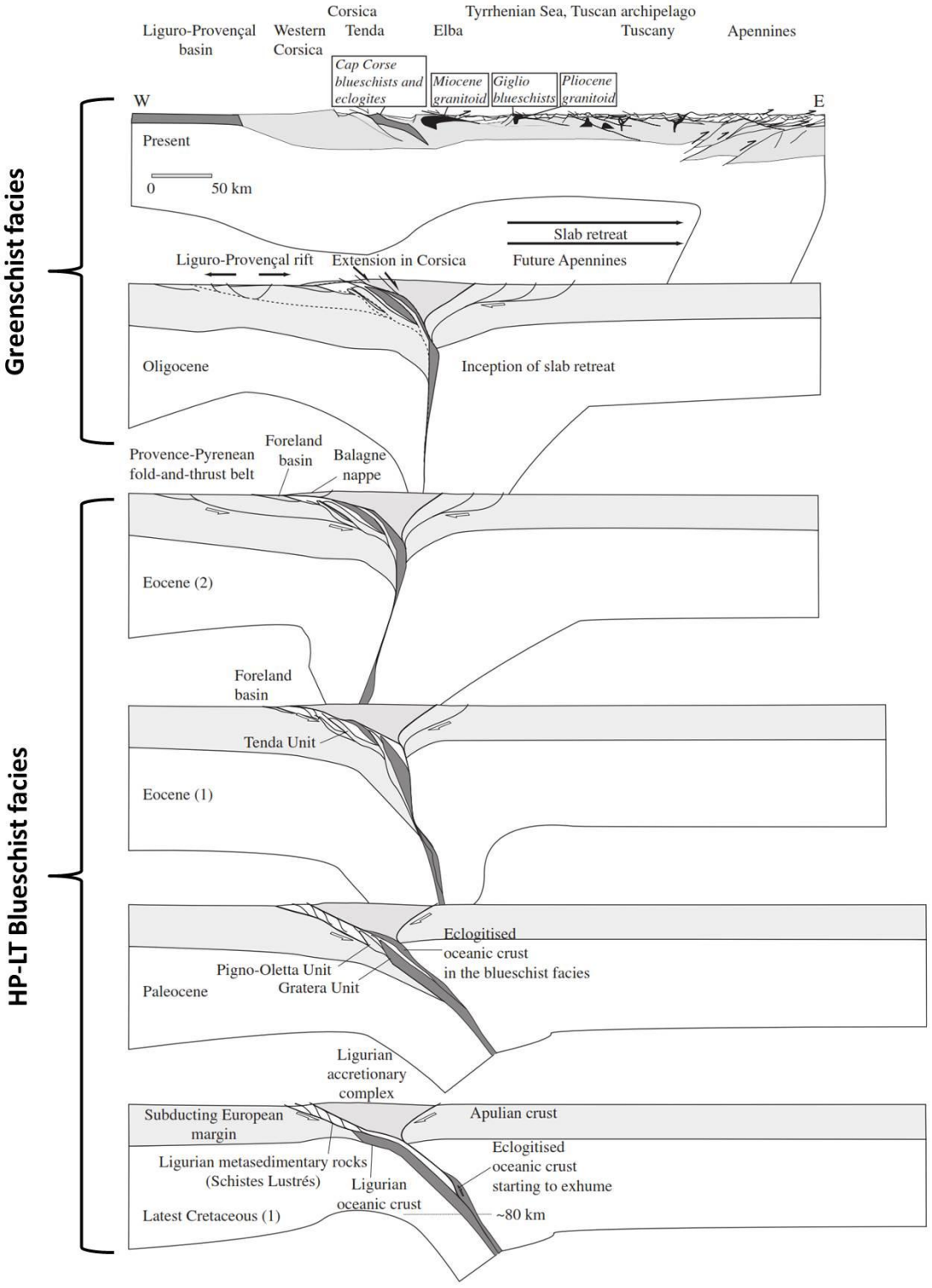


Fig. 2.1 Model of the HP-LT evolution of the metamorphic complexes in Cape Corse, after Ravna et al. (2010). During the Late Cretaceous until the Eocene west-vergent overthrusting dragged oceanic units onto the European Continental Basement, generating nappe stacks. During this period HP-LT (1.5 GPa, 420 ˚C) blueschist facies metamorphism took place, retrogressing the oceanic eclogites. During the Oligocene, eastward simple shear was dominant, associated with extensional deformation, where pre-existing compressional structures were commonly re-activated. The Oligocene deformation is associated with a greenschist overprint on blueschists and eclogites.

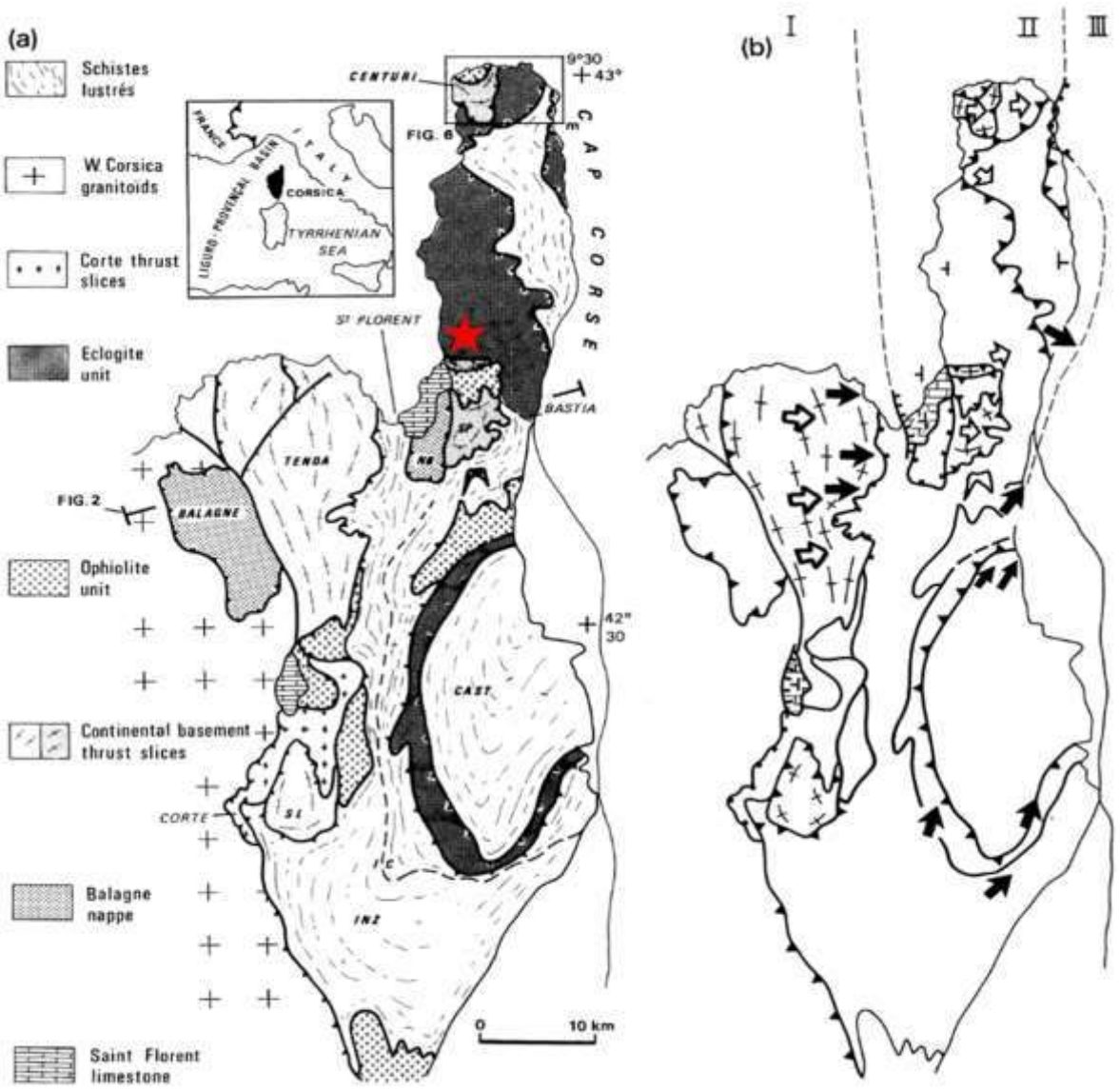


Fig. 2.2 Geological map of Corsica, after Jolivet (1993). a) shows the different lithological units and general sense of ductile shear during greenschist facies retrogression of the various units. The red star indicates the approximate location of Cima di Gratera, the study area. b) illustrates the three deformation phases involved in generating nappes as the European basement was thrust beneath the ophiolite. Arrows indicate the eastward simple shear thrust direction of rock packages.

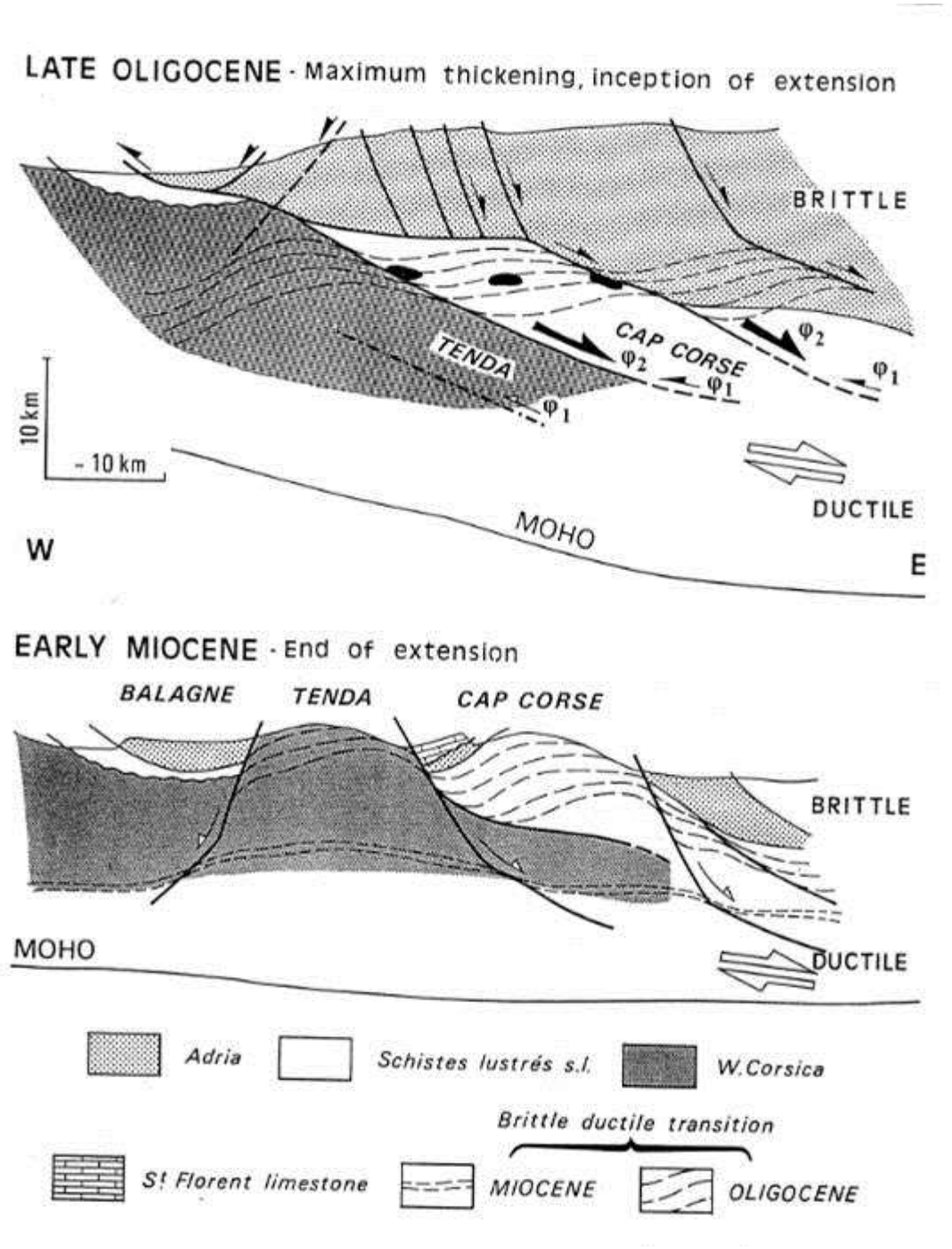


Fig. 2.3 Detail of geometry of Alpine Corsica during the Late Oligocene until present. Both ductile and brittle strain distributions are shown, with predominant shear top-to-the-east. The greatest degree of deformation associated with simple shear is focused in the east-dipping shear zones. After Jolivet (1993).

2.2 Study area

The study area is located on the SSW side of Cima di Gratera, Cape Corse. The PST occur within lenses of gabbro and mantle peridotite enclosed by serpentinite (Figs. 2.3 - 2.5). These rocks form part of the Schistes Lustres Complex (part of the Alpine high pressure-low temperature Subduction Complex) and are incorporated within nappes of exhumed Ligurian oceanic lithosphere, which has slivers of crystalline continental material. This rock package has been thrust onto the continental margin of Europe (Fig. 2.1) (Agard et al., 2002; Fournier et al., 1991; Jolivet, 1993). Within the thrust stacks is an ophiolite, comprising ultramafic rocks (peridotite), gabbro, pillow lavas and metasedimentary schists, as well as allochthonous blueschist and eclogite facies rocks (Austrheim and Andersen, 2004).

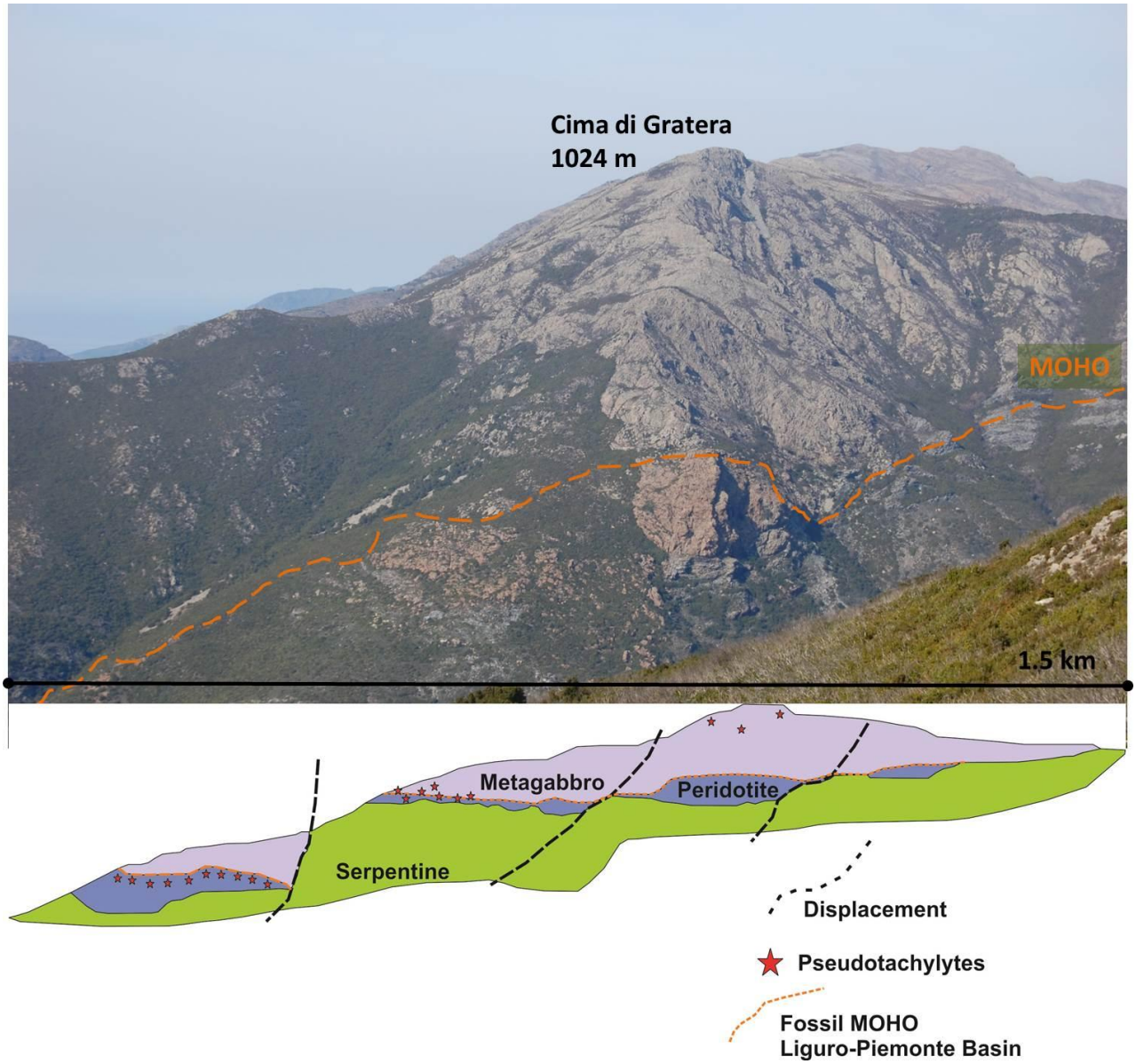


Fig. 2.4 Simplified geological sketch and cross-section of the study area on Cima di Gratera. The PST occur within lenses of preserved peridotite enclosed by serpentinite as well as in the vicinity of the gabbro-peridotite, gabbro-serpentinite contact higher up the hill. After Andersen et al. (2014).

The gabbros are heterogeneous and range from cumulate-layered to varied-textured, whereas the peridotites are relatively uniform in terms of their texture and grain size (Austrheim and Andersen, 2004; Deseta et al., 2014). The fault rocks have been partially metamorphosed to blueschist and greenschist facies only in patches, except within the shear zones where the metamorphic reactions have fully equilibrated (Andersen and Austrheim, 2006; Jolivet, 1993; Ravna et al., 2010). The PST tend to occur within the pristine areas of gabbro and peridotite that are relatively undeformed and metamorphosed.

3. Previous work

3.1 Pseudotachylyte

Pseudotachylytes (PST) were originally defined based on the black, glassy, anastomosing veins observed to pervade the Archaean gneisses of the Vredefort impact structure (Shand, 1916). The name comes from the glassy (tachylytic) nature of the PST, but distinguishes it from true volcanic basalt (pseudo). While the etymological origin of PST originated in association with exogenic hyper-velocity impacts, they are also associated with endogenic coseismic earthquakes (Spray, 2010). On the whole, fault-related PST is a fairly common rock type, defined by sharp and distinct margins, a dark grey/black aphanitic matrix and angular survivor clasts (Sibson and Toy, 2006; Spray, 1992; Swanson, 1992). The dark glassy groundmass of PST is generally considered to be dominated by frictional melt (altered to varying degrees) (Sibson, 1975; Sibson and Toy, 2006; Spray, 2010). PST can form along syndeformational fault planes (fault veins) or as injections shooting off of parent faults (injection veins) (Figs. 3.1 - 3.3). PST are typically associated with shallow faulting in the seismogenic zone of continental upper crust (Magloughlin and Spray, 1992). In order to produce the thicknesses of PST observed in the field (> 1mm – 3500 mm), energy budget calculations indicate that localised shear heating, due to high strain rates, in the fault zone is required (Di Toro et al., 2005; John et al., 2009; Sibson, 1977; Sibson and Toy, 2006; Swanson, 1992). As temperature increases with high strain rates, the transient localisation of heating within a narrow fault zone can induce disequilibrium fusion along the slip plane (Hobbs et al., 1986; Orowan, 1960; Sibson, 1975, 1980a; Spray, 1992). As the fault vein is increasingly lubricated by PST formation, stress along the fault drops and frictional heating is reduced. The resultant stress relaxation permits the fault plane to return to ambient hostrock temperatures, quenching the PST (Sibson, 1975; Spray, 2010). The volume of PST veins is affected by dilation and constriction of the fault zone, causing melt to be pumped out of the fault zone into pre-existing and/or syndeformational fractures. Hence, the volume of PST in a given fault vein cannot be accurately estimated by directly measuring the width of

the vein (Sibson, 1977; Sibson, 1975; Spray, 1992, 2010). PST formation typically destroys deformation features associated with the moments leading up melt production, obfuscating direct observation of precursory deformation (Fig. 3.3) (Spray, 2010). On top of this, the low preservation potential of quenched melt and the tendency of pre-existing faults to be re-activated by later deformation and fluid ingress can also obliterate features that would be useful in determining conditions leading to PST formation (Magloughlin and Spray, 1992).

3.2 High pressure pseudotachylytes

High pressure pseudotachylytes (those formed under blueschist to eclogite facies conditions) from various localities (Blue Ridge Province, North Carolina, the Ivrea-Verbano zone, Italy, the Kråkeneset gabbro and Holsnøy, Norway) have been studied on a number of scales and from various aspects in order to ascertain the mechanism by which they form (Lin 1994a; Lin 1994b; Camacho et al. 2001; John et al. 2009; Austrheim and Boundy 1994; Lund and Austrheim 2003). The majority of pseudotachylytes are generated under relatively shallow crustal conditions and are hence associated with a brittle deformation regime (Figs. 3.4 and 3.5) (Jin et al., 1998; Magloughlin and Spray, 1992; O'Hara, 1992; Spray, 1992). Generally viewed as frictional melts (Sibson, 1977b, 1975, 1980a; Spray, 1992), the formation of high pressure pseudotachylytes in mafic and ultramafic rocks appears paradoxical, as they should be inhibited by high confining stresses (Fig. 3.6). However, it needs to be taken into account that the brittle-ductile transition zone of mafic and ultramafic rocks is controlled by olivine, rather than quartz and feldspar, and can therefore extend beyond the brittle-ductile zone determined for crustal rocks (Fig. 3.4) (Kirby, Durham, and Stern, 1991; Swanson, 1992). With regard to the mafic and ultramafic rocks hosting the Corsican PST, eclogites from Cape Corse record ambient temperatures of 420 ˚C at 1.8 – 2.6 GPa, showing the geotherm to be cold and steep, pushing the brittle-ductile transition down to 80 km (Fig. 3.7) (Ravna et al., 2010).

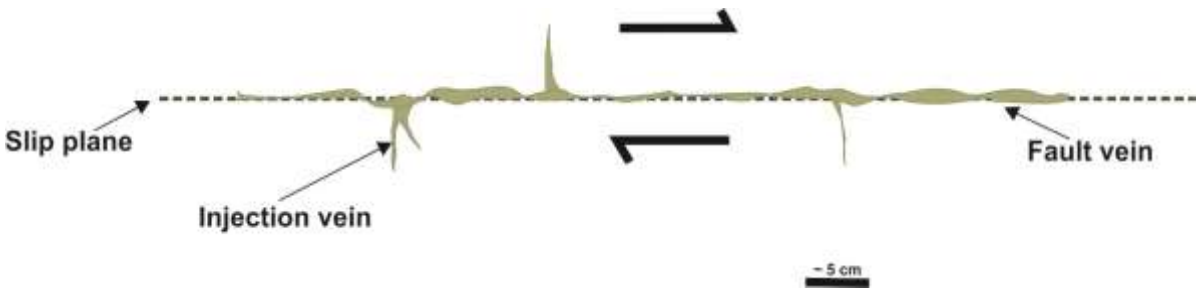


Fig. 3.1 Schematic fault-related pseudotachylyte perpindicular to the slip plane. Fault veins form parallel to slip planes, along which PST are generated. Injection veins shooting off the fault vein impregnate the wallrock with melt, enhancing deformation.

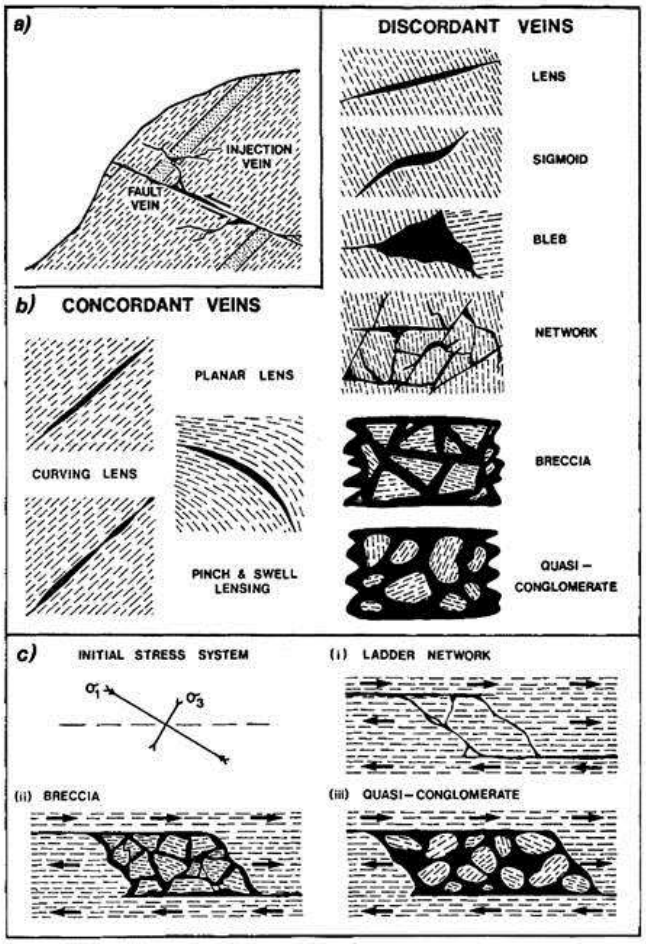


Fig. 3.2 Sketch of PST fault and injection vein relationships. a) General relationship of fault and injection veins. b) Geometry of various PST forms. c) Schematic process of formation of clast-based PST. After Sibson (1975)

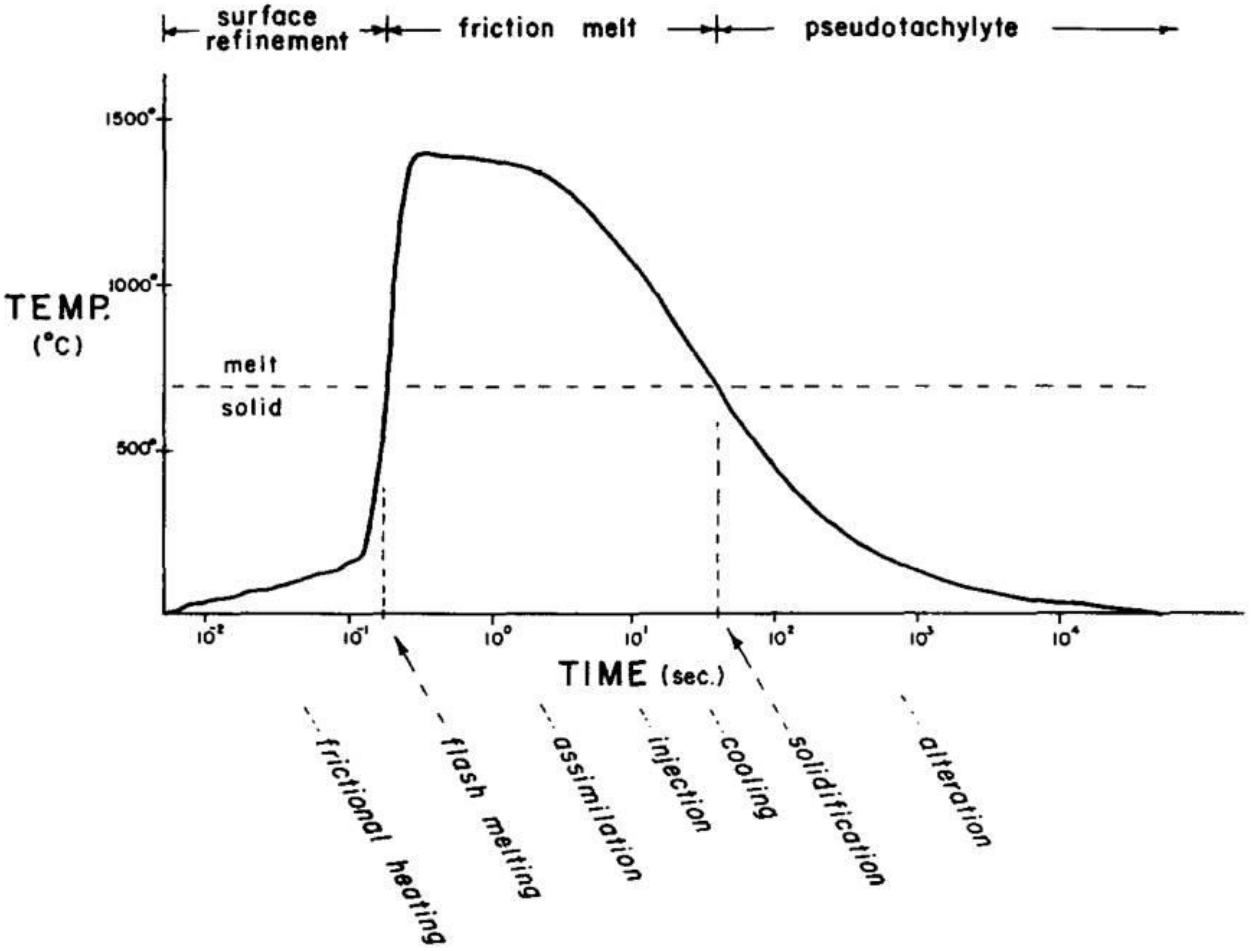


Fig. 3.3 Model of coseismic PST generation in terms of time and temperature. The variation in observed PST can be attributed to different stages of PST development within the fault zone. After Swanson (1992)

3.3 Rheological controls deformation along the fault plane

It is debated whether PST are the products of ultra-comminution or fusion, and whether they can be directly linked to earthquake generation and seismicity (Di Toro et al., 2009, 2005; Pec et al., 2012; Wenk, 1978). The confirmation of the presence of truly amorphous glass is the principal proof of this debate. However, while glass appears to have been identified in many pseudotachylytes by several independent methods (Electron-backscatter diffraction, high resolution (sub-nanometre) X-ray diffraction, transmission electron microscopy, micro-Raman and cathodoluminescence, these results have recently been disputed (Pec et al., 2012). The basis of the dispute is that, at the limit of the resolution of the instruments used in these studies, the signal of the PST groundmass/glass appears

similarly homogeneous, making it impossible to distinguish between a glass and an utltra-comminuted groundmass (Wenk, 1978; Zhang et al., 2004). Microtextural and mineralogical analyses of PST and their surrounding wallrock have been used to infer the production, at some point during deformation, of a melt, in association with positive adiabatic thermal excursions of more than 1000 ˚C (typically beyond the melting point of wallrock minerals). Thermal degradation of minerals in the fault plane, and the formation of melt/vapour vesicules and high temperature microlites have also been used to corroborate that PST are the products of frictional melting (Andersen and Austrheim, 2006; Andersen et al., 2008; Di Toro and Pennacchioni, 2004; Di Toro et al., 2009; Lin, 1994a, 1994b; Spray, 1992; Swanson, 1992). Based on previous work and the mineralogical and microtextural observations made on the PST discussed in this thesis, I propose that these results indicate the presence of a melt phase associated with PST generation and that PST are coseismic features representing paleo-earthquakes (Di Toro et al., 2009; John et al., 2009; Lin, 1994a; Magloughlin and Spray, 1992; Sibson, 1975; Spray, 1992).

3.3.1 The brittle-ductile transition

The brittle-ductile transition marks the depth limit of a material's ability to fracture and the onset of ductile flow. Rocks are generally polymineralic, silicates, comprising assemblages of minerals in different amounts, so the brittle-ductile transition for a rock is partly controlled by the flow (creep) laws of its constituent minerals (Handy, 1990). The formation of PST appears to be intrinsically linked to brittle-ductile transition zones where stress and strain are strongly partitioned based on the proportion of minerals in the hostrock, their shape and distribution (Hobbs et al., 1986; Kim et al., 2010; Swanson, 1992, 1992), to induce frictional melting (Magloughlin and Spray, 1992; Spray, 2010; Swanson, 1992).

It is important to note that frictional melting is a disequilibrium adiabatic phenomenon that occurs over brief periods of microseconds to seconds (Sibson, 1977b; Spray, 2010). Hence, modelling based on equilibrium isothermal partial melting of rocks cannot be used to infer the controls on how PST

are formed (Spray, 2010). PST formation under high pressure should be inhibited because the crystal-plastic deformation that produces frictional melting and seismic failure is predicted to become more ductile with depth, as background heat in the subducting slab and confining pressure increase (Figs. 8 and 9) (Abers et al., 2013; Hobbs et al., 1986). Owing to these effects the flow laws of the toughest minerals in the rock are overcome and ultimately ductile flow predominates (Fig. 3.7) (Hacker and Christie, 1990; Handy, 1990; Niemeijer et al., 2012). PST are most commonly found in felsic, crustal rocks where the main mineral constituents are feldspar and quartz (Sibson and Toy, 2006). The rheology of these two minerals will in part control the way the rock deforms under increasing pressures, temperatures and strain rates (Spray, 2010). Quartz and feldspar undergo brittle-ductile transitions at ~ 12 and 18 km depth, respectively, with a brittle-ductile transition in the bulk rock between the two depth limits (Fig. 3.4) (Swanson, 1992). The Corsican PST are hosted by metagabbro and peridotite, mafic and ultramafic rocks that are essentially dominated by olivine and pyroxene and plagioclase to differing degrees (Andersen et al., 2014; Andersen and Austrheim, 2006; Austrheim and Andersen, 2004). Olivine, the strongest of these minerals, undergoes brittle-ductile transition (for a dunite) at about ~ 30 km depth, implying that all things being equal, as olivine, pyroxene content decreases in the rock, its brittle-ductile transition will become shallower (Handy, 1990; Spray, 2010; Swanson, 1992). Hence, PST formation in olivine/pyroxene-rich rocks is expected at greater depths than for felsic rocks (Fig. 3.4). In cold subduction environments with steep geotherms, such as the Corsican Alpine complex, where the PST are proposed to form at 1.5 – 2.6 GPa, low background temperatures (< 500 ˚C), slow diffusion kinetics, inhibiting ductile flow, ultimately causing the slab to behave more rigidly at greater depths (Scholz, 2002). Slow diffusion kinetics in the slab also enable the persistence of metastable minerals below their stability limits (Austrheim and Andersen, 2004; Green, 1995; Hacker et al., 2004).

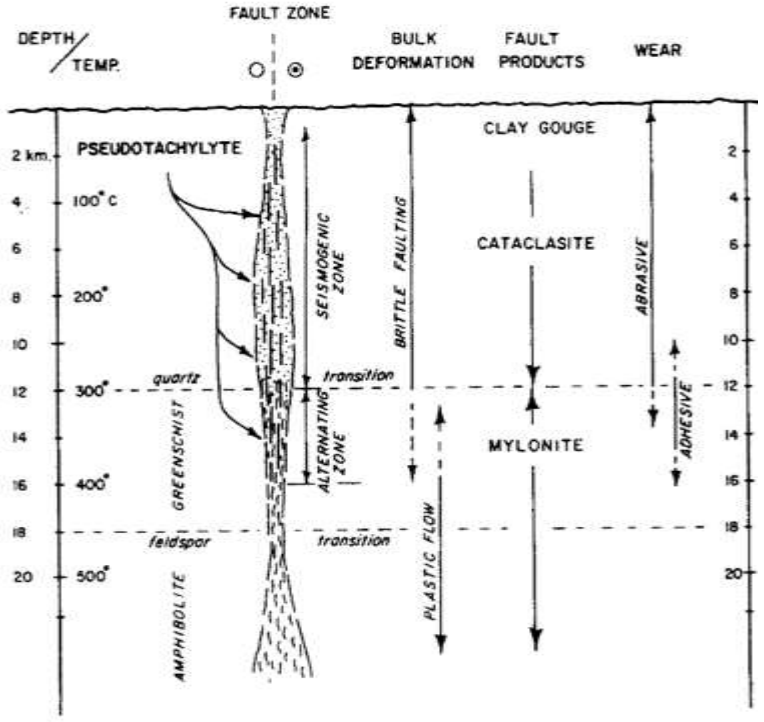


Fig. 3.4 Conceptual depth profile of the quartz brittle-ductile transition in the seismogeneic zone, illustrating the change in deformation and wear mechanisms with increasing pressure. After Swanson (1992)

As the products of frictional melting and comminution, PST are commonly associated with mylonites and cataclasites (Camacho et al., 2001; Dijkstra et al., 2004; Fabbri et al., 2000; Hacker and Christie, 1990; Hobbs et al., 1986; John et al., 2009; Swanson, 1992). These can be syndeformational or indirectly related to the PST forming event (Bestmann et al., 2011; Hobbs et al., 1986; John et al., 2009; Kim et al., 2010; Pec et al., 2012). Syndeformational mylonites and cataclasites are useful indicators of the thermal and stress-strain regime surrounding the period of PST generation, giving clues as to the conditions leading up to their formation (Figs. 3.5 and 3.6).

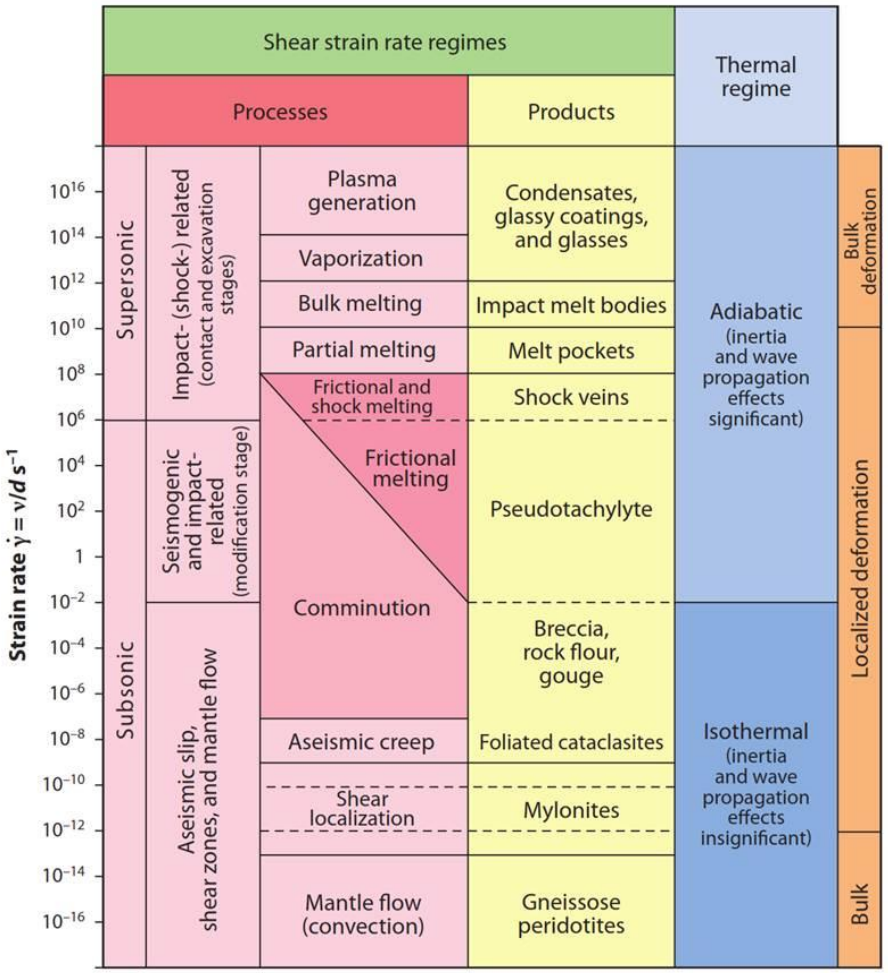


Fig. 3.5 Deformation regime of rocks by strain rate (ẏ), as experimentally determined using ceramics. v = velocity, d = displacement. After Spray (2010)

3.3.2 Comminution and cataclasite

Apart from frictional melting, PST are also intimately associated with cataclasite, gouge and breccia (Sibson, 1975). It is important to understand how these deformational morphologies arise in order to be able to comprehend their relative roles and limitations on generating intermediate-depth seismicity (Handy, 1990; Hobbs et al., 1986; Spray, 2010; Wenk, 1978).

Comminution is an isochemical process by which a solid material is crushed and ground to form smaller particles (Spray, 2010). Typical products of comminution are rock flour, gouge and cataclasite and breccia (Spray, 2010). It is important to note that cataclasite is not synonymous with comminution, as it involves the transformation of the ground up material into a cohesive body

(Spray, 2010). Cementation of comminuted particles may change the grain morphology, texture and composition of the comminuted material, and may not be isochemical (external fluids/melt may have entered the system) (Spray, 2010). The process of comminution results in a particle-size distribution of a highest number of small fragments, an intermediate number of medium fragments and a low number of large fragments (Johnston and McCaffrey, 1996; Spray, 2010; Wenk, 1978). The particle-size distribution is controlled by a fractal, power law relationship, meaning that the distribution is insensitive to grain size and has distinct grain size populations (Johnston and McCaffrey, 1996). However, this relationship breaks down where particle size is << 1 μm, the comminution limit (Spray, 2010). Below this limit the fractal relationship of comminution breaks down for several possible reasons:

1) A critical size limit of particles is reached, whereby particles begin to cushion each other, absorbing compressive and shear stresses, impeding further fracturing.
2) At this limit, particles begin to deform plastically and fracture nucleation is inhibited.
3) The finest particle fraction undergoes agglomeration, producing larger particles. This process may also overprint the original textures in the smallest size fraction.
4) Under conditions of high strain rates and adiabatic heating, fusion of the small size fraction may occur. This is due to the exponential increase in surface area, with decreasing size, as well as heat generated due to viscoelastic deformation.

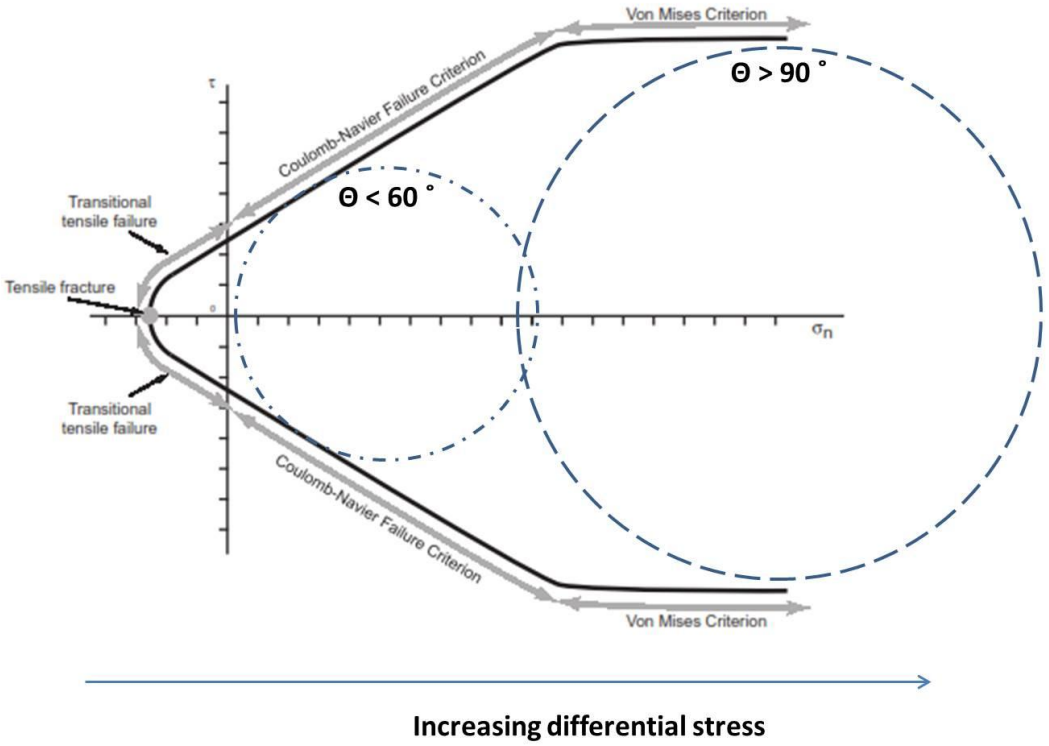


Fig. 3.6 Sketch of a failure envelope illustrating two cases: 1) the Mohr circle touches the failure envelope along the Coulomb-Navier Criterion, where brittle failure will proceed. This case is limited by faulting at a maximum of 30 ˚ (θ = 60 ˚) to σ_1. 2) the Mohr circle touches the failure envelope at the Von Mises Criterion, where ductile failure will occur, forming a shear zone at 45 ˚ to σ_1. As differential stress controls the diameter of the Mohr circles, the greater the differential stress exerted on a rock package the greater the angle of failure relative to σ_1. This moves the circle from left to right, changing the deformation regime from brittle to ductile.

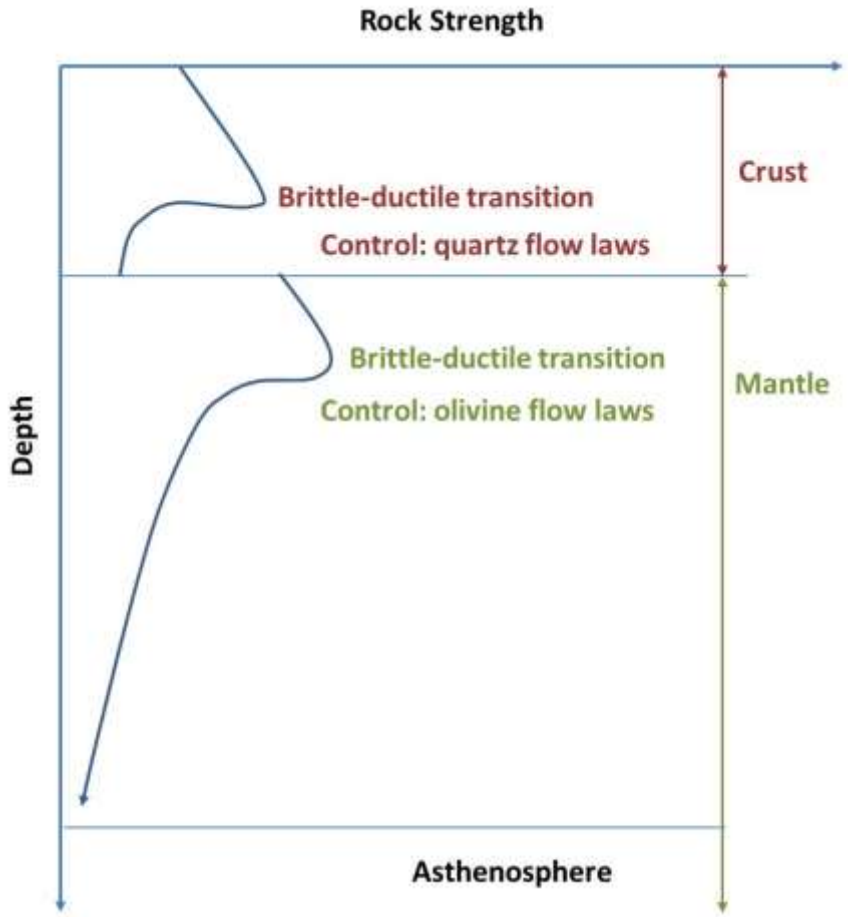


Fig. 3.7 Simplified rock strength profile as controlled by quartz and olivine flow laws, in the crust and mantle respectively. After Regenauer-Lieb et al. (2006).

This is particularly relevant for understanding and modelling PST generation under high pressures via shear localisation, where deformation via comminution and dislocation creep have not been fully considered and grain sizes modelled are ~ 10 µm or not considered at all (John et al., 2009; Kelemen and Hirth, 2007). These studies assume such processes to be inhibited by high confining pressures, favouring stress and strain accommodation by grain-size dependent diffusion creep (John et al., 2009; Kelemen and Hirth, 2007; Ogawa, 1987). However, multiple field examples of high pressure PST show that comminution has taken place (Angiboust et al., 2012; Austrheim and Boundy, 1994; Deseta et al., 2014).

Comminution, and therefore the formation of cataclastites, is controlled by the rheological characteristics (bulk yield strength, shear yield strength, fracture toughness, thermal conductivity and background temperature) arising from the compositions and distributions of participating rocks and minerals, and the stress/strain conditions acting on them (Spray, 2010).

3.3.3 Fracture toughness:

Fracture toughness is the measure of a material's resistance to fracturing. It can be represented by the following equation: $Kc = \sqrt{EGc}$,

Strain intensity factor = $\sqrt{EGc}$,

E = Young's modulus (stress/strain)

Gc = Critical fracture energy

In the case of fast fractures (typically used as an engineering term for catastrophic crack propagation and failure), which exhibit time-dependent strain rates, such as those associated with PST development (Sibson, 1977b; Spray, 1992; Swanson, 1992; Scholz, 2006), stress intensity may be a dynamic factor in fracturing rocks, possibly pulsing through the damage zone. Kc is stress instensity under static

stress intensities and may underestimate the stress intensity factor in natural fracture systems (Spray, 2010).

Critical toughness varies across different material types, with chemical bonding exerting a principal control (Spray, 2010). Natural silicate lattice structures typically comprise covalent (SiO_2), ionic (Fe_2O_3) and ionocovalent (Mg_2SiO_4) bonding combined with van Der Waals forces (phyllosilicates), in order of decreasing toughness (Fig. 3.8). The ordered structure of silicates induces localisation of electrons within specific sites in the lattice structure. This 'pinning' of electrons in the lattice inhibits movement to accommodate strain, causing temperature to rise within the crystal lattice and facilitating dislocation movement (Spray, 2010). This is in contrast to metallic bonding in metals and alloys, in which electrons reside in a delocalised, but interconnected state, increasing their yield strength to above that of most silicates. A comparison of the rheological properties of natural silicates is given in Fig. 3.8.

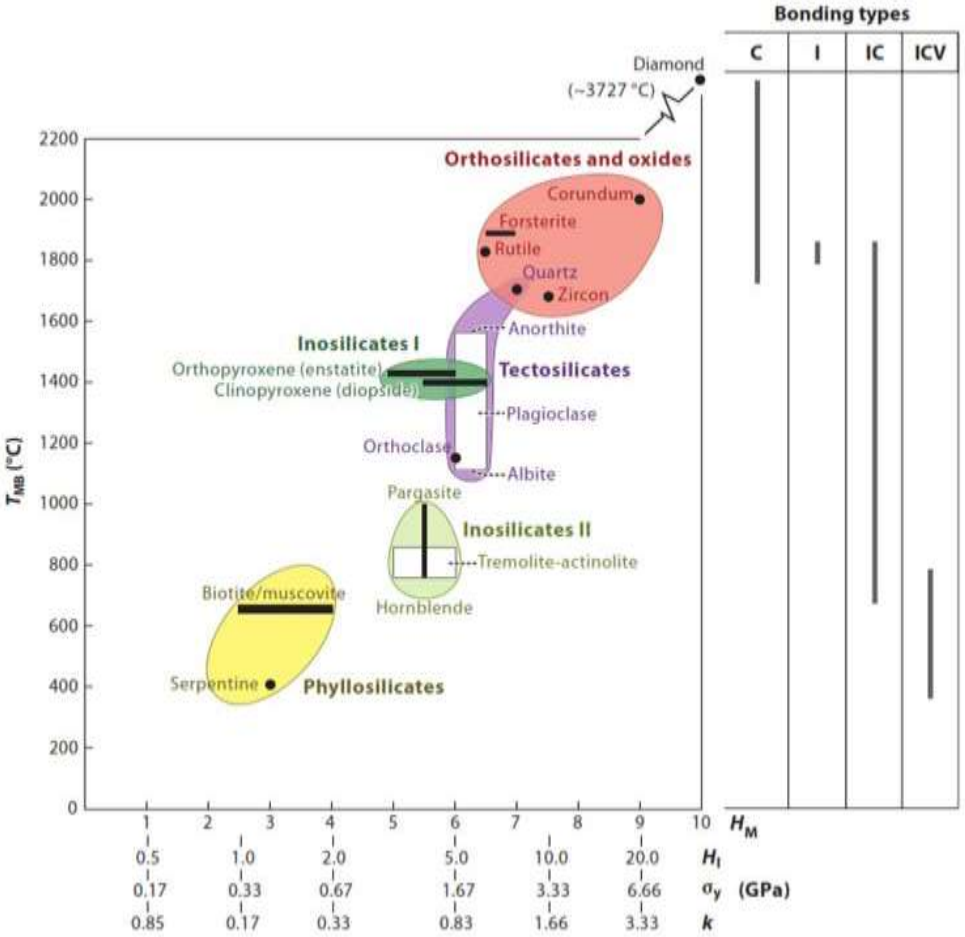


Fig. 3.8 Estimated melting/breaking temperatures for various minerals according to Moh's hardness (H_M). Indentation hardness (H_I), yield stress (σ_Y) and shear yield stress are also indicated. After Spray (2010)

There is a broad positive relationship between fracture toughness and melting/breaking temperature, controlled by bond type and strength. As a result, the relative competencies and abundances of different minerals will influence the response of the bulk rock to stress and strain (Handy, 1990). Silicates have compressive strengths ~ 8 times that of their tensile strengths (Spray, 2010). Owing to this, fracturing generally occurs in the tensile regime, even under compression, localised areas of tension, or relatively lower compressive stress will preferentially form mode I microcracks (Green, 1995; Spray, 2010). Metals however, inhibit crack-tip propagation by strain hardening, forming a zone of plastic deformation that concentrates the strain and induces failure by

ductile flow followed by brittle failure at increasing strain rates (Braeck and Podladchikov, 2007; Spray, 2010). Metallic alloys and minerals with high thermal conductivities do not show any relationships between melting/breaking temperatures, bulk yield strength, shear yield strength and fracture toughness. The fracture strength of silicates is different due to their lower thermal conductivities but ranges from oxides (e.g. magnetite) to orthosilicates (e.g. olivine), Mg- Fe inosilicates (e.g. orthopyroxene) to tectosilicates (e.g. plagioclase), to Ca-Na inosilicates (e.g. diopisde), to double-chain inosilicates (e.g. actinolite), to phyllosilicates and sorosilicates (e.g. muscovite and epidote), (Spray, 2010). In silicates, the influence of vacancies and substitutions on fracture strength is not well constrained, varying up to 20 - 25 ˚C (Spray, 2010). The fracture strength of polycrystalline rocks is virtually temperature independent at low temperatures (25 – 600 ˚C) (Sibson, 1977b; Spray, 1992). Above the 600 ˚C limit the crack tip (of a nucleating slip zone) exhibits plastic behaviour and fracture toughness at that point starts to increase. When temperatures proximal to the crack tip reach 40 – 50 % of the melting points of minerals involved, deformation of individual mineral species is controlled by fracture toughness (controlled by bond strength, type and melting point) (Spray, 2010). The influence of pressure and temperature in crack-tip propagation appears to be secondary to strain rate. At seismic strain rates (> 10^{-2} s^{-1}) fast fracturing (catastrophic fault propagation) is the process that dominates the mechanical response of minerals, even at high temperatures (Spray, 2010). However, the relationship between fast fracturing and strain rate is not well constrained. For long periods of time (> 50 μs) fracture toughness is found to be insensitive to time (Spray, 2010). If this is the case then it implies that if fast fracturing is what causes the generation of PST then lubrication of the fault plane to allow for seismic failure must occur at exceedingly short time scales (< 50 μs) (Spray, 2010). With increasing confining pressure, the bulk fracture toughness of polycrystalline rocks increases, but this has yet to be proven at the individual mineral scale (Spray, 2010).

Under high strain rate deformation conditions resulting in adiabatic heating, a mineral that has a low thermal conductivity will preferentially incur intragranular stresses, subsequently exerting stress onto

contiguous minerals (Spray, 1992). Exponentially increasing strain rate and temperature can easily induce fracturing and melting in such minerals. The combination of high strain rates and consequently high temperatures of resulting melt (> 1000 ˚C), facilitates melting of tougher, more refractory minerals (Sibson, 1977a, 1977b, 1975; Spray, 1992). If the rate of temperature increase is great enough, thermal shocking can result in decrepitation and spalling of clasts (Sibson, 1975). This thermally-dependent break-down can be caused by inter- and intra-granular differential thermal expansion, dehydration of intragranular volatiles and fluid inclusions (Sibson, 1975).

3.3.4 Intracrystalline deformation: creep

Deformation in rocks ultimately comes down to deformation occurring at the granular or sub-granular scale and is controlled by the rheological nature of the deforming material (Handy, 1990; Passchier and Trouw, 2005; Spray, 2010).

At the intragranular scale, deformation within clasts is expressed via two principal mechanisms, dislocation creep and diffusion creep (Passchier and Trouw, 2005). Dislocation creep is manifested as defects in the crystal lattice, *point defects*, singular atoms or molecules (interstitials) and vacancies, and *dislocations*, linear connections of lattice defects within the crystal. Dislocations occur within two end-member types, edge and screw (Davis and Reynolds, 1996; Passchier and Trouw, 2005). *Edge dislocations* are due to the uneven protrusion of individual lattice walls along crystal walls (Fig. 3.9). *Screw dislocations* arise when part of the crystal is displaced relative to another part, distorting the crystal lattice. When dislocations become connected dislocation loops can form (Passchier and Trouw, 2005). Dislocations do not necessarily run continuously throughout the crystal lattice, their propagation can be interrupted by fractures separating them from pieces of undeformed or misoriented crystal lattice. Dislocations are sites of unequilibrated, relatively high energy in the crystal lattice, formed in response to imposed stress and strain (Fig. 3.9) (Passchier and Trouw, 2005).

During a single deformation event, the formation of dislocations and their obliteration occur simultaneously, competing with each other as principal deformation mechanisms. As these forces wane and the diffusion kinetics of the mineral allow the crystal to return to equilibrium, rearrangement in the crystal lattice dominates, reducing dislocations, and moving toward a more stable state of lower internal energy (Davis and Reynolds, 1996; Passchier and Trouw, 2005). Diffusion creep in materials is a type of solid-state deformation, where strain and stress are accommodated by atomic transfer within the crystal lattice by grain-scale diffusive mass transfer (Davis and Reynolds, 1996; Passchier and Trouw, 2005). It typically occurs at lower strain rates, but higher background temperatures to dislocation creep and is grain-size dependent. This process can occur statically or as an evolution under dynamic stress/strain conditions (dynamic recrystallisation). This is manifested as the migration of defects or vacancies within the crystal lattice and is achieved by Coble or Nabarro-Herring creep (Davis and Reynolds, 1996, 1996). Coble creep operates via the migration of defects along grain boundaries, whereas Nabarro-Herring creep exploits internal lattice defects. The strain rate arising in a deforming material is thought to be dependent on the type of deformation mechanism it deforms by (Passchier and Trouw, 2005). It seems that grain size of a deforming rock controls whether diffusion or dislocation creep will predominate, a type of comminution limit (Spray, 2010).

Observed manners of grain recovery in rocks are: grain boundary migration, bulging and subgrain rotation. Grain boundary migration results from the syndeformational clustering of dislocations at grain boundaries (Passchier and Trouw, 2005). When two neighbouring grains are undergoing deformation, dislocations gathered at grain boundaries will move from the boundary or region of a grain with a higher dislocation density (higher internal lattice energy) to a region with a lower dislocation density (lower lattice energy, therefore more stable), or (Passchier and Trouw, 2005). Grain boundary migration involves recovery along the entire grain surface. This is different to bulging, which exhibits localised grain boundary migration, causing a part of one grain's boundary to intergrow, or bulge, into that of another. Bulging occurs at lower temperatures than grain boundary migration (Passchier and Trouw, 2005).

Subgrain rotation occurs when the dislocations within lattices of grains collect via climb in such a way as to break the crystal up into domains (Davis and Reynolds, 1996, 1996). This can occur to such an extent that grain domains will become disparate, forming a cluster of separate grains with different orientations to one another (Fig. 3.10). During the syndeformational evolution of subgrains, such domains can develop collective orientations (lattice preferred orientation, crystallographic preferred orientation and domain preferred orientation) in response to the stress conditions under which they are forming (Fig. 3.10). Petrographically this is shown by textures such as undulose extinction, chessboard, inter- and intragrain fabrics (Fig. 3.10).

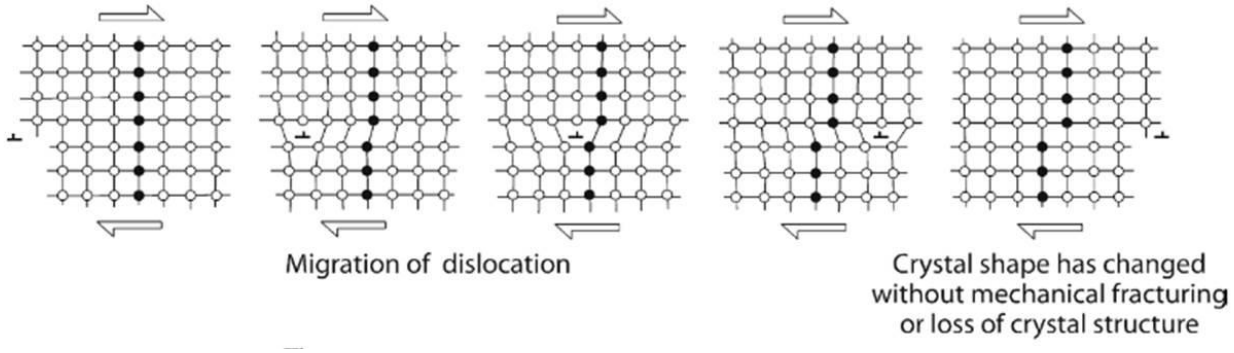


Fig.3.9 Conceptual sketch showing the relative displacement in crystal due to the migration of an edge dislocation (black dots) within the crystal lattice (white dots). Edge dislocation seen normal to displacement direction. After Passchier and Trouw (2005)

Another type of creep, known as Peierl's mechanism, occurs specifically when rocks are deformed at low background temperatures (Kameyama et al., 1999). The migration of dislocations occurs due to thermal activation of dislocations under stress. In particular, this mechanism of deformation is less sensitive to temperature and more sensitive to stress than power law creep (Branlund et al., 2000). This mechanism is relevant to the research on the Corsican PST, as coseismic deformation in these rocks had low initial temperatures (~ 420 ˚C) and power law creep as a potential initial deformation mechanism may have facilitated shear localisation and heating to allow for dislocation glide and climb to take place (Kameyama et al., 1999).

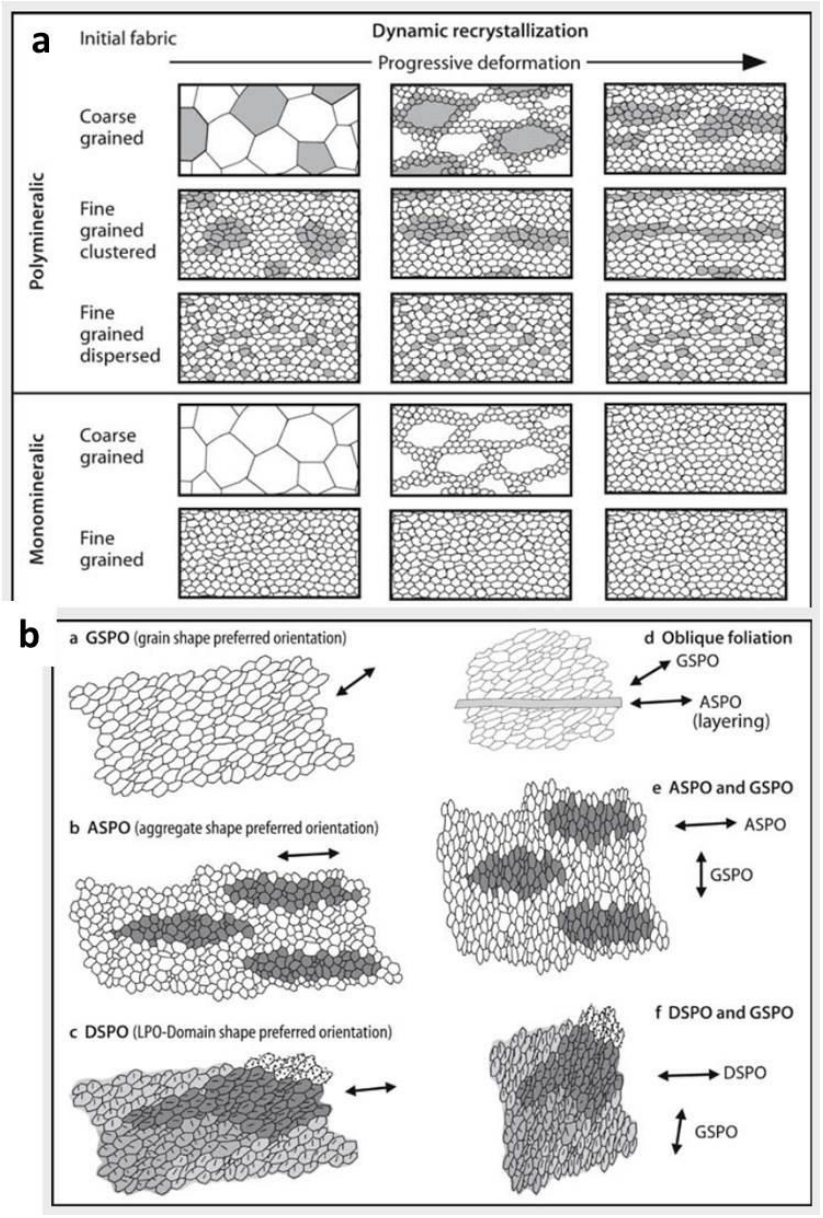


Fig.3.10 Sketches illustrating the appearance of dynamic crystallisation in monomineralic and polymineralic rocks (a). b)Various types and cominations of dynamic subgrain development (*a – f*) in rocks. After Passchier and Trouw (2005).

3.3.5 Transition from comminution to frictional melting:

Frictional melting associated with fracturing can occur in three ways in natural rocks:

1. Fast fracturing of an intact rock to produce a new slip plane (typically a shallow feature)

2. Fracturing and failure along a pre-existing slip plane.

3. Ductile flow and fracture resulting from increasing strain rate and temperature that form localised shear zones along which melting can take place.

All three types can be present within the same fault zone, overprinting one another or occurring in different places along a common slip plane. They can arise as syndeformational features or from distinct events that are unrelated (Sibson, 1975, 1980b; Spray, 1992, 2010).

With regard to slip initiation, the mechanical behaviour minerals is initially controlled by the relationship between yield strength, shear yield strength and melting/breaking temperature (Spray, 2010). This relationship controls the onset of creep (crystal plastic deformation by diffusion or dislocation creep) in different minerals along the slip plane (Spray, 2010). However, at seismic strain rates, fast fracturing overtakes flow and/or exploitation of a pre-existing fracture, inducing comminution (Spray, 2010). Under such conditions fracture toughness is the principal control on deformation in the system. Minerals in the slip plane with the lowest fracture toughness will be ground up preferentially. With increased comminution, possibly beyond the comminution limit, the resistance of these minerals to form fractures increases due to elastic and plastic deformation and their surface areas will increase by a power relation, increasing frictional heating exponentially (Sibson, 1977a, 1975; Spray, 1992; Swanson, 1992). The resulting localised rise in temperature will cause the hot and fine size fraction to fuse, forming a friction melt (PST). It will also facilitate crystal-plastic deformation as the movement of crystal dislocations is thermally activated (Green, 1995). If this process occurs adiabatically, the frictional heat will not be able to escape the slip zone and will increase, and likely go beyond, the melting/breaking limit of the toughest and most refractory minerals in the hostrock (Spray, 2010). If ‘soft’ minerals (phyllosilicates and amphiboles) are present in the hostrock they will fuse preferentially, and consequently enrich the melt in their components (Spray, 1992). Tougher minerals that withstand the initial comminution process will only fuse once they come into contact with melt, forming the greater portion of survivor clasts (e.g. quartz and plagioclase in felsic PST), hence the melt is likely to be depleted in their components (Spray, 1992). Owing to the two different mechanistic controls in forming frictional melt along slip planes, a large

contrast in fracture toughness in the mineral assemblage in the host rocks is likely to result in bulk PST compositions skewed towards 'softer' minerals. If the fracture toughness of the host minerals is comparable then the bulk PST composition will be similar to that of the bulk rock (as shown in Figs. 8.10 – 8.13, Deseta et al. (2014) submitted).

High speed laboratory simulations testing the deformation of polymineralic rocks under seismic strain rates indicate that comminution and fusion in polycrystalline rocks occurs in cycles according to the relative fracture toughness of each mineral in the hostrock, i.e., the softest mineral will comminute first and melt first, followed by the second softest mineral comminuting and melting and so on, until the slip plane is lubricated enough to form a fault (Del Gaudio et al., 2009; Spray, 1992). Consequently, seismic frictional melting and faulting is controlled by the softest mineral, in the highest abundance in the hostrock, i.e., failure in a granite with: quartz > plagioclase > orthoclase > muscovite, will be controlled by feldspars. This is because, while muscovite melts first, as the least abundant mineral, the melt produced might not be sufficient to lubricate the slip zone (Spray, 1992). Therefore, the feldspars as the most abundant and second weakest minerals will control ultimate slip plane lubrication and failure. Unfortunately, to date, no relevant high strain rate experiments of mafic/ultramafic rocks under high pressure have been done.

3.4 *Current models of high pressure pseudotachylyte formation*

To date there are several models of how high pressure pseudotachylytes might form, all of which are based on thermally-activated shear instabilities (John et al., 2009; Kelemen & Hirth, 2007; Ogawa, 1987; Orowan, 1960; Warren & Hirth, 2006). Each model has its own prerequisites and thermal equations; only the general principles of thermal shear instabilities (TSI) will be covered here. TSI is a process by which localised viscous deformation, accompanied by high temperatures, occurs in a visco-elastic material that has been subjected to high stresses (Braeck and Podladchikov 2007). In this Corsican case study the visco-elastic materials would be the metagabbro and

peridotite host rocks of the pseudotachylytes. Localized shear heating caused by increasing strain rates in the seismogenic zone induces a localized reduction in viscosity within the hostrock. The locally reduced viscosity in turn feeds back positively and non-linearly on strain rate and temperature; this feedback may result in a massive release of elastic energy stored in the surrounding rock (or any visco-elastic material), inducing failure (Figs. 3.10 and 3.11) (Braeck and Podladchikov, 2007; Kelemen and Hirth, 2007).

If thermal runaway takes place, the associated strain rates will increase exponentially, increasing the temperature of the fault zone proportionately. Such high strain rates may be sufficiently great to induce seismicity (Figs. 3.5, 3.10, 3.11) (John et al., 2009; Kelemen and Hirth, 2007). At such strain rates the temperature increases too rapidly to be diffused away from the shear zone and the shear instabilities become self-localising (Braeck and Podladchikov 2007; Rice,2006). Owing to the fact that heat can only be transferred out of the shear zone by diffusion, this implies that the peak temperatures are located in the centre of the shear band. The decreasing viscosity of the narrow heated shear zone, as heating increases exponentially, generates a positive feed-back effect (and self-localising), keeping the shear band narrow (Braeck & Podladchikov, 2007; John et al.,2009; Kelemen & Hirth, 2007).

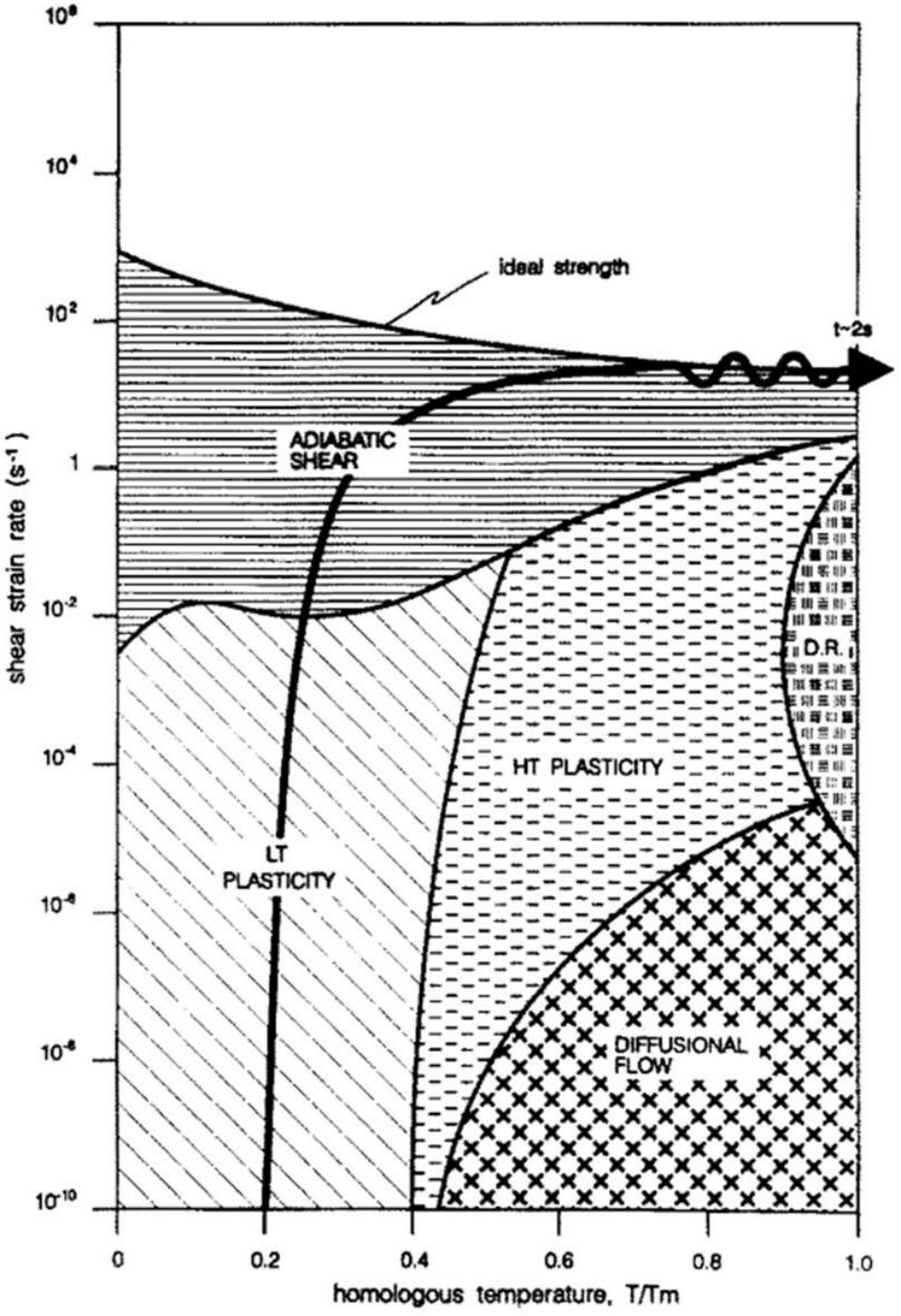


Fig. 3.11 Strain rate vs temperature deformation map for natural ceramics. The arrow indicates a possible strain rate-temperature-time path for coseismic failure and possibly similar to the path of PST formation for Corsican PST. Tm = melting/breaking temperature. After Spray (1992)

Recent experimental research and numerical modeling of TSI processes suggest that, as rocks are heterogeneous materials, the stress imposed will be concentrated in minute domains where the effective viscosity in the rock is locally greatly decreased and acts as a strain concentrator (Kelemen and Hirth, 2007; John et al., 2009, Bestman et al., 2011). Preferential shear heating will take place in these low viscosity zones, resulting in a positive feedback effect, where an exponentially increasing strain rate and temperature will take place, resulting in increasing strain rate, failure, comminution and melting (Fig. 3.11) (Kelemen and Hirth, 2007; John et al., 2009). The perturbations in rheology that result in local viscosity lows are thought to be either reduced grain size and/or the presence of hydrous minerals such as antigorite, chlorite or muscovite (Hacker, 2004; Kelemen and Hirth, 2007; John et al., 2009, Bestman et al., 2011). With regard to the hydrous minerals, it should be noted that, in the case of thermal shear instabilities (TSI), it is their mechanical properties at high pressure that cause the rocks to weaken, not the release of free water. The eclogite facies pseudotachylytes hosted by the Kråkeneset metagabbro, (western Norway) have been suggested as a natural example of SLTR (John et al., 2009). The Kråkenest PST-fault veins occur in domains of the host rock metagabbro where there is a marked decrease in grain size and a relatively high degree of hydration reflected by the presence of phengite, clinozoisite ± amphiboles (Austrheim et al., 1997; Lund and Austrheim, 2003; John et al., 2009).

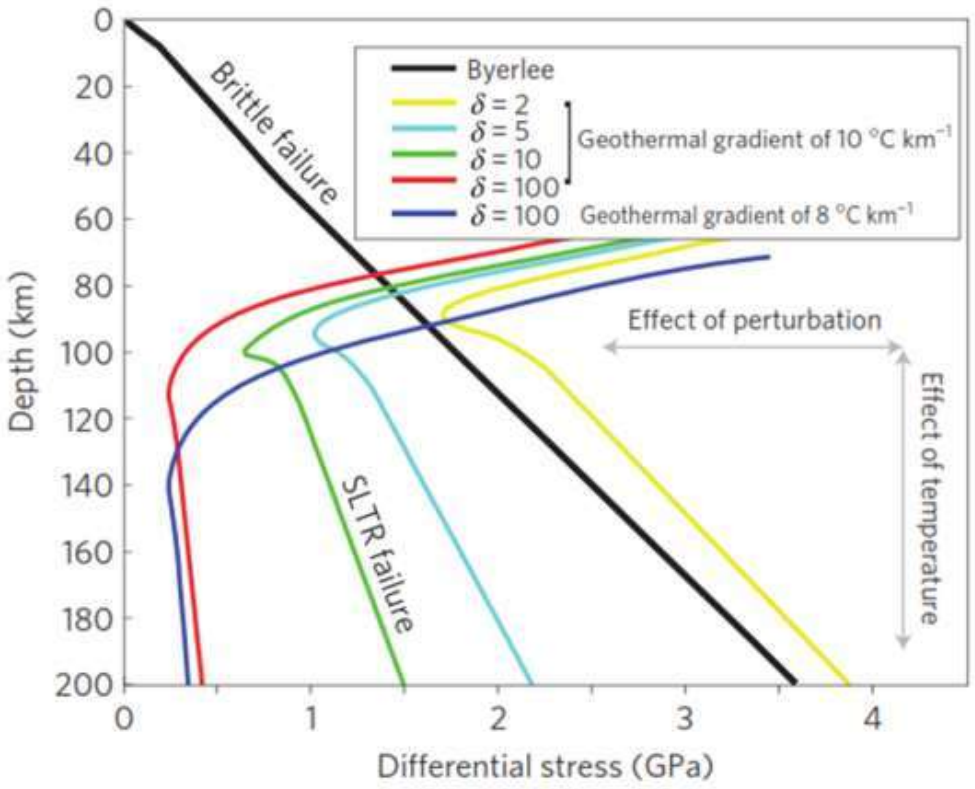


Fig. 3.12 Graph based on numerical modelling derived from the Kråkeneset HP-LT case study illustrating that rock failure at increasing depths is more likely to occur by self-localising thermal runaway (SLTR) rather than brittle failure, as can occur at lower differential stresses. δ represents the viscosity contrast between the host rock and a pre-existing weakness in the rock, e.g. layer of phyllosilicates. Various viscosity values tested are indicated by the different colours. John et al. (2009) found that < 1 % reduction in effective viscosity is sufficient to initiate thermal runaway (Fig. 15 and 16). This equates to a 1 mm thick zone of weakness in the host rock.The model lines cross-cut brittle failure at ~ 80 km; at depths greater than this the model predicts failure by SLTR to predominate. After John et al. (2009)

3.5 Seismiscity and pseudotachylytes

3.5.1 Present-day seismicity: current perspectives on intermediate-depth earthquakes

Seismological studies based on present-day seismic events can inform us about the geometry and mechanics of resultant intermediate-depth earthquakes (Dobson et al., 2002; Green, 2003; Hacker et al., 2010, 2004; Kirby et al., 1995, 1996; Mishra and Zhao, 2004; Nakajima et al., 2009a; Reynard et al., 2010). Seismologically, the definition of intermediate-depth earthquakes is variable.

In general, they are large seismic events occurring in subducting slabs at depths between 60 and 300 km, or any event shallower than 300 km that dips downward from the start of the fracture zone in the slab (Hacker et al., 2004; Kirby et al., 1995). Seismicity typically decreases exponentially below 70 km towards a zone of quiescence between 150 and 300 km (Scholz, 2002). Intermediate-depth earthquakes have fewer seismic aftershocks relative to shallow and deep earthquakes (Green, 1995; Hacker et al., 2004; Houston, 2007). Intermediate-depth earthquakes are identified in planar regions of low seismic velocity that delimit the upper and lower core of the subducting slab and dip approximately 45 ˚ into the mantle (Houston, 2007). Tomographic modelling suggests that the upper seismic plane comprises metastable blueschist facies meta- basalt and gabbro under eclogite facies conditions (Fig. 3.12) (Hacker et al., 2010, 2004). The lower seismic plane is indicated to comprise partially hydrated peridotite and possibly free water or melt (Abers et al., 2013; Dobson et al., 2002; Hacker et al., 2010, 2004; Nakajima et al., 2009a; Reynard et al., 2010; Rondenay et al., 2008). Owing to the temporal and spatial relationship (Fig. 3.13) between hydrated slabs, ntermediate-depth seismicity, and the relationship between partial melting of hydrated slab/mantle wedge, the thermally activated dehydration of hydrous minerals (dehydration embrittlement) in the warming slab has been posited as the ultimate cause of seismic failure (Barcheck et al., 2012, 2012; Dobson et al., 2002; Green, 2007, 2003; Hacker et al., 2004; Jung et al., 2004; Mishra and Zhao, 2004; Yamasaki and Tetsuzo, 2003). Transformational faulting associated with thermal relaxation of the subducting slab as it subducts beyond the stability limit of its constituent hydrous minerals, has also been suggested as a possible mechanism for intermediate-depth seismicity (Hacker et al., 2004; Kirby et al., 1995, 1991, 1996). However, reaction kinetics in warming slabs have been shown to be too sluggish to initiate faulting, causing this mechanism to fall into disfavour (Hacker et al., 2004).

Self-localising thermal shear instabilities were also presented as a possible model for intermediate-depth seismicity (Orowan, 1960), but a paucity of experimental and field data kept it from being considered a viable failure mechanism. Recent studies suggest that the seismic signature of intermediate-depth earthquakes indicates a higher temperature mechanism than that predicted by dehydration embrittlement (Abers et al., 2013; Nakajima et al., 2009a; Prieto et al., 2013; Reynard et al., 2010). Prieto et al. (2013) show that seismicity occurs with a local 600 ˚C to 1000 ˚C increase in temperature, which is likely to be too hot for dehydration embrittlement as hydrous minerals will deform plastically and/or melt at such temperatures rather than dehydrate (Boland and Tullis, 1986; Hacker and Christie, 1990; Hobbs et al., 1986; Jin et al., 1998). Reynard et al. (2012) show that low velocity anomalies associated with the lower seismic plane do not reflect the hydrous V_p/V_s signature of antigorite, but rather partially hydrated peridotite. As a result of these new seismic data, field and experimental data, the hypothesis of thermal shear instabilities has been resuscitated (Hacker et al., 2004; Kelemen and Hirth, 2007; John et al. 2009).

3.5.2 Paleoseismicity

Owing to the great depths at which intermediate-depth earthquakes are initiated, there is a limitation of how directly the fault rocks associated with such seismicity can be studied. Analogues or field examples of shallow earthquakes are much more prevalent as they occur closer to the Earth's surface and are exposed more easily. The presence of PST in fault rocks is considered synonymous with ancient seismic failure/faulting (Sibson, 1975).

While the presence of PST may be used as a general rule of thumb of seismicity, it is still a much-debated assumption (Magloughlin and Spray, 1992; Swanson, 1992; Di Toro et al., 2005; Pec et al., 2012).

PST formed under high pressures in subducting slabs are more rare than shallower PST as subducted slabs are not exhumed in their entirety, and are exposed to both pro- and retrograde metamorphism and deformation, which may obfuscate faulting relationships (Abers et al., 2013; Austrheim and Andersen, 2004; Hacker et al., 2004; Sibson and Toy, 2006). As a result there are few known examples of high pressure faulting (Angiboust et al., 2012; Austrheim and Andersen, 2004; Austrheim et al., 1997; Obata and Karato, 1995). However, the high pressure paleo faults defined by the occurrence of PST and/or breccias can be collated with modelling based on seismology of present-day deep events (Abers et al., 2013; Dobson et al., 2002; Nakajima et al., 2009a; Prieto et al., 2013; Reynard et al., 2010).

Cape Corse is an incomparable area for studying intermediate-depth faulting as the pseudotachylytes record paleoseismicity under blueschist- to lawsonite-eclogite facies conditions in both peridotite and metagabbro (Andersen and Austrheim, 2006; Austrheim and Andersen, 2004; Ravna et al., 2010).

3.6 Water in the subducting slab

Water contained in hydrous minerals can be subducted to depths of more than 170 km (stability limit of clinochlore) (Grove et al., 2006). The fusion or dehydration of hydrous minerals at high pressure could reduce the effective stress on the subducting slab and allow brittle failure to initiate at high pressures that would normally inhibit such behaviour (Figs. 3.6 and 3.11) (Green and Houston, 1995). Hacker et al. (2004) showed through the collation of seismic studies of currently active intermediate-depth seismic zones that are currently active, that the hypocentres of intermediate-depth earthquakes coincide with regions of subducting slabs, where regions characterised by high abundances of hydrous minerals are predicted to be located, through geophysical and numerical models (Fig. 17) (Hacker 2003; Jung et al. 2004; Kelemen and Hirth, 2007; Nakajima etal., 2009a). Hacker (2003) confirms the research of previous workers that suggest that dehydration of hydrous minerals

in the subducting slab is the cause of intermediate-depth seismicity (Green & Houston, 1995; Green & Jung, 2005; Green, 2003; Kirby et al., 1991).

The model involving dehydration embrittlement is based on both theoretical and experimental observations that show that rock materials become weak and brittle upon dehydration of their hydrous minerals (Green, 2007; Green, 2003; Raleigh & Paterson, 1965). This process allows brittle failure to initiate at high pressures, where fracturing would typically be inhibited by high confining pressures (> 1 GPa) (Ogawa, 1987; Sibson, 1977, 1980). The weakening of rock has been attributed to the volume change generated by the production of free water and its thermal expansion resulting from the dehydration of minerals such as serpentine and chlorite (Green & Houston, 1995). The increased pore fluid pressure offsets the high confining pressure on the PST host rocks and on the potential fault planes within them, and thereby facilitates brittle failure (Fig. 3.6) (Green, 2003; Jung et al., 2004; Kirby et al., 1991). Due to volume changes induced by mineral dehydration reactions, the cohesive strength of the host rock is reduced, and this also facilitates brittle failure (Jung et al., 2004, Magloughlin and Spray, 1992; Swanson, 1992; Sibson, 1977).

It is important in this study to note that while dehydration embrittlement is largely thought to induce intermediate-depth seismicity, it has never been observed to be associated with PST. In this thesis, paleofaults, as defined by fusion melts of deformed wallrock material are observed and sampled directly (Andersen & Austrheim, 2006; Jin et al., 1998; John et al., 2009). Dehydration embrittlement is a relatively cold (< 700˚C), monomineralic, solid-state reaction, hence, it is a poor fit to explain high pressure, subduction-related pseudotachylytes (Green & Houston, 1995; Green,2007). This is not to suggest that dehydration embrittlement does not occur at all, but rather that it may be limited to areas of the slab that are rich in hydrous minerals, such as serpentinites. The PST studied here are located in the least hydrated lozenges of metagabbro and peridotite (Fig. 2.1). This has two main implications:

1. There may be two types of intermediate-depth earthquake: one that occurs in the rigid, relatively dry blocks in the subducting slab, and one that occurs in most hydrated regions of the slab.

2. The resolution of the studies collated by Hacker et al. (2003) is too poor to distinguish between areas of the slab that simply dehydrate (e.g. serpentinite) and the rigid rock bodies that actually fracture and produce pseudotachylytes and seismicity. Note that the length of the blocks containing pseudtachylytes in this study is < 1.5 km (Fig. 2.4) and the resolution of the seismic studies used in Hacker et al. (2003) does not go lower than 3 - 5 km.

However, the elimination of dehydration embrittlement as a factor in this study does not reduce the impact of the potential role that hydrous minerals can play in the formation of high pressure pseudotachylytes. Rheologically hydrous minerals such as chlorite, serpentine and amphibole are weak relative to the anhydrous minerals that make up the metagabbro and peridotite, so they may act as strain concentrators (John et al., 2009; Spray, 1992). Furthermore, when hydrous minerals fuse into a pseudotachylyte melt, the dissolved water decreases the viscosity of the melt and increases its thermal expansion (Sibson, 1977).

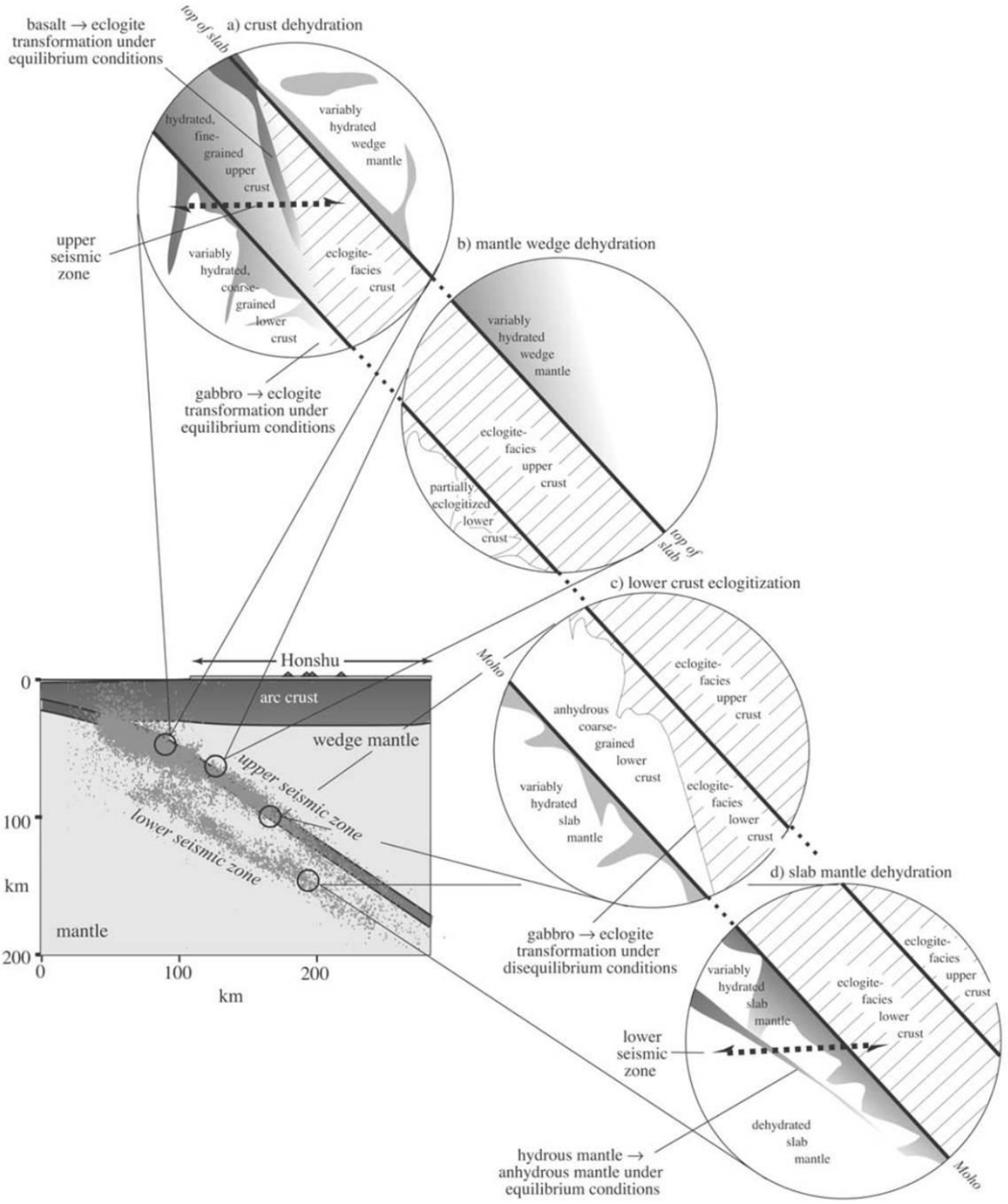


Fig. 3.13 Schematic of subducting crust, with progressive metamorphism of slab rocks from the surface down to eclogite facies conditions. An approximation of slab metamorphism and earthquake hypocentres has been indicated. Not to scale. After Hacker et al. (2004).

3.6.1 Fluids and dehydration

The lawsonite-eclogites and blueschists described in Cape Corse are quite rare, as they are either subducted or overprinted by retrograde metamorphism along the exhumation path as their stability limit is crossed. In order to bring them to the surface intact, steep, rapid exhumation is required. The significance of these rocks in terms of mantle fluid dynamics is that the dehydration of eclogite and blueschist facies minerals is thought to contribute to fluids entering the mantle wedge and the generation of arc magmas as well as possibly intermediate-depth earthquakes (Dobson et al., 2002; Green and Houston, 1995; Hacker, 2003; John et al., 2011; Nakajima et al., 2009b; Ravna et al., 2010). However, it has been shown that the eclogitization process in the subducting slab requires an initial ingress of free fluids generating a chicken-and-egg problem with regard to where and when the fluids enter the system (Figs. 3.13 and 3.14) (Jolivet et al., 2005).

Angiboust et al. (2012) show eclogites in the Monviso ophiolite, Western Alps, which have undergone seismic brecciation due to fluid ingress (Fig. 3.15). Perhaps the dehydration of minerals in the more highly hydrated regions of the slab provides the fluids required for eclogitization and the dehydration of lawsonite-eclogite-blueschists provides further fluids to inititate another stage of intermediate-depth seismicity. If this is the case, the question arises as to whether the fluids produced by the dehydration of low-grade minerals undergo partitioning with some moving through the slab and others moving into the mantle wedge.

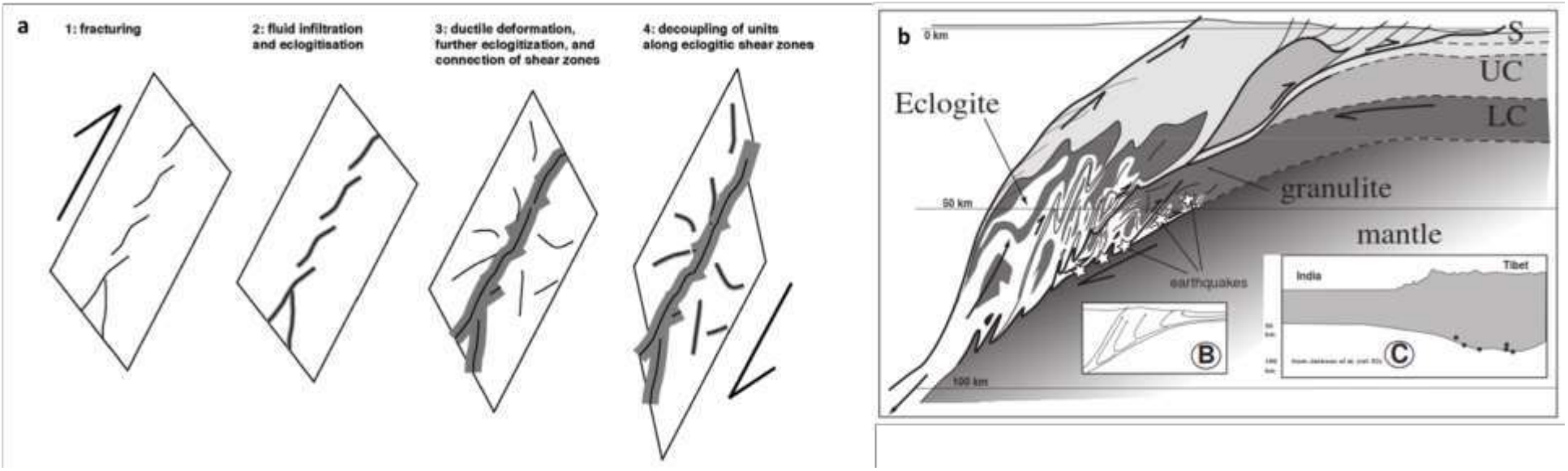


Fig. 3.14 Conceptual model illustrating the manner in which eclogitization takes place, culminating in the formation of eclogite facies shear zones in the Bergen Arc, Norway. a) First fractures form in the granulite host rock, allowing fluid to enter the rock, initiating eclogite mineralization. Eclogite is soft relative the surrounding granulites and this decrease in resistance favours the formation of ductile shear zones in place of the previous fractures. With extensive eclogitization, these shear zones can cause slab detachment and induce exhumation. b) A: Conceptual model of the burial and exhumation of the slab during continental subduction. B: Orientation of rock fabric within the subduction channel. C: Deep earthquake hypocentres in the Himalayan impactogen as another example of continental collision. After Jolivet et al. (2005)

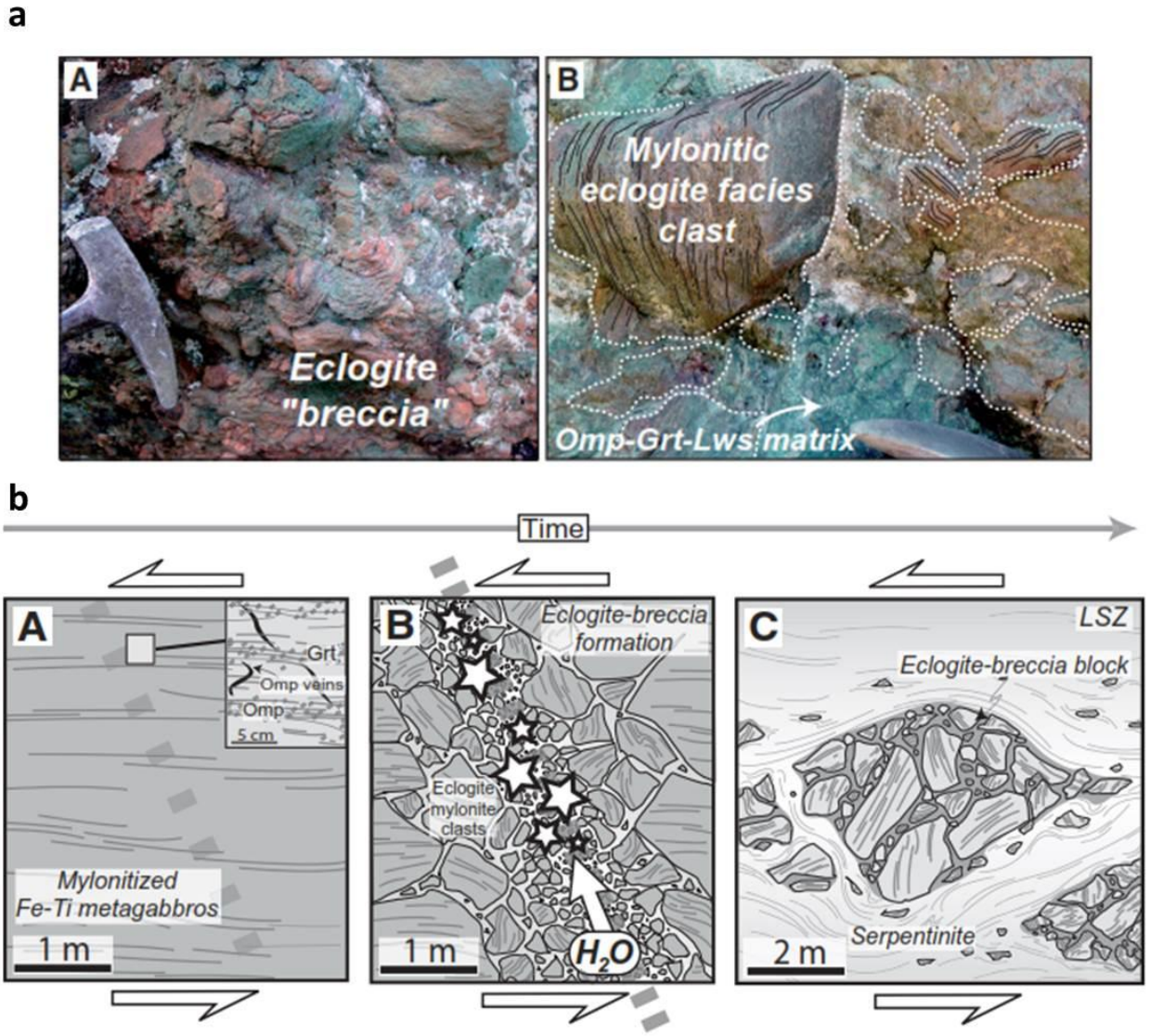


Fig. 3.15 The progressive formation of eclogite breccia in the Monviso Ophiolite, Western Alps, Italy. a) Photographs (A and B) of eclogite breccia enclosed within an Omp-Grt-Laws matrix. A, B and C refer to (b). Illustration of a block of gabbro that has undergone eclogite facies mylonitisation and segregation of garnet- and omphacite-rich zones that are cross-cut by omphacite-rich veins. B: Intermediate-depth earthquake (stars) recorded by eclogite facies brecciation of eclogite mylonite. Blocks of mylonite have been fractured and rotated with the infiltration of fluids derived from outside the shear zone. The white arrow indicates a second generation of omphacite-rich veins between the brecciated segments. C: Sketch of the present- day eclogite breccia enclosed by serpentinite mylonite. The local serpentines do not appear to be the source of the fluids that induced brecciation and the associated seismicity. After Angiboust et al. (2012)

The dehydration of minerals in subducting slabs is a relatively low-temperature process, not likely to exceed 800 ˚C (Green & Houston, 1995; Grove et al., 2006; Kirby et al., 1991). Hence, it does not

seem likely that dehydration could facilitate the formation of these high temperature fusion melts and their associated seismicity. It appears that the generation of intermediate-depth seismicity might not be simple and that it is likely to have multiple mechanisms.

In systems where water is externally-derived from dehydration reactions and expedites the formation of eclogites, 'cold earthquakes' may develop, whereas closed systems with internally derived fluids the formation of high pressure pseudotachylytes may be favoured, generating 'hot earthquakes'(Angiboust et al. 2012; John et al., 2009). This project is primarily focused on hydrous minerals associated with the Corsican high pressure pseudotachylytes and the role they play in generating fusion melts and possible 'hot' intermediate-depth earthquakes.

3.7 Previous work on Corsican PST

The pseudotachylytes (PST) in the Schistes Lustres Complex are present in lenses of peridotite and metagabbro that are surrounded by strongly foliated blueschists, eclogites and serpentinites. The PST occur as fault and injection veins ranging in thickness from < 1 mm - 38 cm (Austrheim and Andersen, 2004). The veins are zoned, comprising glassy to aphanitic chilled margins grading into cores with spherulitic and dendritic textures (Austrheim and Andersen, 2004). Zoned olivine (Fo_{93}-Fo_{89}), orthopyroxene, clinopyroxene and Cr-spinel are the crystallization products from the peridotite-hosted melts (Austrheim and Andersen, 2004). Major element analyses of microlites in peridotite-hosted PST have shown that the compositions of these minerals are indicative of a high temperature of formation (> 1350 ˚C) (Fig. 3.16) (Andersen and Austrheim, 2006). These melts contain micro-vesicles, and could have held up to 4 % water (Andersen and Austrheim, 2006). However, the composition of the fluids in the melt has not been well constrained. Fassaite, glaucophane, pumpellyite, tremolite and chlorite crystallised from the metagabbro-hosted PST (Austrheim & Andersen, 2004). One of the aims of this study was to analyse the crystallisation assemblages of the different

pseudotachylytes in detail to better constrain the conditions under which they formed.

The metagabbro and peridotite PST are located on the same ridge and are thought to have probably formed under similar spatio-temporal conditions, under pressures of 1.6 – 2.8 GPa with ambient slab temperatures of ~ 420 ˚C (Andersen and Austrheim, 2006; Ravna et al., 2010). Austrheim and Andersen (2008) carried out detailed mapping of some of the smaller veins in order to determine small-scale displacement and the volume of peridotite required to melt to produce the local veining, as well as the pressure conditions required. One of their conclusions was that the PST may have formed by localized shear heating, which resulted in a thermal runaway effect to produce these melts (Braeck & Podladchikov, 2007; John et al., 2009; Kelemen & Hirth, 2007; Silkoset, 2013). Major element analysis by electron microprobe of olivine, orthopyroxene and clinopyroxene grains (crystallised from the melt) in the veins and the host rock, and has shown them to be compositionally similar (Andersen and Austrheim 2006). Hence, it was concluded that the parent material of the melts is likely to be similar to their host rocks. Some detailed petrographic descriptions of the veins on the thin section scale were also done (Andersen and Austrheim, 2006).

Systematic whole-rock major and trace element analyses of the PST and the host rock material collated with microstructural features had not yet been done. The new analyses from this study have been collated with those from Andersen and Austrheim (2006) and Austrheim and Andersen (2004) have been used to clarify the amount and style of melting that took place to form these PST.

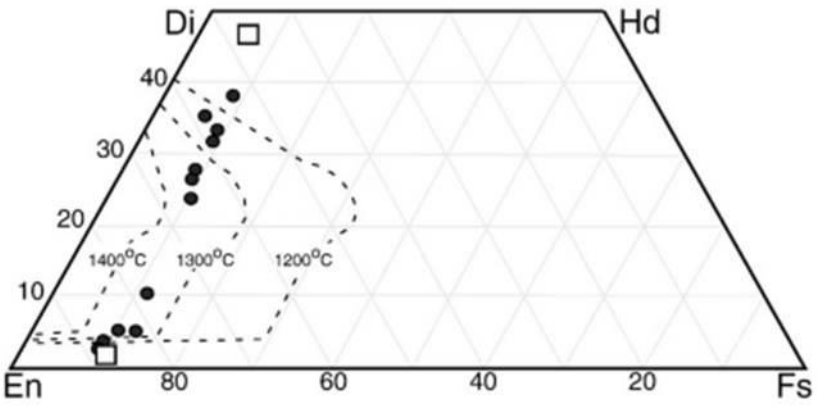


Fig. 3.16 Comparison of pyroxene compositions from peridotite-hosted PST, Cape Corse. White squares are wallrock pyroxenes, black circles are microlite compositions. After Andersen and Austrheim (2006)

4. Aims of study

This project comprises a multi-disciplinary study of the constraints on formation of the Corsican high pressure pseudotachylytes. The geochemical component involves a comprehensive comparison of the pseudotachylytes in the metagabbro and the peridotite and how they compare to the host rock composition. Particular emphasis has been placed on the major and trace element composition of the PST and the minerals within, that can be used to ascertain the mode and extent of melting of the host rock and the mechanisms that initiated it. The influence of fluids in the melting process and degree to which the melts are hydrous are also points of interest, as the presence of hydrous minerals within the host rock may have a predominant influence on the generation of PST. The identification of glass in pseudotachylyte from a metagabbro sample is of great value as the presence of glass indicates undeniably that the PST went through a melt phase. The analysis of this glass in terms of major and trace elements may be particularly useful in understanding the melting processes involved in pseudotachylyte generation.

From a structural perspective, detailed observations of microtextures associated with the pseudotachlytes were made. The purpose of this was to assess the relative stress-strain regime in the PST generation zone. The nature of the grains, in particular their size and form, has been analysed in the host rock immediately adjacent to PST veins. This was done in order to assess if there is a relationship between wallrock grain size and the presence of veins and/or rock strength (Kelemen and Hirth, 2007).

Ultimately, the information gathered from the geochemical and structural analyses has been combined with more recent petrological, geophysical and numerical work on intermediate-depth seismicity to infer a thermal runaway mechanism for the initiation of

high pressure pseudotachylyte generation (John et al., 2009; Reynard et al., 2010; Bestmann et al., 2012; Pec et al. 2012; Silkoset, 2013).

5. Methodology

The research for this study took place from late 2009 to 2013. Initial fieldwork for sample collection and mapping took place in Cape Corse, Corsica, during March 2009, lasting two weeks. The samples were cut for the production of hand specimens and thin sections, and were used for microprobe analyses and comprehensive microstructural and microtextural analysis. Whole rock XRF and ICP-MS analysis were done on the host rock samples at the University of the Witwatersrand.

The microprobe analyses were carried out at the University of Johannesburg and at Oslo University, Norway. XRD synchrotron analysis was performed by Dr. Michael Zolensky at the NASA Johnson Space Center, Houston,Texas.

5.1 Unsuccessful analyses

The original aims of this project involved analysing the timing of PST formation, trace element modelling of fusion melts and detailed microstructural analysis of deformation associated with PST formation. However, for various reasons, not all the proposed methods could be carried out. A summary of unsuccessful analyses follows below:

One of the goals of this project was to analyse the internal structure of thermally degraded clasts in PST using Raman and transmission electron microscopy. Four months were spent doing sample preparation with Prof. Whitcomb at the Microscopy and Microanalysis unit at the University of the Witwatersrand. However, due to the fact that the lab had not yet been set up for geological samples we were unable to produce sufficient samples for analysis. This was mainly due to the soft and brittle nature of the 30 µm thin rock flakes of PST, coupled with the fact that ion-milling had to

be done without the use of a FIB-SEM, as the university had not acquired one yet. The University has now acquired a FEI NOVA FIB-SEM for milling, but it is not fully functional yet.

The Raman study was held back due to the fact that the instrument held by the Wits University Physics department is unable to acquire high resolution (sub-micron) video images, which are necessary for mapping of changes in clast crystallinity. Further, the beam used for Raman is set permanently to blue light (~ 520 nm), for physical and biological analysis. The best beam colour for geological samples is green (~ 780 nm).

^{238}U -^{206}Pb dating of microlites crystallised from the PST had been intended using TIMS (thermal Ionisation mass spectrometry), at the University of Oslo, Norway. However, there were no phases large enough and U-rich enough for analysis. Isotope analysis via isotope dilution was also considered, but once again, microlite size was the limiting factor that prevented analysis, as it was not possible to produce mineral seperates. In any case, due to the cold nature of the Corsican subduction zone, radiogenic dating was not likely to be successful as the ambient temperature of the subduction zone was too cold, inhibiting synmetamorphic transformations in dateable minerals. Previous studies attempting to date preiods of Hercynian metamorphism and deformation in the Schistes Lustres and Tenda Shear Zone have been unsuccessful.

PIXE (Particle-induced Xray emission) analysis was attempted at Ithemba Labs, Gauteng, in order to map the distribution of trace elements in the PST, microlites and proximal regions of fault veins. The data acquired were supposed to have been collated with whole rock ICP-MS data for REE modeling. However, due to the poor live-imaging facilities it was not possible to make the desired element maps at high enough (sub-micron) resolution. The high beam current of the PIXE also destroyed the delicate sample surface, so that the same area could not be studied again using another method.

6. Summary of scientific contributions

This doctoral thesis comprises a multidisciplinary approach of microstructural, petrological and geochemical studies on blueschist facies mafic and ultramafic pseudotachylytes. The main goal of this project was to investigate the style and extent of fusion of the host rocks in producing pseudotachylytes, with the aim of understanding the role that fluids might play in forming them and by association, intermediate-depth earthquakes. This work represents one of the most complete studies characterising pseudotachylytes in detail from the outcrop down to the micron scale. Using detailed microprobe analysis, back-scattered electron imaging, microscopy as well as electron back-scattered diffraction (EBSD), X-Ray Fluorescence (XRF), and Inductively Coupled Plasma Mass Spectrometry (ICPMS), I have tried to cover as many geochemical aspects of the pseudotachylyte-forming process as possible in order to produce a tentative model that suggests a mechanism for the initiation of intermediate-depth seismicity.

My principal contributions to the research on high pressure pseudotachylytes have been divided into two articles. The first is a detailed petrographic and microstructural analysis of both the mafic and ultramafic pseudotachylytes. The second is a detailed geochemical study that investigates and discusses the style of fusion, its extent and the part that hydrous fluids/melts might play in forming these pseudotachylytes.

Manuscript summaries:

6.1 Deseta,N., Andersen, T.B., Ashwal, L. (2014) A weakening mechanism for intermediate - depth seismicity? Detailed petrographic and microtextural observations from blueschist facies pseudotachylytes, Cape Corse, Corsica. Tectonophysics, vol. 610, p.138 - 149.

Indivdual contribution:

Samples analysed were collected by myself during fieldwork in March, 2009 at Cape Corse. All micrographs and BSE images were acquired by myself at the University of the Witwatersrand, University of Johannesburg and the Univeristy of Oslo, Norway. Time was spent on classifying samples based on rock-type, grain size, freshness of PST and identifying fault vs injection veins. This was followed by focusing on certain areas: Undeformed wallrock distal to fault veins, deformed wallrock proximal to fault veins, crystallisation products, bulk matrix, and survivor clasts. Comparisons of the newly collected data with previous work on both natural and experimental PST generation as well as with conceptual models was then carried out.
It was important to break down the observations of each step of PST generation observed in each rock type and describe them in as much detail as possible. By comparing two different rock types, faulted under similar conditions I was able to reduce spurious influences that might be specific to studying only one rock type, and to focus on possible rheological controls. Petrological studies of PST are often not sufficiently complete to evaluate the step-by-step process proposed by numerical models. An important part of this process was determining what petrographic textures would be expected based on previous conceptual models such as thermal run-away, dehydration embrittlement and transformational faulting. No perfect fit to my petrographic and microtextural observations was satisfied by previous work. As a result, I sought out to produce a new model (under the guidance of my supervisors) that was able to bring together previously published observations with my own. The main aim of this study was

to initiate an interdisciplinary dialogue across the disciplines of petrography, numerical modelling and geophysics. This article, its images and discourse are principally my own as the senior author. Suggestions, criticisms and intellectual discussion with my supervisors and co-authors were of course paramount to producing a coherent article.

Article summary:

In order to make meaningful inferences about the mechanism by which high pressure pseudotachylytes are formed, a detailed petrographic and microstructural study of such pseudotachylytes, their wallrocks and microlites was required. The Cape Corse pseudotachylytes, previously determined to have formed at blueschist – to lawsonite – to eclogite facies conditions, are hosted by two different host rock types: a blueschist facies metagabbro and a peridotite. As the two host rocks are spatially and temporally related their corresponding pseudotachylytes likely formed under similar conditions. Therefore, by studying the petrological and microstructural differences and similarities in these fusion melts inferences can be made about the underlying mechanism that generates them. This is one of the first detailed studies using primary data produced by paleo-earthquakes to evaluate the current numerical and geophysical hypotheses on intermediate-depth seismicity.

The results of the study suggest that pseudotachylyte generation was triggered by a thermally activated shear runaway process that is controlled by rheology rather than mineralogy. This is contrary to previously published models proposing dehydration embrittlement or mineral transformational faulting. The documented pseudotachylytes are associated with syndeformational, sheared out, prolate, kinked and twinned wallrock clasts that have been peeled off and entrained into the PST vein as sigmoid survivor clasts. We also noted the presence of unique micro-ultracataclasites at the boundary between the wallrock and fault veins. The ultracataclasites comprise fault gouge, melt and ribbons and stringers of wallrock minerals indicating a subtle

interplay of brittle and ductile deformation. The presence of metastable high temperature crystallisation products in the pseudotachylytes such as hoppers and dendrites of olivine, enstatite and diopside in peridotite-hosted veins, and Al-rich omphacite and Fe-rich anorthite in metagabbro-hosted PST supports the hypothesis of a short-lived high temperature event associated with pseudotachylyte generation. Partial overprinting of these high temperature mineral assemblages by ones indicating lower temperatures, but still high pressures, such as glaucophane, albite and epidote in metagabbro and clinochore, fine-grained granoblastic olivine, enstatite and diopside in peridotite, show a return to low temperature, high pressure ambient conditions (430 ˚C, 1.5 – 2.6 GPa). The pseudotachylyte-generating process is relatively insensitive to grain-size of the host rock and pressure, but strongly dependent on differential stress and temperature. The implication of these relationships is that the mechanism that generates these fusion melts is controlled by power law creep as opposed to diffusion creep, as suggested by previous models (Braeck and Podladchikov, 2007; Kameyama et al., 1999; Kelemen and Hirth, 2007). The observational data compiled from the natural samples in this study corroborate and modify previous hypotheses to inform a new tentative model for high pressure PST generation.

6.2 Initiating intermediate-depth earthquakes: insights from a HP-LT ophiolite from Corsica

Deseta, N., Ashwal, L., Andersen, T.B. (Submitted revision) Intermediate-depth earthquakes: insights from a HP-LT ophiolite from Corsica. Accepted by Lithos

Individual contribution:

As mentioned previously in section 6.1, samples analysed were collected by myself during fieldwork in March, 2009 at Cape Corse. All micrographs and BSE images and microprobe data were acquired by myself at the University of the Witwatersrand, University of Johannesburg and the Univeristy of Oslo, Norway. Sample crushing and preparation and analyses for XRF and ICP-MS data were done at the University of the Witwatersrand. Due to the fact that I could not obtain useable mineral trace element data via PIXE I could not analyse fusion and crystallisation processes using rare earth

element (REE) and ratio/ratio plots as originally intended. Without these data the depth of the study is limited to major element data from EPMA mineral and XRF whole rock analyses. I decided to use loss on ignition (LOI) values from the EPMA and XRF data to estimate H_2O content of hydrous minerals, PST bulk matrix and wallrock analyses. LOI in EPMA can be exaggerated by analytical error, vacancies in hydrous minerals and the Fe2+/Fe3+ ratio assumed in mineral recalculations, the proxy can only be used as an estimate to within ~ 2 wt %. When analysing the PST bulk matrix I focused on the finest-grained, most amorphous representative areas in veins using a broadened beam of 5 – 10 µm. Any EPMA analyses for anhydrous minerals with totals less than 98 wt % were rejected from the dataset. All mineral and bulk matrix EPMA analyses were processed through mineral recalculations in order to facilitate identification and type and degree of stoichiometry. For example, wallrock and survivor clasts of tremolite and chlorite as well as local bulk matrix and glassy melt haloes around survivor clasts were compared. The bulk matrix and glassy halo analyses were found in major element plots (p.f.u) to be clearly non-stoichiometric. Analyses of the microfibrous recrystallised PST matrices were found to be more stoichiometric compared to 'fresher' bulk matrices. This was used as a general assessment for detecting PST matrices that had been recrystallised vs those that were more pristine. I then used Raman spectroscopy on the same PST matrices to confirm the lack of crystallinity in the matrices. Reclassifying microlites in the metagabbro PST from fassaite and edenite (Austrheim and Andersen, 2004) to high Al-omphacite was particularly difficult as the microlites are not large enough to be analysed by petrographic microscopy and the major element compositions among the three minerals are similar. Once run through mineral recalculations, I found that the edenite and fassaite were consistently related in all major element diagrams when recalculated as clinopyroxene.The principal stoichiometric differences between fassaite and omphacite are that fassaite contains more Al, which is tetrahedrally coordinated and has low Na. Omphacite typically has more Na and less Al; however, when it does have Al it is octrahedrally coordinated, i.e. fassaite has a greater Ca-Tschermak component than omphacite and omphacite has a greater Ca-Eskola component (Katayama et al., 2000; Konzett et al., 2007; Smyth, 1980; Zhao et al., 2011). *Prof. Ashwal and I plotted Al vs Na (p.f.u)*

of published fassaite and omphacite compared with our own analyses. We observed a clear trend of our data parallel to published omphacite data, but shifted higher due to higher Al content. There was no relationship between our data and the published fassiate (Deer et al, 1995). This plot led us to conclude that the microlites we had analysed were stoichiometrically akin to omphacite.

After mineral identification and recalculation were completed I broke down the newly collected data into groups according to hostrock type, local outcrop and fault vein vs injection vein. I then subdivided the data according to distal undeformed wallrock, fault vein boundary (+/- ultracataclasite), local PST bulk matrix, local crystallisation products and survivor clasts. Coupled with previous microtextural descriptions (section 6.1) I compared the data with previous work on both natural and experimental PST generation as well as with conceptual models (Bestmann et al., 2011; Branlund et al., 2000; Green and Houston, 1995; Hacker et al., 2010, 2003; John et al., 2009; Jung et al., 2004; Kameyama et al., 1999; Kelemen and Hirth, 2007; Kirby et al., 1991, 1995; Zhang et al., 2004). *The peridotite-hosted PST was of particular interest as it comprises both coarse- and fine-grained examples. The possible role that grain size might play in generating PST is important as it can be used to discern whether diffusion or dislocation creep is the principal influence on fusion and fracturing. In order to do this, detailed BSE and SE imaging of fault vein boundaries was carried out. It was important to break down the observations of each step of PST generation in each rock type and describe them in as much detail as possible. By comparing the results from two different hostrock types (and within them different degrees of hydration) and different grain-sizes within a single rock type, I was able to assess the differences in PST formation in different mineral assemblages, with different amounts of wallrock hydration, different hydrous mineral species and fine and coarse-grain sizes. Petrological studies of PST are often not sufficiently complete to evaluate the step-by-step process proposed by numerical models. An important part of this process was determining what petrographic textures would be expected based on previous conceptual models such as thermal run-away, dehydration embrittlement and transformational faulting. No perfect fit to my petrographic and microtextural observations was satisfied by previous work* (Green and Houston, 1995; John et al.,

2009; Kelemen and Hirth, 2007; Ogawa, 1987). *Under the guidance and suggestions of my supervisors and reviewers, I have proposed my own interpretive model of PST generation. From the results in this study I concluded that the style of high pressure faulting is not that much different from faulting and PST generation at shallower depths, both being controlled primarily by grain-size independent power law creep* (Spray, 1992; Swanson, 1992).*With increasing pressure, temperature and strain rate the limiting factor on brittle failure will be the inter- and intra-granular fracture toughness of the most abundant mineral in the assemblage (in the case of peridotite this is olivine). Facilitating this process is the presence of intracrystalline* H_2O *within anhydrous minerals (inducing hydrolytic weakening) and within hydous minerals, that release* H_2O *and melt when they fuse preferentially* (Bromiley and Keppler, 2004; John et al., 2009; Magloughlin and Spray, 1992; Zhang et al., 2004). *With regard to separating high temperature and low temperature assemblages associated with the quenching and/or recrystallisation of PST, classification in the peridotite-hosted PST was much easier than for the metagabbro-hosted PST. In the peridotite-hosted PST, the crystallisation assemblage of the PST was the same as the annealed neoblasts that succeeded them. In contrast, the metagabbro-hosted PST was initially thought to crystallise/recrystallise fassaite, edenite, plagioclase, albite glaucophane, katophorite and barroisite* (Austrheim and Andersen, 2004). *Plagioclase and fassaite have the highest crystallisation temperatures (~ 1550 ˚C and ~ 1350 ˚C, respectively) followed by the amphiboles (< 600 ˚C)* (Carmen and Gilbert, 1983; Devine and Sigurdsson, 1980; Konzett et al., 2007; Simon and Grossman, 2006; Zhao et al., 2011). *Thermally and texturally the minerals did not all fit into a single paragenesis, which led me to break them down into groups of higher temperature microlites and lower temperature recrystallisation products. The refinement of parageneses was hampered by the paucity of experimental literature on the thermal and barometric stabilities of blue amphiboles and omphacite. Neither of these minerals has been observed before as the products of high temperature fusion. Further, glaucophane has never been properly synthesised experimentally, only mineralogical analogues such as miyashiroite* (Carmen and Gilbert, 1983).

The ambient temperature of the fault zone also appears to influence the brittle-ductile character of different PST (Bestmann et al., 2012; Green & Houston, 1995; Hobbs et al., 1986; Kameyama et al., 1999). *The model produced at the end of the article was based on interpretations I drew in comparison with the model of Bestmann et al. 2012. The aim of this article was to provide a direct study of paleofaults that was sufficiently detailed and complete so that a thorough collation with previous indirect studies of numerical modelling and geophysics could be done. This article, its images and discourse are principally my own as the senior author. Suggestions, criticisms and discussion with my supervisors and co-authors were of course paramount to producing a coherent article.*

Article Summary:

Seismic and numerical modelling studies first noted the potential relationship between intermediate-depth earthquakes and the presence of hydrous minerals and volatile-rich fluids within subducting slabs. This study uses detailed major element analyses, petrography and back-scatter electron (BSE) imaging in order to evaluate whether there is in fact a spatio-temporal relationship between hydrous minerals and fluids and the generation of high pressure pseudotachylytes in subducting slabs, and by extension, of intermediate-depth seismicity. In the Cape Corse PST the wallrocks hosting the pseudotachylytes and the fusion melts themselves contained hydrous minerals in various abundances. BSE imaging, electron microprobe analysis (EPMA) and XRF whole rock analysis of the pseudotachylytes, their constituent glass, microlites and survivor clasts indicate that the hydrous minerals underwent wholesale, preferential fusion due to shear heating. Note that wholesale fusion is disequilibrium fusion and not that same as partial melting. Preferential fusion of hydrous minerals occurs wherever they are present. This is due to their relatively low fracture toughness and significantly lower melting temperature

relative to anhydrous minerals in the assemblage. No evidence of free fluids prior to pseudotachylyte generation was found, nor were any neoblasts formed by prograde dehydration or mineral transformation reactions observed. Water content of bulk pseudotachylyte matrices was found to be heterogeneous, ranging from 0 – 14 wt % H_2O, and was found to be largely controlled by the coarse grain-size (5 – 15 mm) of the wallrock and poor mixing of the melt. Al-rich omphacite microlites were identified in metagabbro-hosted pseudotachylytes after being reclassified from fassaite suggested by Austrheim and Andersen (2004). When recalculated according to the 6-oxygen pyroxene structure these omphacites were found to have significant Ca-Eskola components of up to 25 mol %, indicating an approximate formation temperature of at least 1700 ˚C (Konzett et al., 2007; Smyth, 1980), which is in agreement with the temperature estimate previously obtained from peridotite-hosted pseudotachylytes (Andersen and Austrheim, 2006). Preliminary EBSD analyses of wallrock olivine show them to contain trace amounts of H_2O (Silkoset, 2013). From these data we concluded that in the case of producing intermediate-depth pseudotachylytes, it is likely that intracrystalline H_2O is a fundamental requirement as it induces hydrolytic weakening of wallrock minerals, facilitating the preferential fusion of water-bearing minerals.

6.3 Large subduction earthquakes along the fossil MOHO in Alpine Corsica
Andersen, T.B., Austrheim, H., Deseta, N., Silkoset,P., Ashwal., L. (2014) Large subduction earthquakes along the fossil MOHO in Alpine Corscia. Geology, vol. 42, p. 395 – 398.

Individual contribution:

As third author in this article, my role was to assist in providing background information with regard to micro-scale textures observed and how they might inform larger scale features observed in the field. This article focuses on an area in Cima Di Gratera where metagabbro and peridotite are in contact, delineating a possible paleo-Moho. Proximal to this contact is a wall of peridotite, approximately 2 m high and 3 m wide, containing swarms of PST within a larger fault zone. One of the initial aims of my project was to try to determine what processes led to initiation of seismic-induced fusion in these rocks. Initially, I had thought that dehydration embrittlement was the principal mechanism by which faulting was initiated. However, upon detailed analysis using BSE, SE, EPMA, and petrography I was able to de-convolute the microtextures in the fault rocks and give them an interpretive time-line. The sequence of events involved in generating these high-pressure PST does not fit previous models of dehydration embrittlement and transformational faulting, or a purely ductile shear-heating mechanism (Braeck and Podladchikov, 2007; Green and Houston, 1995; Kelemen and Hirth, 2007). Instead, I refined the model of developing a thermal shear instability based on my observations of crystal plastic behaviour in these fault rocks. It is important to note that the work of Braeck and Podlachikov (2007), on which much of the recent shear-heating modelling is based, provides results on the high strain rate deformation of metallic glasses. At the atomic level, metallic atoms reside in a delocalized sea of electrons; this is in contrast to ceramics and rocks where atomic bonding is ionic or covalent, and electrons are more securely captured in ligand complexes. Consequently, and coupled with the higher thermal conductivity of metallic glasses, metals may deform in a more ductile manner to crystalline rocks at seismic strain rates. Originally localised shear

heating was not specifically ascribed to ductile or brittle deformation (Drury et al., 1991; Jessell and Lister, 1991; Orowan, 1960; Swanson, 1992).

The detailed descriptions of microtextures and petrography reported in this thesis and my manuscripts, allowed me to delineate the process by which fluids were introduced into the seismogenic zone and how they may or may not facilitate faulting. My results clearly indicate that dehydration embrittlement is not directly associated with initiating high pressure faulting in these rocks.This is not to say that dehydration does not take place in the seismogenic zone, only that it is not a principal faulting mechanism and may be more important in generating arc magmas. Previously the literature has paired intermediate-depth seismisicity and the production of arc magmas on the basis of dehydration of intra-slab hydrous minerals. The interpretation of our findings suggests that these processes may be fundamentally separate.

Article Summary:

The third manuscript discusses the occurrence of exceedingly large melting events along the paleo-Moho in the Ligurian Basin. As with previously identified pseudotachylytes, it is assumed that these large melt events are associated with large releases of seismic energy into the surrounding crust and mantle lithosphere. The products of such seismic events are rarely observed in the field, as they are normally subducted. The abrupt release of energy along the paleo-Moho is due to localised shear heating that melted and brecciated the adjacent metagabbro and peridotite wallrocks. The energy required to induce wholesale fusion of metagabbro and peridotite wallrocks is combined with previous estimates of seismic stress releases in the area, and shows that the deformation observed in this area was likely produced by several (less than three) very large earthquakes. These seismic events took place along the paleo-Moho at the lower end of the seismogenic zone (assuming they formed at ~ 80 km depth (Andersen et al., 2008, 1991; Ravna et al., 2010) analogous to present-day subduction at continental margins such as in the Himalayas .

A weakening mechanism for intermediate-depth seismicity? Detailed petrographic and microtextural observations from blueschist facies pseudotachylytes, Cape Corse, Corsica.

Tectonophysics (2014) Vol. 610, p. 138 - 439

N. Deseta[1,*], T.B. Andersen[2], L.D. Ashwal[1]

[1]Department of Geosciences, University of the Witwatersrand, Private Bag 3, 2050, Johannesburg, South Africa.

[2]Department of Geosciences, CEED, University of Oslo, P O Box 1047, Blindern, 0316, Oslo, Norway.

Abstract

Gabbro- and peridotite-hosted pseudotachylytes from the Alpine Schistes Lustres Unit in Corsica, previously determined to have formed at blueschist to - lawsonite – eclogite facies conditions, have been causally linked to the generation of intermediate-depth earthquakes, which occur at depths of 50 – 300 km. Detailed petrographic and microtextural analyses of these pseudotachylytes suggest that their initiation may be controlled by a thermally-activated shear runaway process that is controlled by rheology rather than mineralogy. This is documented by sheared out, prolate, kinked and twinned wallrock clasts that have been peeled off and entrained into the pseudotachylyte vein as sigmoid survivor clasts. The presence of metastable high temperature crystallisation products in the pseudotachylyte, such as hoppers and dendrites of olivine, enstatite and diopside (peridotite) and Al-rich omphacite and Fe-rich anorthite in metagabbro, are suggestive of a short-lived high-temperature event resulting from thermal instability. These high temperature mineral assemblages are overprinted by ones indicating a return to ambient conditions of lower temperatures, but still high pressures: glaucophane, albite and epidote in metagabbro and clinochore; and fine-grained granoblastic olivine, enstatite and diopside in peridotite. The observations from this detailed study of natural samples suggest that intermediate-depth seismicity may be generated by a thermal runaway process.

Keywords: Shear localisation, intermediate-depth earthquakes, pseudotachylyte.

7.1. Introduction

The initiation of intermediate-depth earthquakes has long been a subject of debate. These phenomena occur at depths from 50 km to 350 km, which, due to high confining pressures, preclude traditional brittle failure (Green and Houston, 1995; Hacker et al., 2004; Jung et al., 2004; Ogawa, 1987). In order to address this problem researchers have put forth several hypotheses, which include dehydration embrittlement, transformational faulting and thermal runaway processes. These hypotheses can be divided into brittle - (solid-state dehydration embrittlement and transformational faulting) and crystal-plastic - (shear-heating and thermal runaway) controlled processes. These models are based on experimental, numerical and geophysical modelling, with no field observations and little work on natural samples (Green and Houston, 1995; Hacker et al., 2004; John et al., 2009; Kelemen and Hirth, 2007; Ogawa, 1987). In the past two decades however, several discoveries of high pressure pseudotachylytes associated with intermediate-depth earthquakes have been made (Austrheim and Boundy, 1994, 1994; Jin et al., 1998, 1998; John and Schenk, 2006; Kanamori et al., 1998), providing researchers with natural material with which to evaluate previous models. This paper presents detailed petrographic and microstructural observations of peridotite- and metagabbro-hosted pseudotachylytes associated with subduction zone seismicity, in the Cima di Gratera area of Cap Corse, Corsica. Previous work suggests that faulting and pseudotachylyte generation took place during subduction at blueschist to-lawsonite-eclogite facies conditions under pressures of 1.8 – 2.6 GPa (Andersen and Austrheim, 2006; Ravna et al., 2010; Vitale Brovarone et al., 2011). A detailed discussion on the geochemistry of these rocks and the role that water plays in earthquake generation will be addressed in a separate paper.

7.2. Geological setting

The study area is located on the SSW side of Cima di Gratera, Cape Corse, northern Corsica (Fig. 1). The pseudotachylytes, first described by Austrheim and Andersen (2004), occur within lenses of gabbro and mantle peridotite enclosed by serpentinite (Fig. 2). These rocks form part of the Schistes Lustres Complex (part of the Alpine age high pressure-low temperature subduction complex), and which has been interpreted as either nappes of exhumed Ligurian oceanic lithosphere, which have slivers of crystalline continental material, or hyper-stretched continental lithosphere interleaved with mantle imbricates (Agard et al., 2002; Beccaluva et al., 1977; Jolivet, 1993; Mohn et al., 2009; Vitale Brovarone et al., 2011). This rock package was thrust onto the continental margin of Europe during the Late Cretaceous to Tertiary Periods (Fig. 7.1) (Jolivet, 1993).

The metagabbros are compositionally uniform and encompass a range of igneous textures marked by differences in grain size. Common textures are cumulate layering and the interfingering of irregularly shaped domains of fine- and coarse-grained gabbro. Conversely, the peridotites are relatively uniform in terms of composition, texture and grain size. The pseudotachylyte-bearing fault rocks have been partially metamorphosed to blueschist and greenschist facies only in patches, except within the shear zones where the metamorphic reactions are fully equilibrated. The pseudotachylytes occur within the pristine lenses of gabbro and peridotite that are relatively undeformed and least affected by the regional HP-LT metamorphism (Andersen and Austrheim, 2006).

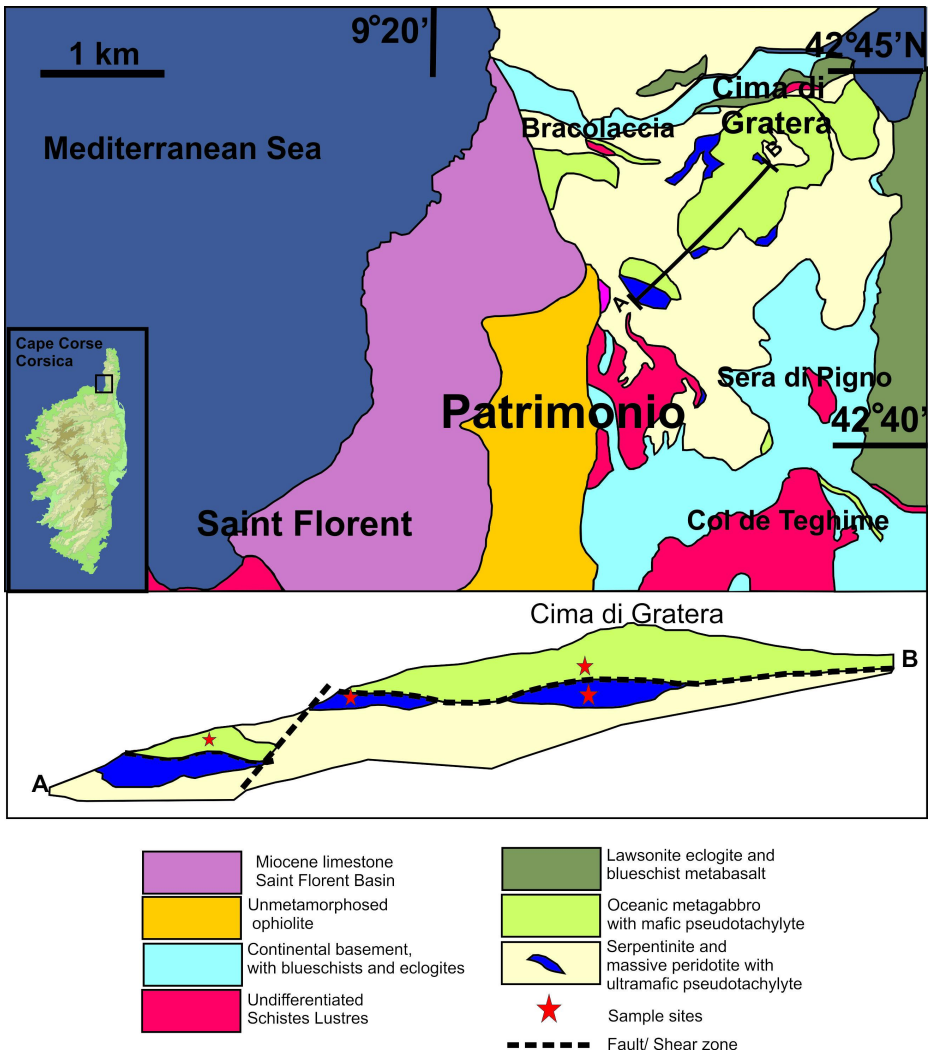


Fig.7.1 Simplified geological map of the study area in Cima di Gratera. Modified after Andersen and Austrheim (2006).



Fig. 7.2 Photographs of pseudotachylyte hosted by peridotite. (a) shows one of the thickest (up to 25 cm) pseudotachylyte fault veins observed in the field. The thickness of this vein is principally due to multiple generations of pseudotachylyte that have nucleated along the same plane. (b) Explosive network veining of pseudotachylytes that radiate in all directions away from the centre of the fault plane. (c) Cross-cutting relationships of pseudotachylyte self-injecting.

7.2.1 Field observations

In outcrop the pseudotachylytes typically have a positive relief with respect to the host rocks. The pseudotachylyte veins weather to a rust-red colour but on fresh surfaces are black-grey and aphanitic (Fig. 7.2). Comminuted wallrock clasts and flow banding are commonly observed. In the peridotite, the pseudotachylytes occur in two sets that extend for up to 1 km: a sub-vertical set and a sub-horizontal set. Within the vein sets the pseudotachylytes form complex vein networks that over-print and re-inject

one another, indicating multiple generations of pseudotachylyte (Fig. 7.2). In the peridotite, the pseudotachylyte veins occasionally form radial 'explosive' networks. These veins are thicker than other injection or fault veins and contain more re-injections and comminuted wallrock material (Fig. 7.2b). In contrast with the peridotite-hosted veins, those in the gabbro are thinner and more discrete, commonly (but not always) occurring along the boundary between the very coarse-grained (< 15 mm) metagabbro and fine-grained (< 2 mm) metagabbro (Fig. 7.2). The peridotite pseudotachylytes show cross-cutting relationships with serpentinised host rocks, which have been entrained into the veins as sigmoidal lozenges, indicating a brittle-ductile overprint relationship. In the metagabbro fault rock, the pseudotachylytic crystallisation products (glaucophane) have formed CPO (crystallographic preferred orientation) fabrics and contain boudinaged wallrock clasts, indicating a ductile overprint post-dating pseudotachylyte generation (Fig. 7.12) (Andersen and Austrheim, 2006). Many of the pseudotachylytes are cut by later serpentine veins and show a hydration overprint. Care was taken to analyse only pristine, unaltered pseudotachylytes.

7.3. Materials and methods

Detailed thin section petrography and back-scatter electron (BSE) imaging for mineral identification and microtextural analysis were done on both gabbro- and peridotite-hosted pseudotachylyte. Electron microprobe analyses were conducted using a Cameca SX-100 instrument at Spectrau Laboratory, University of Johannesburg, South Africa. Analyses of the bulk matrix (wide beam (10 µm) and narrow (1 µm)), wall rock, entrained minerals as well as crystallisation products (glass and crystallites) were done. The beam current was reduced to minimise sodium loss on glass, but tests on higher currents showed loss to be negligible. Analyses were run at 20kV, 10nA. The reference standard used was a Ni-bearing glass. Refer to Merlet (1994) for more detailed operating parameters.

7.4. Petrographic and microtextural observations

Detailed petrographic microtextural analyses were carried out on the pseudotachylyte and the adjacent wallrock in both the metagabbro and peridotite in order to ascertain the rheological behavior of the rock at the time of fusion. Features of the host rocks and microtextures common to both rock types will be discussed in the first section, followed by those characteristic to only the metagabbro or the peridotite.

7.4.1 *Metagabbro host rock*

The metagabbro hostrock is heterogeneous in grain size with large, irregular domains (up to approximately a metre in outcrop) of very coarse-grained (up to 15 mm) gabbro occurring in contact and inter-fingering with a much more fine-grained (~ 1mm) gabbro. The margin between the coarse- and

fine-grained domains is consistently sharp, less than 5 mm thick. Despite the large grain-size variability in the metagabbro, the constituent mineral assemblage is not significantly variable.

The primary gabbro mineralogy is largely preserved and comprises plagioclase, diopside, olivine and minor ilmenite. In thin section the gabbro adjacent to pseudotachylyte faults retains little of its original igneous texture, most of which has been transformed into an annealed granoblastic texture with poikiloblasts of olivine and diopside. Grain boundary migration and dynamic recrystallisation are common, particularly in diopside. Early greenschist facies metamorphism of the hostrock has led to variable replacement and recrystallisation of diopside by actinolite, bastite and Mg-hornblende. Plagioclase alteration to sericite has also taken place, causing the grains to become cloudy and grey. Alteration of the olivine to serpentine, magnetite or iddingsite has also been observed. Post-dating the early greenschist alteration is the development of blueschist facies assemblages, which manifest in the replacement of diopside, actinolite, Mg-hornblende and plagioclase by glaucophane, barroisite, albite and epidote. Late blueschist facies metamorphism that post-dates pseudotachylyte generation at these conditions is associated with ductile deformation and pseudotachylte recrystallisation (Fig. 7.12). Late retrograde metamorphism, particularly marked by serpentine veins and the presence of epidote, clinochlore and pumpellyite overprints the blueschist assemblages phase and patches of the pristine material (Fig. 7.3).

The early greenschist metamorphism of the hostrock may be associated with seafloor hydration and/or hydration-associated fracturing in the slab bend, as well as earlier hydration associated with extensional tectonics (Mohn et al., 2009; Vitale Brovarone et al., 2011). The late greenschist metamorphic overprint has been observed in thin section and BSE images and is interpreted to be associated with hydration and faulting upon slab exhumation. This late retrograde metamorphism overprints some of the pseudotachylyte veins and is not cut by later pseudotachylyte generations (Fig. 7.3).

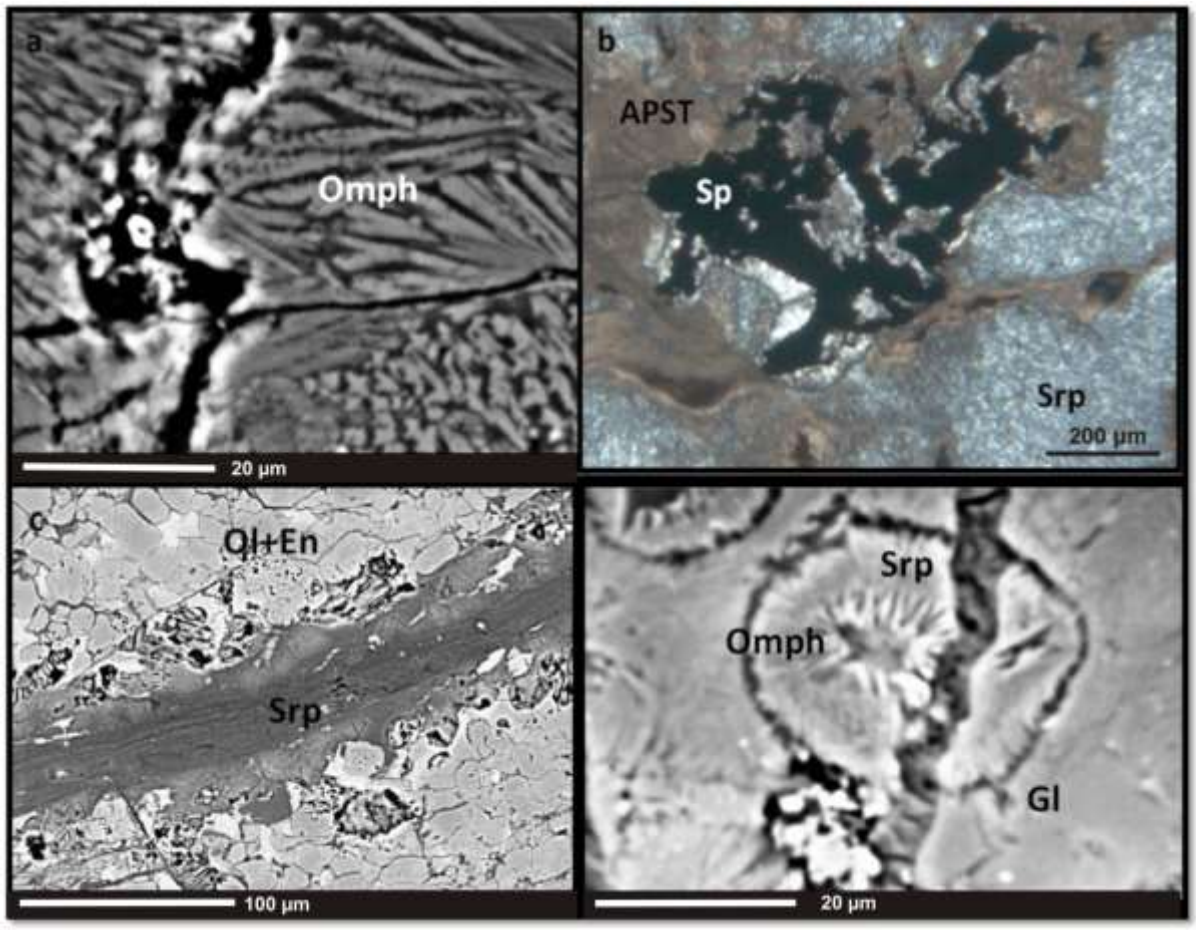


Fig.7.3 BSE images and a photomicrograph (b), of hydrated/altered pseudotachylyte. In all images serpentine and associated spinel is the principal late alteration mineral (as is the case in both host rocks), but late epidote and actinolite are also present in the metagabbro. These images show how serpentinisation destroys the delicate textures associated with the pseudotachylyte forming event (dendrites and vein boundaries) and bleaches the pseudotachylyte, removing magnesium. (a) a black vein crosscuts a pristine pseudotachylyte matrix of omphacite in a metagabbro. The boundaries of the vein can be seen on BSE to have bleached the matrix enriching it in Fe. (b) Serpentinised peridotite pseudotachylyte where all microscopic crystallization textures have been obliterated. (c) A late serpentine vein cuts through a recrystallised peridotite pseudotachylyte. Microfibres of serpentine can be seen eroding the fine-grained granoblastic texture. (d) Serpentine vein crosscutting spherulitic omphacite in an otherwise glassy pseudotachylyte matrix. Ol: olivine, En: enstatite, Srp: serpentine, Omph: omphacite, Gl: glass, Sp: spinel APST: altered pseudotachylyte.

7.4.2 *Peridotite host rock*

The peridotite host rocks show gradational transitions from fine- to coarse-grained (< 1 mm – 7 mm) textures. The mineralogy corresponds to that of a plagioclase lherzolite with olivine > diopside > enstatite, as well as minor plagioclase and magnetite. The rocks exhibit a granoblastic texture with annealed poikiloblasts and some grain boundary migration. The diopside and enstatite commonly show exsolution lamellae of each other and twinning of the diopside and olivine has been observed. There is some early greenschist facies metamorphism of diopside and enstatite to fine-grained clinochlore and tremolite by dynamic recrystallisation. The clinochlore has a plumose and feathery texture. Various generations of serpentinisation (including magnetite and Cr-spinel) overprint all pre-existing features and are variably distributed throughout the rock; occasionally associated with late reactivation of pseudotachylyte veins (Fig. 7.12c). The peridotite shows no blueschist facies mineral assemblages; only multiple stages of early and late greenschist metamorphism are observed prior to and after the period(s) of pseudotachylyte generation. The early greenschist metamorphism has been attributed to events occurring prior to pseudotachylyte generation associated with ocean-continent hyperextension and hydrothermal alteration due to prograde subduction (Vitale Brovarone et al., 2011). The late greenschist facies metamorphism is likely associated with slab exhumation processes.

7.4.3 Fault vein characteristics

Fault veins form parallel to displacement surfaces in the host rock. Wallrock clasts locally underwent crystal plastic deformation in proximity to vein boundaries or melted along/with the fault plane (Fig. 7.4). Microscope- and BSE-based observations of the pseudotachylyte vein boundaries reveal a syndeformational zone in the associated wallrock that begins several grain widths from the vein 'proper'. This region is dominated by highly strained, sheared, kinked, elongate wallrock grains (Figs. 7.4

and 7.7). The vein boundary is sharply cut by the pseudotachylyte and has commonly been observed to be dragged or peeled off into the vein and is surrounded by injecting melt (Fig. 7.4b).

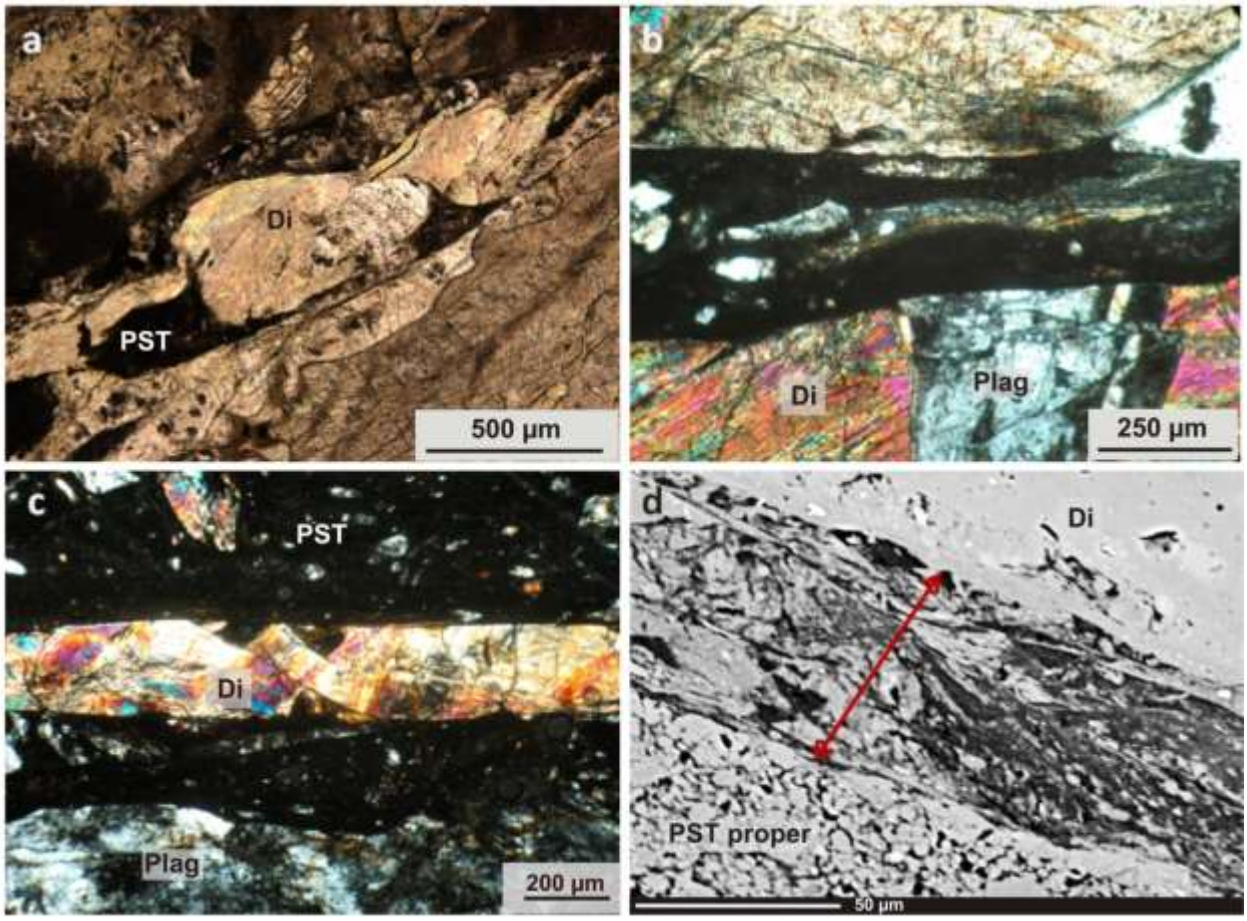


Fig. 7.4 Images of microstructures at fault vein boundaries in metagabbro. All these images clearly show that wallrock material at these boundaries has been subjected to crystal plastic deformation. (a) shows a boudinaged, kink-banded diopside enclosed in a dark brown, glassy pseudotachylyte matrix. (b) Pseudotachylyte vein with entrained, boudinaged, wallrock aggregate of plagioclase and clinopyroxene. The wallrock diopside and plagioclase clearly show kinking and deformation twinning, respectively. (c) A sliver of thermally rounded, prolate and deformed diopside-dominated clast derived from the wallrock has been peeled away by intruding PST and lies within the quenched PST matrix. In the BSE image (d) the red arrow indicates a transition zone of ultracataclasite, melt and minerals ribbons between a wallrock clinopyroxene clast (upper right) and PST proper (lower left). EPMA data show that this transitional zone comprises wallrock clinopyroxene and chlorite.

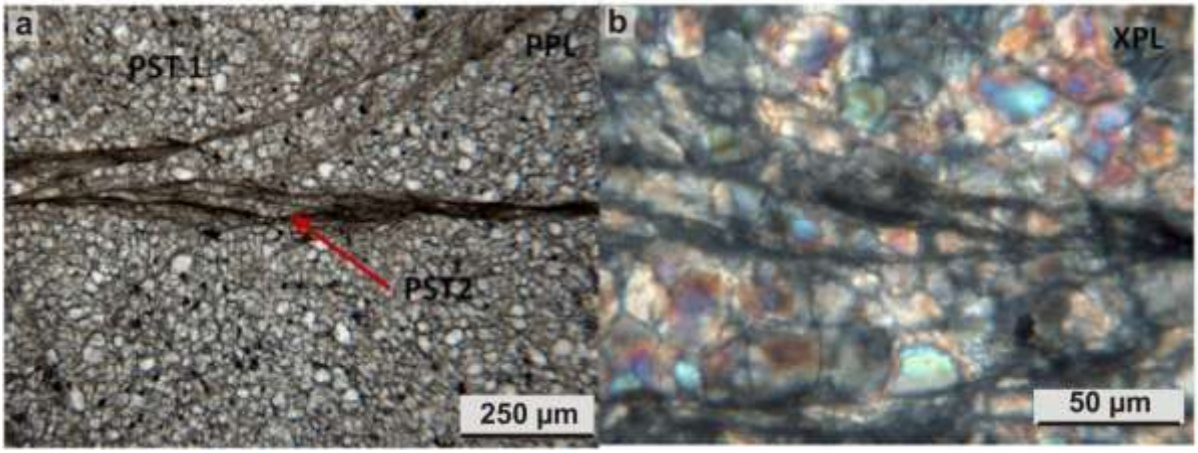


Fig.7.5 Micrographs of fine-grained, recrystallized peridotite-hosted pseudotachylyte (PST 1) cut by later pseudotachylyte (PST 2). (b) is a high magnification view with crossed nicols of where the red arrow is pointing to in (a). In (b) the grains enclosed by the glassy black melt veins are prolate and lozenge-shaped compared to those grains not in contact with PST 2. Grain boundary migration is suggested by the grain boundary alignment of grains enclosed by fault veins. In contrast to the previous figure (Fig. 5), where coarser-grained wallrock was deformed, these photomicrographs show fine-grained recrystallised peridotite-hosted pseudotachylyte cut by a later generation of pseudotachylyte.

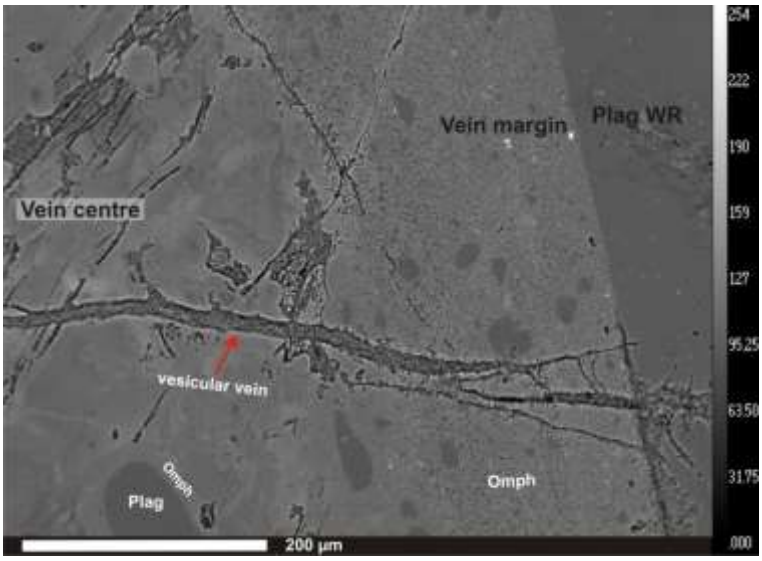


Fig. 7.6 BSE image of a pseudotachylyte fault vein hosted by metagabbro. The dark grey thermally rounded clasts are plagioclase upon which dendrites of omphacite have crystallised with interstitial

glass. The smaller veins cross-cutting the main pseudotachylyte vein in this image, are contemporaneous with the molten pseudotachylyte, as can be seen by the lobate-cuspate boundaries enclosing the dendrites. These cross-cutting veins appear, by their low atomic numbers and low totals (on EPMA analysis) to have contained dissolved hydrous fluids that later vesiculated. Plag: plagioclase, Plag WR: Wallrock Plagioclase, Omph: omphacite

Creep textures associated with the formation of the pseudotachylytes were observed in the full range of grain sizes observed in the wallrock; from 20 mm to 30 µm (Fig. 7.4 and 7.5), from shearing and kinking as seen in the coarser-grained material (Fig. 7.4) to what appears to be grain boundary creep in fine-grained re-crystallised pseudotachylytes that were subsequently reactivated to generate a melt (Fig. 7.5).

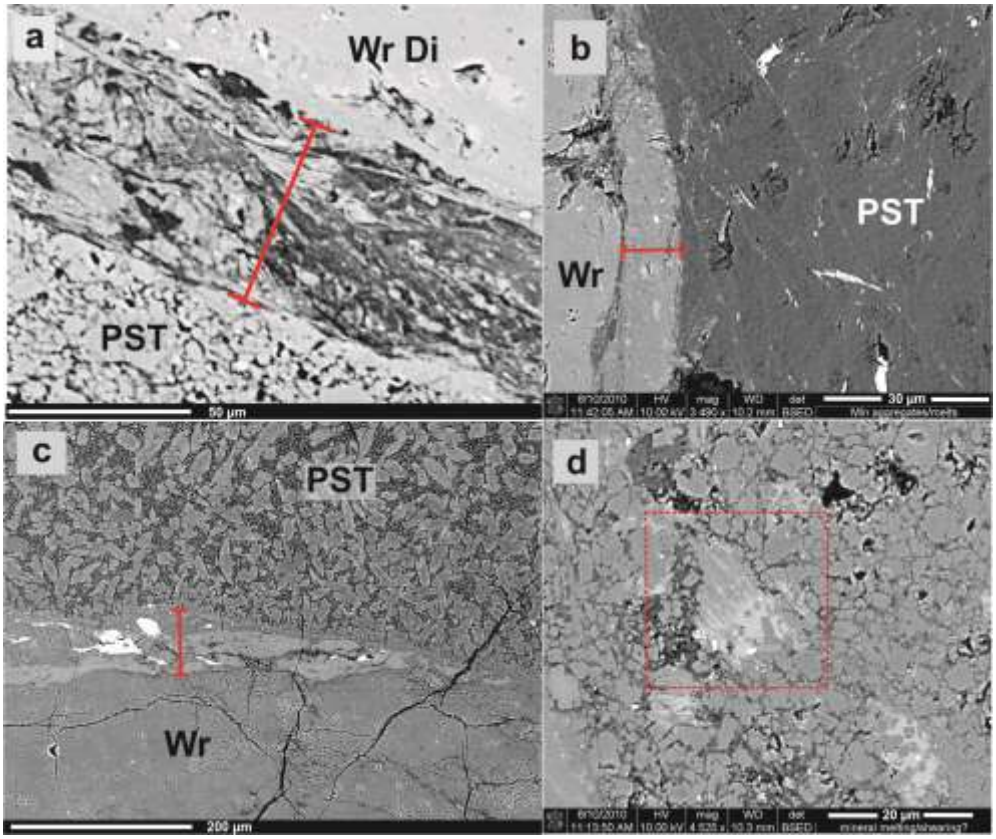


Fig. 7.7 BSE images a – c of ultracataclasites at fault vein boundaries in peridotite. A range of brittle – ductile textures are present in the ultracataclasite, the width of which is shown by the capped red line. a) Close-up of the ultracataclasite; the black areas are an hydrous Al-rich melt, the dark grey areas are a sheared out pseudotachylyte matrix, and the lighter grey is a combinations of sheared out survivor clasts of wallrock diopside and pseudotachylyte matrix . Image d) shows a pseudotachylyte matrix

crystallising olivine (grey) and diopside (light grey) in a hydrous matrix (dark grey). The red box encloses an olivine-diopside crystal complex being sheared out prior to total solidification indicating continued displacement along fault veins post melt production and failure. c) Shows a similar feature; brittle-looking ultracataclasites with a matrix hosting ribbons of stretched out diopside microlites (in white). Wr: Wallrock, Wr Di: Wallrock diopside grain.

The thickness of fault veins ranges from less than 1 mm to more than 30 cm. Fault veins were typically formed by a single event. However, reactivation and multiple fusion events are exemplified by older pseudotachylyte survivor clasts entrained into younger veins (Fig. 7.4 and 7.5) and by cross-cutting relations. The lack of offset markers as well as the injection of melt into dilational fractures precludes the determination of the true dimensions of the fault zone during a single pseudotachylyte-forming event. However, due to the pristine nature of the pseudotachylyte matrices studied, we have concluded that no significant post- pseudotachylyte vein deformation occurred.

7.4.4 Injection vein characteristics

The injection veins are secondary pseudotachylyte veins that emanate from parent fault veins into the adjacent wallrock. Injection veins cannot in all instances be traced to their sourcing fault vein. This is due to chaotic networks of nearby multiple injection veins in proximity and arching self-injections that cross-cut one another. The veins vary widely in thickness, ranging from 200 μm, thinner than the average fault vein, to > 20 cm, thicker than the average fault vein. They inject at all angles from their parent veins, from near-parallel to perpendicular. They cut between and through wallrock grains and are not associated with or dependent on precursory wallrock deformation or foliations.

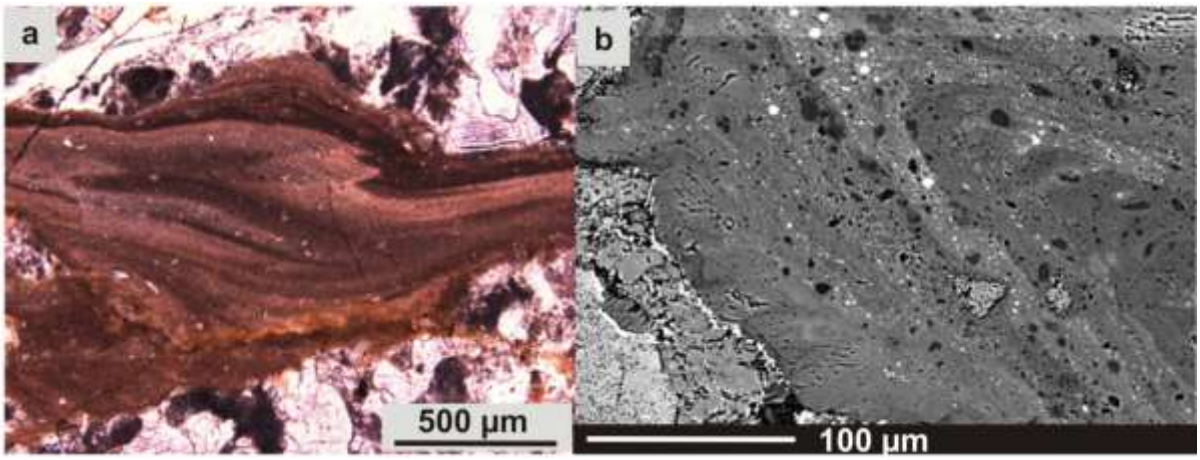


Fig. 7.8 Micrograph (a) and BSE image (b) of pseudotachylytes matrix in a metagabbro. Colour bands in these veins are evident in both images and are attributed to zones where individual minerals or aggregates have fused and become decrepitated and sheared out. Clusters of microlites and glassy material are also observed to form bands. However, the crystallisation products of the melt are strongly controlled by its composition, and hence the pre-existing minerals that fused will be the dominant control over the formation of these colour bands. Minimal physical sorting or fractionation has been observed in these veins, so this is not considered to be a significant factor.

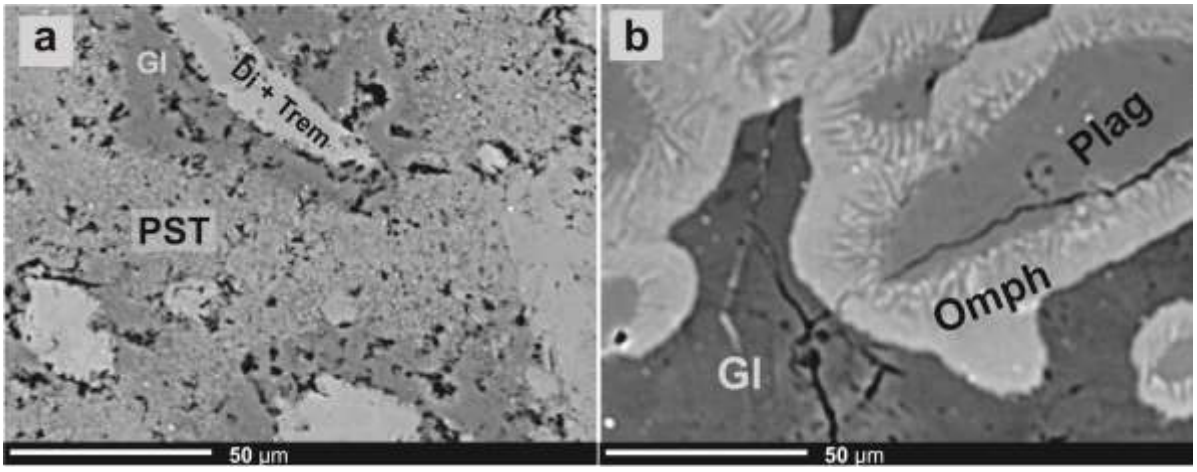


Fig. 7.9 BSE images of individually fusing clasts enclosed in a pseudotachylyte matrix. a) the matrix is dominated by microlites and minute relict clasts. However, at the boundary of melting clasts there is a zone of Al-rich, hydrous glass (Gl). Conversely, in b) the matrix is glass dominated (anhydrous) and the fusing grains are bounded by a crystallisation front of Al-rich omphacite (Omph) nucleating on plagioclase (Plag) derived from wallrock. Di + Trem: aggregate clast of wallrock diopside and tremolite.

7.4.5 Microtextures of ultracataclasite

Syndeformational ultracataclasite at the margins of coarse-grained pseudotachylyte fault veins is a common feature in both the metagabbro and peridotite hostrocks. The ultracataclasite comprises a mixture of comminuted clasts, melt and plastic ribbons (Fig. 7.7). The size range in comminuted wallrock material is from 30 μm < 1 μm. The mineral assemblage in the ultracataclasite matches that of the adjacent wallrock. The deformation of different mineral species in the ultracataclasite appears to be determined by fracture toughness, as predicted by Spray (1992). Minerals with greater relative fracture toughness such as diopside, plagioclase, Mg-hornblende and olivine typically form the portion of comminuted grains and mineral ribbons. Softer minerals such as clinochlore, tremolite, serpentine and actinolite comprise the melt and the rest of the ribbon portion in the ultracataclasite (Fig. 7.7). It is possible that some of the displacement in the fault veins is accommodated by preferential crystal plastic deformation and fusion within the ultracataclasite, explaining the lack of kinematic markers between the fault vein pseudotachylyte and wallrock (Kim et al., 2010; Sibson, 1980a; Spray, 1992). The microtextures of this unusual crystal-plastic ultracataclasite may hold information regarding the earliest stages of pseudotachylyte generation. It is important to take note that no ultracataclasite appears to form in pseudotachylyte fault veins hosted by equigranular, fine-grained rock (~ 20 μm) in both the peridotite and metagabbro.

7.4.6 Microtextures of the pseudotachylyte matrix

The matrices of the metagabbro and peridotite pseudotachylytes are typically dominated by crystallisation products of the melt, with interstitial crypto-crystalline material or glass and entrained wallrock clasts that vary greatly in size and can constitute up to 20% of the vein, but are normally much less. The presence of interstitial glass was confirmed with XRD synchrotron analysis on the sample

shown in Fig. 7.9b (refer to A1 – A5 for Laue patterns). The veins are commonly marked by streaks or colour bands that indicate compositional variation, predominantly due to clusters of spinel, and inefficient mixing of the melt (Fig. 7.8). The crystallisation products have various habits: hopper crystals, simple acicular laths, and feathery plumes, which nucleate on clastic material in the vein forming dendrites or along vein boundaries. A principal control on microlite size is the presence or absence of a nucleation surface and the size of this surface. When the nucleating surface is particularly small it generally forms the core of a larger than average complex dendrite composed of several mineral species. Space may also exert a control on crystallisation; areas that appear to be absent of any nucleating surface are typically host to some of the largest crystals.

7.4.7 Microtextures of survivor clasts

Survivor clasts comprise wallrock material that has been dragged into the pseudotachylyte during its formation. These can be monomineralic or composed of aggregates of minerals. They are typically angular or tabular in shape, with thermally rounded margins. The larger tabular forms are aggregates from the deformed wallrock that have been scoured away from the vein boundary by injecting melt (Fig. 7.4). The composition of the clasts is the same as that of the adjacent wallrock mineralogy, but not in the same proportions. Hydrous minerals such as Mg-hornblende, clinochlore and serpentine occur only in rare aggregates with anhydrous minerals and are thus inferred to have melted preferentially. Monomineralic olivine, diopside, magnetite, ilmenite and plagioclase have all been observed in the matrix of both types of host rock. Diopside and plagioclase are the most common clasts derived from the metagabbro hostrock, whilst olivine and diopside are those abundantly found in the peridotite. Survivor clasts commonly exhibit undulose extinction and kink-banding similar to that observed just beyond fault vein boundaries in the wallrock, suggesting that they may be derived from the wallrock and

underwent similar crystal plastic deformation. Sieve textures in sheared out wallrock and partially resorbed survivor clasts of older pseudotachylyte have also been observed (Fig. 7.10).

Further detailed petrographic data have been divided according to the metagabbro and peridotite host rocks. Within those groups the most pristine samples were selected for microtextural and geochemical analysis (refer to A11 – A44 for compositional data used). The pseudotachylytes are highly heterogeneous in composition down to the micron scale, so this separation is the best way to gain information from these veins and interpret their mechanism of formation meaningfully.

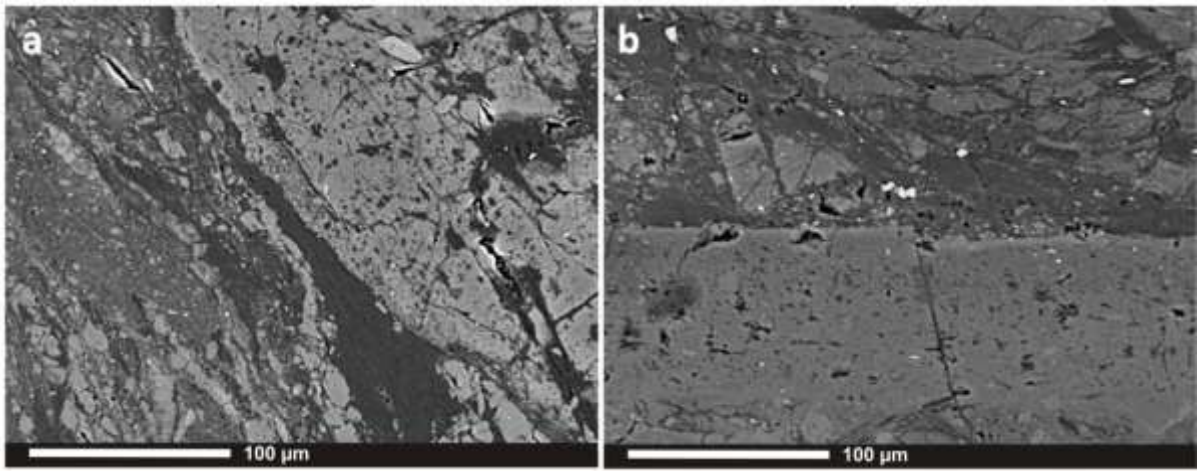


Fig. 7.10 BSE images of sieve textures in a peridotite-hosted pseudotachylyte matrix. Both (a) and (b) show at least two generations of pseudotachylyte. The sieve textured material in both images is the oldest generation that has been deformed and partially digested by a younger pseudotachylyte generation into which sheared out clasts of the older pseudotachylyte have been entrained. The oldest generation of pseudotachylyte contains inclusions of relative low atomic number (and low totals when analysed with EPMA; ~ 86%), suggesting that these are quenched melt inclusions with fluids dissolved in them to varying degrees. Preliminary raman spectroscopy shows these vesicles to contain glassy material and empty cavities, presumably once filled with fluid.

7.4.8.1 Metagabbro: Pseudotachylyte

Compositionally the pseudotachylytes hosted by metagabbro are highly heterogeneous, strongly reflecting local mineral compositions of the adjacent wallrock and survivor clasts. However, despite the compositional variability of the melt, the mineralogy of the crystallisation products in the pseudotachylytes is simple albeit showing great chemical variability. The pseudotachylyte matrix is defined as a combination of glass, crystallisation products and comminuted material that are too small to be resolved by electron microprobe analysis (EPMA) beam (< 1 μm). The crystallisation products are divided into two groups: a high temperature quench assemblage with pockets of interstitial glass, and a lower temperature assemblage in which devitrification of the glass and recrystallisation of the pseudotachylyte matrix has taken place.

7.4.8.1.1 *Microlite assemblage in the metagabbro pseudotachylytes*

This microlite assemblage is dominated by omphacite and plagioclase, with minor ilmenite (Fig. 7.9). This is the first reported evidence of natural crystallisation of omphacite directly from a melt. Omphacite has been reclassified from fassaite, as it was termed by Andersen and Austrheim (2006). The composition of the minerals is highly variable and is strongly controlled by melt composition in the matrix or by fusing clasts on which the microlites have nucleated. The omphacite is characterised by significant Al-enrichment relative to typical omphacite, which could be due to the high temperature and pressure of crystallisation (average Al_2O_3: 17.3 wt%). The plagioclase is characterised by high FeO_{total} and MgO contents (average FeO_{total} = 1.3 wt%, MgO = 1.1 wt%), possibly due to the rapidity or high temperature of crystallisation, or inclusions of unresolvable omphacite or ilmenite. These microlites take the form of laths, dendrites and skeletal hoppers crystallising freely in the pseudotachylyte matrix or nucleating on vein boundaries or on survivor clasts. The omphacite is clearly zoned with Mg-rich cores and Fe-rich rims (Fig.7.9b and Fig. 11).

7.4.8.1.2 *Metagabbro*: *Devitrification and recrystallisation of pseudotachylytes*

Devitrification of glass and recrystallisation of the higher temperature minerals that quenched directly from the pseudotachylyte melt produces its own assemblage of blueschist facies minerals: glaucophane, Fe-rich albite, epidote and minor sphene (Fig. 7.11a, b). The crystals in this assemblage are commonly coarser than those in the higher temperature assemblage (up to 2 mm). They are also more irregular and blocky in form, no longer exhibiting the dendritic habits of the replaced minerals. They occasionally show a deformation fabric expressed as folds and boudins of pseudotachylyte at the thin section scale, indicating a ductile blueschist facies overprint (Fig. 7.13a).

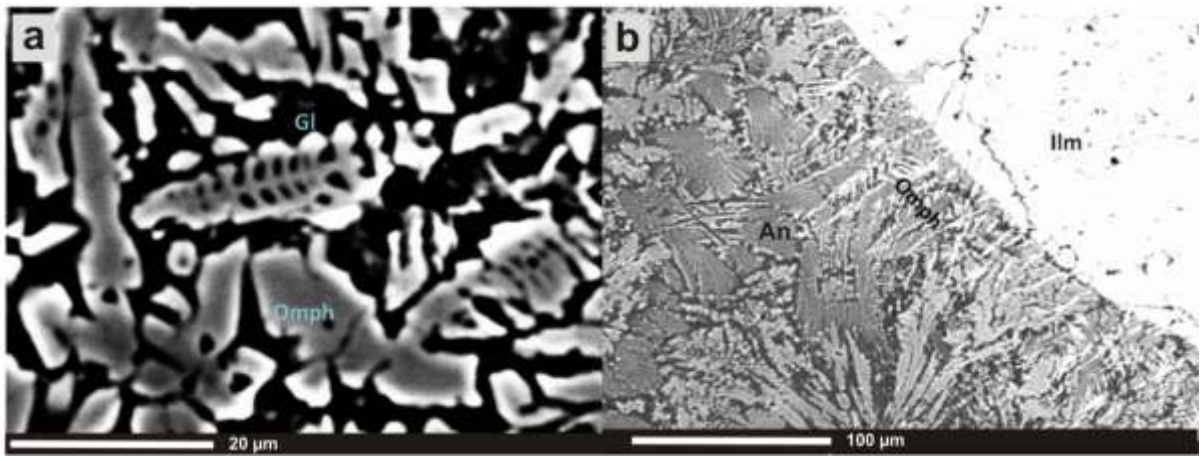


Fig. 7.11 Omphacite is the principal high temperature mineral crystallising from gabbroic pseudotachylyte, with anorthite and ilmenite to lesser degrees. (a) shows delicate, zoned hopper crystals of omphacite enclosed by glass; this crystal habit is an indicator of rapid, high temperature quenching. (b) shows omphacite in white and light grey with feathered and dendritic textures. The dark grey dendrites are anorthite. The variation in the composition of omphacite is controlled by the mineral that it nucleates on, as shown by the change in greyscale; its local melt composition and zoning in the crystals. Omph: omphacite, Ilm: Ilmenite.

7.4.9.1 *Peridotite: Pseudotachylyte*

At the millimetre to micron scale the peridotite pseudotachylytes show great variability in composition and abundance of bulk matrix, glass and crystallisation products. Despite this variability, the microlites consistently comprise diopside, olivine and enstatite. As with the metagabbro, the peridotite fusion products can be divided into a high temperature quench assemblage and a lower temperature devitrification assemblage.

7.4.9.1.1 Microlite assemblage in peridotite-hosted pseudotachylytes

Olivine, diopside and enstatite occur as clusters of monomineralic blocky microlites (particularly olivine) or as dendritic complexes. Also common are larger, polymineralic laths and dendrites (Fig. 7.12). The interstitial material of the bulk matrix ranges is a variable mixture of olivine and enstatite and has an H_2O content ranging from 0 - 14.2 wt % H_2O.

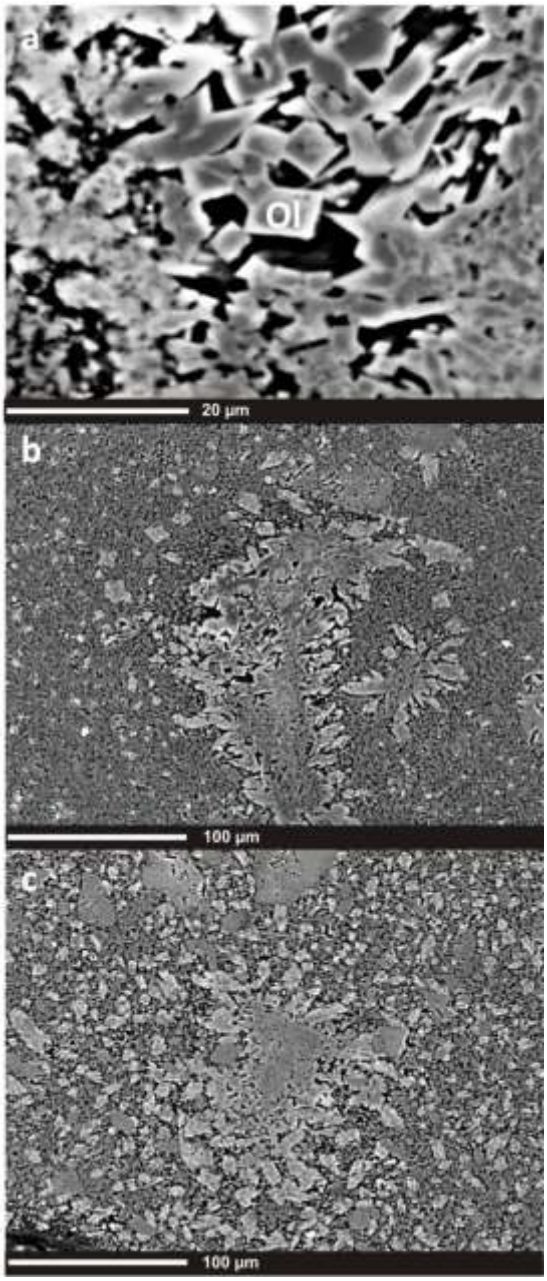


Fig. 7.12 BSE images showing the three principal types of crystallisation styles in peridotite hosted pseudotachylyte. (a) shows blocky microlites of olivine surrounded by glass (black in images). The olivine crystals show strong Mg-Fe zoning from core to rim. (b) shows pure olivine dendrites clustered in an aggregate with interstitial glass in a matrix of blocky olivine crystals and complex laths of diopside (light gray) and olivine (darker grey). (c) This image shows an aggregate of crystallised material in the centre. Close inspection shows the aggregate is composed of three minerals; enstatite (darkest grey), olivine (mid-grey) and diopside (light grey). The aggregate is dominated by these complex, tri-mineralic dendrites. The black interstitial matrix in all three images was analysed to be a variably Al-, H_2O-enriched glassy material.

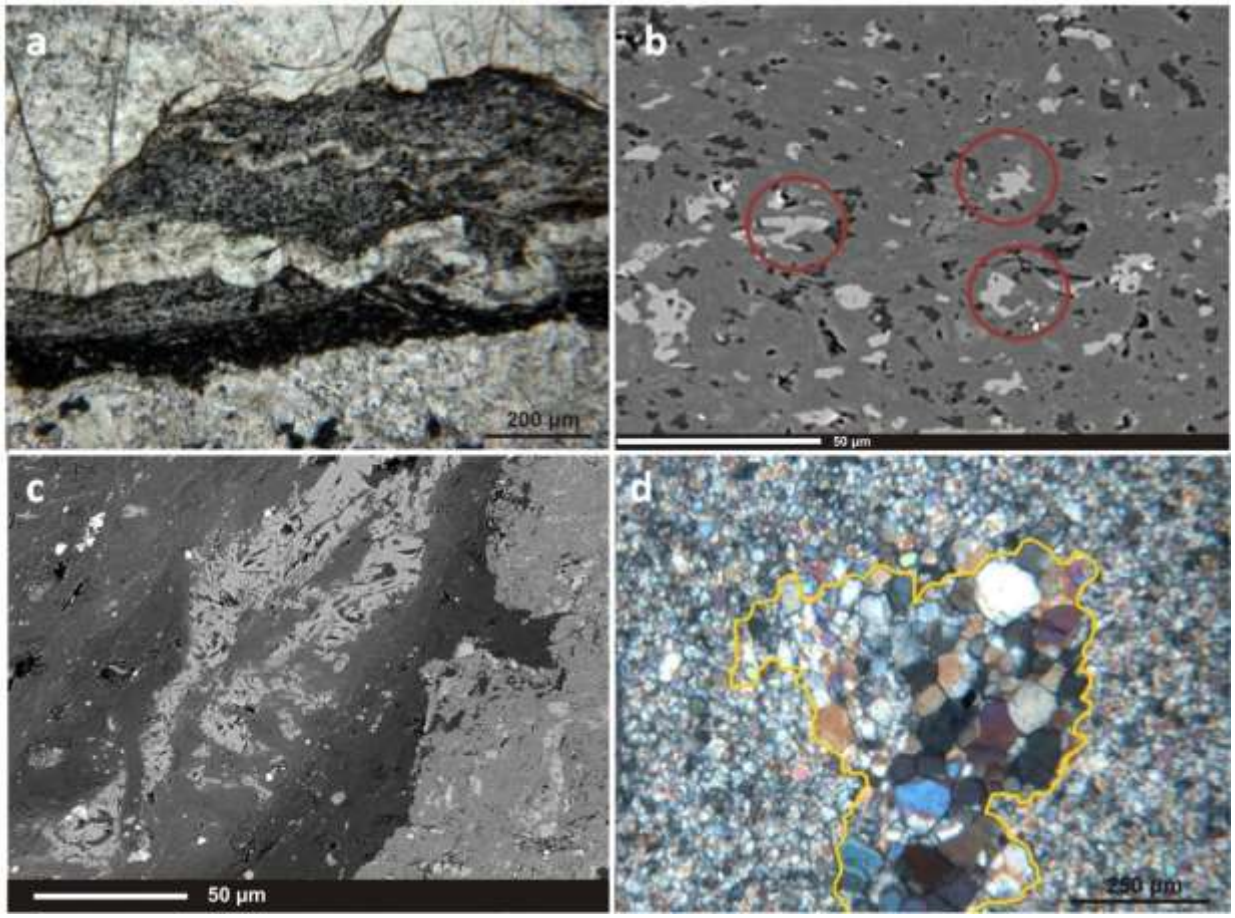


Fig. 7.13 Micrographs and BSE images showing the various recrystallisation textures in pseudotachylytes from both host rocks. (a) and (b) metagabbro pseudotachylyte (a) from the same thin section sample as (b), only at a lower magnification. (a) folding of the recrystallised pseudotachylyte. The microlites in (b) are blocky, no longer the dendritic forms shown in previous examples. EPMA analyses show the mineral assemblage to be glaucophane, sphene (light grey crystals), albite (dark grey crystals) and epidote (darkest grey). The crystals are subhedral and deformed and aligned in a subtle fabric due to folding, as shown in (a). Images (c) and (d) peridotite- pseudotachylyte. (c) a devitrified pseudotachylyte matrix that has an ultrafine (< 1 µm) of clinochlore composition. The matrix is not recrystallised as pristine quenched dendrites of diopside are observed (light grey dendrites (c) and stretched out, deformed clasts are evident along with zoning/colour banding in the vein that are preserved. (d) shows a recrystallised matrix; the yellow line indicates the form of a recrystallised wallrock aggregate that was entrained into the pseudotachylyte. The surrounding fine-grained material comprises olivine and enstatite clasts which have replaced earlier dendrites and upon stage rotation under the microscope, shadows of now replaced dendrites can be observed. The clasts in this photomicrographs are annealed, forming a granoblastic texture and show no evidence of deformation. It is important to note that peridotite pseudotachylyte recrystallises to a harzburgitic composition.

7.4.9.1.2 Peridotite: Devitrification and recrystallisation of pseudotachylytes

Devitrification of glass and recrystallisation of the higher temperature minerals that quenched directly from the pseudotachylyte. Typically the devitrified melt is characterised by the formation of microfibrous clinochlore, serpentine and tremolite (Fig. 7.10). In contrast, pseudotachylyte that has completely recrystallised comprises fine-grained (< 50 μm) granoblastic diopside, olivine and enstatite (Figs. 7.5 and Fig. 7.13d).

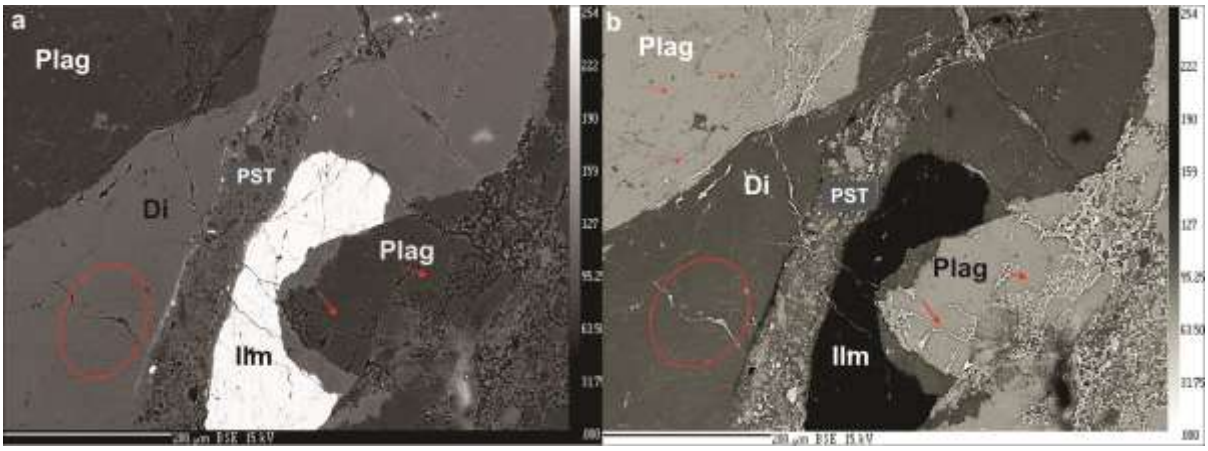


Fig. 7.14. BSE image of metagabbro with several generations of pseudotachylyte. The image on the left is the original BSE image and the image on the right has been inverted to highlight some features. The red circle highlights kinkbanding in wallrock diopside (Di). A minute fault vein has formed within a kink plane. The arrows indicate preferential fusion in the plagioclase (Plag) along certain planes. The white clast in the centre is ilmenite (Ilm).

7.5. Discussion

The microtextures analysed in this study are spatially and temporally associated with pseudotachylyte generation. The observed crystal-plastic phenomena observed that are considered to be causally linked to fusion and seismic failure include: dislocation creep/glide, deformation twinning, kinking, bending

and ultracataclasite/melt formation (Figs. 7.7, 7.13 and 7.14). The ultracataclasite observed in these rocks is unusual in that it contains angular comminuted wallrock minerals as well ribbons and strings of minerals exhibiting syndeformational ductile features (Fig. 7.7). The interstitial areas of the ultracataclasite contain glassy pockets of preferentially melted hydrous minerals, e.g. tremolite and clinochlore. Together, these textures suggest that the wallrock minerals may have undergone power law creep-dominated deformation that reached seismic strain rates, to induce the heating and fusion of the wallrock that is characterised by the presence of pseudotachylyte in these rocks (John et al., 2009; Kameyama et al., 1999).

The quench products of the pseudotachylytes indicate initially very high temperatures (~ 1600 °C), followed by a return to blueschist to – lawsonite- eclogite conditions (~ 430 °C – 550 ˚C, 1.8 - 2.6 GPa) (Andersen and Austrheim, 2006; Ravna et al., 2010). When the pseudotachylytes devitrify or recrystallise, the resulting mineral assemblages (glaucophane, albite and epidote in the metagabbro and diopside, olivine, enstatite and clinochlore in the peridotite) indicate a high pressure, low temperature environment (Ravna et al., 2010).

7.5.1 Precursors to pseudotachylyte formation

To date, several mechanisms have been put forward to explain the initiation of intermediate-depth seismicity. They all share the commonality of being fundamentally dependent on precursory conditions (Green and Houston, 1995; John et al., 2009; Kelemen and Hirth, 2007). Therefore, we need to investigate in detail the evidence of any preserved pre-existing elements that may elucidate the sequence of events that culminate in the production of these high pressure pseudotachylytes. A close spatial relationship between pseudotachylyte formation and fabric development is observed in the host rocks. This is not a unique occurrence and has been noted by previous workers in other pseudotachylyte

studies (Bestmann et al., 2011; Hobbs et al., 1986; Jin et al., 1998; Kim et al., 2010; Lin, 1994a; Lund and Austrheim, 2003). Hobbs et al. (1986) were amongst the first to propose the possibility that in high pressure cases, pseudotachylyte and mylonite formation may be inter-related processes; suggesting that at the highest deformation rates pseudotachylyte would form, followed by cataclasis and then fabric development, potentially culminating in mylonite at the lowest deformation rates.

Incipient fabric development prior to and after pseudotachylyte formation has been observed (Fig. 7.7d, and 7.13a). Detailed EBSD analysis of a peridotite fault section from the same field area shows that the wallrock minerals are exposed to increasing strain towards pseudotachylyte fault veins. The wallrock has undergone recrystallisation to form an incipient lattice preferred orientation (LPO) prior to and/or during fault vein development (Silkoset, 2013). Crystal plastic deformation such as folding, boudinaging, annealing and foliation development occurring after fault vein formation has been observed within veins and the associated wallrock (Fig. 7.7d, 7.13, 7.14). The time lapse between pseudotachylyte generation and fabric development (before and after) is unknown. However, the simplest explanation of the observations involves: recrystalllisation in the wallrock with increasing strain towards vein boundaries as well as rotation of elongate wallrock clasts into parallelism with developing fault vein boundaries. Continued shearing (Fig. 7) occurs after displacement and fusion have taken place, at which point the fault zone had cooled enough to crystallise glaucophane (in the metagabbro) and clinochlore (in the peridotite). We suggest the following sequence of events to explain our observations:

The majority of wallrock material for both metagabbro and peridotite is coarse-grained and partially deformed due to previous events. As a result the wallrock grains will likely contain numerous crystallographic imperfections that can be exploited when in the right orientation in the stress field to form the locii of fault nucleation and initial fusion due to low temperature creep, followed by power law creep.

The fault wall rocks developed a damage zone with synchronous recrystallisation and an increasing strain-gradient towards the future fault plane as also observed by Silkoset (2013).

2. Anisotropic wall rock fragments have rotated so that long axes become parallel with the developing slip surface.

3. Deformed wall-rock fragments become entrained, as survivor clasts in the pseudotachylyte melt and their deformation is associated with the shearing event that produced the melt. Some undergo near complete to complete fusion.

4. In some veins, shearing and displacement continued after fusion, locally attested to by deformed and recrystallised pseudotachylyte.

5. Pseudotachylyte and fault damage zones cooled down sufficiently to devitrify or recrystallise to glaucophane (in metagabbro) and clinochlore (in peridotite).

It is possible that at lower deformation rates foliations may develop in the pseudotachylyte and wallrock between major faulting events.

Based on the observations and sequence of events presented above, we suggest the following model for pseudotachylyte generation:
The metagabbro and peridotite were mostly coarse-grained rocks, but both host rocks had structural and mineralogical heterogeneities inherited from earlier events.
During subduction-related deformation, pre-existing zones with numerous crystallographic imperfections at favourable orientation relative to the new stress field become the loci of enhanced deformation (Jessell and Lister, 1991; Kameyama et al., 1999; Sibson, 1980a). Low temperature and subsequent power-law creep, induced by seismic strain rates eventually

gave rise to fusion. It is possible that several loci in the same orientation underwent contemporaneous strain-induced fusion. These individual melt spots may in turn have linked up to form primitive fault planes. Stick-slip action along such plane will be preferentially activated for further slip and facilitate comminution and fusion. As the stress is released by comminution, displacement and fusion, the temperature of the fault and damage zone will remain elevated until the stress has dropped below the strength of the transient melted material of the fault. Thereafter, heat is dissipated by diffusion beyond the cooling vein and damage zone to facilitate crystallisation of the wall rocks. The delicate preservation of quench textures in pseudotachylytes suggests neglible post-quenching deformation in most of the pseudotachylyte veins except in those areas where later regional deformation and metamorphism are penetrative.

7.5.1 Possible influence of grain size on pseudotachylyte formation:

The grain size of both the metagabbro and the peridotite ranges from approximately 20 μm - 260 μm. The principal deformation mechanism of the wallrock material and entrained survivor clasts that have been sheared and kinked but show no evidence of crystallographic recovery prior to pseudotachylytic fusion is interpreted to be dislocation creep/glide. EBSD analysis in a recent study indicates that the wallrock encountered rapidly increasing strain towards the pseudotachylyte boundaries, with weakly developed LPOs (Silkoset, 2013). The incipient LPO development could be due to localised stresses in the rock being accommodated by high dislocation densities in different grains (Branlund et al., 2000; Kameyama et al., 1999; Newman et al., 1999). EBSD analysis by Silkoset (2013) and intracrystalline microtextural observations (Figs. 7.4 and 7.7) in this study suggest dislocation creep as a possible dominant deformation mechanism associated with pseudotachylyte formation. If this is the case then there would be little grain size reduction through dynamic recrystallisation associated with the

instability as diffusion creep would be a secondary deformation mechanism (Kameyama et al., 1999; Kelemen and Hirth, 2007).

In finer-grained material (grain-size approximately 20 μm) strain has been accommodated by grain boundary sliding as opposed to intra-grain deformation; grain boundaries associated with the pseudotachylyte are aligned and grains appear squamous in shape as opposed to equant (Fig. 7.5).

It appears that higher volumes of melt are formed in the coarser-grained host rock. Of course, the current fault and injection vein thicknesses are not expected to be an exact indication of melt volume. However, taking vein dilation, draining and deformation into account the melt volume produced by coarse-grained rock relative to fine-grained rock is orders of magnitude greater; refer to Fig. 7.2a vs Fig. 7.4 where an outcrop scale image of an average fault vein is compared to the largest fault vein observed in the finest grained hostrock, seen in thin section as it is so small. This may correspond with power-law creep as a principal deformation mechanism as coarser-grained material would be easier to deform than finer-grained material. Coarser grains can accumulate more dislocations and higher dislocation densities in local areas of slip than can finer grains suggesting a greater potential for localised heating (Kameyama et al., 1999). Images of pseudotachylyte in the finer-grained host rock (Fig. 7.4) suggest grain boundary sliding occurs preferentially over intra-grain deformation to resolve the applied stress.

Furthermore, our geochemical results show that grain size influences melt composition such that the bulk composition of a pseudotachylyte derived from a fine-grained host rock will better approximate fusion akin to that of an equilibrium melt (this is due to melt formation occurring primarily along grain boundaries), whereas in pseudotachylyte derived from a coarser-grained host, the bulk melt composition tends to reflect wholesale fusion of individual minerals such as olivine or diopside.

Grain size reduction adjacent to vein boundaries was observed from the outcrop scale to the micron scale. Microtextural relationships suggest that this change in grain size is a feature contemporaneous

with pseudotachylyte generation and is due to intense shearing along the fault surface, whereby the heat released by shearing facilitates recrystallisation and the shearing itself induces the reorientation of wallrock clasts and/or their comminution. This is in contrast with the results of Kelemen and Hirth (2007) and John et al. (2009) where a pre-existing fine-grained zone in the host rock was proposed in order to provide a nucleation site for shear instabilities to take place.

7.5.2 Present model compared to previous mechanisms

The Corsican pseudotachylytes contain up to 15 wt% H_2O. This coupled with the large melt volumes produced by these events, apparently precludes dehydration embrittlement as a mechanism for the observed paleofaults. There is no evidence that free water or other fluids were available before faulting. Previous work by Green (1973), Jung et al. (2004) and Kirby et al. (1991), indicates that dehydration embrittlement is related to a solid-state monomineralic reaction. Its occurrence in polymineralic materials such as those studied here has to our knowledge not been tested experimentally. Instead we suggest that the high temperature deformation related to local shear-heating was more significant for failure than a solid-state dehydration reaction weakening. Previously published shear heating models (John et al., 2009; Kelemen and Hirth, 2007) are not perfect fits either. Both these models prescribe precursory mylonites or fine-grained zones that act as strain concentrators in order to initiate self-localisation. Our observations from the rocks in
Corsica however, indicate that, despite various differences in the hostrocks, seismic faulting and fusion took place regardless of grain size, rock fabric or composition. The only discernible restriction on mineralogy is fracture toughness; minerals must have a shear yield strength great
enough to allow for a sufficiently large stress build-up (Spray, 1992), which explains

why no pseudotachylytes occur in the serpentinites surrounding the peridotite and metagabbro blocks. A non-quantified and speculative option may be that the rheological behaviour of rocks traditionally predicted at high pressure may not be simply constrained by visco-elasticity or Von Mises Criterion as suggested by (Mancktelow, 2006).

7.6. Conclusions

Both shear instabilities and dehydration reactions are thermally activated processes. However, the activation of thermal instability is derived from local rheological heterogeneities that provide a viscosity contrast in the host rock material at sufficiently high stresses that it behaves as a non-linear viscoelastic material (Braeck and Podladchikov, 2007; John et al., 2009; Kameyama et al., 1999; Ogawa, 1987). Conversely, dehydration embrittlement is induced by warming of the previously hydrated slab making it dependent on the presence of pre-existing hydrous mineralogy and an efficiently warmed slab. In addition, there is no evidence in the petrographic data to support the hypothesis of a dehydrated precursor to pseudotachylyte nucleation. This is not to say that dehydration embrittlement does not occur; it may well occur in the serpentinite enclosing the blocks of peridotite and metagabbro. The results from this study suggest that these pseudotachylytes produced at high pressure and seismic strain rates, in different host rocks, with different degrees of hydration, may have been generated by a high temperature crystal-plastic shear process. Detailed petrographic analysis suggests that low temperature and power law creep may play dominant roles in producing thermal instabilities and high pressure pseudotachylytes. Deformation of wallrock grains at the boundary of fault veins results in the formation of subtle LPOs in olivine grains and grain size reduction due to comminution (Silkoset, 2013). These features form at the onset of and during pseudotachylyte generation, not before, and they are not the precursory elements that form the nucleation sites of pseudotachylyte generation in previous models

(John et al., 2009; Kelemen and Hirth, 2007). Future work to test this interpretation might involve high pressure fusion experiments, numerical modelling, detailed EBSD on more complex fault veins and geochemical analysis.

Acknowledgements

This work is supported Wits University, the National Research Foundation and the Mellon Foundation as well as the Centre of Excellence grants to Physics of Geological Processes, Oslo University.Thanks to Prof. M. Zolensky of NASA for assisting with EBSD and XRD synchrotron analysis of some samples.

Initiating intermediate-depth earthquakes: insights from a HP-LT ophiolite from Corsica

Accepted by Lithos July (2014)

N. Deseta[1,*], L.D. Ashwal[1], T.B. Andersen[2]
[1]Department of Geosciences, University of the Witwatersrand, Private Bag 3, 2050, Johannesburg, South Africa.
[2]Department of Geosciences and CEED, University of Oslo, P O Box 1047, Blindern, 0316, Oslo, Norway.

Abstract

The hypocentres of intermediate-depth earthquakes have been shown to overlap with the regions in subducting slabs that contain high abundances of hydrous minerals. This relationship was initially revealed using geophysical and numerical modelling and until recently has lacked corroboration from direct field-based research. We evaluated the relationship of the coincidence of intermediate-depth earthquakes with hydrous minerals in the slab by undertaking detailed geochemical analyses of blueschist to lawsonite to eclogite facies pseudotachylytes and their hostrocks located within an exhumed ophiolite, the Eocene Schistes Lustres Complex in Corsica. These units comprise incompletely metamorphosed metagabbro and peridotite. The wallrocks of the pseudotachylytes contain variable amounts of hydrous minerals: tremolite, Mg-hornblende, glaucophane in the metagabbro, and serpentine, tremolite and chlorite in the peridotite. Back-scatter-electron images show that the hydrous minerals entrained in the melt undergo fusion rather than dehydration. Vesicular and H_2O-rich melt veins are observed cross-cutting partially molten pseudtachylyte fault veins and show evidence of H_2O exsolution during melt solidification. The crystallisation products of these melts indicate formation under high temperature, high pressure conditions (1400 - 1700 ˚C; 1.5 GPa). The peridotite-hosted pseudotachylytes crystallised olivine, orthopyroxene and diopside, which are surrounded by interstitial Al- and H_2O-rich glass. The metagabbro pseudotachylyte is dominated by Al-rich omphacite, ilmenite and high-Fe anorthite. XRF bulk analyses of the wallrock of the pseudotachylyte and electron microprobe analyses of the pseudotachylyte matrix, entrained survivor clasts and the crystallisation

products show that near-total disequilibrium melting took place. The peridotite-hosted pseudotachylyte composition is skewed strongly towards chlorite; however, the preservation of delicate dendritic diopside and olivine hopper crystals suggests that the pseudotachylyte is unaltered, indicating that preferential fusion of chlorite took place. The metagabbro-hosted pseudotachlyte matrix composition is very similar to the bulk wallrock composition but slightly skewed by the preferential melting of Mg-hornblende and tremolite. Not all the pseudotachylytes are hydrous as the H_2O content of the melts vary highly; the metagabbro-pseudotachylyte ranges from 0 - 4 wt % and the peridotite-pseudotachylyte ranges from 0 – 14 wt %. The range in H_2O content of the pseudotachylytes has led us to conclude that the localised dehydration of hydrous minerals may be a second-order factor in initiating intermediate-depth seismicity. However, we have observed that the pseudotachylytes with the most chaotic vein networks, thickest fault veins and most comminuted material have the highest abundances of hydrous wallrock minerals, possibly owing to repeated fluid ingress in between pseudotachylyte-generating events. This implies that free fluids enhance pseudotachylyte generation and possibly seismicity, but are not a first-order requirement. Microtextural and geochemical results from this study suggest that the presence of abundant H_2O-rich minerals in the slab exerts a strong rheological control during high strain-rate deformation, facilitating thermally-triggered localising shear instabilities. These field-based observations allow us to explore the assumption of the causal link between slab hydration and earthquake nucleation, and offer fresh insight into the debate of how intermediate-depth earthquakes take place.

Keywords: Intermediate-depth seismicity, pseudotachylyte, dehydration, melting, hydrous minerals

8.1. Introduction

Intermediate-depth earthquakes occur in subduction zones at depths of 60 – 300 km. This is contrary to the expectation that brittle failure should be inhibited by the high pressure and temperature conditions in the subducting slab (Green and Houston, 1995; Hacker et al., 2004). Seismic data show that the hypocentres of such earthquakes occur in the regions where sinking slabs are likely to have high contents of hydrous minerals (Hacker et al., 2004; Yamasaki and Tetsuzo, 2003). Whether these earthquakes and hydrous minerals are causally linked remains uncertain, although experimental and numerical studies have put forward several hypotheses: dehydration embrittlement, mineral transformational faulting and thermally-induced shear instabilities (Dobson et al., 2002; Green, 2003; Hacker et al., 2004; John et al., 2009; Jung et al., 2004). The aim of this study was to test the link between hydrous minerals and intermediate-depth seismicity using direct analysis of paleofaults. We present the first combined detailed geochemical and microstructural study of the blueschist to eclogite facies pseudotachylytes from Corsica, which have been interpreted as relicts of intermediate-depth seismic events (Andersen and Austrheim, 2006; Austrheim and Andersen, 2004). The pseudotachylytes are hosted in metagabbros and perodotites in an Eocene Alpine subduction complex and comprise both mafic and ultramafic fusion melts (Austrheim and Andersen, 2004). The pseudotachylytes are quenched fusion melts formed at pressures of 1.5 – 2.6 GPa and ambient slab temperatures of ~ 420 – 500 ˚C, with melting temperatures of 1400 ˚C upward, and are variably hydrous, with 0 – 14 wt % H_2O (Andersen and Austrheim, 2006; Deseta et al., 2014; Ravna et al., 2010; Vitale Brovarone et al., 2011, 2013).

By analysing the fault rocks of intermediate-depth earthquakes directly we can evaluate the proposed importance of hydrous minerals in generating these phenomena. Do they facilitate dehydration embrittlement, weakening in wallrock or does the H_2O released by dehydration of these minerals act as a flux for melting?

8.1.1 Pseudotachylyte formation and flash melting:

High pressure pseudotachylytes from various localities (Blue Ridge Province, North Carolina; the Ivrea-Verbano zone, Italy; the Krakeneset gabbro, Norway) have been studied on a number of scales and from various aspects in order to ascertain the mechanism by which they form (Camacho et al., 2001; Jin et al., 1998; John et al., 2009; Lin, 1994b; Lund and Austrheim, 2003). The majority of pseudotachylytes are derived from relatively shallow crustal lithologies and are hence associated with a brittle deformation regime (Jin et al., 1998; Magloughlin and Spray, 1992; O'Hara, 1992; Spray, 1992). However, ultramafic pseudotachylytes occurring in association with lower crustal metagabbro in contact with mantle peridotite (as observed in Corsica) implies that these melts can form at depths greater than 50 km (Jin et al., 1998; Kelemen and Hirth, 2007; Ravna et al., 2010). Generally viewed as the products of coseismic frictional melting, the formation of high pressure fault-related pseudotachylytes in mafic and ultramafic rocks appears paradoxical, as they should be inhibited by high confining stresses. However, it needs to be taken into account that the brittle-ductile transition zone of mafic and ultramafic rocks is controlled by olivine creep laws (Boland and Tullis, 1986; Demouchy et al., 2009), rather than quartz and feldspar, and can therefore extend beyond the brittle-ductile zone determined for crustal rocks (Kirby et al., 1991; Swanson, 1992). When it is further considered that the geotherm for the Corsican pseudotachylytes was cold and steep, and eclogites from Cape Corse record ambient temperatures of 420 ˚C at 1.5 – 2.6 GPa, it becomes apparent that the brittle-ductile transition in the slab extended to nearly 80 km in some places (Vitale Brovarone et al., 2013).

8.1.2 Current models of high pressure pseudotachylyte formation:

*S*everal mechanisms have been proposed to explain intermediate-depth seismicity and associated pseudotachylyte generation under blueschist and eclogite facies conditions. These mechanisms encompass a range between two end-member processes, which will be discussed in more detail:

dehydration embrittlement and a-thermally induced shear instability end-member (TSI). The hypothesis tested in this study is that a form of TSI is the initiating process of intermediate-depth seismicity and associated PST generation, as implicated by the observations discussed in this paper. The principles of these two mechanisms are summarized briefly below.

Dehydration embrittlement is based on experimental observations that show that rock materials become weak and brittle upon dehydration of their hydrous minerals, facilitating unstable faulting and inducing seismic failure (Green, 1995; Jung et al., 2006; Kirby et al., 1995, 1996). This process allows brittle failure to initiate at high pressures where fracturing would typically be inhibited by high confining pressures (> 1 GPa) (Jung and Green, 2005; John et al., 2009). The weakening of rock under such conditions has been attributed to the volume change generated by the production of free water and its thermal expansion resulting from the dehydration of minerals such as serpentine and chlorite (Green, 1995). The increased pore fluid pressure offsets the high confining pressure on the PST hostrocks and on the potential slip planes within them, thereby facilitating brittle failure (Hacker et al., 2004; Jung et al., 2004). Due to dehydration-induced volume changes in individual minerals, the cohesive strength of the hostrock is reduced and this also facilitates brittle failure (Hacker et al., 2004).

To date there are several models of how high pressure pseudotachylytes might form, all of which are based on thermally-activated shear instabilities (John et al., 2009; Kelemen and Hirth, 2007; Ogawa, 1987; Orowan, 1960; Warren and Hirth, 2006). Each model has its own prerequisites and thermal equations; only the general principles of thermal shear instabilities (TSI) will be covered here.

Unlike dehydration embrittlement, TSI is a process by which coseismic shear heating under high differential stresses induces localized viscous deformation, in a visco-elastic material, such as silicate rocks (Braeck and Podladchikov, 2007; Spray, 2010). As viscous deformation progresses, there is a reduction in viscosity along the slip plane, which in turn feeds back positively and non-linearly on strain rate and temperature. This results in a massive release of elastic energy stored in the surrounding rock

(or any visco-elastic material), inducing failure (Braeck and Podladchikov, 2007; Hogan et al., 2011; John et al., 2009; Kelemen and Hirth, 2007; Ogawa, 1987).

At such high strain rates (> $10^{-2}s^{-1}$) the temperature increases too rapidly to be diffused away from the shear zone and the shear instabilities become self-localising (Braeck and Podladchikov, 2007). Due to the fact that heat transfer away from the shear plane occurs by diffusion, peak temperatures located in the centre of the shear plane. As temperature increases exponentially in the narrow shear zone, viscosity decreases generating a positive feed-back effect (and self-localising effect), keeping the shear band into which strain is being focused, narrow (less than ~ 200 µm) (Braeck and Podladchikov, 2007; Kelemen and Hirth, 2007; Rice, 2006).

There may be several alternatives for precisely how TSI is initiated, but current experimental research and numerical modeling suggest that as rocks are heterogeneous materials, the stress imposed will be concentrated in minute domains where the effective viscosity in the rock is locally greatly decreased and acts as strain concentrators (Kelemen and Hirth, 2007; John et al., 2009, Bestman et al., 2011). Preferential shear heating will take place in these low viscosity zones, eventuating in a positive feedback effect where an exponentially increasing strain rate and temperature will take place resulting in failure, melting and or comminution (Kelemen and Hirth, 2007; John et al., 2009). The perturbations in rheology result in extremely localised regions of low viscosity expressed in the rock as either reduced grain size and/or the presence of hydrous minerals such as serpentine, chlorite or muscovite (Hacker, 2004; John et al., 2009, Bestman et al., 2011). With regard to hydrous minerals it should be noted that, in the case of TSI, it is their mechanical properties at high strain rates that causes the rocks to weaken and fail, not the release of free water (Sibson, 1977a; Spray, 2010). The eclogite facies pseudotachylytes hosted by the Krâkeneset metagabbro, western Norway have been suggested as a natural example of TSI (John et al., 2009). The Krâkenest pseudotachylyte-fault veins occur in domains of the hostrock metagabbro,

within which there is a marked decrease in grain size towards the fault plane and a relatively high degree of hydration reflected by the presence of phengite, clinozoisite ± amphiboles (Austrheim et al., 1997; Lund and Austrheim, 2003; John et al., 2009). TSI ultimately differs from dehydration embrittlement, as fault weakening is rheologically controlled rather than being solely dependent on the initial production of free water to overcome high effective pressures, and achieve catastrophic failure (Handy, 1990; John et al., 2009; Kelemen and Hirth, 2007; Spray, 2010).

8.2. Geological Setting

The study area is located on the SSW side of Cima di Gratera in Cape Corse, northern Corsica (Fig. 8.1a). The pseudotachylytes are preserved within lozenge-shaped blocks (~ 500 – 1000 m long) of partially metamorphosed mantle peridotite and more continuous blocks of lower crustal metagabbro; these are enclosed by serpentinite and blueschist to eclogite facies schists (Fig. 8.1b) (Austrheim and Andersen, Vitale Brovarone et al., 2011). These rocks form part of the high pressure – low temperature (HP – LT) Schistes Lustres Complex, which contains nappes of the Piemont-Liguria oceanic basin as well as vestiges of the hyperextended ocean-continent transition and lithospheric mantle (Agard et al., 2002; Beccaluva et al., 1977; Jolivet et al., 2005; Vitale Brovarone et al., 2011). The Corsican Schistes Lustres Complex was thrust onto the European continental margin and the resulting thrust stack contains an ophiolite, comprising ultramafic rocks (peridotite), gabbro, pillow lavas and metasedimentary schists, as well as allochtonous blueschist and eclogite facies rocks (Fig. 1b) (Andersen et al., 2014; Austrheim and Andersen, 2004; Jolivet et al., 2005; Mohn et al., 2009; Vitale Brovarone et al., 2011).

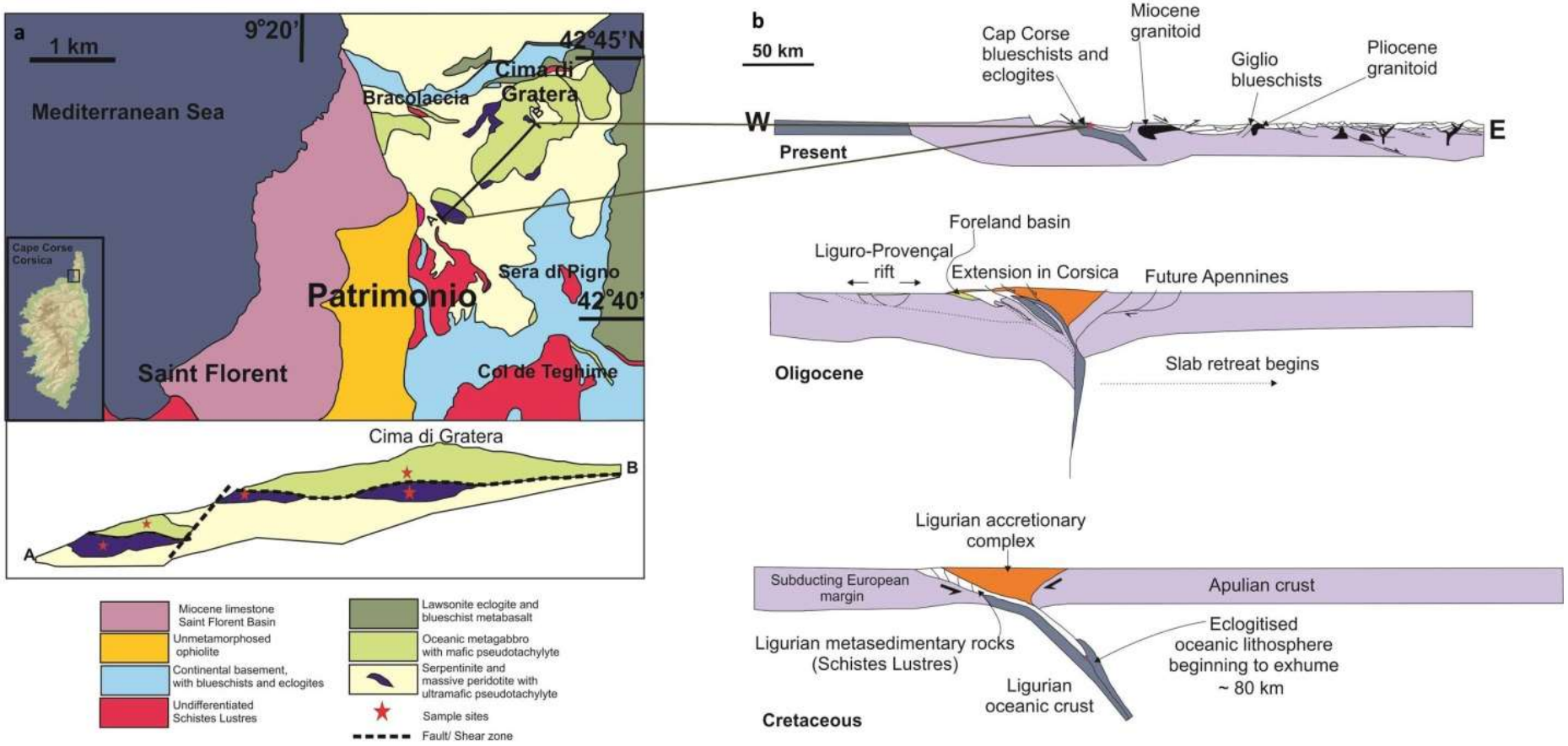


Fig.1 a) Simplified geological map and cross-section of the study area in Cima di Gratera. Modified after Andersen and Austrheim (2006). b) Abridged model of the tectonic evolution of the LT-HP Corsican metamorphic complexes. The diagrams illustrate the formation of the eclogitised oceanic lithosphere, during the Cretaceous, and follows its exhumation through the Oligocene to its present day position at the Earth's surface. The hyperextension during the Oligocene resulted in enhanced exhumation of subducted lithosphere. Modifed after Ravna et al. 2010.

The studied metagabbros are compositionally uniform, but display a range of igneous textures marked by changes in grain size and igneous layering; interfingering of irregularly shaped textural domains is common (Fig. 8.2c and d). Conversely, the peridotites are relatively uniform in terms of their texture, composition and grain size. The pseudotachylyte-bearing fault rocks have been patchily metamorphosed and/or retrogressed to eclogite, blueschist and greenschist facies, except within the bounding shear zones that mark places where the metamorphic reactions have gone to completion and retrograded to greenschist facies (Austrheim and Andersen, 2004). The blueschist and eclogite facies metamorphism are thought to be diachronous and represent peak metamorphic conditions of the subduction complex (Vitale Brovarone and Herwartz, 2013). The pseudotachylytes are located within the lenses of metagabbro and peridotite that are relatively undeformed and least affected by the regional HP-LT metamorphism (Andersen and Austrheim, 2006). We have interpreted the metagabbro and peridotite lozenges hosting the pseudotachlytes to represent the base of what was potentially a double seismic zone, where the pseudotachylytes hosted by the metagabbro and peridotite are proposed to have been part of the lower fault zone at the contact between the crust and mantle lithosphere, i.e. the Moho (Andersen et al., 2014). Double seismic zones are defined as two planes of slab seismicity that typically coincide with the hydrated upper and lower sections of the slab, separated by an aseismic slab core (Hacker et al., 2004; Houston, 2007; Reynard et al., 2010; Yamasaki and Tetsuzo, 2003). These zones are a relatively common feature of intermediate-depth earthquakes and tend to occur in older, rapidly subducting slabs, e.g. Japan, Chile, Taiwan and the Aleutians (Hacker et al., 2004; Yamasaki and Tetsuzo, 2003). Previous researchers have drawn a link between dehydration of minerals in the upper and lower parts of the slab and double planar seismicity, arguing that a lack of hydrous minerals in the core of the slab accounts for its lack of seismicity (Hacker et al., 2004; Nakajima et al., 2009b; Yamasaki and Tetsuzo, 2003).



Fig. 8.2 Field photographs of pseudotachylytes in outcrop. a) and b) are peridotite-hosted pseudotachylyte fault veins; the thickness of the fault veins reaches up to 30 cm. The peridotitic veins are more resistant to weathering and stand out in positive relief. c) and d) are pseudotachylyte fault and injection veins hosted in metagabbro; these fault veins rarely exceed thicknesses of 0.5. The metagabbro pseudotachylytes are aphanitic and black.

8.2.1 *Field observations and sampling:*

In outcrop the pseudotachylytes typically have a positive relief with respect to the hostrocks. The veins weather to a rust-red colour (in the peridotite) or to a navy blue-black (in the metagabbro), but on fresh surfaces the pseudotachylytes are black-grey and aphanitic (Fig. 8.2 a - d). The peridotite-hosted pseudotachylyte form two broad sets of fault vein networks that extend for up to 1 km and include a sub-vertical set and a gently dipping set parallel to the metagabbro – peridotite contact. Within these sets the pseudotachylytes form complex fault and injection vein networks that can overprint and re-

inject one another, due to the large melt volume produced and multiple fault generations. In outcrop, some of the peridotitic pseudotachylytes are observed to form intensive, penetrative fault networks that can extend for metres, and have been interpreted as features from the lower seismogenic zone (Andersen et al., 2014). These veins are thicker than other injection and fault veins and contain more re-injections and comminuted wallrock material than those in the metagabbro. In contrast with the peridotite-hosted veins, those in the metagabbro are thinner and more discrete, commonly (but not always) occurring along the boundary between the very coarse-grained (< 15 mm) metagabbro and fine-grained (< 2 mm) metagabbro (Fig. 8.2 c and d). The peridotite-hosted pseudotachylytes show cross-cutting relationships with serpentinised hostrocks, fragments of which have been entrained into the veins as sigmoidal lozenges. In the metagabbro fault rocks, pseudotachylyte crystallisation products have formed shape preferred orientation fabrics (SPOs) and contain boudinaged wallrock clasts, indicating blueschist facies conditions both pre- and post-date PST generation. Many of the pseudotachylytes are cut by later serpentine veins and show a hydration overprint. Samples of the pseudotachylytes and their hostrocks were taken from sites indicated by the red stars in Fig. 8.1. Care was taken to separate the most pristine pseudotachylyte samples from the altered ones, and both were analysed in detail petrographically in order to classify the various microtextures, mineral assemblages and processes observed.

8.3. Materials and methods

Detailed thin section petrography and back-scatter electron (BSE) imaging for mineral identification and microtextural analyses were performed on both gabbro- and peridotite-hosted PST. Electron microprobe analyses were done on a Cameca SX-100 instrument housed at Spectrau Laboratory, University of Johannesburg, South Africa. Analyses include bulk matrix (wide beam), wallrock, entrained

minerals as well as crystallisation products (glass and crystallites). The beam current was reduced so as to minimise Na loss on glass, but tests on higher currents (> 10 nA) showed Na loss to be negligible. Analyses were run at 20kV, 10nA. The reference standard used was a Ni-bearing glass. Detailed operating parameters can be found in Merlet (1994). XRF analyses were carried out on whole rock samples of pseudotachylyte wallrocks, metagabbro and peridotite. The analyses were performed at the University of the Witwatersrand School of Geosciences Earthlab and the operating parameters are given in Wilson (2012).

8.4. Results:

8.4.1 Petrographic analysis:

Detailed petrographic and microtextural analyses were carried out on both metagabbro- and peridotite-hosted pseudotachylytes. The results following from those analyses were published in a separate paper (Tables 8.1 and 8.2), (Deseta et al., 2014). Only those petrographic data that are relevant to evaluating the influence of hydrous components and grain size will be presented here.

8.4.1.1 Metagabbro: Hostrock:

The metagabbro hostrock has a bimodal grain size distribution, with metre wide irregular domains of very coarse-grained (maximum grain diameter up to 15 mm) gabbro occurring in contact and inter-fingering a fine-grained (~ 1 mm) gabbro (Fig. 8.2c and d). The contact between the coarse- and fine-grained domains is always sharp, less than 5 mm. Despite the range in grain size, the constituent mineral assemblage does not appear to be significantly variable.

The igneous mineralogy of the metagabbro that hosts the pseudotachylytes is partially preserved and consists of plagioclase, clinopyroxene, olivine and minor ilmenite (Table 8.1). In other regions the metagabbro is hydrated and foliated, but does not contain pseudotachylytes. In thin section the gabbro adjacent to PST faults retains little of its igneous texture, most of which has been annealed to a granoblastic texture with poikiloblasts of olivine and clinopyroxene. Grain boundary migration and dynamic recrystallisation are common, particularly in clinopyroxene. Early greenschist facies metamorphism of the hostrock has led to variable replacement and recrystallisation of clinopyroxene by tremolite, bastite and Mg-hornblende. Plagioclase alteration to sericite has also taken place, causing the grains to become cloudy and grey. Alteration of the olivine to serpentine, magnetite and iddingsite has also been observed (Fig. 8.4). Post-dating the early greenschist alteration is the development of blueschist facies assemblages, which are manifest by the replacement of clinopyroxene, tremolite, Mg-hornblende and plagioclase by glaucophane, barroisite and albite (Fig. 8.3). The blueschist metamorphism is associated with alternating periods of ductile deformation of the gabbro and PST generation at these conditions. The PST itself is commonly observed to be folded and boudinaged in places due to later deformation (Fig. 8.3f – h). Late retrograde metamorphism, particularly marked by serpentine veins and the presence of epidote, chlorite and pumpellyite, overprints the blueschist phases and patches of the pristine material (Fig.8. 3a - e).

The early greenschist to upper greenschist metamorphism of the hostrock may be associated with sea floor hydration and/or hydration-associated fracturing in the slab bend, as well as earlier hydration associated with pre-Alpine extensional tectonics (Mohn et al., 2009; Vitale Brovarone, 2011b). The late greenschist metamorphic overprint was observed in thin section and BSE and is thought to be associated with hydration and faulting upon slab exhumation. This late retrograde metamorphism overprints some of the PST veins and is not cut by later PST generations. These observations corroborate and expand upon previous observations made by Andersen and Austrheim (2006).

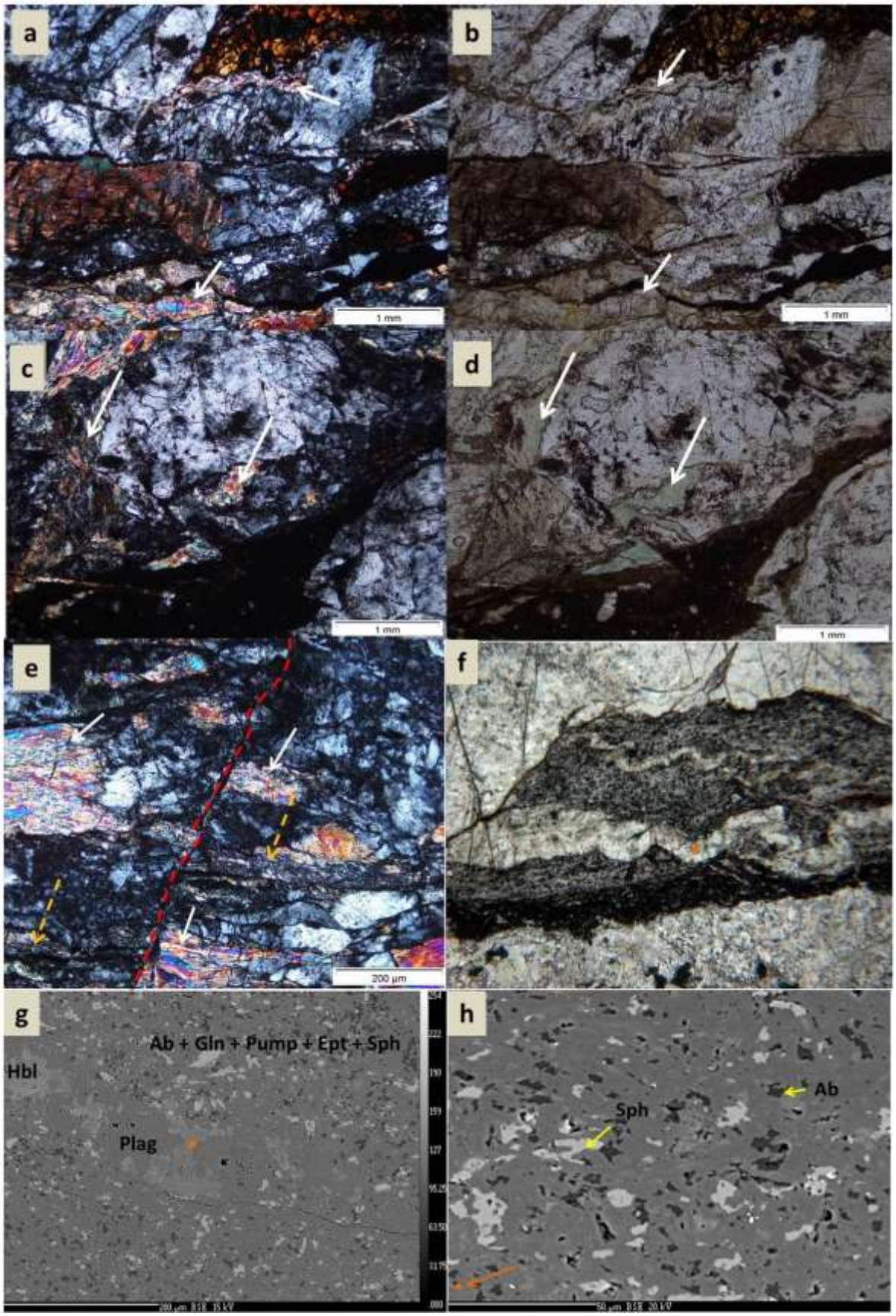

a
1 mm
b
1 mm
c
1 mm
d
1 mm
e
200 µm
f
g
Ab + Gln + Pump + Ept + Sph
Hbl
Plag
h
Ab
Sph

Fig. 8.3 Micrographs of metagabbro-hosted pseudotachylyte fault veins. a) and b) are the same area in XPL and PPL respectively. c) and d) are the same area in XPL and PPL, respectively. White and orange arrows in each image indicated the presence of hydrous minerals adjacent to pseudotachylyte fault veins (White: tremolite and bastite, orange, dashed arrow: chlorite). e) XPL micrograph of microfault (shown by red dashed line) cross-cutting an older pseudotachylyte containing hydrated and recrystallised clasts of clinopyroxene (white arrows) and olivine (orange arrows) Metagabbro pseudotachylyte fault vein with a ductile overprint at increasing magnification from f) to h). Orange dot indicates the same spot at different magnifications. f) Recrystallised fault vein with folded and boudinaged relict survivor clast within vein matrix. g) and h) are BSE images of folded survivor clasts. The matrix has recrystallised to a blueschist facies assemblage of albite (Ab), glaucophane (Gln), Pumpellyite (Pump), Sphene (Sph) and epidote (Ept). h) Recrystallised matrix shows neoblasts are deformed and weakly aligned due to ductile overprint.

8.4.1.2 Peridotite: Hostrock

The peridotite hostrocks show gradational transitions from fine- to coarse-grained varieties (< 1 mm – 7 mm), with local layers rich in pyroxene and olivine, but massive overall (Fig. 8.2). The mineralogy corresponds to that of a plagioclase lherzolite, with olivine > clinopyroxene > orthopyroxene, minor plagioclase, Cr-spinel and magnetite (Table 8.1). The rocks exhibit a granoblastic texture, with annealed poikiloblasts and some grain boundary migration. The clinopyroxene and orthopyroxene commonly show exsolution lamellae of each other and twinning of the clinopyroxene and olivine has been observed. Locally the early greenschist facies metamorphism, deformation and dynamic recrystallisation have resulted in the conversion of clinopyroxene and orthopyroxene to fine-grained aggregates of chlorite, tremolite and bastite (Fig. 8.4). The chlorite has a plumose and feathery texture. Various generations of serpentinisation overprint all pre-existing features and are variably distributed across the rock, locally associated with late reactivation of PST veins (Fig. 8.4). The peridotite shows multiple stages of hydration, observed to have occurred before, after and in between pseudotachylyte

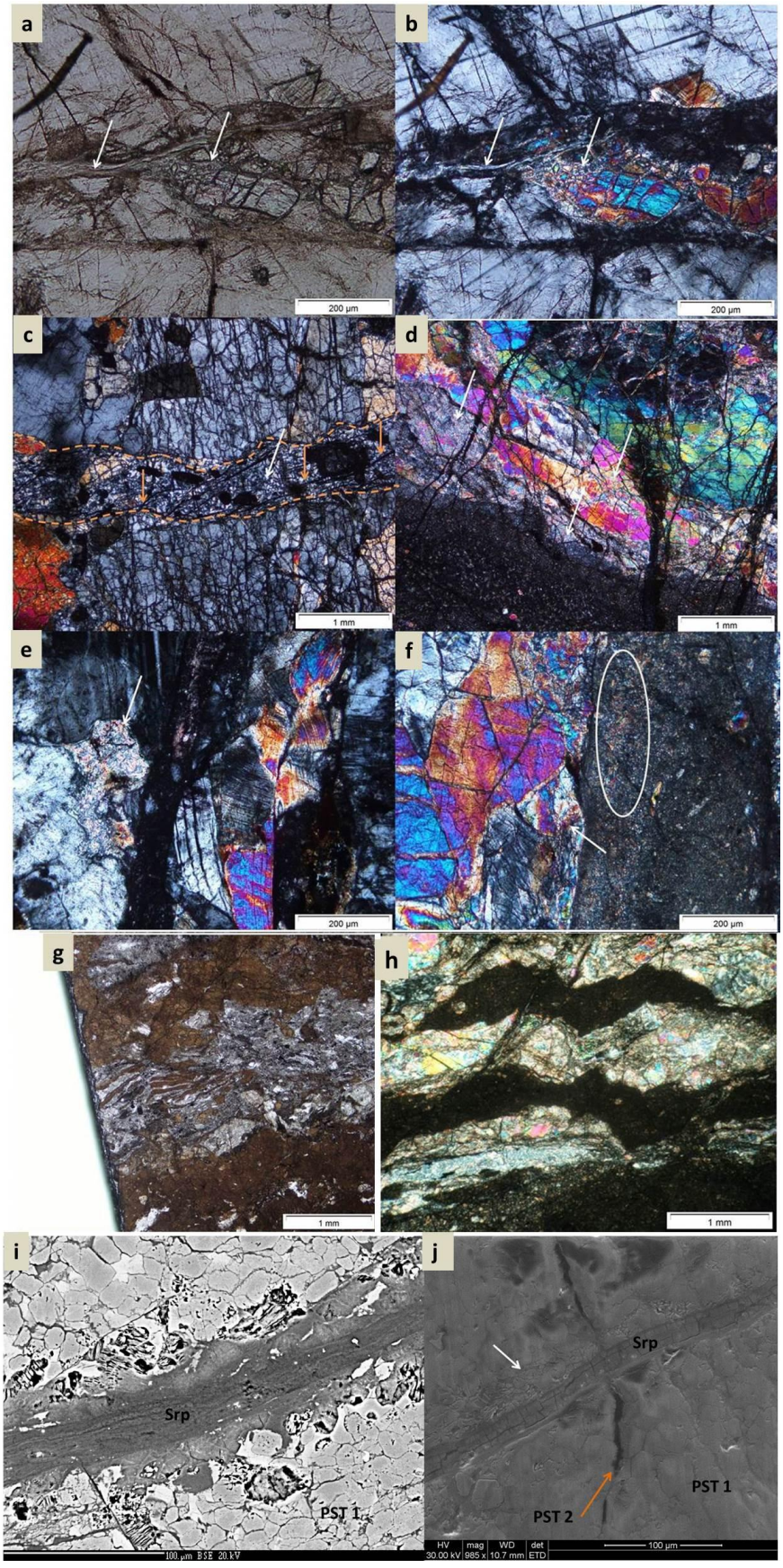

a
200 µm
b
200 µm
c
1 mm
d
1 mm
e
200 µm
f
200 µm
g
1 mm
h
1 mm
i
Srp
PST 1
100 µm BSE 20 kV
j
Srp
PST 1
PST 2
HV mag WD det
30.00 kV 985 x 10.7 mm ETD
100 µm

Fig. 8.4 Micrographs of peridotite-hosted pseudotachlyte fault veins incorporating hydrated wallrock into the melt. a) and b) are the same section in XPL and PPL respectively. White arrows indicate serpentised and chloritised wallrock olivine and clinopyroxene dragged into the fault vein. b) Isotropised areas in the wallrock orthopyroxene, which coincide with its cleavage. c) A micrograph of recrystallised pseudotachylyte (bounded by dashed lines) crosscut by isotropic melt patches and microveins (orange arrows). d) and e) XPL micrograph of sheared out, recrystallised and hydrated wallrock clasts proximal to fault vein. f) XPL micrograph of deformed olivine and clinopyroxene at vein boundary with still intact, partially fused wallrock olivine in the pseudotachylyte matrix (white circle). g) is amicrograph showing two successions of fault vein development that are overprinted by ductile folding. The dark brown (g areas are the later generation of pseudotachylyte that has been incorporated into an earlier generation. The younger pseudotachylyte is fractured and comminuted and its injections into the older pseudotachylyte have been folded. h) XPL micrograph of alternating pseudotachylyte matrix (black) and highly altered wallrock clasts that have undergone progressive deformation and recrystallisation within a larger fault zone. i) BSE image of serpentinised fault vein in fine-grained peridotite-hosted PST. Dark sheets of serpentine have crystallised at the vein margins at the expense of olivine neoblasts. j) SE image of Serpenitinised pseudotachylyte vein cross-cutting two generation of pseudotachylyte. White arrow indicates comminuted and partially fused wallrock neoblasts at the vein margin.

generation events (Fig. 8.4). The early greenschist metamorphism has been attributed to events occurring prior to PST generation, associated with ocean-continent hyperextension and hydrothermal alteration due to prograde subduction (Vitale Bravorone, 2011b). The late greenschist facies metamorphism is likely associated with slab exhumation processes.

8.4.2 Presence of hydrous minerals in the wallrock:

Hydrous minerals are present in irregular patches in both the peridotite and metagabbro wallrocks and in proximity to the boundaries of pseudotachylyte veins. The abundance of hydrous minerals in both wallrock lithologies does not have a spatial relationship with the pseudotachylytes (e.g. increasing towards vein boundaries) and appears incidental. Hydrous minerals show evidence of having formed prior to, after and in between pseudotachylyte-forming events (Fig. 8.4).

8.4.3 Pseudotachylyte:

As mentioned previously, the detailed petrographic analyses have already been published in a separate paper (Deseta et al., 2014). However, the relevant details are summarised in Tables 8.1 – 8.3 for reference. In this study we have focused on the major element results from EPMA and XRF analysis.

Fault and injection veins of pristine pseudotachylytes from both hostrock lithologies were analysed using detailed thin section petrography followed by analysis of the same samples by electron microprobe (EPMA). Fault veins are classified as those that form parallel to displacement orientation; injection veins are secondary and originate at parent fault veins and extend into the adjacent wallrock. For all vein types the boundary between the vein and the wallrock is always sharp. Fault vein boundaries are commonly marked by the presence of ultracataclasite, approximately 50 μm thick (Fig. 8.5). This gouge is unusual in that it contains a mixture of comminuted wallrock material as well as mineral ribbons and melt (Deseta et al., 2014). Compositionally the pseudotachylyte veins are highly variable at the sub-millimetre scale. This heterogeneity has been attributed to the coarse-grained nature of the wallrock (wallrock clasts are typically > 1000 μm in length and width), the disequilibrium melting of these clasts and inefficient mixing of the resultant melt (Fig. 8.6). The wallrock minerals, matrix, clasts entrained into the matrix and crystallisation products were analysed using EPMA. The fine-grained matrix of the pseudotachylyte is a bulk composition, acquired using a broad defocused beam, comprising melt and any crystallisation products or comminuted material too small to resolve and analyse with the beam (< 1 μm) (Tables 1 and 2).

BSE imaging of the pseudotachylytes reveals the presence of fluid/melt-bearing vesicles Fig. 8.7. The vesicles are indicated by black (low Z) irregularly shaped regions within the pseudotachylyte matrix. Fig. 8.7c shows multiple generations of fluid/melt-rich veins that crosscut one another, Note the cuspate and lobate rims of dendrites extending into the fluid/melt veins (white circle), indicating that the pseudotachylyte was still molten to some degree when the veins formed.

Crosscutting pseudotachylytes with matrices that contain clasts of comminuted and sheared out pseudotachylytes are indicative of multiple generations of pseudotachylyte that have formed along the same fault planes (Fig. 5).

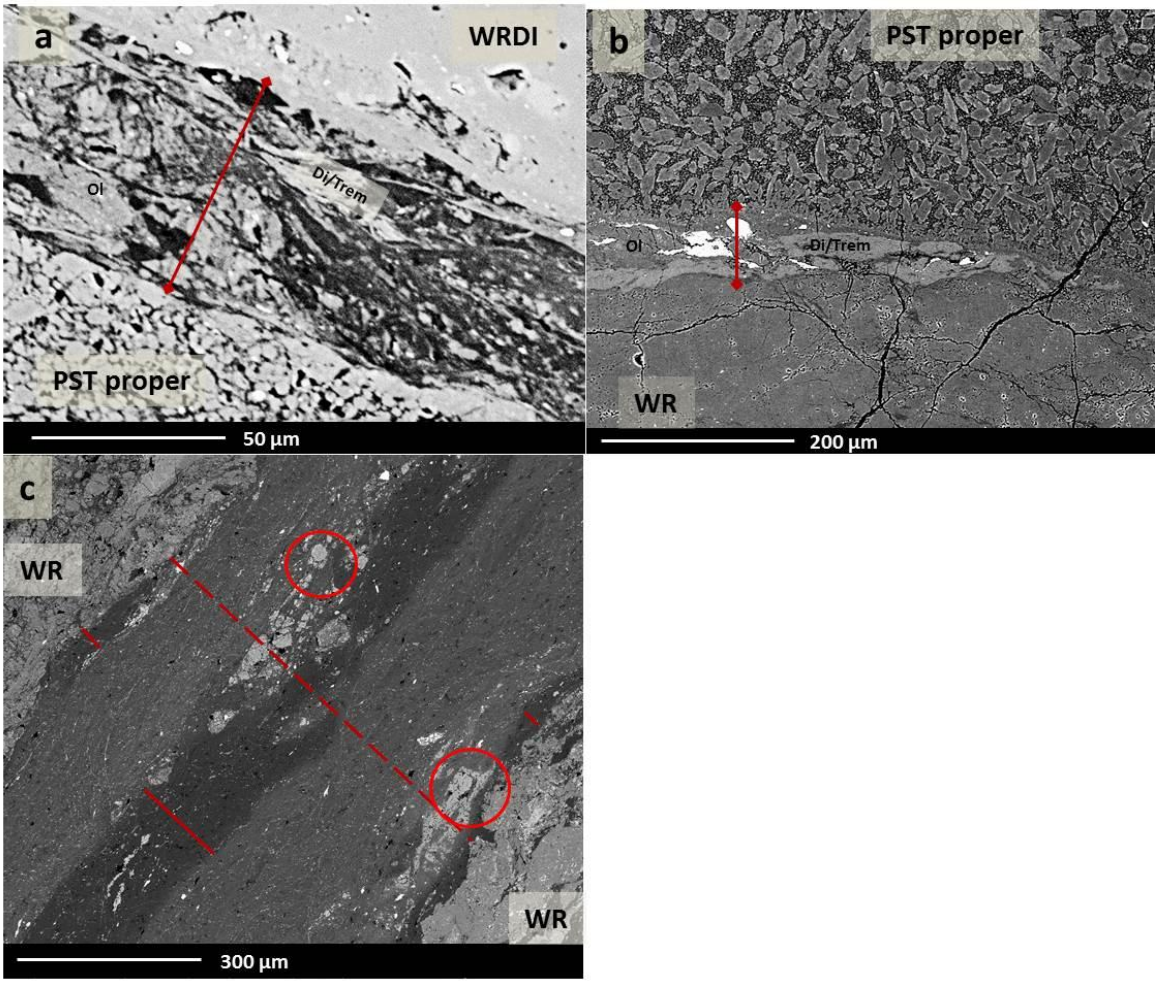


Fig. 8.5 BSE images of peridotite-hosted pseudotachylytes. a) and b) show the occurrence of ultracataclasite (width indicated by red line), which formed between the wallrock (WR) and the pseudotachylyte fault vein (PST proper). This ultracataclasite is unusual as it contains glassy material and ribbons of deformed wallrock minerals, olivine (Ol), clinopyroxene and or tremolite (Di/Trem). c) Poorly mixed; pseudotachylyte fault vein, containing microlites of diopside (circled). The melt was poorly mixed, it comprises dark, glassy regions (width shown by solid lines) with a composition of chlorite and light grey regions similar to diopside except they are non-stoichiomteric. The width of the vein is indicated by the dashed line.

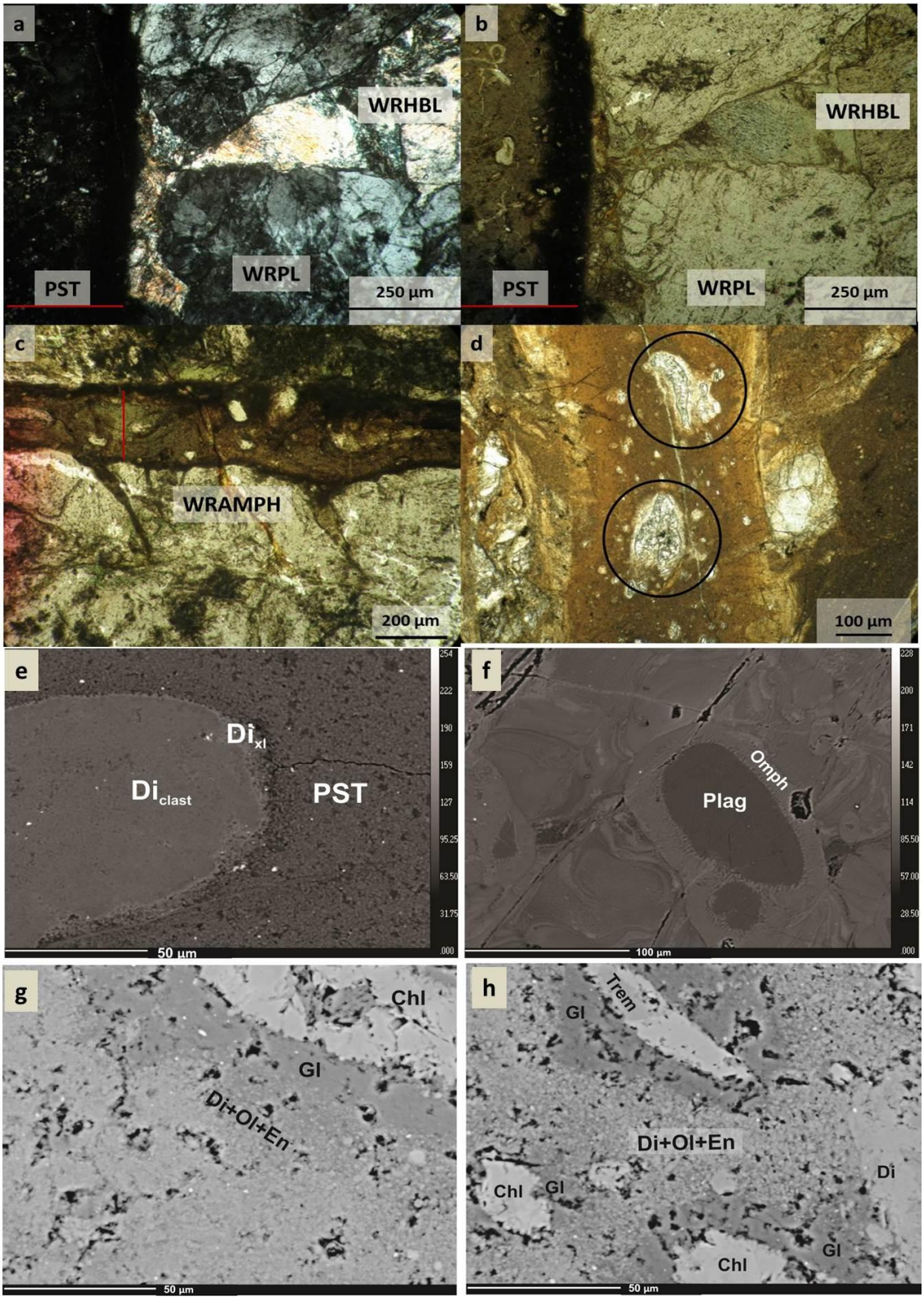

a
WRHBL
WRPL
PST
250 µm
b
WRHBL
PST
WRPL
250 µm
c
WRAMPH
200 µm
d
100 µm
e
Di$_{xl}$
Di$_{clast}$
PST
50 µm
f
Omph
Plag
100 µm
g
Chl
Gl
Di+Ol+En
50 µm
h
Trem
Gl
Di+Ol+En
Di
Chl
Gl
Gl
Chl
50 µm

Fig. 8.6 Micrographs of pseudotachylyte fault veins. Images a - c show hydrous wallrock minerals, Mg-hornblende (WRHBL) (b) and a combination of tremolite and glaucophane (WRAMPH) (c) in the wallrock that are cut by the pseudotachylytes. a) is the same as b) but under crossed polarisers. WRPL indicates wallrock plagioclase grains. d) shows a peridotite-hosted pseudotachylyte containing survivor clasts of serpentine and olivine with glassy haloes containing microlites. e) – h) are BSE images of entrained wallrock clasts fusing in a pseudotachylyte matrix. f) is from a metagabbro-hosted pseudotachylyte. The images show that grains underwent disequilibrium fusion and melt individually into the matrix. e) shows a fused clinopyroxene clast (Di_{clast}) and clinopyroxene daughter microlites (Di_{xl}). f) shows poorly mixed quenched melt showing irregular regions where individual clasts have fused. A plagioclase wallrock clast (Plag) has fused and Al-rich omphacite (Omph) has nucleated on its surface. g) and h) show partially fused wallrock minerals tremolite (Trem) and chlorite (Chl). These clasts are surrounded by glassy haloes that grade into a complex matrix of glass, microlites and comminuted wallrock material. Note the black, irregular bodies emanating off the fusing hydrous clasts. Preliminary Raman spectroscopy has shown these areas to be Al- and H_2O-rich; they are likely H_2O-rich vesicles.

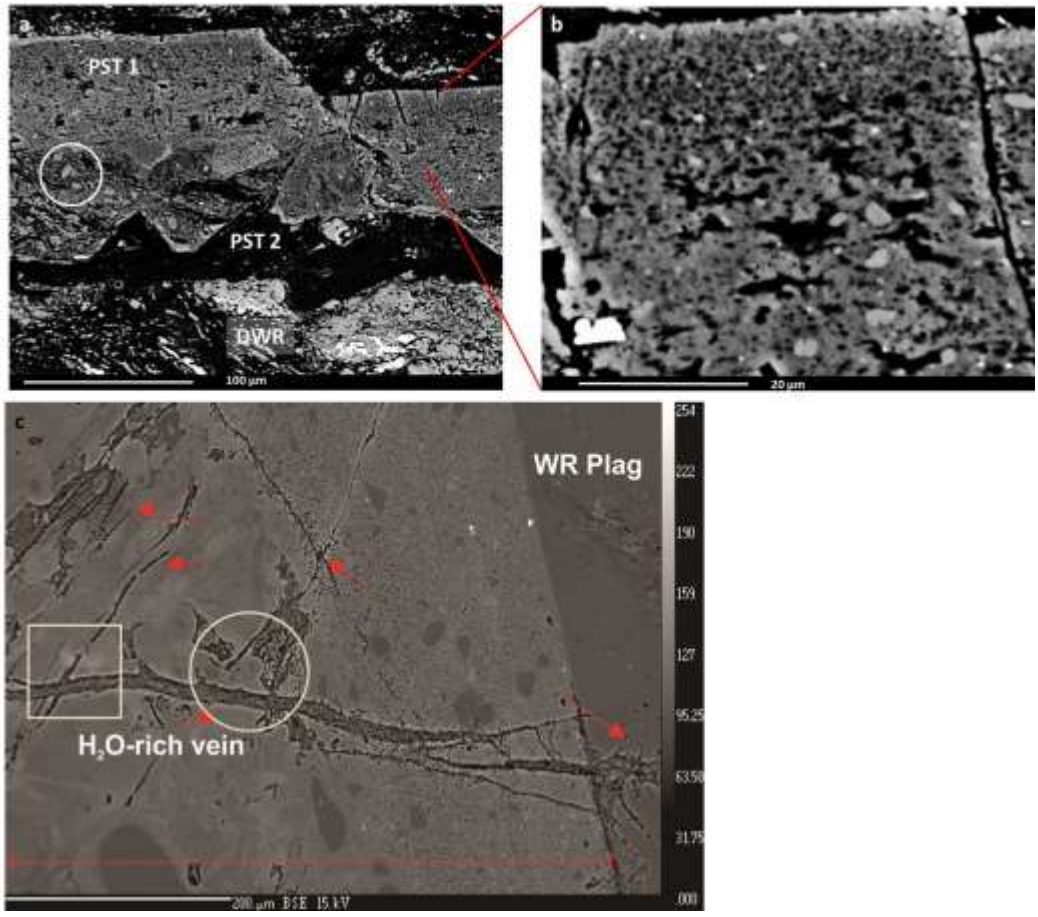


Fig. 8.7 BSE image of a peridotite-hosted pseudotachylyte. a) High contrast image showing two pseudotchylyte generations, PST 1 is the earlier generation of pseudotachylte that was reactivated to form PST 2, which has exploited the contact between PST 1 and the wallrock (DWR). Grey, irregular-shaped fragments in PST 1 are derived from an even earlier pseudotachylyte generation (white circle). b) Close up of vesiculated PST 1; the black areas indicate the presence of an H_2O-rich melt phase. Note the decrease in vesicle size, but increase in number, towards the vein boundary. This is suggestive of rapid quenching of fluids at the vein margin, whereas the longer-lived melt pockets in the centre of the vein were able to coalesce and enlarge to due greater flow stresses within the middle of vein. c) H_2O-rich vein crosscuts a pseudotachylyte vein and moves beyond the vein boundary into the wallrock (WR Plag; wallrock plagioclase grain). Pseudotachylyte vein width is indicated by the red base line; red arrows indicate H_2O-rich veins. Note that the veins form and crosscut the pseudotachylyte, while microlites are still forming as shown in the encricled area (cuspate and lobate rims of spherulites push into the H_2O-rich vein boundaries). The area enclosed by the square shows that the H_2O-rich veins crosscut one another, forming early and late generations.

8.4.3.1 Fine-grained wallrock derived pseudotachylyte

Within the peridotite hostrock, there are fault veins derived from older pseudotachylytes that have recrystallised and annealed back to a fine-grained (5 – 30 µm) peridotitic assemblage (Fig. 8.8a), (Deseta et al., 2014). The occurrence of small pseudotachylyte fault systems (veins < 100 µm across) within fine-grained peridotite (Fig. 8.8) provides an ideal contrast to the coarse-grained examples discussed in previous sections. Further, these veins are dominated by a relatively simple crystallisation assemblage of olivine, orthopyroxene and clinopyroxene. These veins have previously been interpreted to have formed through repeated fault reactivation, whereby high temperature crystallisation assemblages of olivine-diopside-clinopyroxene microlites (Fig. 8.8f, unstrained microlites) anneal to form an equigranular matrix as the fault zone returns to ambient temperatures to from peridotite again (~ 420 ˚C), (Fig. 8.8 a and c), (Deseta et al., 2014). Fig. 8.8a is an example of such an annealed fault vein matrix, dominated by olivine. Subtle variations in the birefringence of the minerals show the annealed neoblasts have inherited their orientations from the dendrites in the matrix. The degree to which the neoblasts have annealed is heterogeneous and incomplete in some places, allowing us to observe relict spaces in the neoblasts inherited from the original microlites (Fig. 8.8c, white arrows). Focusing on deformation at the boundary between the fault veins and the wallrock, we observe both inter- and intra-granular deformation (Fig. 8.8d, e, f). We measured angles between conjugate fracture sets occurring inter- and intra-granularly in grains adjacent to fault veins and compared them with healing gaps in unstrained annealing neoblasts (Fig.8.8 c and f, yellow lines). In unstrained grains, measurement of angles between sets of incompletely annealed neoblasts results in two consistent sets of angles, ~ 50 ˚ and ~ 80 ˚. The inter- and intra-granular fracture sets in the strained olivines proximal to the fault veins exhibit higher angle sets, ranging between 70 ˚ – 85˚. We also compared the fracture set angles with decorated dislocations observed in coarser-grained olivine adjacent to a fault vein (Fig. 8.9). We report two sets of dislocations; the first set is indicated by angles of ~ 75 ˚ and the second set, that overprint the first have conjugate

angles of ~ 60 ˚. Fluid/melt fronts have been observed to have moved into the wallrock from the fault veins (Fig. 8.9b, yellow arrows indicate vesicle-decorated fractures) and appear to have exploited these dislocation sets in order to move into the wallrock. Preliminary electron back-scattered diffraction (EBSD) analysis of similar coarse-grained fault veins was done (see A6 – A9 for orientation contrast maps) (Silkoset, 2013). The results of this study show that neoblasts in annealed pseudotachylyte have a random orientation and that no clear lattice preferred orientation is observed in grains proximal to fault veins. Incipient preferred domain orientation was observed, with domains rotating to parallelism with fault planes (Silkoset, 2013). The conjugate fracture sets identified in Fig. 8.8 exploit several inter- and intra-grain relationships in order to accommodate high strain rate, seismic conditions. Fractures are observed to emanate from grain boundaries inwards and from any incompletely annealed area within the neoblasts towards/away from the crystal faces. These areas constitute pre-existing weaknesses in the neoblasts and are remnants of the former dendrites, from which they may inherit their random orientation (Fig. 8.8). Fractures propagate parallel to crystal faces, suggesting slip along b and c planes and probably the a plane (Ave'Lallemant and Carter, 1970; Jung et al., 2006; Katayama and Karato, 2006). Comminution and localised melting are observed between and within neoblasts; the intergranular fusion and comminution is much more pronounced (Fig. 8d and c). Less common localised areas of wavy grain boundaries akin to grain boundary diffusion have also been observed.

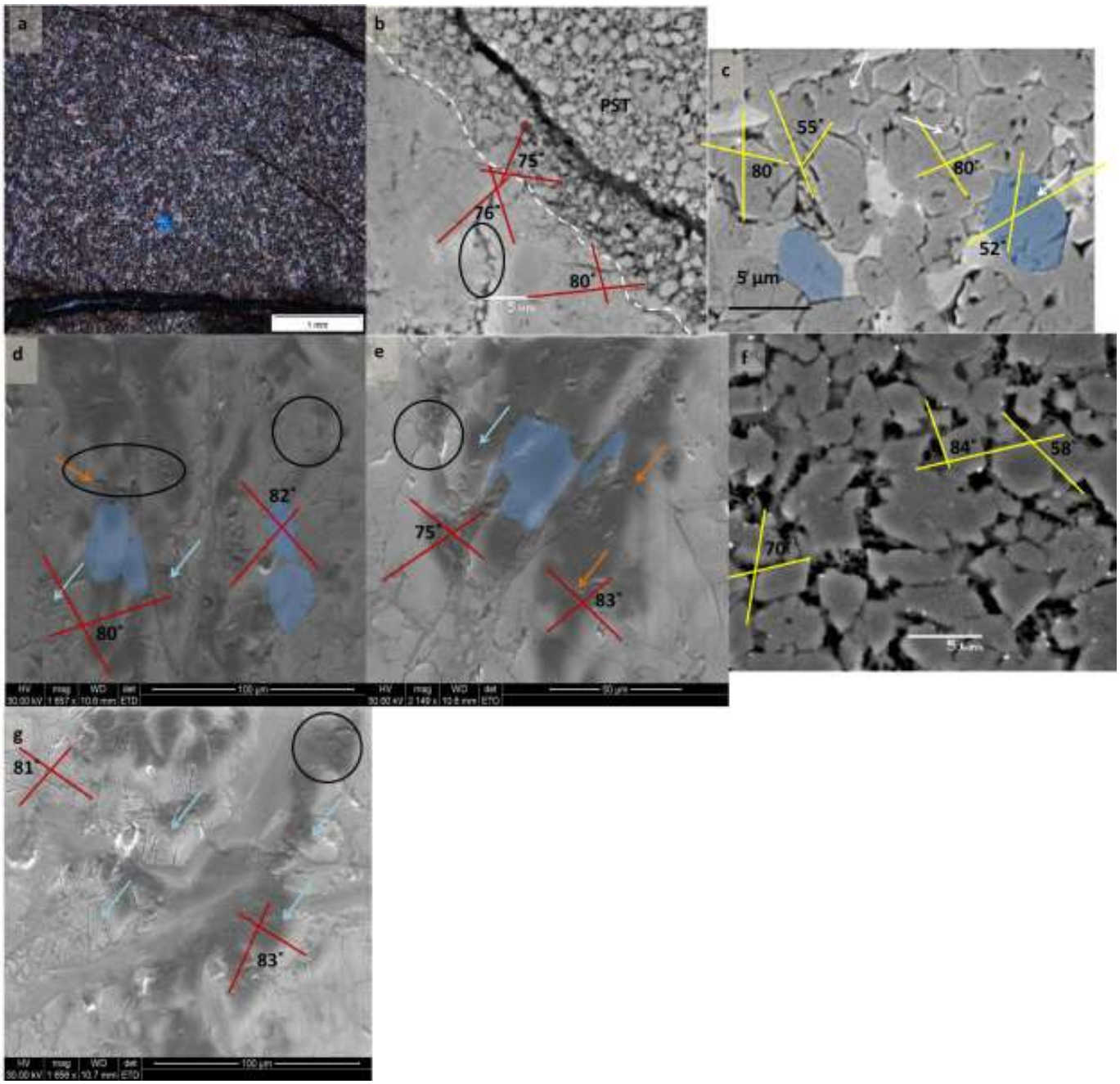


Fig. 8.8 Images of pseudotachlyte fault veins hosted by a pre-existing fault vein. a) Micrograph in XPL of a fault vein recrystallised to produce a fine-grained (5 – 30 µm) annealed matrix of olivine neoblasts, which can be seen to have overgrown the microlites quenched from the melt. The black veins crosscutting the pseudotachylyte are due to later serpentinisation. This matrix forms the wallrock for later pseudotachylytes (b – g) . b) BSE image of a pseudotachylyte fault boundary (white dashed line). Note the fracture sets in the wallrock grains (red lines), with two principal sets arising at different angles. Black circles indicates localised fusion at grain boundaries in the wallrock, accompanied by the production of angular clasts. c) Incompletely annealed olivine neoblasts (grey) with intercumulus clinopyroxene (white). The neoblasts are euhedral (blue) and retain some features of the dendrites they

have overgrown (white arrows). The planes along which annealing is incomplete in the grains produce two sets of potential planes of weakness in the crystals are shown by yellow lines. d) SE image of fault vein with strained grains at fault boundary (blue). Predominant fracture sets of internally deformed grains (blue arrows) shown by red lines. Black circles indicate wavy grain boundaries possibly produced by diffusion creep. e) SE image close-up of fault vein, showing fractured and strained wallrock neoblasts (blue). Red lines indicate predominant fracture sets. Orange arrows indicate wavy grain boundaries of neoblasts. Blue arrow indicates intragranular fractures. Black circle shows localised intergranular comminution and melting. f) BSE image of relatively unstrained olivine microlites enclosed in a vesiculated matrix of high-Al glass. Several dihedral angles are indicated by yellow lines. g) SE image of highly strained neoblasts entrained into fault vein. Intragranular fractures are pronounced. Black circle indicates saw-toothed grain boundaries. Red lines indicate intragranular fracture sets (blue arrows). Dark shadows in SE images due to sample charging.

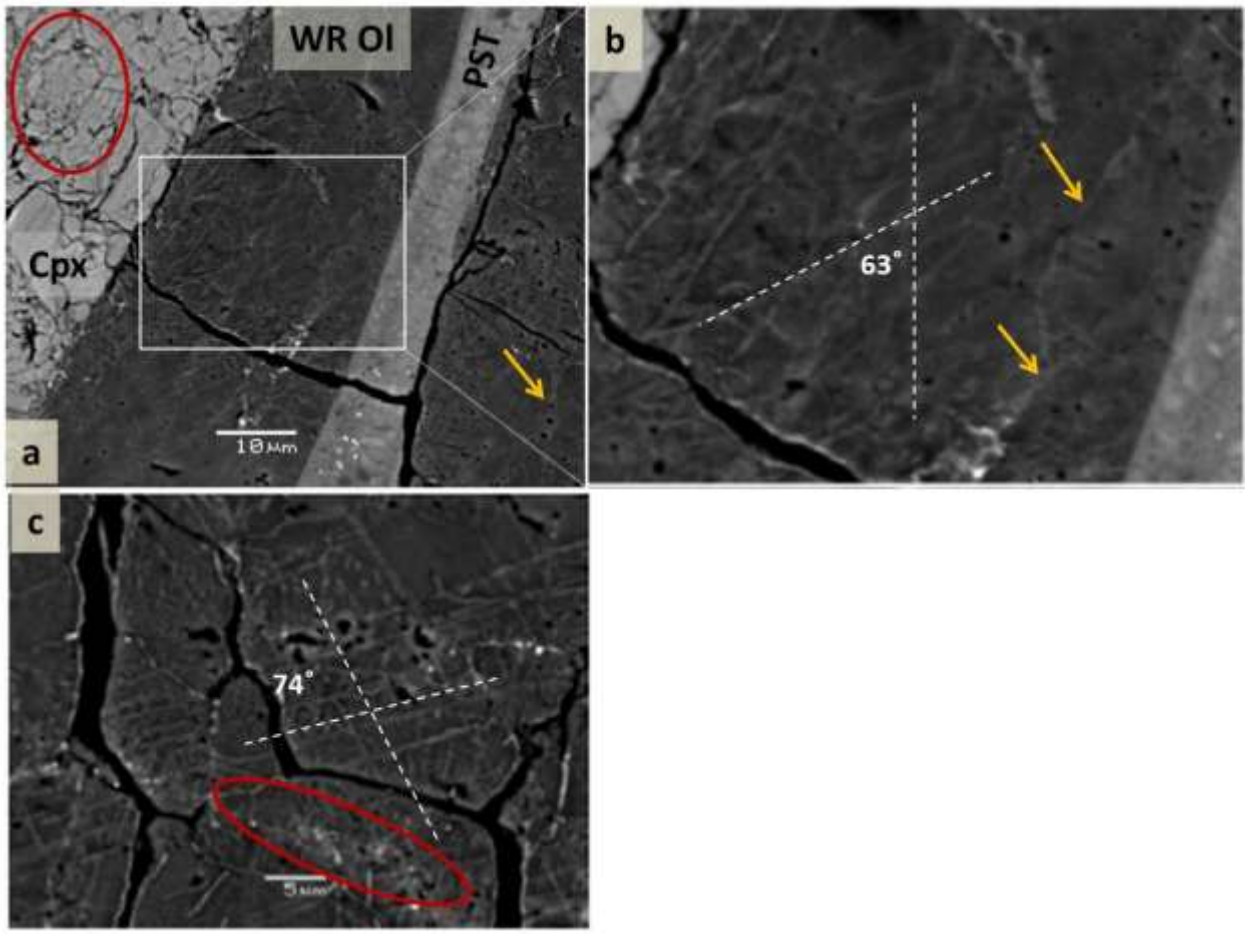


Fig. 8.9 BSE images of pseudotachylyte fault veins in peridotite. The sample contains dislocations decorated due to alteration of the fault vein to form oxides. a) Contiguous olivine (WR Ol) and clinopyroxene (Cpx) wallrock clasts, with a fault vein (PST) cutting through the wallrock olivine. Two sets of dislocations. Note the localised fusion at the boundary between the clinopyroxene and the olivine. The red circle indicates localised intragranular comminution and melting in the clinopyroxene. Yellow arrow indicates fluid/melt trails infiltrating the wallrock grains, they are marked by localised vesiculation/pocks with lighter Z values, possibly indicating fusion. b) Close-up of a). The two sets of dislocations are shown more clearly. A high angle set, cross-cut by a lower angle set (shown by white dashed lines). Yellow arrows indicate a fluid/melt front moving from the pseudotachylyte into the wallrock clasts. c) BSE imaging showing the higher angle set of dislocations in the wallrock olivine (white dashed lines). Red circle indicates localised melting of the grain. Dark shadows in SE images due to sample charging.

8.4.4 Bulk rock and mineral compositions

Ternary diagrams of wallrock minerals and the pseudotachylyte matrix for both metagabbro- and peridotite-hosted pseudotachylytes are plotted (Figs. 8.10 and 8.11). XRF analyses of wallrock samples from both hostrocks (Table 8.3) are overlain with bulk matrix analyses from the pseudotachylytes (Figs. 8.12 and 8.13). Fusion glass from the pseudotachylytes was also analysed and confirmed as non-crystalline using XRD synchrotron (refer to A1 – A5 for Laue pattern). The metagabbro-hosted glass is anhydrous and has the same approximate composition as the bulk matrix, whole rock XRF analyses and omphacite microlites (Table 8.2). In contrast, the glass from the peridotite-hosted pseudotachylytes has a large hydrous component (up to 14 wt %), a strong chlorite component, and a high Mg# of 93 (Table 8.1). The variablilty in the range of the H_2O content of the pseudotachylytes is given in Figs. 8.12 and 8.13. The microlite assemblages for both the metagabbro and peridotite pseudotachylytes have been divided into two groups: a high temperature quench mineralogy and a low temperature recrystallization/devitrification assemblage. The former assemblage constitutes those minerals crystallised immediately after the pseudotachylyte was generated, at temperatures much higher (> 1700 ˚C) than the ambient conditions (420 ˚C). The latter assemblage comprises minerals formed from glass devitification or pseudotachylyte recrystallisation once the fault zone had cooled and returned to ambient temperatures and pressures. Only the high temperature crystallisation assemblages are discussed here; the devitrification/recrystallisation products of these pseudotachylytes have already been discussed in detail (Deseta et al., 2014).

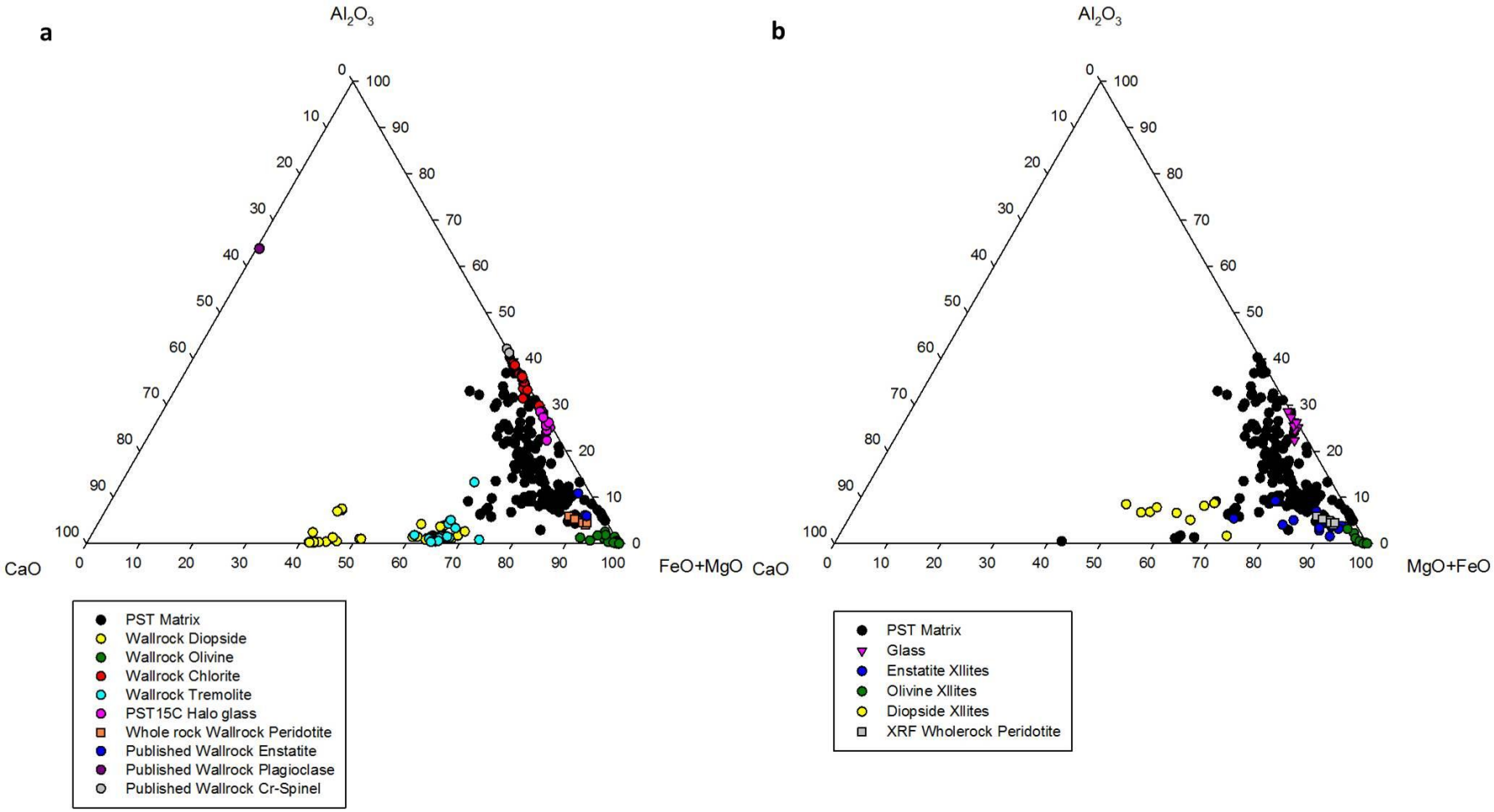


Fig. 8.10 ACF diagrams of metagabbro wallrock minerals (a) and microlites (b) compared to the pseudotachylyte bulk matrix composition (PST Matrix) and wholerock XRF data of the wallrock metagabbro (orange squares).

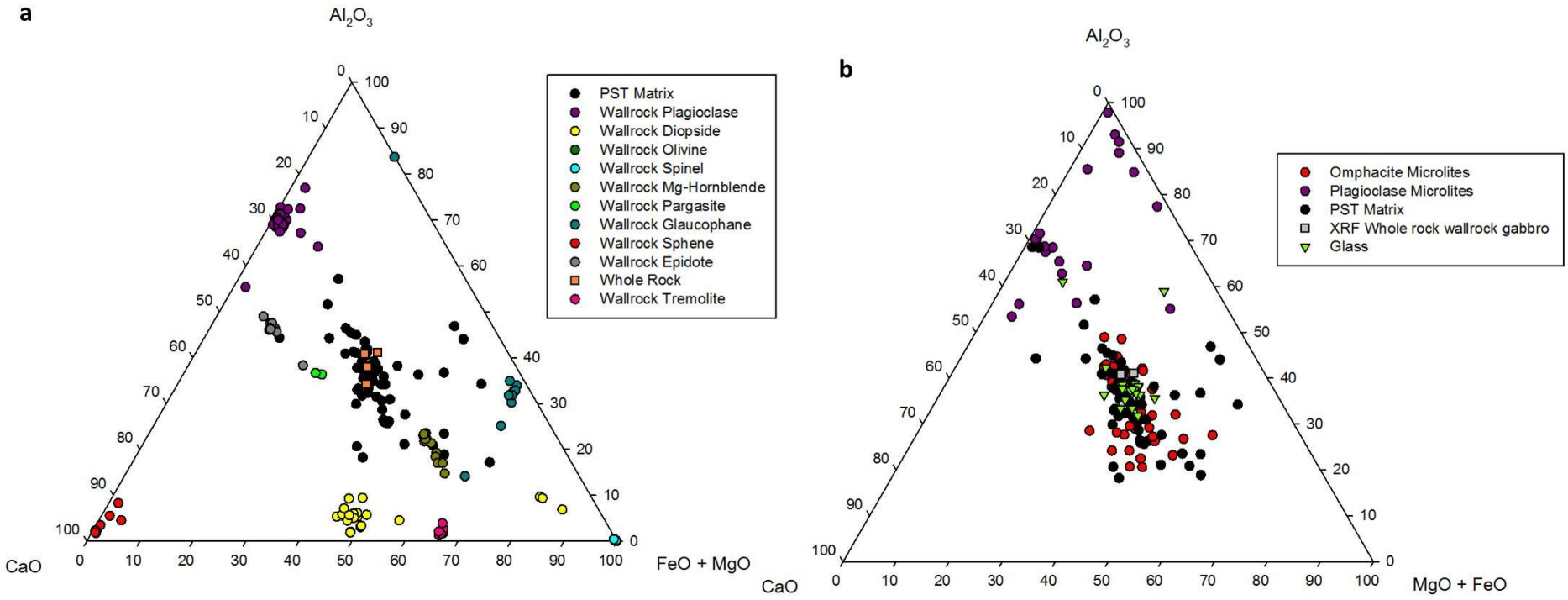


Fig. 8.11 ACF diagrams of peridotite wallrock minerals (a) and microlites (b) compared to the pseudotachylyte bulk matrix composition (PST Matrix) and Wholerock XRF data of the wallrock peridotite (orange squares).

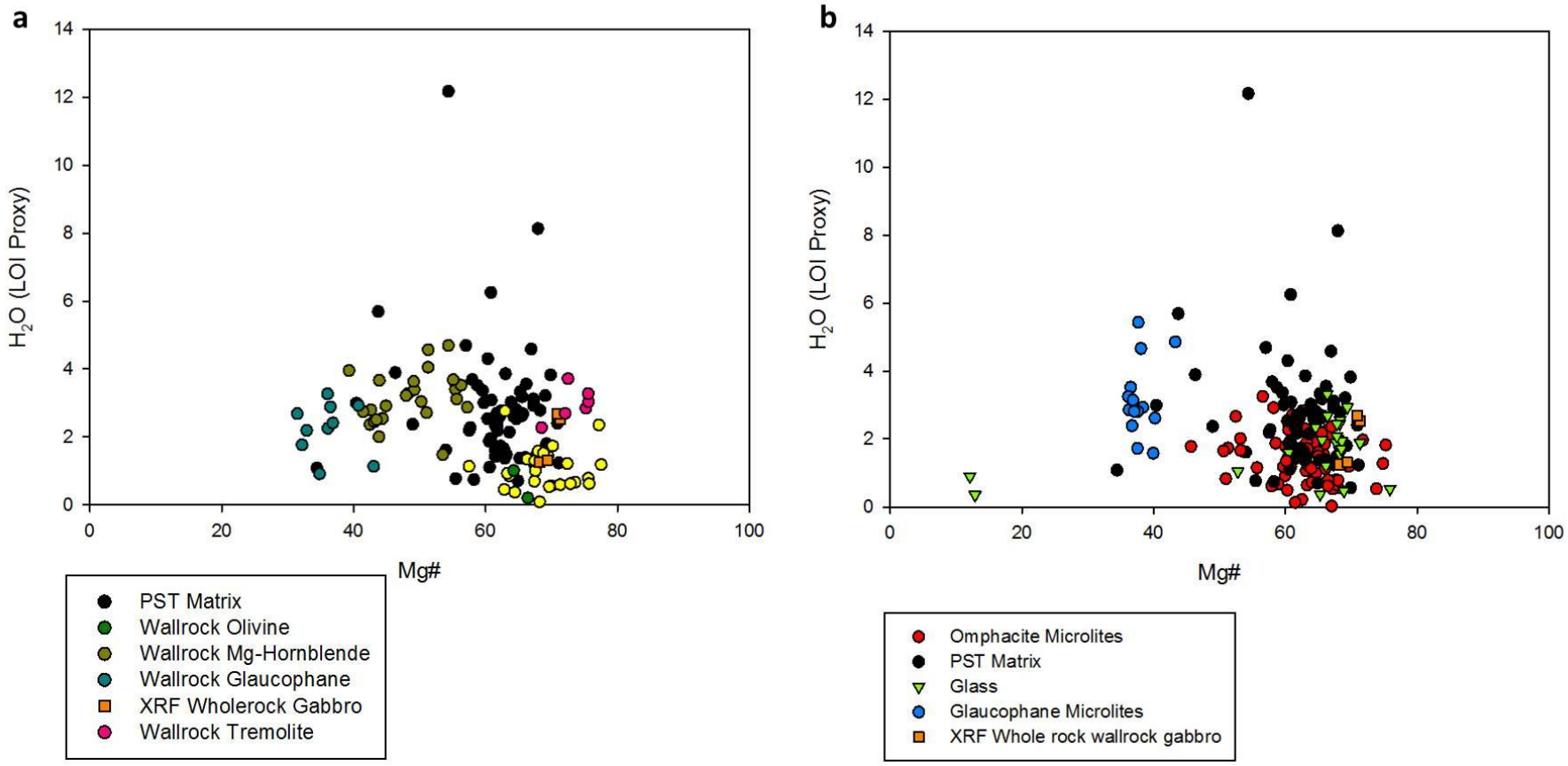


Fig. 8.12 H_2O content vs Mg # of metagabbro wallrock minerals (a) and microlites (b) compared to bulk metagabbro wallrock (orange squares) and pseudotachylyte bulk matrix (black cirlces). Loss on ignition (LOI) of XRF whole rock samples and EPMA analyses has been used as a proxy for H_2O content.

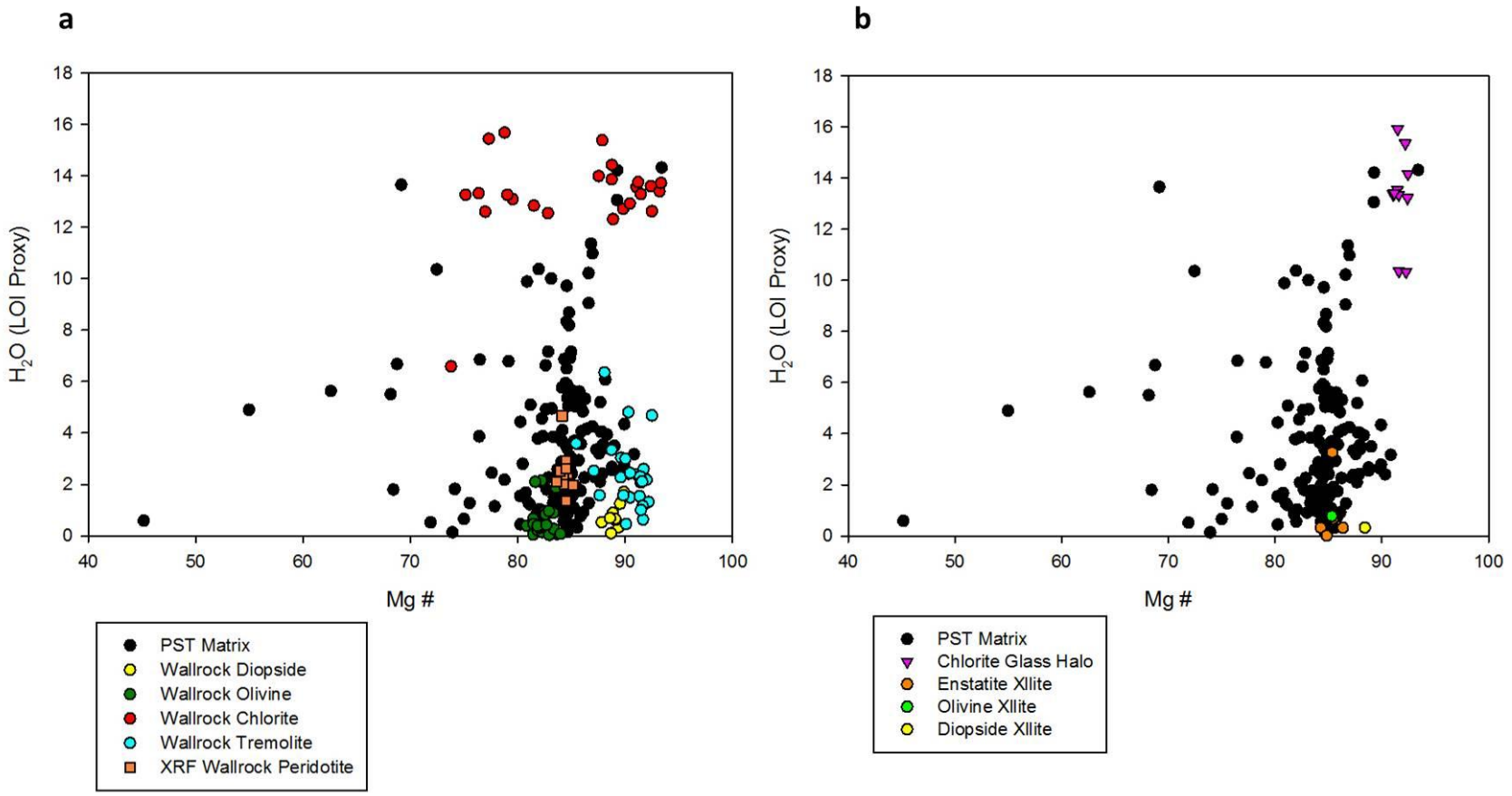


Fig. 8.13 H_2O content vs Mg # of peridotite wallrock minerals (a) and microlites (b) compared to bulk peridotite wallrock (orange squares) and pseudotachylyte bulk matrix (black cirlces). Loss on ignition (LOI) of XRF whole rock samples and EPMA analyses has been used as a proxy for H_2O content.

8.4.4.1 Metagabbro - pseudotachylyte microlites:

The crystallisation products of the metagabbro-hosted pseudotachylytes comprise a consistent, but unusual mineralogy of Al-rich omphacite and Fe-rich plagioclase, with minor accessory ilmenite. This Al-rich omphacite was previously classified as fassaite by Austrheim and Andersen (2004), but detailed EPMA revealed a closer stoichiometric affinity with the structure of sodic pyroxenes (Fig. 8.14, Table 8.4). Al in this omphacite appears to be located in the M1 (octahedral) position, rather than in the T (tetrahedral) position, indicating a large Ca-Eskola component, which, combined with the skeletal structure of the omphacite crystals, indicates a high temperature of formation (> 1700 ˚C) (Katayama et al., 2000; Konzett et al., 2007; Smyth, 1980).

8.4.4.2 Peridotite - pseudotachylyte microlites:

The high temperature crystallisation products of peridotite-hosted pseudotachylytes comprise clinopyroxene, olivine and orthopyroxene, with interstitial glass (Table 8.1). However, the entire assemblage does not crystallise uniformly within pseudotachylyte veins. Veins are populated with irregular patches of monomineralic quench material (only clinopyroxene or only olivine) and patches comprising complex laths of olivine decorated with clinopyroxene and orthopyroxene (Fig. 8.8f) (Deseta et al., 2014).

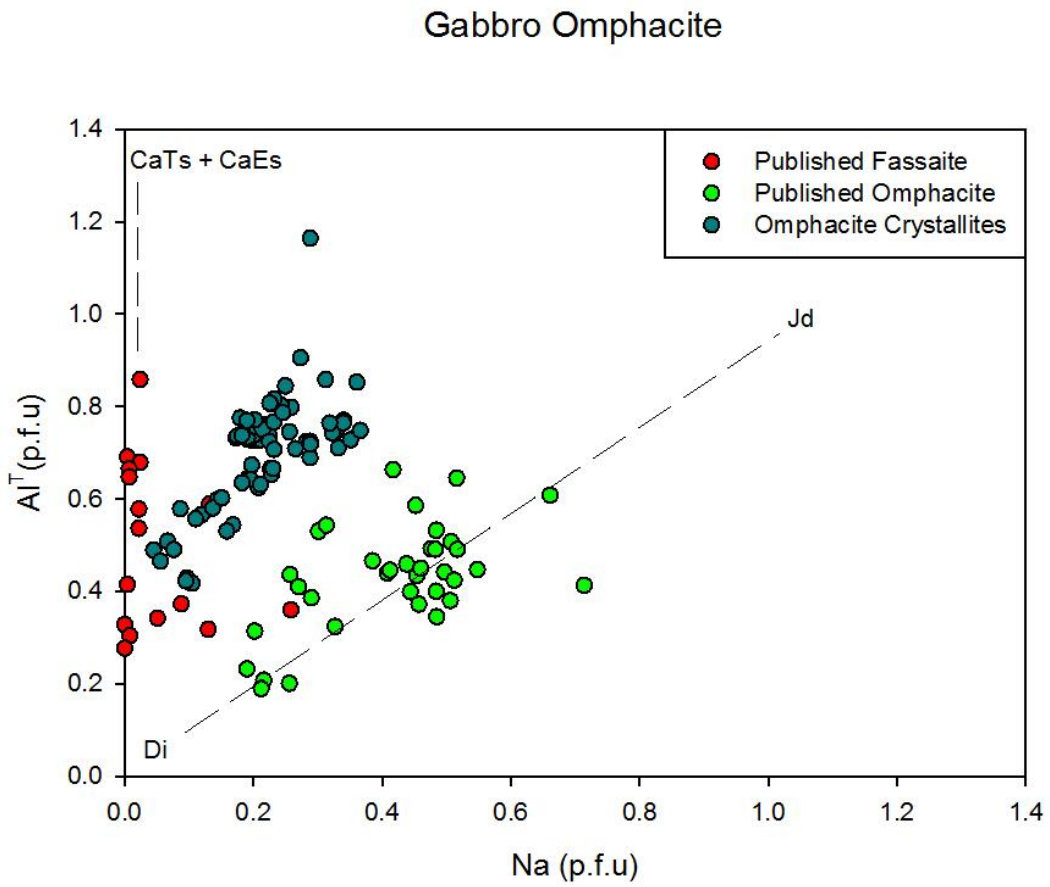


Fig.8.14 Total Al and Na of omphacite crystallites, per six oxygens, from metagabbro-hosted pseudotachylytes (blue) compared to the spectrum of published omphacites (green) and fassaites (red) from Deer et al. (2001). The dashed lines indicate the range between clinopyroxene (Di) and jadeite (Jd) end members, as well as Ca-Tschermak's and Ca-Eskola components.

8.5. Discussion

8.5.1 Style of melting and principal components involved:

The composition diagrams of the metagabbro and peridotite pseudotachylytes show wallrock compositions that overlie the bulk pseudotachylyte compositions (Figs. 8.10 – 8.13). The distributions of the pseudotachylyte bulk matrix compositions are well constrained by constituent wallrock minerals. However, in the case of the peridotite pseudotachylyte, the bulk matrix distribution is skewed towards tremolite and chlorite compositions, suggesting preferential melting of these minerals relative to others in the same assemblage due to their relatively low fracture toughness and melting temperatures (Spray, 2010). Late alteration of the pseudotachylytes, to chlorite, tremolite and serpentine, might explain the skewed distribution of the bulk matrix. However, this is considered to be unlikely as the veins are texturally pristine and thermally rounded clasts containing both chlorite and tremolite clasts have been observed (Fig. 8.6). From the data distributions in Figs. 8.10, 8.11, 8.13 and 8.14, we interpret that the pseudotachylytes formed via highly localised disequilibrium melting of wallrock minerals proximal to the fault plane, which was influenced by the relative fracture toughness of minerals participating in the reaction (Spray, 1992).

8.5.2 Influence of grain size on pseudotachylyte formation: a fine-grained peridotite vs coarse-grained peridotite case study:

SE and BSE imaging of the coarse- and fine-grained peridotite-hosted pseudotachylyte fault veins reveal that both inter- and intra-granular syndeformational faulting took place (Figs. 8.4, 8.8 and 8.9). Conjugate fracture sets for both fine- and coarse-grained examples appear to coincide approximately with crystallographic planes of weakness in neoblasts, which they inherited when they annealed microlites (Fig. 8.8). The conjugate fractures observed are suggested to coincide with activation of a, b and c slip planes and approximately coincide with those of the pseudohexagonal orthorhombic morphology

of the observed olivine neoblasts (Fig. 8.8) (Ave'Lallemant and Carter, 1970; Jung et al., 2006; Katayama and Karato, 2006; Twis and Moores, 2007).

Melt and fluids escaping the pseudotachylyte fault veins have exploited pre-existing intragranular fractures and induced locaslied melting (Figs.8.6 and 8.10). In the peridotite-hosted pseudotachylytes, at both inter- and intra-granular levels, and coarse- and fine-grain sizes, we observed fracture propagation to be controlled principally by olivine and its pseudohexagonal structure (Cmiral et al., 1998; Jin et al., 1994). From the observations in Figs. 8.6, 8.8 and 8.9 we interpret that the principal deformation mechanism in these rocks is power law creep (via dislocation creep and glide). This is in contrast to the studies of Bestmann et al. (2011) and Bestmann et al. (2012), where the authors studied the development of pseudotachylytes and associated mylonites in quartzites and tonalites. They observed wallrock grains deformed via dynamic recrystalisation along grain boundaries, forming microshear zones along which pseudotachylytes and cataclasites formed at peak shear stress and strain rate in the seismic cycle. They interpreted that the observed microshear zones were generated in association with fluid-rich conditions. Bestmann et al. (2012) observed fluid-mediated grain size reduction with increasing strain intensity towards the shear plane. In this case study we observe microcataclasites and melting (Fig. 8.9), as opposed to microshear zones. On a larger scale the observed fault zones are decorated with cataclastic transition zones (Fig. 8.6).

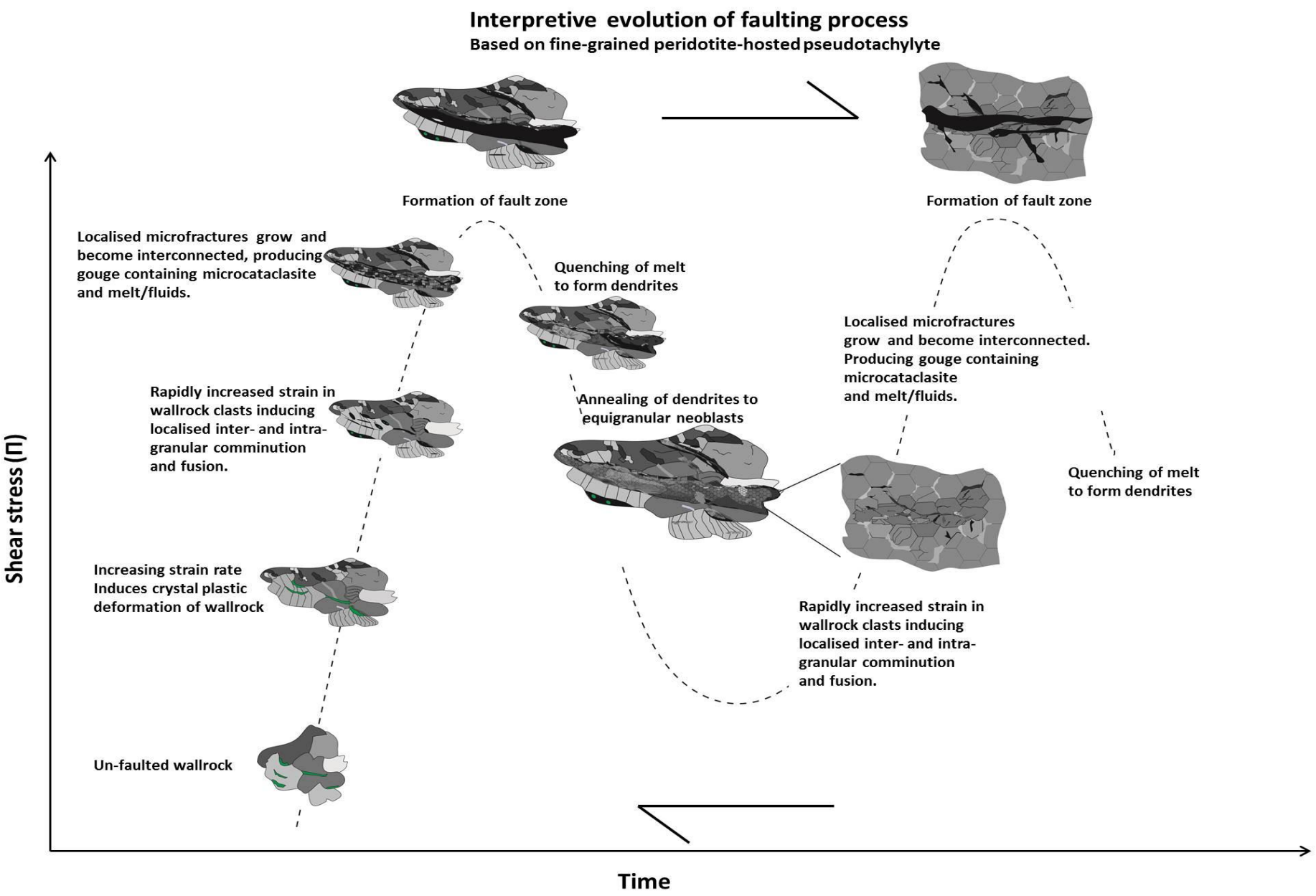

Interpretive evolution of faulting process
Based on fine-grained peridotite-hosted pseudotachylyte
Formation of fault zone
Formation of fault zone
Localised microfractures grow and become interconnected, producing gouge containing microcataclasite and melt/fluids.
Quenching of melt to form dendrites
Localised microfractures grow and become interconnected. Producing gouge containing microcataclasite and melt/fluids.
Rapidly increased strain in wallrock clasts inducing localised inter- and intra-granular comminution and fusion.
Annealing of dendrites to equigranular neoblasts
Quenching of melt to form dendrites
Increasing strain rate Induces crystal plastic deformation of wallrock
Rapidly increased strain in wallrock clasts inducing localised inter- and intra-granular comminution and fusion.
Un-faulted wallrock
Shear stress (Π)
Time

Fig. 8.15 Interpretive schematic of the faulting process based on observations from the slightly hydrated fine- and coarse-grained peridotite pseudotachylytes. The green patches represent the presence of hydrous minerals in the wallrock. The hydrous minerals are sites of weakness and undergo preferential melting during coseismic deformation, introducing H_2O in the fault system. Note that initial melting of hydrous minerals and wallrock does not initiate failure (step 4 in sketch). Enough fusion and comminution must occur to link up disparate regions of melt and comminuted materal to form a fault plane. When the PST quenches and anneals some of the fluids in the melt move into neoblasts as intracrystalline components (step 8). During later coseismic reactivation, the intracrystalline H_2O acts as sites of hydrolytic weakening, facilitating the formation of a new fault plane (step 8 - 10).

Possible reasons for these observations are that the Corsican PST evolved from mafic bulk rocks (meta-gabbro and peridotite) where deformation is controlled by olivine and pyroxene flow laws, and the rate of change in strain rate during the seismic cycle (Hobbs et al., 1986). Another possibility is the relative difference and degree of hydrolytic weakening between the two cases. Quartz, for example, can contain much more H_2O in its lattice than olivine and may also require less intra- or intercrystalline H_2O to initiate ductile flow over brittle fracturing (Spray, 2010; Karato, 1987; Boland and Tullis, 1986).

In the fine-grained peridotite-hosted PST, strained olivine neoblasts may have contained significant amounts of intra-granular H_2O due to high H_2O activity in the melt (Fig. 8.8c), and in the coarse-grained peridotite wallrock grains have been injected by local fusion melts/fluids that exploited previously activated slip planes in the grains (Fig. 8.9b) (Jung et al., 2006; Wang, 2010). As temperature increases with strain rate, the low initial temperature of the fault zone (~ 420 ˚C), coupled with a seismic strain rate may have further reduced the influence of diffusion creep in the Corsican PST (Hansen et al., 2012; Pec et al., 2012). The development of the incipient LPO observed adjacent to fault veins was possibly inhibited by the low ambient temperature of the surrounding undisturbed wallrock (420 ˚C), relative to the fault vein (> 1400 ˚C), causing diffusion kinetics to slow rapidly after faulting/stress release. Deformation experiments of forsterite at low strain rates and a sustained temperature of 1200 ˚C show evidence of grain size reduction towards the shear zone via diffusion creep and grain boundary sliding as the predominant deformation mechanisms (Hansen et al., 2012). Grain size reduction in the peridotite may have been achieved through repeated fault cycles progressively inducing the wallrock to fracture and melt, recrystallising finer-grained neoblasts (Fig. 8 8). However, there is insufficient recovery and fabric development in the fault rocks to form a well-developed mylonite zone, as observed in other case studies (Bestmann et al., 2012, 2011; Hobbs et al., 1986; John et al., 2009; Kim et al., 2010). An interpretive model summarizing the faulting process observed in this case study is shown in Fig. 8.15.

8.5.3 H_2O content of the melt:

Low totals for EPMA of bulk pseudotachylyte matrices have been confirmed for both the metagabbro- and the peridotite-hosted pseudotachylytes; these, combined with the associated BSE images of areas analysed, have been interpreted to indicate the presence of water in these melts (Figs. 8.13 and 8.14). Wallrock clasts containing hydrous minerals have been incorporated into the melts and BSE micrographs of these clasts show evidence of thermal fragmentation and fusion into the melt (Fig. 8.9). It is important to note that no evidence of solid state dehydration of minerals has been observed; hydrous minerals simply melt into the PST matrix and are enclosed by haloes of H_2O-rich melt (Fig. 8.9). Melts with variable compositions, that have not mixed efficiently are attributed to the in-situ melting of clasts and poor melt transport. The volatile content of the melts is highly variable, ranging from 0 - 4 wt % in the metagabbro pseudotachylyte, and 0 - 14 wt % in the peridotite pseudotachylyte. Not all water in the melt existed in dissolution during pseudotachylyte formation; amygdules and veins comprising exsolved hydrous fluid and melt have been observed (Figs. 8.7 and 8.9).

The exsolution of such fluids into the pseudotachylytic matrix implies that at some point after fusion of minerals and prior to the total solidification of the melt, fluids (and some melt) reached supersaturation. This is in agreement with observations made in a high pressure melting experiment by Zhang et al. (2004), who observed immediate separation of fluids from melt during fracturing. They also noted that the exsolved fluids formed veins oriented parallel to the σ_1 stress orientation. Our natural samples show that multiple stages of fluid exsolution may occur within the history of a single PST, where vesicle-rich micro-veins cross-cut one another within a single fault vein. It could be argued that the distinct orientation of the initial hydrous veins might have been parallel to σ_1, whereas the orientations of later veins were influenced by relict flow stresses after pseudotachylyte generation (Fig. 8.7). If this is the case then the first hydrous melt/veins might be produced when H_2O and melt immediately separate at the surface of fusing clasts (Fig. 8.6 e – h), in response to heating from shear stresses. The later hydrous

veins, which crosscut the pseudotachylytes, might form due to the supersaturation of H_2O in the melt as anhydrous minerals crystallise (Fig. 8.7c, white square).

Comparatively, the peridotite-hosted pseudotachylytes have more H_2O than the metagabbro-hosted pseudotachylyte (Tables 8.1 and 8.2). This is due to the higher water-content of the hydrous minerals (serpentine, chlorite and tremolite) in the wallrock peridotite relative to the metagabbro, and the preferential melting of such minerals (Table 8.3, Figs. 8.12 and 8.13). There does not appear to be any indication that there was external fluid influx during faulting; there are no obvious veins or fluidised zones associated with the pseudotachylytes or hydrous mineral-rich bleached margins at the borders of fault veins to indicate the passage of an externally derived fluid during faulting. This is not unexpected and has been observed in other studies (Mittempergher et al., 2014; Sibson, 1977b, 1975). If there was indeed no external fluid contribution, then the fluids present in the pseudotachylyte matrices would have been sourced exclusively from the melting of hydrous minerals incorporated from the wallrock (Figs. 8.4 and 8.6). The variable nature of H_2O distribution in the pseudotachylytes is consistent with the patchy distribution of hydrous minerals in the wallrock. If fluid ingress before or during faulting had occurred, one would expect to see continuous H_2O-rich zones or bands (Lund and Austrheim, 2003).

8.5.4 High-Al Omphacite:

The EPMA analyses of the metagabbro omphacite microlites show the minerals to be unusually enriched in Al_2O_3 (Fig. 8.14) (average: 16.2 wt %, range: 25.6 – 9.6 wt %; compared with ~ 8 wt % according to (Deer et al. (1992). Stoichiometry based on 6 oxygens indicates that the excess Al has an octahedral coordination, implying a tetrahedral vacancy, i.e. a dominant Eskola component of up to 20 mol % (Table 8.4). The amount of Eskola component in these omphacites is indicative of their high temperature of formation, possibly more than 1400 ˚C, as shown by experiments (Smyth, 1980; Zhang et al., 2004;

Zhao et al., 2011). Andersen and Austrheim (2006) acquired similar temperature results from microlites of clinopyroxene and orthopyroxene hosted by the same peridotitic pseudotachylytes as in this study. The high degree of vacancies in the omphacite, may act as sites hosting intracrystalline H_2O. An anhydrous mineral, inherently associated with formation in the presence of fluids, omphacite has been shown to have a relatively high capacity for intracrystalline H_2O (Angiboust et al., 2012; Jolivet et al., 2005; Moghadam et al., 2010; Smyth, 1980; Spandler et al., 2011; Zhang et al., 2004). In possible coseismic events post-dating PST formation and crystallisation in the metagabbro, hydrolytic weakening of omphacite at low temperatures (420 ˚C) may facilitate Peierls creep, and subsequent power law, creep, allowing grains to act as sites for fracture nucleation (Moghadam et al., 2010; Spandler et al., 2011; Zhang et al., 2004). As for pressure constraints, its influence on the Al content of omphacites remains uncertain (Konzett et al., 2007; Zhao et al., 2011). The crystallisation of omphacite rather than diopside in the metagabbro pseudotachylytes is principally due to a compositional control of Na in the melt, and possibly the coupled substitution of Na and Al in the pyroxene structure. The Na_2O content of the omphacite microlites is quite low, not exceeding 8 wt %. The low Na_2O, but high Al_2O_3 (and Mg and Fe) (Table 8.4) of the omphacite may be due to the slow diffusion kinetics of Na, relative to Al, in the rapidly cooling melt, such that it remained behind in the interstitial glass (Brady, 1995). In the case of the peridotite-hosted pseudotachylyte, there are not enough Na-bearing phases in the system to fuse and allow omphacite to form. In fact, even though there is sufficient Al in the peridotitic melt from the fusion of chlorite, clinopyroxene microlites do not have more than 2.3 wt % Al_2O_3 on average (Table 8.3). In contrast to the omphacite microlites, the low Al_2O_3 in peridotitic pyroxene microlites is attributed to the relatively slow diffusion kinetics of Al, compared to Mg and Fe relative in the quenching melt (Brady, 1995). The absence of Na-rich melts/fluids in these rocks may be consistent with a lack of external fluids infiltrating the fault system (Mittempergher et al., 2014).

8.5.5 Implications:

A recent high resolution tomographic study of intermediate-depth earthquakes in Hokkaido, Japan (Reynard et al., 2010) reported that the V_p/V_s (where V_p represents compressional wave velocity and V_s represents shear wave velocity) value for seismic events in the lower seismic plane in lithospheric mantle is $V_p/V_s < 1.73$. They also found that V_p varies more than V_s so that the principal control on seismicity is due to rheological anisotropy rather than composition, temperature or pressure (Reynard et al., 2010). The observed V_p/V_s values do not fit with the presence of abundant serpentine at the hypocentres ($V_p/V_s > 1.73$) but rather implies a slightly altered lherzolitic peridotite. As the stability limit of serpentine (and other hydrous minerals) resides at the approximate depth of the lower seismic plane, these results contradict the likelihood of dehydration embrittlement taking place as implied by previous studies (Hacker et al., 2004; Iyer et al., 2010; Kirby et al., 1995; Nakajima et al., 2009b; van Keken et al., 2011).

The observations made in this study are in broad agreement with the results of Reynard et al. (2010), because they suggest that hypocentres of intermediate-depth earthquakes occur in relatively dry peridotite from the lower seismic plane, as opposed to in serpentinite. This is important because it indicates that the earthquakes are generated in hostrocks that behave rigidly on the whole, faulting instead of undergoing ductile flow, as would be expected in serpentinite (Chernak and Hirth, 2011). At seismic strain rates, small amounts of hydrous minerals, altering pyroxene and olivine, act as minute regions of high viscosity contrast in the rock, focusing shear heating and nucleating sites of thermally-induced shear instabilities.

Curiously, despite the presence of serpentine in the hostrocks, in this case study, chlorite and tremolite/actinolite, and not serpentine, are the principal hydrous minerals participating in the seismic generation of high pressure peridotite-hosted pseudotachylytes. This is likely due to the composition of the peridotite hostrock, a plagioclase-spinel lherzolite, dominated by clinopyroxene, which alters more

readily to chlorite and amphibole than serpentine. Grove et al. (2009) showed that the stability limit of chlorite in the subducting slab approaches depths of up to 125 km, showing that this mineral can be subducted to intermediate-depths.

The intercalation of comminuted and altered wallrock and old PST with younger PST in coarse-grained peridotite-hosted pseudotachylytes indicates the fault zone has been repeatedly reactivated. Altered and hydrated PST cut by younger pristine PST suggests that between periods of seismicity the fault zone was exposed to fluid influx. This characteristic is only observed in the coarse-grained peridotite PST, where the thickest veins (up to 30 cm) comprise alternating layers of PST and cataclasite (for images refer to A10). Hence, it is not surprising that these thickened veins have the highest water relative to the drier fine-grained peridotite-hosted and metagabbro-hosted pseudotachylytes. An alternative example of the amplification effect of water in such fault zones would be the eclogite breccias of the Monviso Ophiolite, Italy, reported by Angiboust et al. (2012), which are also proposed to be a record of intermediate-depth paleoseismicity. These breccias are tectonic correlatives of the Schistes Lustres Complex in Corsica (Andersen et al., 2014). The brecciated eclogites lie within an eclogite facies shear zone that is 30 – 150 m wide. The mylonite comprises omphacite pseudomorphs after lawsonite and garnet containing fluid inclusions and evidence of polyphase crack-seal events, leading the authors to suggest an external fluid source to explain these high pressure breccias (Angiboust et al., 2012; Spandler et al., 2011).

Energy budget and source parameter modelling of recent magnitude 4 – 5 earthquakes in the Bucaramanga Nest, Colombia have been studied as analogues of intermediate-depth earthquakes (Prieto et al., 2013). The results from this study suggest the formation of narrow shear zones of less than 3 cm, rapid stress drops and localized positive temperature excursions of up to 600 ˚C above ambient temperatures, leading the authors to conclude that shear heating, rather than dehydration embrittlement as the more likely mechanism. The observations made by Prieto et al. (2013) are in agreement with those based on interpretations from Andersen et al. (2008).

Intracrystalline H_2O observed in incompletely annealed olivine neoblasts, and coarser-grained wallrock olivine proximal to PST fault veins formed by repeated faulting in the peridotite (Figs. 8.8 and 8.9) is another suggestion of hydrolytic weakening aiding the production of these pseudotachylytes (Green and Houston, 1995; Green and Jung, 2005; John et al., 2009; Silkoset, 2013; Zhang et al., 2004). Melting experiments performed by Zhang et al. (2004) involving 'wet' eclogite (containing 500 – 800 ppm H_2O) and 'dry' eclogite (up to 150 ppm H_2O) suggest that intracrystalline H_2O may facilitate the change in deformation mechanism, from diffusion to dislocation creep. They observed that the 'dry' eclogite was ductile under all strain rates and temperatures tested. However, the 'wet' eclogite deformed under the same conditions showed a step-wise change from ductile deformation to faulting that was dependent on high strain rates. These results are in agreement with independent modelling and tomography by John et al. (2009) and Reynard et al. (2010). Detailed analysis of intracrystalline H_2O content of clasts participating in fusion has not yet been investigated sufficiently in these rocks to determine with certainty the role that intracrystalline water may play in the production of these pseudotachylytes.

It has been assumed that intermediate-depth earthquakes and the presence of high abundances of hydrous minerals in the subducting slab are causally linked (Green and Jung, 2005; Jung et al., 2004; Kirby et al., 1995; Pec et al., 2012), and spatially associated, as demonstrated by seismological studies (Hacker et al., 2004; Nakajima et al., 2009a; Reynard et al., 2010). However, seismic studies can only be resolved down to a certain scale; earthquake hypocentres are commonly reported with vertical and horizontal errors of ~ 4 -5 km (Faccenda, 2014; Hacker et al., 2004). Given that the size of the rock packages that host the pseudotachylytes is less than 1 km in thickness and length, and the fact that they are enclosed by serpeninite, seismic analysis would not be able to resolve between the relatively dry rocks that contain the pseudotachylytes and the serpentine-rich rocks that surround them. This excludes any shortening of the rock package that may have occurred during the subduction/exhumation process. As a result, the site of intermediate-depth earthquakes, of hydrous minerals in the slab and the site of

fluids derived for hydrous arc magmas have all been placed at the same location within subducting slabs. However, by directly observing the exhumed slab rock we can resolve that this is not the case. This study, and others like it (Jin et al., 1998; John et al., 2009; Lund and Austrheim, 2003; Prieto et al., 2013), show that high pressure pseudotachylytes form in relatively dry and pristine rock packages in ophiolite lithologies and vary in degree of H_2O content from 0 – 14 wt %. The range in H_2O contents of the PST and the observations of anhydrous PST suggests the mechanism that explains these melts is not simply dependent on the presence of hydrous minerals in the wallrock, but their relative quantity and toughness within the deforming bulk assemblage (Spray, 2010). A recent experimental study by Chernak and Hirth (2011), aimed at inducing syndeformational antigorite dehydration at high shear stresses in order to test if the associated faulting instabilities predicted by thermal modeling were produced (Jung et al., 2004). The experimental conditions of 1.0 – 1.5 GPa, 400 ˚C – 700 ˚C are similar to the lower pressure limit and ambient temperatures of the rocks in this case study. The results of Chernak and Hirth (2011) indicate that at high strain rates, high temperatures and pressures, antigorite exhibits stable faulting, or aseismic slip, without melting.

With regard to the mechanism that produces high pressure pseudotachylytes, we are increasingly observing that the rheological behaviour of the deforming bulk rock may be the principal control (John et al., 2009; Spray, 2010). In this study, 'wet' peridotite fault veins are generally the thickest veins, featuring more brittle characteristics than their drier counterparts, with pseudotachylyte matrices rich in angular and comminuted survivor clasts. These veins locally contain the greatest abundance of chlorite and tremolite wallrock clasts. The 'dry' peridotite and metagabbro hostrocks typically yield finer, more discrete vein networks, due to the relatively higher fracture toughness of the anhydrous wallrock minerals (Spray, 1992). By comparing two rock types that contain high pressure pseudotachylytes likely formed under the similar pressure conditions of 1.5 – 2.6 GPa, and external stresses up to > 600 MPa

(Andersen et al., 2008), we can identify and distinguish the compositional charactertistics of pseudotachylyte generation. The presence of a moderate abundance of hydrous minerals in an anhydrous wallrock will enhance deformation due to their lower relative viscosity and fracture toughness, resulting in fusion and strongly contributing to thermal runaway. However, free H_2O produced through localised dehydration or otherwise, is not a prerequisite. The rock package must remain rigid in order to allow the build-up of stresses that produce pseudotachylytes. Dehydration of the surrounding serpentinite mylonites could well take place, but there is no evidence for it in those parcels of rock that host pseudotachylytes. Further, the production of high pressure pseudotachylytes need not be linked to hydrous melt production for arc magma sources. Dehydration reactions of the more hydrated regions of the subducting slab are more likely to be the source of hydrous material for arc magmas than the relatively anhydrous rock packages that host the pseudotachylytes. Hence, the generation of intermediate-depth earthquakes might not be fundamentally related to arc magma sources other than the fact they the both occur in similar spatial-temporal localities in subducting slabs.

8.5.6 Summary of conclusions:

In order to better understand the role of water in intermediate-depth earthquakes we performed a detailed geochemical, mineralogical and micro-textural analysis of high-pressure pseudotachylytes reported as relicts of such events. We suggest that the studied seismic rupture events took place along the lower plane (intra-plate position) of a double seismic subduction zone. From this study we conclude:

- There is no indication that free water was present prior to generation of pseudotachylytes, suggesting that the abundant water dissolved in the pseudotachylyte melts (up to 14 wt%) was locally generated by shear-heating and melting of pre-existing hydrous minerals and water-bearing minerals within the fault zones.

- Fluids were present in the hostrocks as hydroxyl ions in water-bearing minerals and as intracrystalline impurities but not chemically-bound water in anhydrous wallrock minerals.
- Evidence for prograde metamorphic dehydration reactions has not been observed.
- Increasing amounts of water present in the pseudotachylyte melts correspond with increasing fault-vein complexity, vein thicknesses and the thickness of the fault damage zones. This is exemplified by the comparison of peridotite and metagabbro fault-veins, where the ultramafic pseudotachylytes are both more complex, show more cataclastic deformation features and have higher water contents.
- Relative fracture toughness and melting/breaking temperature of wallrock minerals influences the bulk composition of PST.
- Presence of water in rocks that otherwise are dominated by coarse-grained anhydrous minerals (olivine, pyroxenes) is a fundamental facilitator in generating pseudotachylytes through the preferential melting of hydrous wall-rock minerals, as well as by the hydrolytic weakening of dissolved water in anhydrous minerals.
- Fault vein orientation at nucleation sites in fine-grained examples suggests a crystallographic control on fault propagation. In the case of the peridotitic pseudotachylytes, olivine as the most abundant and toughest mineral in the rock assemblage is likely to exert a principal control on the orientation of pseudotachylyte fault and associated injection veins.
- Al-rich omphacite microlites that crystallised directly from mafic pseudotachylytes in metagabbro provide additional evidence to quantify the thermal excursion (1400 - 1700˚C) associated with the shear heating that formed pseudotachylytes, from a regional temperature of approximately 420˚C.

Acknowledgements

This work is supported by Wits University, the National Research Foundation and the Mellon Foundation as well as the Norgwegian Research Council Centre of Excellence grants (No. 223272) to CEED, Oslo University. Thanks to Petter Silkoset and Prof. M. Zolensky of NASA Space Johnson Center for assisting with EBSD data and XRD synchrotron analysis of some samples (see A1 – A10 for reference images).

List of tables

Metagabbro-hosted		Pseudotachylyte											
		Wallrock mineral averages							Microlite mineral averages				
Wt% analysis	Diopside	Plagioclase	Mg-Hornblende	Olivine	Glaucophane	Tremolite	Epidote	Sphene	Sphene	Plagioclase	Omphacite	Glass	Bulk Matrix
SiO_2	51.78	53.33	47.57	38.75	55.42	56.47	39.40	29.79	30.88	52.53	50.49	51.62	49.35
Al_2O_3	2.45	28.33	7.81	0.01	10.22	0.89	25.17	1.16	1.98	26.51	16.23	17.10	15.59
FeO	6.70	0.46	13.74	20.73	13.87	7.05	4.77	0.39	1.34	1.27	5.59	4.95	6.46
MnO	0.23	0.01	0.22	0.32	0.08	0.28	0.20	0.01	0.02	0.02	0.12	0.09	0.12
MgO	15.07	0.22	12.67	39.75	8.52	19.27	1.84	0.06	0.16	1.08	9.74	10.44	10.28
CaO	21.36	11.53	11.92	0.05	3.01	12.81	22.88	28.24	28.00	12.52	12.60	11.96	12.15
Na_2O	0.43	5.07	1.53	0.01	5.98	0.16	0.13	0.03	0.08	4.51	3.17	1.98	2.48
K_2O	0.01	0.05	0.10	0.00	0.03	0.02	0.00	0.00	0.01	0.03	0.04	0.04	0.10
TiO_2	0.67	0.07	1.32	0.02	0.37	0.02	0.08	40.15	35.86	0.12	0.52	0.38	0.70
Cr_2O_3	0.20	0.01	0.05	0.01	0.02	0.00	0.06	0.01	0.02	0.01	0.07	0.06	0.08
NiO	0.01	0.01	0.02	0.12	0.01	0.05	0.01	0.02	0.01	0.01	0.02	0.03	0.03
Total	**98.82**	**99.10**	**96.95**	**99.78**	**97.54**	**97.03**	**94.55**	**99.87**	**98.36**	**98.59**	**98.59**	**98.65**	**97.35**

Table 8.1. Average EPMA for minerals associated with metagabbro-hosted pseudotachylyte. . Individual analyses can be found in A11 – A28.

Peridotite-hosted	Pseudotachylyte								
	Wallrock mineral averages				Microlite mineral averages				
Wt% analysis	Olivine	Diopside	Chlorite	Tremolite	Olivine	Diopside	Enstatite	Glass	Bulk Matrix
SiO_2	41.33	54.23	32.69	57.32	43.32	55.16	51.21	38.05	42.35
Al_2O_3	0.16	0.65	18.96	0.81	0.45	2.36	2.36	12.58	9.15
FeO	10.06	3.97	5.16	2.61	8.21	3.57	5.71	2.87	6.88
MnO	0.15	0.09	0.02	0.07	0.10	0.07	0.10	0.02	0.08
MgO	47.57	22.98	29.34	24.04	47.00	27.37	35.62	31.98	33.36
CaO	0.32	17.87	0.29	12.45	0.34	11.04	3.75	0.37	4.00
Na_2O	0.01	0.03	0.05	0.04	0.02	0.02	0.04	0.02	0.21
K_2O	0.00	0.00	0.01	0.01	0.00	0.00	0.00	0.02	0.01
TiO_2	0.01	0.03	0.03	0.04	0.01	0.08	0.05	0.19	0.16
Cr_2O_3	0.02	0.06	0.20	0.10	0.27	0.15	0.69	0.44	0.33
NiO	0.36	0.09	0.14	0.10	0.31	0.11	0.19	0.17	0.21
Total	**100.00**	**100.00**	**86.89**	**97.58**	**100.04**	**99.92**	**99.72**	**86.70**	**96.82**

Table 8.2. Average EPMA for minerals associated with peridotite-hosted pseudotachylyte. Individual analyses can be found in A29 – A40.

SAMPLE	Rock type	SiO2	Al2O3	Fe2O3	FeO	MnO	MgO	CaO	Na2O	K2O	TiO2	P2O5	Cr2O3	NiO	LOI	TOTAL	Mg#
H7	**Metagabbro**	50.27	18.22	0.55	4.53	0.10	9.74	12.12	2.77	0.04	0.28	0.03	0.08	0.03	1.25	100.01	68.24
H8	**Metagabbro**	50.29	14.96	0.56	4.47	0.10	11.11	13.18	2.33	0.03	0.29	0.02	0.09	0.02	2.53	99.98	71.29
COR-09-05	**Metagabbro**	48.91	18.47	0.55	4.49	0.10	10.93	11.05	2.64	0.03	0.18	0.02	0.05	0.03	2.68	100.13	70.90
COR-25-05	**Metagabbro**	50.39	16.78	0.57	4.60	0.10	10.40	12.35	2.85	0.03	0.35	0.03	0.05	0.02	1.32	99.84	69.34
H1	**Peridotite**	43.93	2.54	0.89	7.21	0.13	39.26	2.40	0.06	0.00	0.07	0.01	0.38	0.28	2.92	100.08	84.48
H2	**Peridotite**	44.75	3.08	0.87	7.04	0.14	38.38	3.34	0.09	0.00	0.09	0.01	0.51	0.28	1.35	99.93	84.50
H3	**Peridotite**	43.71	2.13	0.90	7.28	0.14	40.25	2.22	0.12	0.01	0.05	0.01	0.40	0.29	2.41	99.90	84.68
H4	**Peridotite**	43.51	2.37	0.93	7.52	0.14	40.46	2.41	0.06	0.00	0.06	0.01	0.39	0.30	1.99	100.15	84.33
H5	**Peridotite**	42.94	2.36	0.94	7.58	0.14	40.62	1.97	0.08	0.00	0.06	0.01	0.46	0.30	2.38	99.83	84.28
H6	**Peridotite**	43.59	2.68	0.87	7.07	0.13	37.49	2.87	0.08	0.00	0.07	0.01	0.38	0.29	4.66	100.18	84.14
COR-31-05	**Peridotite**	43.93	2.67	0.92	7.42	0.15	38.86	2.51	0.09	0.01	0.07	0.02	0.45	0.30	2.53	99.92	83.97
COR-32-05	**Peridotite**	43.08	2.42	0.92	7.40	0.14	40.26	2.11	0.12	-0.01	0.06	0.01	0.32	0.30	2.61	99.73	84.47
COR-41-05	**Peridotite**	43.81	2.09	0.87	7.09	0.13	40.68	2.20	0.10	0.00	0.05	0.01	0.44	0.30	1.97	99.73	85.16
Mg # formula: (MgO)/(MgO+FeO+Fe2O3)*100																	

Table 8.3. Wholerock XRF data for metagabbro and peridotite wallrocks.

Omphacite microlite recalculation										
Formula	$M2_1M1_1T_2O_6$									
Name	Omph1	Omph2	Omph3	Omph4	Omph5	Omph6	Omph7	Omph8	Omph9	Omph10
SiO_2	50.2	50.29	51.66	50.57	50.35	48.81	51.29	52.76	50.63	49.87
TiO_2	0.44	0.45	0.43	0.4	0.41	0.68	0.37	0.43	0.63	0.45
Al_2O_3	16.98	16.78	17.34	16.98	16.9	11.81	18.44	20.03	13.28	16.78
Fe_2O_3										
FeO										
FeO_T	4.97	5.11	5.31	4.94	5.15	4.94	4.25	4.67	5.09	5.09
MnO	0.12	0.09	0.08	0.12	0.13	0.12	0.11	0.06	0.1	0.09
MgO	9.8	9.82	8.09	8.97	9.39	13.92	7.8	7	12.6	9.87
CaO	13.36	12.95	10.85	12.87	12.56	18.15	12.34	9.59	16.16	12.9
Na_2O	2.61	2.78	4.64	3.13	3.07	0.94	3.63	4.43	1.71	2.97
K_2O	0.03	0.06	0.06	0.03	0.03	0.02	0.02	0.03	0.04	0.05
P_2O_5										
Cr_2O_3	0.09	0.08	0.08	0.07	0.08	0.08	0.08	0.08	0.07	0.07
Total	**98.6000**	**98.4100**	**98.5400**	**98.0800**	**98.0700**	**99.4700**	**98.3300**	**99.0800**	**100.3100**	**98.1400**
Si	1.80	1.81	1.85	1.82	1.82	1.78	1.83	1.85	1.81	1.80
Al	0.72	0.71	0.73	0.72	0.72	0.51	0.78	0.83	0.56	0.72
Ti	0.01	0.01	0.01	0.01	0.01	0.02	0.01	0.01	0.02	0.01
$Fe^{2+}T$	0.15	0.15	0.16	0.15	0.16	0.15	0.13	0.14	0.15	0.15
Mn	0.00	0.00	0.00	0.00	0.00	0.00	0.00	0.00	0.00	0.00
Mg	0.53	0.53	0.43	0.48	0.51	0.75	0.42	0.37	0.67	0.53
Ca	0.51	0.50	0.42	0.50	0.49	0.71	0.47	0.36	0.62	0.50
Na	0.18	0.19	0.32	0.22	0.21	0.07	0.25	0.30	0.12	0.21
K	0.00	0.00	0.00	0.00	0.00	0.00	0.00	0.00	0.00	0.00
P	0.00	0.00	0.00	0.00	0.00	0.00	0.00	0.00	0.00	0.00
Cr	0.00	0.00	0.00	0.00	0.00	0.00	0.00	0.00	0.00	0.00
Total	**3.91**	**3.92**	**3.93**	**3.91**	**3.92**	**3.99**	**3.89**	**3.87**	**3.95**	**3.93**

Table 8.4.A representative group of ompahcite microlite compositions recalculated per 6 oxygens.

Large Subduction Earthquakes along the fossil MOHO in Alpine Corsica

Geology (2014) Vol. 42, p. 395 - 398

Torgeir B. Andersen[1*], Håkon Austrheim[2], Natalie Deseta[3], Petter Silkoset[1] and Lewis D. Ashwal[3]
[1]Centre of Earth Evolution and Dynamics and [2]Physics of Geological Processes, University of Oslo, P.O. Box 1047, Blindern 0316 Oslo Norway
[3]School of Geosciences, University of Witwatersrand, Wits 2050 Johannesburg, South Africa
*Correspondence to: t.b.andersen@geo.uio.no

Abstract

Subduction earthquakes release vast amounts of energy to crust and mantle lithosphere. The products of such drastic deformation events can rarely be observed in the field because they are mostly lost by subduction. We present new observations of deformation products formed by fossil subduction earthquakes in Alpine Corsica. Deformation products of a few very large and numerous small intermediate-depth earthquakes are preserved along the exhumed palaeo-Moho in the Alpine Liguro-Piemontese basin. The abrupt release of energy resulted in localized shear heating events that completely melted both gabbro and peridotite along the Moho. The large volume of melt that were generated by at most a few very large earthquakes can be studied in the fault- and injection vein breccia complex along the Moho fault. The energy required for wholesale melting of a large volume of peridotite pr. m^2 fault plane, combined with previous estimates of stress-drops show that very large earthquakes took place at the Moho of the subducting plate. Since these fault rocks represent intra-plate seismicity we suggest they formed at the lower seismogenic zone by analogy with present-day subduction.

9.1. Introduction

Pseudotachylytes (PST) are melt rocks formed by shock events such as extra-terrestrial impacts or more commonly earthquake faulting. Such sudden release of strain energy may be associated with very high temperature and may melt rocks irrespective of bulk-composition (Sibson, 1977; Spray, 1995). Exhumed high-pressure and low-temperature (HP-LT) provinces are regions recording low geotherms characteristic of subduction and collision. Wadati-Benioff-zones are the most seismically active domains on Earth and host the largest known earthquakes. Ancient HP-LT terrains may therefore provide windows for making direct observation of deformation phenomena produced by the processes related to collision and subduction earthquakes (Austrheim and Boundy, 1994). Previous studies in the blueschist- to lawsonite-eclogite terrains of Alpine Corsica (Ravna et al., 2010; Vitale Brovarone et al., 2011) have documented co-seismic slip evinced by numerous but mostly small PST fault- and injection veins (Andersen and Austrheim, 2006; Austrheim and Andersen, 2004; Deseta et al., 2014). These studies have also shown that complete melting and HP-quenching of gabbro and peridotite took place and that very large stresses (>570 MPa) were released by small (< 5 cm) slip-events in the peridotite (Andersen et al., 2008). Field examples of PST produced by intermediate depth earthquakes are rare (Austrheim and Boundy, 1994; John and Schenk, 2006; Lund and Austrheim, 2003), not because the processes they record are rare, on the contrary, but the likelihood of exhumation of such fault-rocks to the surface enabling direct observation is very small indeed. Such rocks will normally be lost permanently by densification (Bjornerud et al., 2002) and subduction or be restructured and recrystallized during exhumation. Therefore, only a handful occurrences worldwide are known (Sibson and Toy, 2006). Here we present new observations of PSTs that formed along the ancient Moho by much larger earthquakes than those described previously from Corsica. Their formation is related to the Alpine closure of the Liguro-Piemontese oceanic basin and its adjacent hyperextended margin (Martin et al., 2011; Meresse et al., 2012).

9.2. Field observations

Subduction earthquakes along the palaeo-Moho in the studied area (Fig. 9.1) caused melting of large volumes of spinel- and plagioclase-bearing mantle peridotite (Fig. 9.2) as well as the gabbro of the lower crust (e.g. Austrheim and Andersen, 2004; Deseta et al., 2014). Evidence for dramatic PST generation events can be studied within several preserved peridotite lenses (up to 140 m thick, 850 m long), which define a horizon traceable approximately 2.5 km along the fossil Moho at Chima di Gratera (Fig 9.1). The exposed Moho is offset by later down to-west faults also truncating the Miocene Saint Florent Basin (Fig.9.1). The Moho is a sharp, gently dipping contact between variably serpentinized to well-preserved mantle peridotite and the overlying layered to varied-textured meta-gabbro. The PST faulting occurred along 2 main fault systems, a steep and a gently dipping (~30^{o}) system parallel to the Moho fault zone (Andersen and Austrheim, 2006; Silkoset, 2013).

The PSTs are pristine in the least hydrated parts, and occur as relicts in areas with more hydration. PSTs are not preserved in the sheared serpentinites that forms most of the mantle rocks of the HP-LT units in Corsica. Prograde dehydration of the serpentinites has not been observed, and serpentinization mostly post-dates earthquake faulting (Deseta et al., 2014). The Moho fault is strongly overprinted by ductile shearing at locality 1, but the former presence of large PSTs is shown as large porphyroclasts in the blueschist mylonites (Fig. 9.1 (A45, S3). The PST veins increases in abundance at the palaeo-Moho in both localities 1 and 2. In the best preserved areas (loc. 2) the upper ~6 m of the mantle consists of a PST network breccia, which may contain ~50% ultramafic PST (Fig. 9.2). The largest melt volumes form a dense network of mutually intruding veins ranging from mm to several 10´s of cm in thickness (Fig. 9.3 and 9.4).

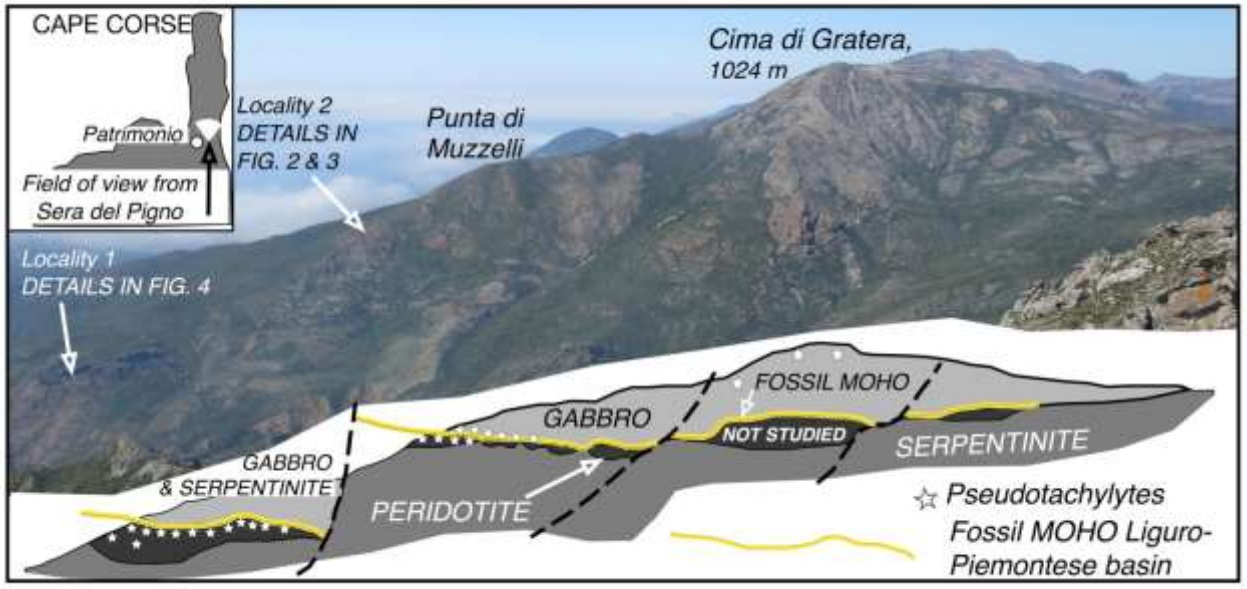


Fig.1.9 View and sketch showing the south face of Cima di Gratera in Cape Corse, where the fossil Moho of the Liguro-Piemontese ocean (yellow line) is well preserved along a distance of 2.5 km. The best-preserved Moho fault breccias in the peridotite are found at locality 2 with details in Fig. 2 and 3. All visited outcrops along the contact have large volumes of ultramafic pseudotachylyte. Some areas have not yet been visited because of steep topography.

Locally, this produces a breccia with PST matrix without an obvious hierarchy of individual veins (Figs. 9.2 and 9.4). A number of variably oriented minor faults with PST post-date the large vein breccia (Fig. 9.2, A41 - A44, S1). Other localities along the Moho fault have massive and thicker fault-veins that may be up to 1 m in cumulative thickness (Figs. 9.3, 9.4, A40 – A42, S1). These are formed by at most a few major ruptures succeeded by several minor events as shown by re-injection of younger PST (A45 – A46, S2). The fault veins and dense vein-network constitute the several meter wide damage zone along the Moho fault. The distribution of PST along this fault zone varies considerably with an apparent maximum in areas where the vein-network is thickest at locality 2. From the lateral thickness variation it is obvious that redistribution by flow of ultramafic melt along the fault took place after generation but before complete solidification. This flow, partial solidification, re-mobilization and back-veining relationships produce a “sponge-like” vein-network where PST occupies space in veins and between fragments (Fig. 9.2, A43 and A44, S2).



Fig.9.2 The main Moho-fault vein complex with >6 m thick damage zone in peridotite below Punta di Muzzelli (Fig 9.1). The cliff-face (a) constitutes a net-veined, 'sponge' like breccia with dominantly sub-parallel, but mutually cross cutting ultramafic pseudotachylyte veins dipping gently to the left. Notice that some veins coalesce into massive injection veins up to 15 cm thick. Notice also that the vein complex is truncated by a later steeply (~60^{o}) dipping fault also decorated by pseudotachylyte as seen by 2-4 cm wide fault veins at arrows. The vein complex is without an obvious vein hierarchy. b) Detail (frame in a) showing the intensity of the brecciation/net veining with more than 50% melt. The positive surface features are mostly formed by hair-thin to cm wide melt accumulations and a pseudotachylyte matrix also without an obvious sequence of emplacement. The lichen covered (darker) negative surface features are disintegrating host-peridotite fragments. Notice some larger veins up to 8 cm wide above the hand and lack of later faults cutting the vein-complex. c) Detail (frame in a) of glassy bifurcating and coalescing net-veins making positive topography on the weathered surface showing ~40% melt in the peridotite (fingertip for scale). With exception the late steep fault seen in (a) there is no suggestion that this vein complex was formed by multiple, distinctly time-separated and cross cutting events as would be the case if the Moho fault-vein complex was formed by a number of individual fault episodes.



Figure 9.3 The MOHO fault: (a) Close-up of the Moho at the locality 2 (Fig. 1). The gabbro-peridotite contact is sharp (surface at the left hand of person). Both rocks are strongly affected by pseudotachylyte melting. The damage zone in the peridotite is more than 2 m wide (limited by outcrop) and consists mostly of pseudotachylyte as intensely net-veined material with up to 80% melt in 2b and as massive fault veins, see in detail in 2c showing the lower part of a 0.3m wide massive ultramafic pseudotachylyte.

Where best preserved (locality 2) the melt zone is several meters thick, hosting up to 50% ultramafic PST. The network/breccia in Fig. 9.2 (A43 and A44, S2) is more than 6 m thick. It is truncated by several minor faults with PST, truncating and re-melt older PST. We suggest that these represent aftershocks succeeding the main rupture and melting events.



Fig.9.4 Details from the Moho fault damage zone at locality 1 (Fig. 9.1). Another example of the large melt production in a single-stage event along the Moho is shown. Width normal to the veins from lower left to upper right corner is 1.1 m, and the pseudotachylyte constitute 75% of this thickness, corresponding to nearly 2.4 tons of melted mantle pr. m^2 fault surface. Only a segment of the fault damage zone is exposed in this locality. Hammer for scale is 32 cm.

9.3. Melt volumes, energy budget and earthquake magnitude

The spectacular outcrops at locality 2 have not been described before. It is obvious that explosive release of energy accompanied by melting has fractured the wall rocks intensely. Wall rock fragments and xenocrysts were incorporated and progressively assimilated in the PST producing domains of variable composition and banding at mm-scale (Deseta et al. 2014). Thin melt channels kept open and the bifurcating and coalescing network could effectively funnel m^3 of melt from the generation zone in the fault-core several meters into the wall rocks (Fig. 9.2). In order to transport PST melts several meters in thin channels and sheets, the ultramafic melt must have had a low viscosity (Suzuki et al., 2001) or the melt would have solidified towards the cold wall rock. The melts may also have been superheated and indeed supercritical (Kanamori et al., 1998) during their

explosive formation and drainage from the generation zone, in which case additional melts may have been produces within the vein complex during injection. The melt breccia with up to 50% PST formed by complete disequilibrium melting of the peridotite. An up to 3 m thick melt layer shows that ~ 9500 kg of the peridotite may have melted per m^2 of the fault plane.

Because most of the thick net-vein complex is without an obvious cross cutting vein-hierarchy, it is possible that it may have formed in just one major event? Even after careful examination, it is however, difficult to ascertain if the thick breccia formed by one - or by a few major events, in addition to the many smaller events described previously (Andersen et al., 2008; Deseta et al., 2014). Because veins of different generations have different characteristics (A10, A40 - A42, S1) our preferred interpretation is that most of the thick melt zone was formed by at most a few (up to 3?) large event? There are examples of rootless, cross cutting injection veins, which perhaps suggest that more than one major melting event took place (Fig 9.2a, A41 – A42, S1a - e). In the calculation of earthquake magnitude we assume that most of the Moho melt breccia with a cumulative melt-thickness of up to 3 m formed by a few large melt-generating events. It is not possible to be more specific about relative importance and magnitude of the large event(s).

Using standard values for heat capacity and heat of fusion for an olivine rich mantle (Weatherley and Katz, 2012) the release of energy must have been more than 1.9×10^{10} J m^{-2} along the fault plane in order to melt the observed volumes of ultramafic PST (Fig. 9.2). In adjacent areas PSTs are more concentrated in thicker veins and the cumulative thickness is apparently less, more commonly 1 to 1.5 m (Figs. 9.3 and 9.4). We also observed smaller branching veins, which have 3-dimensional star-shaped vein pattern (A42, S1g). We interpret these to be reminiscent of local explosive production and injection of melts on a smaller scale but similar to the thick sponge-like melt breccia described above. Both structures demonstrate that melt-volumes stored on generation surfaces are much smaller than the total volume generated, and that in most cases melt volumes will be underestimated.

If we use mantle strength (Δσ) of 500 MPa (Andersen et al., 2008; Obata and Karato, 1995), mantle density (ρ3200 kg m^{-3}, heat capacity (C_p) 1200 J kg^{-1} $^oC^{-1}$, temperature change δT=1250^{o}C from 420^{o}C to complete melting at 1670^{o}C (Katz et al., 2003), heat of fusion (H) of 5 x 10^5 J kg^{-1} (C_p and H (Weatherley and Katz, 2012)) and assume that more than 95% of the seismic energy is dissipated as heat (McGarr, 1999) it is possible to make an estimate of the shear strain ɣ- d/h (d- displacement and h- thickness of fault core) if we assume that a single earthquake produced the melt. From the equation for 100% melting: $\Delta\sigma = \rho[C_p \delta T + H]\ \gamma^{-1}$ (Di Toro et al., 2005) we obtain ɣ≈ 12.8. If displacement took place across a 1.5 m wide slip zone as indicated by the massive PST fault veins, co-genetic fault-vein ladder networks and breccias (Sibson, 1977) (Fig 3), the displacement along the Moho fault may have been more than 19 m. If this was a single event the earthquake it must have had a moment magnitude (Mw) of ~8. Generation by 2 to 3 successive large events would reduce the displacement for the individual earthquakes by up to 1/3, which still suggest displacements of more than 6 m and magnitude ~7.5 earthquakes. The rupture length associated with the largest estimates may have been up to several hundred kilometers (Bonilla et al., 1984). The fossil earthquakes seen in Corsica may therefore have affected a large part in the early Alpine subduction zone and been effective on a basin-scale in the relatively small Liguro-Piemontese oceanic basin (Handy et al., 2010). Subduction earthquakes exposed in Corsica may therefore have been co-genetic with other deeper HP-LT co-seismic events described from the western Alps (Angiboust et al., 2012).

9.4. Discussion

A major discussion concerning subduction earthquakes is the weakening mechanism for seismic events at depth. The main hypothesis used to explain the weakening (Rice, 2006) involves high pore-fluid pressures (Green and Houston, 1995; Kirby, 1996). Fluid pressure reduces effective stress and may cause failure and a run-away stress-drop of the system. High fluid pressures in this model are nourished by prograde metamorphic dehydration of subducted sediments and serpentinized mantle (Hacker et al., 2003). There may be a close link between metamorphism and seismicity in subduction

zones (Rondenay et al., 2008). Our initial work strategy in Corsica was strongly influenced by the dehydration embrittlement hypothesis, but in spite of careful studies, we found no mineralogical or textural evidence that dehydration reactions were common in the fault zones. We have not observed formation secondary dry minerals produced by dehydration of serpentine, talc, chlinoclore or amphiboles in the gabbro and peridotite, which could be used as an argument for dehydration embrittlement. Secondary dry minerals produced within the PST veins are very common, but it is the shear heating, melting and crystallization and not prograde metamorphism that gave rise to their formation.

Consequently alternative weakening mechanisms (Rice, 2006) are investigated from the textural/mineralogical evidence. Deseta et al. (2014) recently described in detail localized ductile precursors to the faulting along smaller faults from Corsica. Evidence for precursor deformation by dislocation systems in olivine characteristic of intermediate- to high water contents and stresses of 120 to 340 MPa in experiments at ~1250^{o}C (labeled type E in Jung et al. (2006)) have recently been described by electron backscatter diffraction studies (Silkoset, 2013). We therefore infer shear heating as the most likely weakening mechanism (Kelemen and Hirth, 2007). Viscous dissipation of heat resulted in a thermal run-away and earthquake faulting. Thermal run-away has been investigated theoretically (Braeck and Podladchikov, 2007) and numerical simulations (John et al., 2009) show that it requires lower differential stresses than frictional faulting at the ambient conditions of intermediate and deep earthquakes in the absence of a free fluid.

9.5. Conclusion

Observations from natural examples in the HP-LT metamorphic rocks in Corsica show that one or a few very large earthquakes produced thick PST melt(s) along a Moho fault during Alpine subduction. The commonly used mechanism for subduction earthquakes is embrittlement by dehydration of seawater-altered rocks (Green and Houston, 1995). The embrittlement related to dehydration of serpentinite in the mantle of the subducting slab produces the lower seismogenic zone (Hacker et

al., 2003; Rietbrock and Waldhauser, 2004). After examination of a large number of thin sections, no evidence for prograde metamorphic dehydration has been found. We therefore support previous interpretations (Braeck and Podladchikov, 2007; John et al., 2009; Kelemen and Hirth, 2007) that shear heating was the most likely weakening mechanism that released the large earthquakes along the palaeo-Moho in Corsica

Acknowledgements

Norwegian Research Council Centre of Excellence grants to PGP and CEED financed this work.

10. Discussion and Conclusions

The principal aim of this project was to provide detailed constraints on the formation of high pressure pseudotachylytes of the Schistes Lustres Complex, Corsica. One of the issues with previous studies involving pseudotachylytes is the lack of consistency and detail in description and analysis of all microscale features. Pseudotachylytes are notoriously compositionally complex and this has been a barrier to understanding the factors of their formation. Beginning with detailed petrography I undertook an iterative process of using electron microprobe analysis (EPMA) and back-scatter electron (BSE) imaging to acquire detailed major and trace element and microstructural data of PST and associated wallrock to evaluate the pseudotachylyte generating process. In order to evaluate the mechanism by which these pseudotachylytes form and the role that fluids play in their production, pseudotachylytes were analysed from both types of host rock: metagabbroic and peridotitic. The resulting analyses have resulted in the form of a large database for a single pseudotachylyte occurrence. From these data I have been able to make several conclusions regarding the style of melting these rocks undertake, the role of water in their production and the principal factors leading up to their formation, resulting in a tentative mechanistic model:

10.1 Style of fusion

- BSE imaging, EPMA, XRF analysis and detailed petrography indicate for both host rocks that their pseudotachylytes form by disequilibrium melting. To expound, wallrock clasts underwent near-total wholesale fusion instead of partial melting. In the case of polymineralic survivor clasts, embayments in clasts caused by preferential fusion of lower temperature minerals have been observed (Fig. 10.1). This is principally due to the coarse- grained nature of the hostrocks, where intracrystalline fusion of wallrock clasts dominates inital melt generation.

Fine-grained granoblastic recrystallized pseudotachylyte that is cross-cut by younger pseudotachylytes produces a melt more characteristic of normal partial melting. This is because grains melt along their boundaries as opposed to internally. This change in the character of melting has an important bearing on the mechanism by which these high pressure pseudotachylytes form, but also indicates that grain size is not a barrier to melting induced by localised shear heating as previously thought (Fig. 10.1) (John et al., 2009; Kelemen and Hirth, 2007).

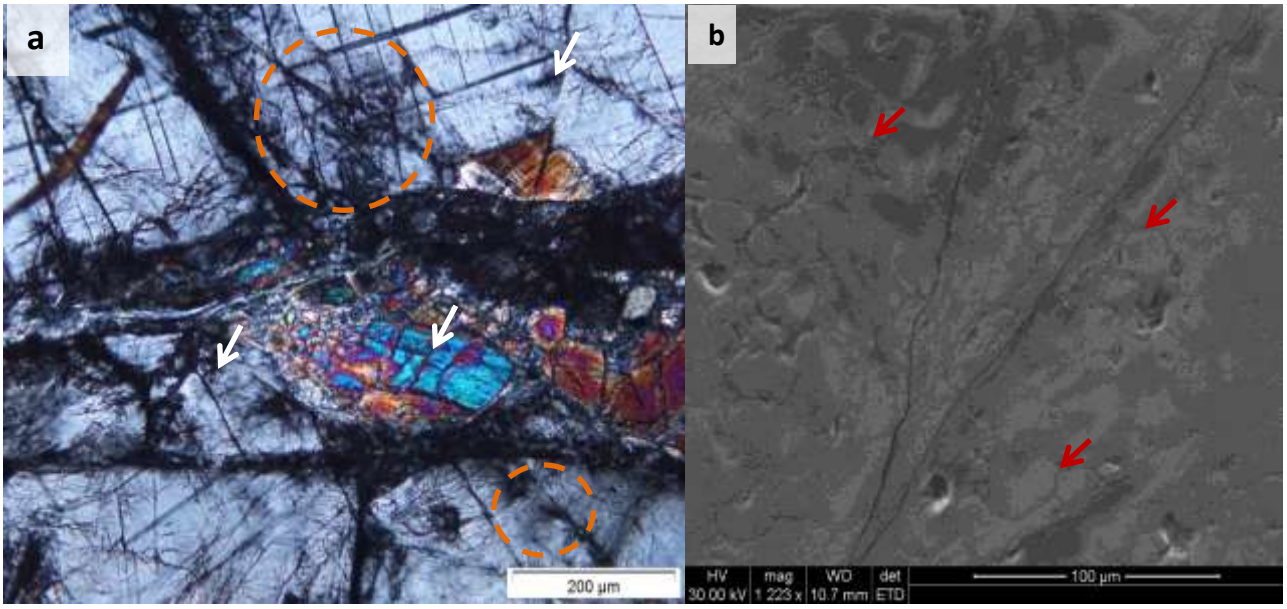


Fig. 10.1 Images of peridotite-hosted PST fault veins. a) Micrograph (XPL) of PST fault vein formed in a coarse-grained hostrock. Orange circles and white arrows indicate areas of localised intragranular fusion. b) SE image of a PST fault vein in a fine-grained hostrock. Red arrows indicate sites of intergranular melting. Inter- and intra-granular comminution shown in both a) and b).

10.2 Role of water in seismic failure: decoupling dehydration from shear heating

- Taking analytical error and the influence of Fe and cation vacancies into account, detailed petrography, EPMA and XRF analysis have allowed me to estimate that these pseudotachylytes range from 0 – 14 wt % H_2O. The H_2O content in the pseudotachylytes is widely heterogeneous across distances as small as 300 μm and is principally attributed to the coarse-grained nature of the fusing clasts, the contrast in fracture toughness between phyllosilicates and amphiboles with anhydrous minerals (plagioclase, clinopyroxene, olivine and orthopyroxene) the pre-existing distribution of hydrous minerals within the wallrock immediately adjacent to fault veins and poor mixing of the melt.
- There is no evidence of fluid ingress during faulting or freely available hydrous fluids prior to fusion, leading to the conclusion that all the fluids in the pseudotachylytes came from the fusion of hydrous wallrock minerals. This is in agreement with (Mittempergher et al., 2014) who demonstrated experimentally that fluids are first introduced to the fault system by the fusion of proximal hydrous minerals in the wallrock.
- Petrography, EPMA and BSE imaging all indicate that the hydrous minerals in the pseudotachylytes undergo fusion rather than dehydration.
- Water content in the wall rock appears to be a fundamental requirement for producing higher quantities of these high pressure melts. The H_2O typically occurs as a hydroxyl or trace component of minerals that induces hydrolytic weakening (Zhang et al., 2004). Within PST melt, increased dissolved fluids dissolved, will decrease its viscosity. Assuming the activity of the H_2O in the melt is high enough it may act as a flux, facilitating fusion of contiguous clastic material (Sibson, 1977a, 1977b; Spray, 2010).
- Both the metagabbro and peridotite host rocks are populated by patches of hydrous minerals. The contrast between the relative viscosities and melting/breaking temperature of

phyllosilicates, amphiboles, and H_2O-enriched nominally anhydrous, relative to anhydrous olivine, orthopyroxene, clinopyroxene and plagioclase causing the strain bulk rock to behave as a viscoelastic material at increasing strain rates (John et al., 2009; Kameyama et al., 1999; Kelemen and Hirth, 2007; Newman et al., 1999). Further, background temperatures in the slab can range from 400 – 700 ˚C, at such temperatures and high confining pressures (> 1.5 GPa), antigorite exhibits ductile flow and stable aseismic failure (Chernak and Hirth, 2011). If this relationship is extended to other hydrous species in the hostrock, at coseismic strain rates and associated temperature increase (up to 1000 ˚C) the adiabatic loci of these species undergo preferential fusion. On the bulk rock scale, mm-scale localised areas with high temperatures, enclosed in cooler bulk rock, the initial stage of preferential fusion, might be equated with activation of Peierl's mechanism (Kameyama et al., 1999). The resultant hot (> 1000 ˚C) melt spots, enriched in dissolved fluids, thermally degrade contiguous anhydrous minerals (clinopyroxene, plagioclase, olivine, orthopyroxene). Observations of olivine comminution in the fine-grained peridotite case suggest that strain rates in the Corsican earthquakes did not exceed the ductile flow limit of olivine (Chernak and Hirth, 2011; Handy, 1990), but was higher than the limit for dislocation glide and climb.

- Free water has been observed to be present in some subduction planes (Nakajima et al., 2009a). However, while changes in pore fluid pressures might induce faulting, they cannot produce the high volumes of melt observed in this study (Hacker et al., 2004; Prieto et al., 2013; Zhang et al., 2004). The expression of high pressure faulting in the presence of free water appears to be distinct from pseudotachylytic fault zones, as is illustrated in Fig. 10.2 by the observation of brecciated eclogite, overprinted by eclogite-facies ductile features in the Monviso Ophiolite, Italy (Angiboust et al., 2013). Free H_2O appears to have been present in the Coriscan PST as both a fluid dissolved in the melt, and as a free vapour (Fig. 10.10). Within the metagabbro at least we can estimate an upper limit on the localised conditions of H_2O exsolution in fusing clinopyroxene and albite (Luth and Boettcher, 1986). At pressures of

~ 1.5 GPa, clinopyroxene becomes vapour-saturated at 1350 ˚C and albite at 700 ˚C. The disparity in exsolution temperature for the two minerals demonstrates that localised fluid exsolution in the fault zone can occur at wide range of temperatures (Luth and Boettcher, 1986).

- With particular regard to dehydration embrittlement (DE), petrographic and microtextural observations, in this case, preclude this process as the principal cause of pseudotachylyte-associated intermediate-depth seismicity. The primary control generating seismic melting is the combined influence of exponentially increasing strain rate and temperature; it is not simply dependent on high temperature and pressure (Barcheck et al., 2012; Green, 2007; Scholz, 2002; Spray, 2010; Zhang et al., 2004). Experimental studies do not support the coupling of large melt volumes in the fault zone (PST generation) and DE. Lastly, DE is most likely to occur in regions of the slab richest in hydrous minerals, i.e. hydrated shear zones at the Moho and completely serpentinised peridotite. However, these regions are not structurally competent enough to embrittle at a sufficient rate in a single event, to induce seismic failure (Chernak and Hirth, 2011). Dehydration will occur as the slab warms and subducts deeper, regardless of strain rate, but it will be facilitated by increasing strain rate due to the production of frictional heat from shear stress (Barcheck et al., 2012; Chernak and Hirth, 2011; Green, 2007; Prieto et al., 2013). Reynard et al. 2010, show that the low velocity anomaly associated with the lower seismic plane, does not reflect the hydrous V_p/V_s (where V_p is compressional velocity and V_s is shear wave velocity) signature of antigorite, but rather partially hydrated peridotite (Fig. 10.5). They also suggest that the increased fluctuations in compressional wave velocity relative to shear wave velocity, reflects a rheological rather compositional control. Lastly, Prieto et al. 2013 show that seismicity occurs with a local 600 ˚C to 1000 ˚C increase in temperature.

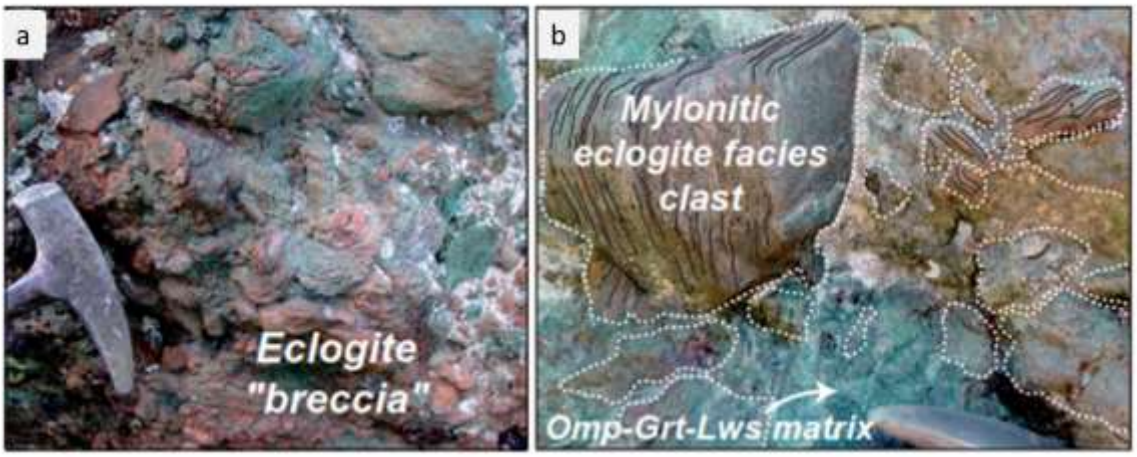


Fig. 10.2 Multiscale fracturing recorded in brecciated eclogites from the lower shear zone in the Monviso Ophiolite, Italy. a) Brecciated eclogite. b) cm-scale mylonitic eclogite clasts cemented by lawsonite under eclogite facies conditions, After Angiboust et al. (2012)

- The release of water into melt by fusing minerals occurs in two stages: The water produced by initial fusion immediately separates from the melt to form primary Mode I veins. Secondary H_2O-rich veins exsolve later from the melt owing to the supersaturation of H_2O in the melt as anhydrous minerals crystallise from the melt, progressively enriching it in H_2O. The secondary vein orientation was influenced by concurrent flow stresses acting on the pseudotachylytes as they quenched.
- Anydrous pseudotachylyte fault veins have been observed in both the metagabbro and peridotite pseudotachylytes. These veins are typically thinner and simpler than their more hydrous counterparts, comprising fewer chaotic re-injections (Figs. 10.3 and 10.4). It remains to be tested whether these veins are truly anhydrous or have trace amounts of H_2O. In-situ analysis of the H_2O content of these veins and the survivor clasts within them is something that remains to be investigated. Hydrogen isotopic and fourier transform infrared analyses of experimentally generated high pressure PST indicate that fluids in the fault zone have a genetic relationship between the contiguous catacalasite and wallrock, rather than from externally derived meteoric fluids (Mittemperger et al., 2014).



Fig. 10.3 Photographs indicating water-rich versus water-poor pseudotachylyte fault veins hosted by metagabbro and peridotite. a) Water-poor PST in Metagabbro. b) Water-poor PST in peridotite. c) Water-rich PST in metsgabbro, not the sub-parallel tablets of comminuted wallrock cemented by younger fault veins. d) Water-rich PST fault vein in peridotite. Note that the vein comprises sub-parallel anastomosing layers of PST comminuted wallrock. e) Close-up of a water-rich PST vein in metagabbro, note the increased damage zone diameter at the vein boundary as compared to a). f) Close-up of wallrock of PST in d). Both e) and f) show a boundary zone beyond the water-rich fault veins, where deformation and hydration of the wallrock is greater than that seen in a) and b) (water-poor PST).

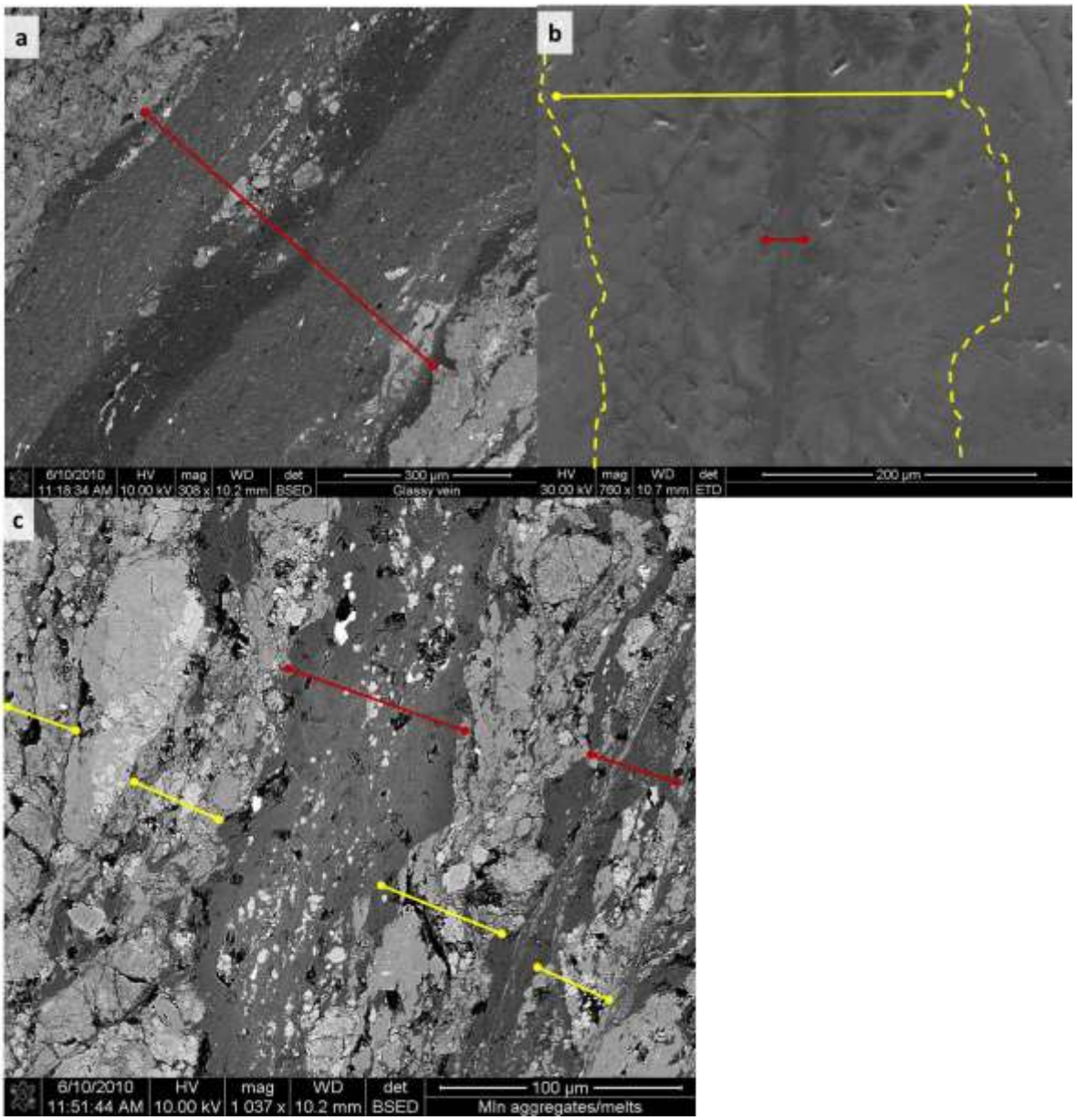


Fig. 10.4 BSE and SE images of coarse- and fine-grained peridotite-hosted fault veins. a) Close-up of a water-rich PST fault vein complex. Red line indicates the width of the latest PST generation. b) Close-up SE image of a PST hosted by a water-poor, fine-grained peridotite. Red line indicates fault vein width. Dashed yellow lines indicate the alteration/damage zone beyond the fault vein. d) PST fault vein complex comprising alternating and anastomosing sub-parallel zones of the latest PST generations (width shown in red), as shown in a) and older ultracataclasite and melt aggregates (width shown in yellow).

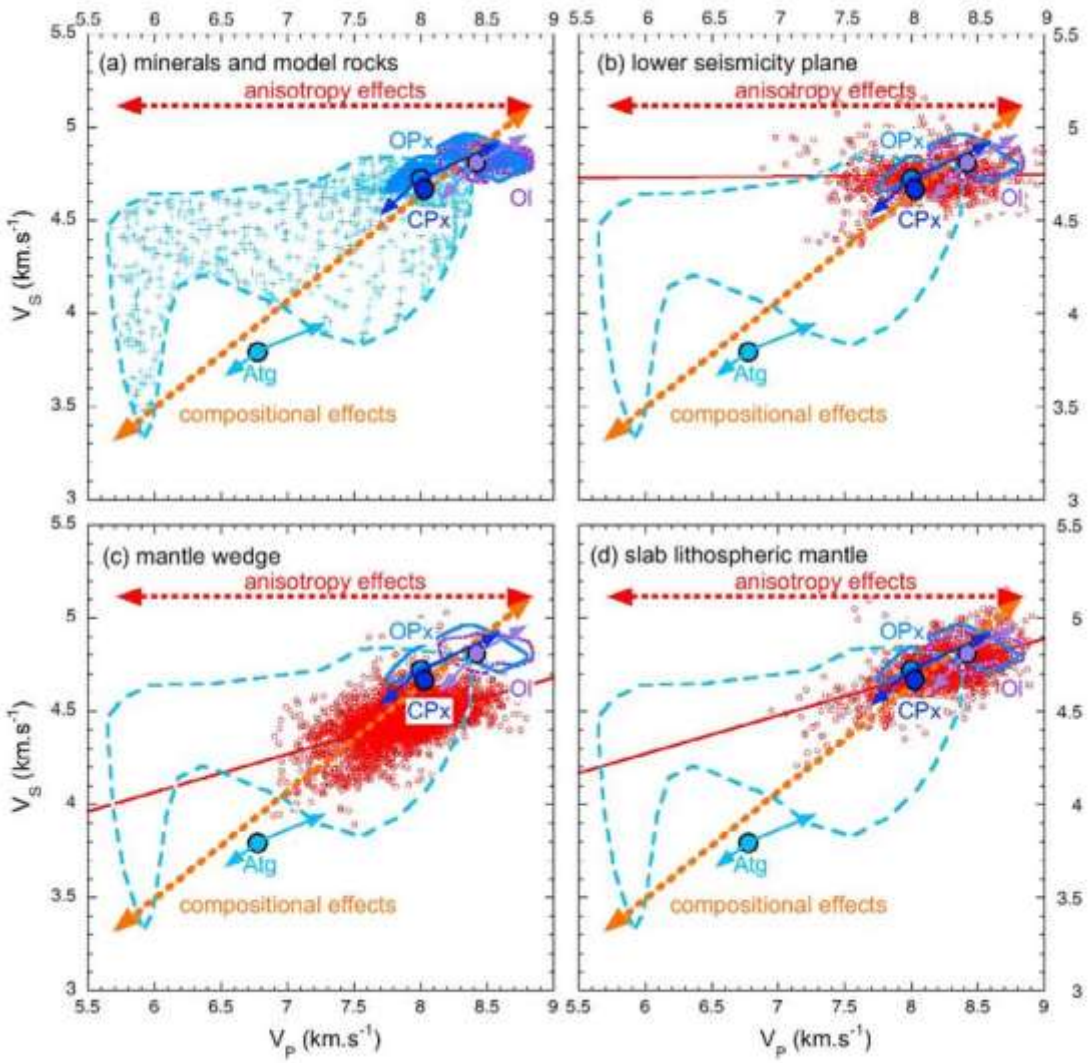


Fig.10.5 Graphs of seismic velocities in subduction-related rocks and minerals, comparing the anisotropic and compositional signature of minerals representing totally hydrated slab (Atg, antigorite), anhydrous peridotite comprised of clinopyroxene (Cpx), orthopyroxene (Opx), and olivine (Ol). a) Mineral and rock signatures; purple symbols are olivine aggregate; blue, lithospheric mantle (Opx + Ol); light blue, foliated serpentinite. Arrows indicate temperature and pressure effects. Red line is a regression of seismic velocities of each rock type. b) Seismic velocities in the lower plane (red) overlie olivine aggregates and anhydrous lithospheric mantle. c) Within the mantle wedge, the broad dispersion of seismic events is principally due to thermal effects. d) Within the slab lithospheric mantle (the region between the lower seismic plane and oceanic crust). The variability in seismic velocities indicates partial hydration and is controlled by a combination of thermal and anisotropic effects. After Reynard et al. (2010)

10.3 Character of pseudotachylyte generating mechanism

- The detailed observations in this study present a unique opportunity to evaluate pre-existing models of high pressure faulting, which are based on indirect observations and geophysical modelling. In general, the observations made in this study are congruent with the model of shear-localised thermal runaway (John et al., 2009).
- Ultracataclasites observed at fault vein-wallrock boundaries (Fig. 10.4) record the brittle-ductile interplay arising from the distinct rheologies of coarse-grained wallrock mineral species; i.e., phyllosilicates and amphiboles underwent preferential fusion to form glassy melt pockets (Sibson, 1977b, 1975; Spray, 2010). In contrast, anhydrous minerals such as olivine and diopside were sheared to form mineral ribbons.
- EPMA and BSE imaging of survivor clasts in pseudotachylytes show that all minerals, including hydrous species underwent fusion. H_2O released by fusing minerals appears to have dissolved into the melt and upon reaching supersaturation, exsolved to produce fluid-rich veins. These observations preclude previously suggested mechanisms for generating high pressure PST, such as dehydration embrittlement and transformational faulting and support a shear-heating mechanism.
- Microtextural analysis of wallrock survivor clasts associated with pseudotachylyte fault veins suggests a mechanism controlled principally by power law creep, rather than diffusion creep (Fig. 10.6). A shear heating mechanism controlled by power law creep precludes a truly ductile shear heating process and suggests a mechanism relatively insensitive to grain-size and rather a dependence on background temperature and strain rate (Braeck and Podladchikov, 2007; Green, 1995; Spray, 2010). Figs. 10.8 – 10.9 show that the transitional ultracataclasite associated with fault vein PST is present at both in coarse and fine grain sizes. The development of the ultracataclasite appears to be

facilitated by the presence of phyllosilicates and amphiboles in the wallrock (Fig. 10.8 compare a and b with c) (Scholz, 2002; Spray, 2010). This may be due to the contrast in fracture toughness between hydrous minerals and anhydrous minerals in the wallrock (Handy, 1990; Kameyama et al., 1999; Spray, 1992, 2010). Repeated reactivation of the fault plane may also facilitate the thickness and maturity of the ultracataclastic transition zone as wallrock adjacent to the fault plane becomes increasingly fractured and previously formed ultracataclasite and PST are recycled (Figs. 10.4; 10.7 b and d). The thickness of the ultracataclasite may be limited as it is peeled off and digested by the PST melt.

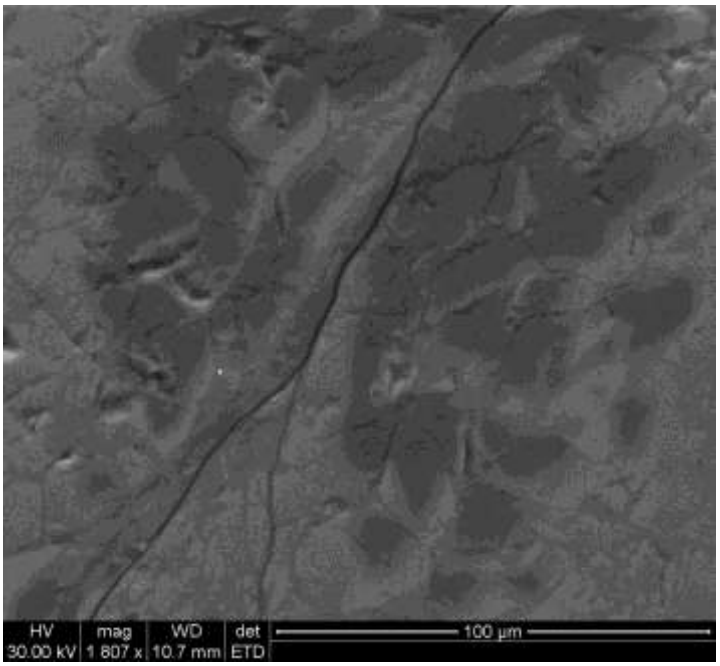


Fig. 10.6 SE image of a PST fault vein in fine-grained peridotite. Grains shown are euhedral to subhedral olivine neoblasts cut by darker grey fusion melt. Black line is a serpentine vein. Both intra- and inter-granular fracturing, comminution and fusion are shown.

- The case study of PST hosted by fine-grained peridotite allowed me to beyond assigning power law creep as the principal deformation mechanism for PST generation. Focusing on the relationships between intra- and inter-granular fractures in olivine neoblasts distal and proximal to fault veins, it was observed that fracturing took place along grain boundaries and a,b, and c axes of olivine grains (Fig. 7.6). This implies a crystallographic control on PST

development such that in a near-monomineralic condition fracturing is controlled by weaknesses along the grain boundaries and within the olivine crystal lattice, i.e. fracturing is controlled by the pseudo-orthorhombic habit of the olivine neoblasts. Ultimately the neoblasts inherit their orientation from the dendrites that they have overgrown, which were randomly oriented (Fig. 10.6).

- Poorly developed diffusion creep in the olivine neoblasts (fine-grained peridotite-hosted PST) (Fig. 10.7d) indicates that the fault zone had not yet reached a bulk condition of pressure, temperature and strain rate to allow for diffusion creep to be the dominant deformation mechanism. Olivine has been demonstrated to exhibit power law creep at high pressures (~ 1 Gpa) and seismic strain rates (10^{-5} s^{-1}), at temperatures above 1200 ˚C. Under the same conditions, olivine undergoes diffusion creep at temperatures above 1400 ˚C) (Demouchy et al., 2009). The difference in aticvation temperature between these two mechanisms can hence be used to show that the sheared wallrock olivine proximal to the melt zone did not exceed a bulk temperature of 1400 ˚C (Demouchy et al., 2009).
- The background or ambient temperature of the PST hostrock prior to fault generation appears to exert some control on subsequent crystal-plastic deformation features (Hacker and Christie, 1990). Monomineralic studies of high pressure failure indicate that at sub-solidus temperatures the fault zone is dominated by plastic deformation, whereas at hypersolidus conditions crystal-plastic deformation and cataclastis with melt formation predominates (Hacker and Christie, 1990). The Corsican PST studied here present a case study of intermediate-depth seismicity generated in a low temperature (~ 420 ˚C) environment. The majority of research on high pressure seismicity and PST generation typically use higher background temperatures (~ 600 – 1000 ˚C) (Abers et al., 2013; Bestmann et al., 2012; Di Toro et al., 2009; Green, 2007; Hobbs et al., 1986; John et al., 2009; Prieto et al., 2013; Zhang et al., 2004). Owing to this, the Corsican PST provide a window on

intermediate-depth coseismic deformation at low temperatures, elucidating the potential influence of temperature change on the coseismic mechanism that operates. Further, under colder geotherms, subducting slabs are likely to carry more H_2O to greater depths (Abers et al., 2013). In the Corsican case, background temperatures were ~ 420 ˚C, and the fault damage zones experienced elevated temperatures up to 1420 ˚C (in the peridotite hosted PST, temperature, limited to the thermal limit of olivine flow) and up to 1270 ˚C (in the metagabbro-hosted PST, temperature estimated based on the thermal limit of diopside flow) (Boland and Tullis, 1986; Demouchy et al., 2009) prior to fusion. The fault zone is dominated by crystal-plastic deformation of olivine, orthopyroxene and clinopyroxene, in perdotite and clinopyroxene and plagioclase in metagabbro and fusion of hydrous minerals (chlorite, tremolite, serpentinte, glaucophane). i.e. the anhydrous minerals had not been heated beyond the flow limit of each species, but the hydrous minerals were heated to melting/breaking point. The high temperature crystallisation products ($olivine_{Fo89\text{-}93}$, Al-rich omphacite) from the PST show that the temperature in the damage zones of both the metagabbro and peridotite eventually reached at least 1400 ˚C (Andersen and Austrheim, 2006; Hacker and Christie, 1990; Konzett et al., 2007; Smyth, 1980).

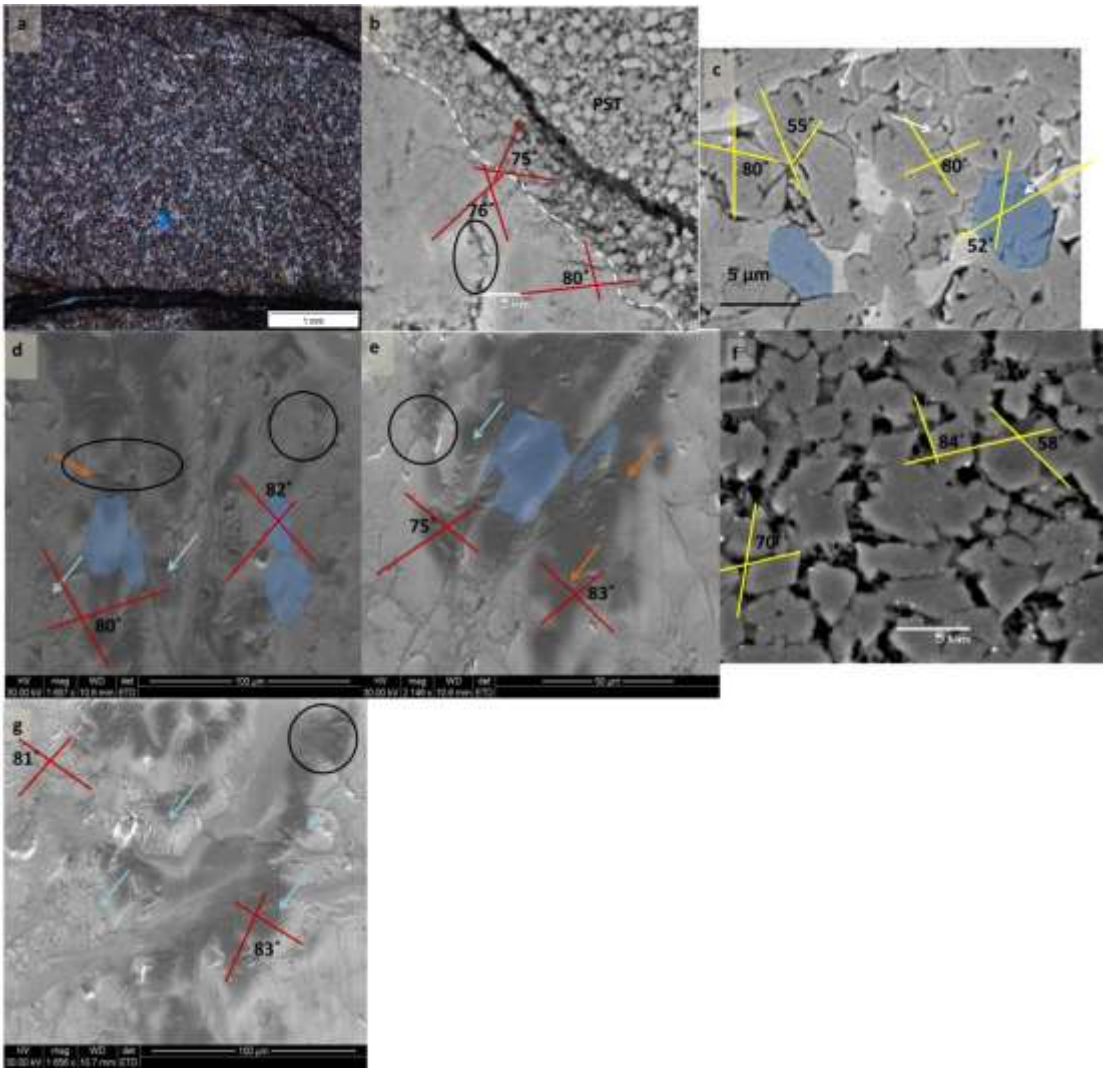


Fig. 10.7 Images of pseudotachlyte fault veins hosted by a pre-existing fault vein. a) Micrograph in XPL of a fault vein recrystallized to produce a fine-grained (5 – 30 µm) annealed matrix of olivine neoblasts, which can be seen to have overgrown the microlites quenched from the melt. The black veins crosscutting the pseudotachylyte are due to later serpentinisation. This matrix forms the wallrock for later pseudotachylytes (b – g) . b) BSE image of a pseudotachylyte fault boundary (white dashed line). Note the fracture sets in the wallrock grains (red lines), with two principal sets arising at different angles. Black circles indicates localised fusion at grain boundaries in the wallrock, accompanied by the production of angular clasts. c) Incompletely annealed olivine neoblasts (grey) with intercumulus clinopyroxene (white). The neoblasts are euhedral (blue) and retain some features of the dendrites they have overgrown (white arrows). The planes along which annealing is incomplete in the grains produce two sets of potential planes of weakness in the crystals are shown by yellow lines. d) SE image of fault vein with strained grains at fault boundary (blue). Predominant fracture sets of internally deformed grains (blue arrows) shown by red lines. Black circles indicate wavy grain boundaries possibly produced by diffusion creep. e) SE image close-up of fault vein, showing fractured strained wallrock neoblasts (blue). Red lines indicate predominant fracture sets. Orange arrows indicate wavy grain boundaries of neoblasts. Blue arrow indicates intragranular fractures. Black circle shows localised intergranular comminution and fusion. f) BSE image of relatively unstrained olivine microlites enclosed in a vesiculated matrix of high-Al glass. Several dihedral angles are indicated by yellow lines. g) SE image of highly strained neoblasts entrained into fault vein. Intragranular fractures are pronounced. Black circle indicates saw-toothed grain boundaries. Red lines indicate intragranular fracture sets (blue arrows). Dark shadows in SE images due to sample charging.

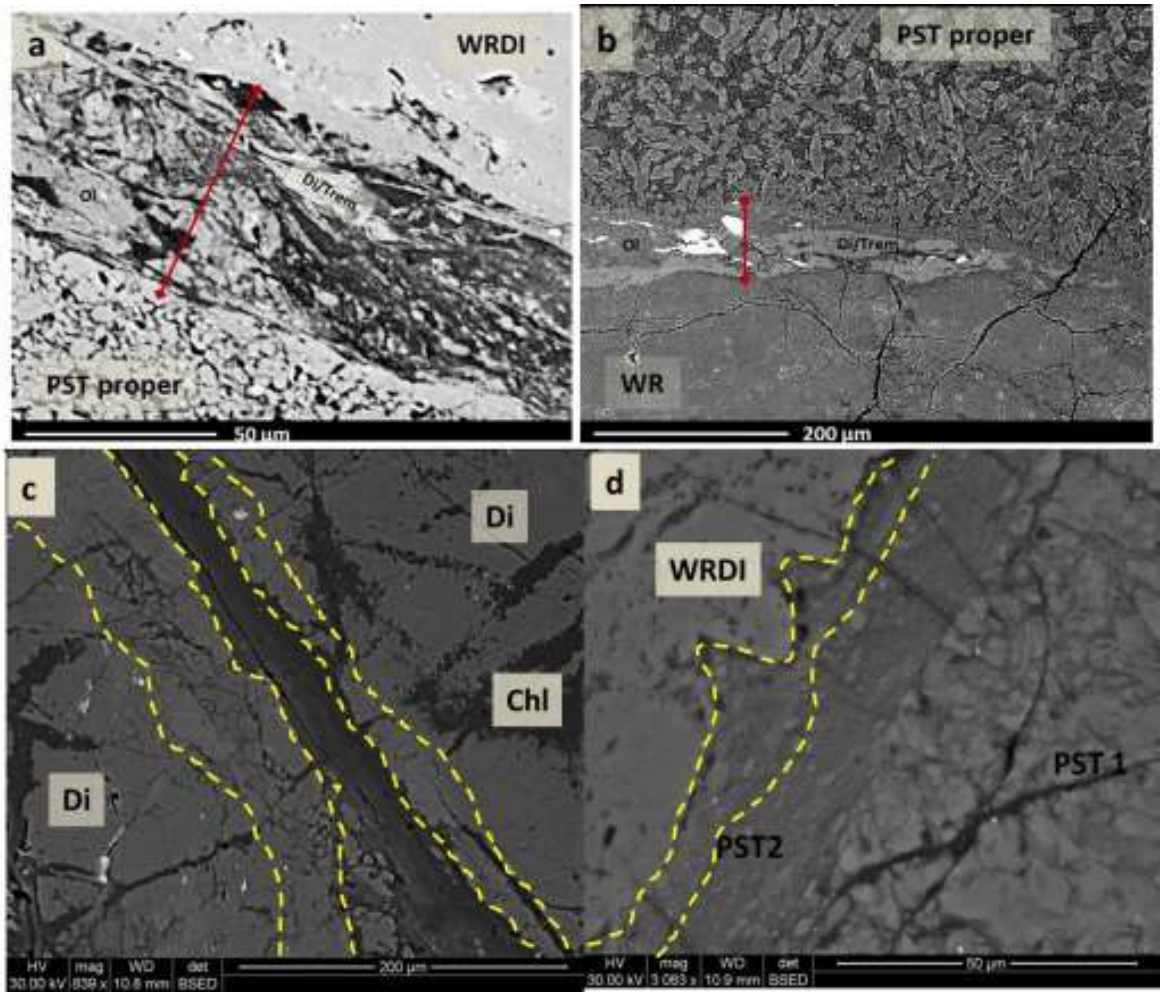


Fig. 10.8 BSE images of ultracataclasite transition zone at PST fault vein boundaries in coarse-grained hostrocks. a) Peridotite-hosted PST: Ultracataclasite between PST proper and wallrock diopside (WRDI) The width of the transition zone is indicated by the red line. The transition zone contains black patches of melt with lighter grey slivers of sheared out aggregates of diopsode and tremolite (Di/Trem) and olivine (Ol) derived from the adjacent wallrock. b) Peridotite-hosted PST: Width of ultracataclasite transition zone shown by red line. This transition zone lies between the PST proper and wallrock (WR). Crystal plastically deformed wallrock minerals olivine (Ol), diopside (Di) and tremolite (Trem) are indicated. c) Metagabbro-hosted PST: Dark vein in the middle of the image indicates the PST proper. Yellow dashed lines indicate the approximate extent of the ultracataclasite. Wallrock minerals adjacent to PST are diopside and chlorite (Chl). d) Metagabbro-hosted PST with two generations, PST 1 followed by PST 2. Yellow dashed lines indicate the approximate extent of the ultracataclasite (sheared out PST 1 in this case). Note the difference between the extent of development between the metagabbro- and peridotite-hosted PST; The metagabbro is less hydrous and its transition zones are less distinct.

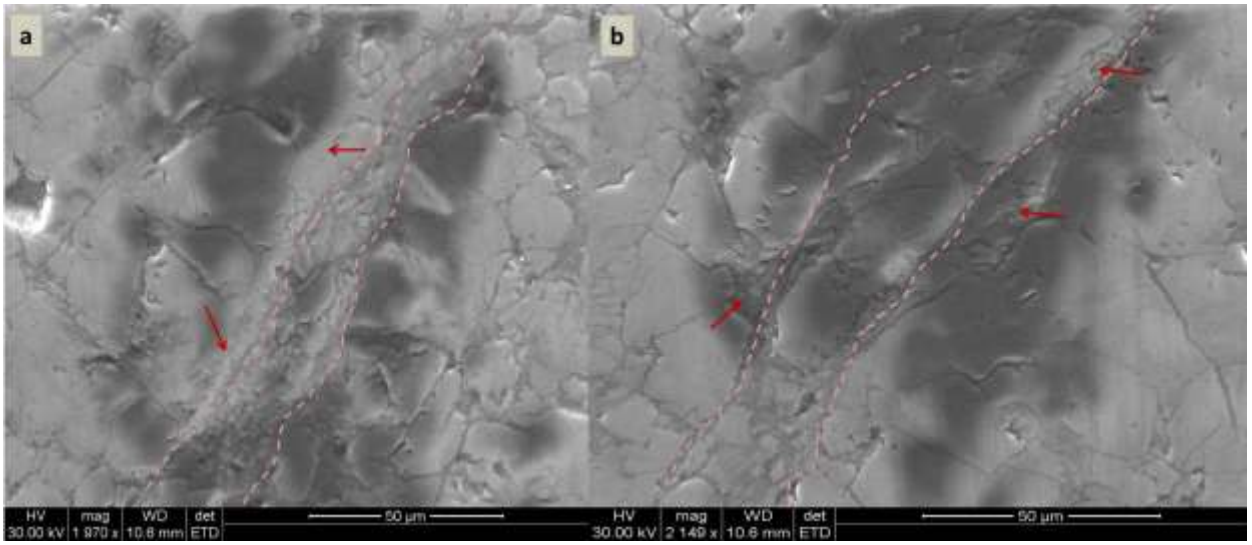


Fig. 10.9 SE images of incipient fault vein PST in fine-grained peridotite hostrock. Pink dashed lines indicate the approximate extent of the fault plane containing PST and cataclastic wallrock neoloblasts of olivine, examples of which are indicated by red arrows. Dark shadows in images are due to sample charging. a) Single distinct clast-based PST rich in angular clasts of comminuted olivine. Red arrows indicate inconsistently developed ultracataclasite. b) Single PST fault vein, developed to a lesser extent than a). PST matrix is clast-based, containing angular clasts of comminuted wallrock neoblasts.

- The collation of data in this thesis suggest that the PST generating mechanism for intermediate-depth earthquakes appears to be controlled by the same principals as shallow earthquakes, i.e. fracturing or flow is determined by strain rate, the fracture toughness and melting/breaking point of the most abundant mineral in the host rock, and the background temperature of the would-be host rock and damage zone (Braeck and Podladchikov, 2007; Hobbs et al., 1986; Kameyama et al., 1999; Sibson, 1975, 1977; Spray, 1992). The presence of intracrystalline H_2O in the fault system appears to have a secondary control on the failure process. If the fault zone experience fluids ingress or is under hydrostatic conditions, where the H_2O exists as a separate component in the system, then its control on deformation will become primary as the H_2O (or other fluids) is a distinct phase in the bulk rock. In the case of the Corsican PST studied here, no indications of fluid ingress were recorded. Fluids were introduced into the system via fusion of variably hydrated clasts. Hence, H_2O was not initially a separate component in the deformation zone, only exsolving once the melt in fault zone

had enough space to accommodate vapour phases, was supersaturated in fluids, and had cooled sufficiently (exsolution potential of a melt is inversely related to background temperature) (Fig. 7.10). H_2O and melt first enter the fault system when the weakest minerals (chlorite, tremolite, serpentine, glaucophane) and hydrated minerals fuse. It may be that with increasing heat and strain rates, in such platy, hydrous minerals, the H_2O, localised in lattice layers becomes mobilized, localizing strain within the mineral layers (Fig. 7.10). As the H_2O begins to move out of the crystal and induce dehydration, the fluxing capability of H_2O, the strong directionality of hydrogen bonds, latent heat of phase change, strain localisation and temperature rise within the mineral facilitates melting of contiguous anhydrous components.

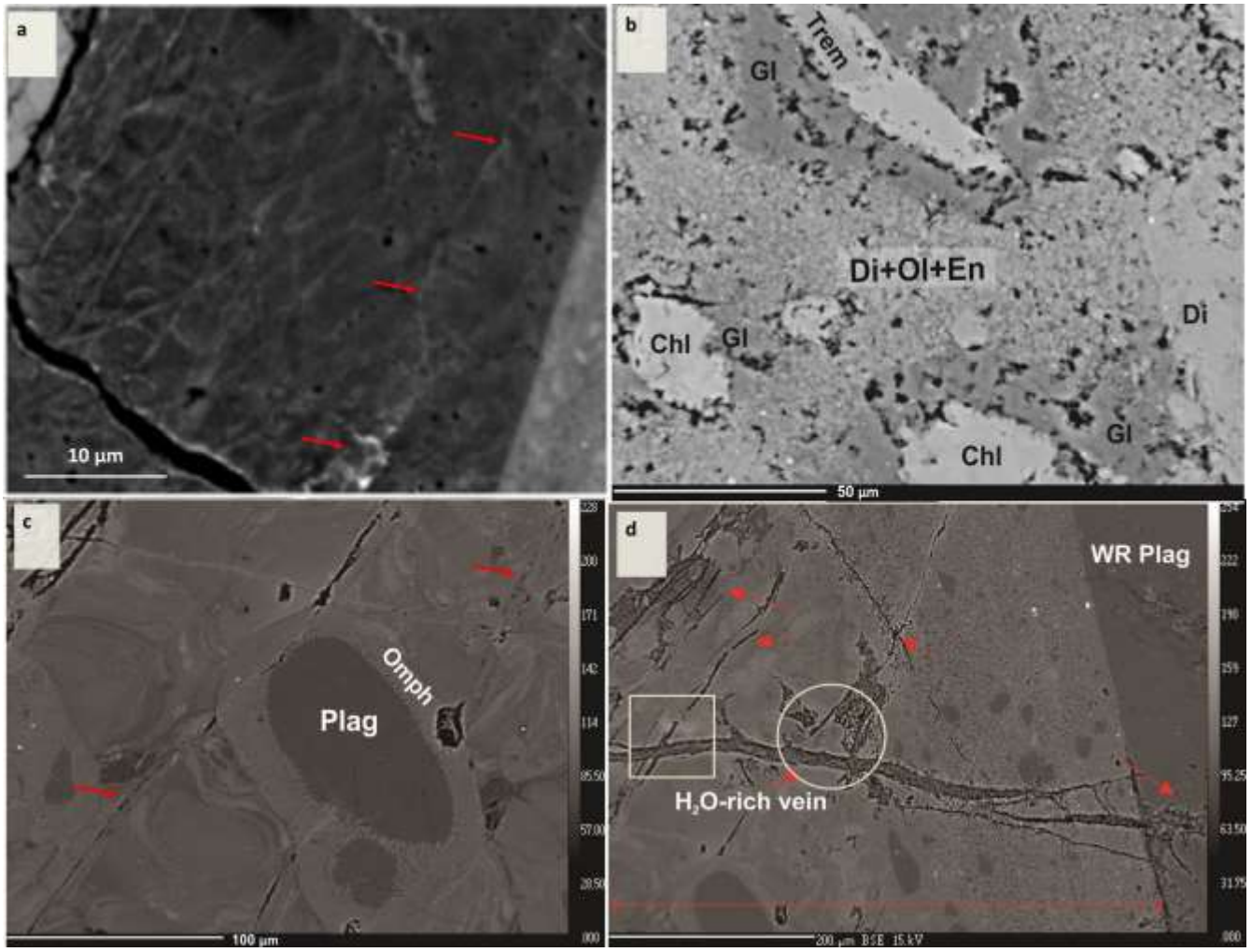


Fig. 10.10 BSE images illustrating fluid mobility associated with PST generation in peridotite (a and b) and metagrabbro (c and d). a) Dark grey area is a wallrock olivine grain in contact with PST (light grey) in the lower right corner. Red arrows indicate a melt/diffusion front of fluids entering the olivine from the PST. Sub-circular black patches interpreted as vesicles of fluid/melt. b) PST bulk matrix shown with thermally degrading wallrock minerals, chlorite (Chl), clinopyroxene (Di) and tremolite (Trem) enclosed by a glassy halo (Gl). Olivine (Ol), orthopyroxene (En) and clinopyroxene (Di) microlites dominate the matrix. Irregularly shaped black patches emanating off of survivor clasts are interpreted as fluid/melt vesicles related to the fusion of hydrous minerals. c) PST fault vein matrix where hydrous fluids crosscut still mushy crystallisation products (red arrows). d) Different section of the same vein shown in c, multiple sets of crosscutting (white square) fluid-rich veins are evident (red arrows). The white circle encloses a hydrous vein overgrown at the edges by omphacite dendrites.

11. Future outlooks

While the discovery of natural relics of intermediate-depth seismicity has guided researchers in the revision of their mechanistic and geochemical models regarding how these phenomena occur (Green and Houston, 1995; Green, 2007; John et al., 2009; Jung et al., 2004; Prieto et al., 2013; Reynard et al., 2010; Zhang et al., 2004), much remains to be done before we fully understand these processes. It is clear from the various case studies (Green, 1973, 2007; Jessell and Lister, 1991; Kirby et al., 1995, 1991; Zhang et al., 2004) based on natural laboratories that intermediate-depth earthquakes come in several varieties and a unifying model has yet to be constructed. In the case of the Corsican pseudotachylytes future possible studies are suggested:

1. Detailed analysis and quantification of the H_2O and halogen content in hydrous and anhydrous minerals at the ppm level and the location of hydroxyls within the deformed wallrock and survivor clasts of the pseudotachylytes. This could be done using in-situ XRD and EBSD analysis and would be relevant in terms of documenting the process of hydrolytic weakening.

2. Detailed EBSD analysis on the preferred orientation of wallrock minerals at pseudotachylyte vein boundaries to assess the progression of dislocation creep/glide at the fine scale. This would be fundamental in providing constraints for shear localization and thermal runaway models, which at this stage are largely theoretical and based on the results of high pressure ceramic experiments.

3. In-situ LA-ICPMS analysis and mapping of survivor clasts, their glassy haloes and pseudotachylyte bulk matrix in order to understand the diffusion and partitioning of trace elements as they move from deformed fusing crystalline phases into the melt phase. This could also be of use in determining natural partition coefficients for olivine, orthopyroxene and clinopyroxene at high pressures.

4. In-situ analysis of H_2O, CO_2 and halogens by XRD synchrotron and micro-raman spectroscopy, in fresh and altered pseudotachylyte veins in order to evaluate how much diffusion has taken place across veins and the manner in which this has taken place. Of particular interest is the movement of fluids in association with observed vesicles.

5. Higher resolution imaging of the gouge and ultracataclasite using TEM and better SEM facilities, in order to better understand the mechanism by which these veins form and the rheological controls on this process, regarding the fusion of different minerals at different grain sizes. Due to the inconsistent operation of the TEM and SEM equipment at my disposal, I could not achieve higher resolution images myself.

References

Abers, G.A., Nakajima, J., van Keken, P.E., Kita, S., Hacker, B.R., 2013. Thermal–petrological controls on the location of earthquakes within subducting plates. Earth Planet. Sci. Lett. 369-370, 178–187. doi:10.1016/j.epsl.2013.03.022

Agard, P., Monié, P., Jolivet, L., Goffé, B., 2002. Exhumation of the Schistes Lustrés complex: in situ laser probe 40Ar/39Ar constraints and implications for the Western Alps. J. Metamorph. Geol. 20, 599–618.

Andersen, T., B., Austrheim, H., Deseta, N., Silkoset, P., Ashwal, L., David, 2014. Large subduction earthquakes along the fossil MOHO in Alpine Corsica. Geology 42, 395 – 398.

Andersen, T.B., Austrheim, H., 2006. Fossil earthquakes recorded by pseudotachylytes in mantle peridotite from the Alpine subduction complex of Corsica. Earth Planet. Sci. Lett. 242, 58–72. doi:10.1016/j.epsl.2005.11.058

Andersen, T.B., Mair, K., Austrheim, H., Podladchikov, Y.Y., Vrijmoed, J.C., 2008. Stress release in exhumed intermediate and deep earthquakes determined from ultramafic pseudotachylyte. Geology 42, 395 – 398. doi:10.1130/G25230A.1

Angiboust, S., Agard, P., Yamato, P., Raimbourg, H., 2012. Eclogite breccias in a subducted ophiolite: A record of intermediatedepth earthquakes? Geology. doi:doi:10.1130/G32925.1

Austrheim, H., Andersen, T.B., 2004. Pseudotachylytes from Corsica: fossil earthquakes from a subduction complex. Terra Nova 16, 193–197. doi:10.1111/j.1365-3121.2004.00551.x

Austrheim, H., Boundy, T., 1994. Pseudotachylytes generated by seismic faulting and eclogitization of the deep crust. Science 265, 82 – 83.

Austrheim, H., Erambert, M., Engvik, A.K., 1997. Processing of crust in the root of the Caledonian continental collision zone: the role of eclogitization. Tectonophysics 273, 129–153.

Ave'Lallemant, H.G., Carter, N.L., 1970. Syntectonic recrystallisation of olivine and modes of flow in the upper mantle. Geol. Soc. Am. Bull. 81, 2203 – 2220.

Barcheck, C.G., Wiens, D.A., van Keken, P.E., Hacker, B.R., 2012. The relationship of intermediate- and deep-focus seismicity to the hydration and dehydration of subducting slabs. Earth Planet. Sci. Lett. 349-350, 153–160. doi:10.1016/j.epsl.2012.06.055

Beccaluva, L., Ohnenstetter, D., Ohnenstetter, M., Venturelli, G., 1977. The trace element geochemistry of Corsican ophiolites. Contrib. Miner. Pet. 64, 11–31.

Bestmann, M., Pennacchioni, G., Frank, G., Göken, M., de Wall, H., 2011. Pseudotachylyte in muscovite-bearing quartzite: Coseismic friction-induced melting and plastic deformation of quartz. J. Struct. Geol. 33, 169–186. doi:10.1016/j.jsg.2010.10.009

Bestmann, M., Pennacchioni, G., Nielsen, S., Göken, M., de Wall, H., 2012. Deformation and ultrafine dynamic recrystallization of quartz in pseudotachylyte-bearing brittle faults: A matter of a few seconds. J. Struct. Geol. 38, 21–38. doi:10.1016/j.jsg.2011.10.001

Boland, J.N., Tullis, T.E., 1986. Deformation behaviour of wet and dry clinopyroxenite in the brittle to ductile transition region. Geophys. Monogr. Am. Geophys. Union 36, 35 – 49.

Brady, J.B., 1995. Diffusion data for silicate minerals, glasses, and liquids. Miner. Phys. Crystallogr. Handb. Phys. Constants 269–290.

Braeck, S., Podladchikov, Y., 2007. Spontaneous Thermal Runaway as an Ultimate Failure Mechanism of Materials. Phys. Rev. Lett. 98. doi:10.1103/PhysRevLett.98.095504

Branlund, J.M., Kameyama, M.C., Yuen, D.A., Kaneda, Y., 2000. Effects of temperature-dependent thermal diffusivity on shear instability in a viscoelastic zone: implications for faster ductile faulting and earthquakes in the spinel stability field. Earth Planet. Sci. Lett. 182, 171–185.

Camacho, A., McDougall, I., Armstrong, R., Braun, J., 2001. Evidence for shear heating, Musgrave Block, central Australia. J. Struct. Geol. 23, 1007–1013.

Chernak, L.J., Hirth, G., 2011. Syndeformational antigorite dehydration produces stable fault slip. Geology 39, 847–850. doi:10.1130/G31919.1

Cmiral, M., Fitz Gerald, J.D., Faul, U.H., Green, D.H., 1998. A close look at dihedral angles and melt geometry in olivine-basalt aggregates: a TEM study. Contrib. Miner. Pet. 130, 336 – 345.
Davis, G., H., Reynolds, S., J., 1996. Structural geology of rocks and regions. Wiley, United States of America.
Deer, W.A., Howie, R.A., Zussman, J., 1992. An introduction to rock-forming minerals, 2nd ed. Longman Scientific and Technical.
Del Gaudio, P., Di Toro, G., Han, R., Hirose, T., Nielsen, S., Shimamoto, T., Cavallo, A., 2009. Frictional melting of peridotite and seismic slip. J. Geophys. Res. 114. doi:10.1029/2008JB005990
Demouchy, S., Schneider, S., E., Mackwell, S., J., Zimmerman, M., E., Kohlstedt, D.L., 2009. Experimental deformation of single olivine crystals at lithospheric temperatures. Geophys. Res. Lett. 36.
Deseta, N., Andersen, T.B., Ashwal, L., 2014. A weakening mechanism for intermediate-depth seismicity? Detailed petrographic and microtextural observations from blueschist facies pseudotachylytes, Cape Corse, Corsica. Tectonophysics 610, 138 – 149.
Di Toro, G., Pennacchioni, G., 2004. Superheated friction-induced melts in zoned pseudotachylytes within the Adamello tonalites (Italian Southern Alps). J. Struct. Geol. 26, 1783–1801. doi:10.1016/j.jsg.2004.03.001
Di Toro, G., Pennacchioni, G., Nielsen, S., 2009. Pseudotachylytes and earthquake source mechanics. Int. Geophys. 94, 87–133.
Di Toro, G., Pennacchioni, G., Teza, G., 2005. Can pseudotachylytes be used to infer earthquake source parameters? An example of limitations in the study of exhumed faults. Tectonophysics 402, 3–20. doi:10.1016/j.tecto.2004.10.014
Dijkstra, A., H., Drury, M.R., Vissers, R.L.M., Newman, J., Herman, V.R., L.M., 2004. Shear zones in the upper mantle: evidence from apline- and ophiolite-type peridotite massifs. Geol. Soc. Lond. Spec. Publ. 224, 11 – 24.
Dobson, D.P., Meredith, P.G., Boon, S.A., 2002. Simulation of subduction zone seismicity by dehydration of serpentine. Science 298, 1407 – 1410.
Fabbri, O., Lin, A., Tokushige, H., 2000. Coeval formation of cataclasite and pseudotachylyte in a Miocene forearc granodiorite, southern Kyushu, Japan. J. Struct. Geol. 22, 1015–1025.
Faccenda, M., 2014. Water in the slab: A trilogy. Tectonophysics 614, 1–30. doi:10.1016/j.tecto.2013.12.020
Green, D.H., 1973. Experimental melting studies on a model upper mantle composition at high pressure under water-saturated and water-undersaturated conditions. Earth Planet. Sci. Lett. 19, 37–53.
Green, H.W., 2003. Earth science: Tiny triggers deep down. Nature 424, 893–894.
Green, H.W., 2007. Shearing instabilities accompanying high-pressure phase transformations and the mechanics of deep earthquakes. Proc. Natl. Acad. Sci. 104, 9133–9138.
Green, H.W., Houston, H., 1995. The mechanics of deep earthquakes. Annu. Rev. Earth Planet. Sci. 23, 169 – 213.
Green, H.W., Jung, H., 2005. Fluids, Faulting, and Flow. Elements 1, 31 – 37.
Green, H., W. II, 1995. The mechanics of deep earthquakes. Annu. Rev. Earth Planet. Sci. 23, 169 – 213.
Hacker, B.R., Andersen, T.B., Johnston, S., Kylander-Clark, A.R.C., Peterman, E.M., Walsh, E.O., Young, D., 2010. High-temperature deformation during continental-margin subduction & exhumation: The ultrahigh-pressure Western Gneiss Region of Norway. Tectonophysics 480, 149–171. doi:10.1016/j.tecto.2009.08.012
Hacker, B.R., Christie, J., M., 1990. Brittle/ductile and plastic/cataclastic transitions in experimentally deformed and metamorphosed amphibolite. Geophys. Monogr. Am. Geophys. Union 56, 127 – 147.

Hacker, B.R., Peacock, S., Abers, G.A., Holloway, S., 2004. Subduction factory 2. Are intermediate-depth earthquakes in subducting slabs linked to metamorphic dehydration reactions? J. Geophys. Res. 108. doi:10.1029/2001JB001129

Handy, M., R., 1990. The solid-state flow of polymineralic rocks. J. Geophys. Res. 95, 8647 – 8661.

Hansen, L.N., Zimmerman, M.E., Kohlstedt, D.L., 2012. The influence of microstructure on deformation of olivine in the grain-boundary sliding regime. J. Geophys. Res. 117. doi:10.1029/2012JB009305

Hobbs, B.E., Ord, A., Teyssier, C., 1986. Earthquakes in the ductile regime? Pure Appl. Geophys. 124, 309–336.

Hogan, J.D., Spray, J.G., Rogers, R.J., Boonsue, S., Vincent, G., Schneider, M., 2011. Micro-scale energy dissipation mechanisms during dynamic fracture in natural polyphase ceramic blocks. Int. J. Impact Eng. 38, 931–939. doi:10.1016/j.ijimpeng.2011.06.004

Houston, H., 2007. Deep earthquakes, in: Treatise of Geophysics. Elsevier, pp. 321 – 347.

Iyer, K., Rüpke, L.H., Morgan, J.P., 2010. Feedbacks between mantle hydration and hydrothermal convection at ocean spreading centers. Earth Planet. Sci. Lett. 296, 34–44. doi:10.1016/j.epsl.2010.04.037

Jessell, M.W., Lister, G.S., 1991. Strain localization behaviour in experimental shear zones. Pure Appl. Geophys. 137, 421–438.

Jin, D., Karato, S., Obata, M., 1998. Mechanisms of shear localization in the continental lithosphere: inference from the deformation microstructures of peridotites from the Ivrea zone, northwestern Italy. J. Struct. Geol. 20, 195–209.

Jin, Z.-M., Green, H.W., Zhou, Y., 1994. Melt topology in molten mantle peridotite during ductile deformation. Nature 372, 164.

John, T., Medvedev, S., Rüpke, L.H., Andersen, T.B., Podladchikov, Y.Y., Austrheim, H., 2009. Generation of intermediate-depth earthquakes by self-localizing thermal runaway. Nat. Geosci. 2, 137–140. doi:10.1038/ngeo419

John, T., Schenk, V., 2006. Interrelations between intermediate-depth earthquakes and fluid flow within subducting oceanic plates: Constraints from eclogite facies pseudotachylytes. Geology 34, 557. doi:10.1130/G22411.1

Johnston, J.D., McCaffrey, K.J.W., 1996. Fractal geometries of vein systems and the variation of scalingrelationships with mechanism. J. Struct. Geol. 18, 349–358.

Jolivet, L., 1993. Extension of thickened continental crust, from brittle to ductile deformation: examples from Alpine Corsica and Aegean Sea. Ann. Geofis. 36, 139 – 153.

Jolivet, L., Raimbourg, H., Labrousse, L., Avigad, D., Leroy, Y., Austrheim, H., Andersen, T.B., 2005. Softening trigerred by eclogitization, the first step toward exhumation during continental subduction. Earth Planet. Sci. Lett. 237, 532–547. doi:10.1016/j.epsl.2005.06.047

Jung, H., Green, H.W., Dobrzhinetskaya, L., 2004. Intermediate-depth earthquake faulting by dehydration embrittlement with negative volume change. Nature 428, 545 – 549.

Jung, H., Katayama, I., Jiang, Z., Hiraga, I., Karato, S.-I., 2006. Effect of water and stress on the lattice-preferred orientation of olivine. Tectonophysics 421, 1 – 22.

Kameyama, M., Yuen, D.A., Karato, S.-I., 1999. Thermal-mechanical effects of low-temperature plasticity (the Peierls mechanism) on the deformation of a viscoelastic shear zone. Earth Planet. Sci. Lett. 168, 159–172.

Kanamori, H., Anderson, D., Heaton, T., 1998. Frictional melting during the rupture of the 1994 Bolivian earthquake. Science 279, 839 – 842.

Karato, S., 1987. Scanning electron-microsope of dislocations in olivine. Physics and chemistry of minerals. 14, 245 - 248.

Katayama, I., Karato, S.-I., 2006. Effect of temperature on the B- and C-type olivine fabric transition and implications for flow patterns in subduction zones. Phys. Earth Planet. Inter. 157, 33 – 45.

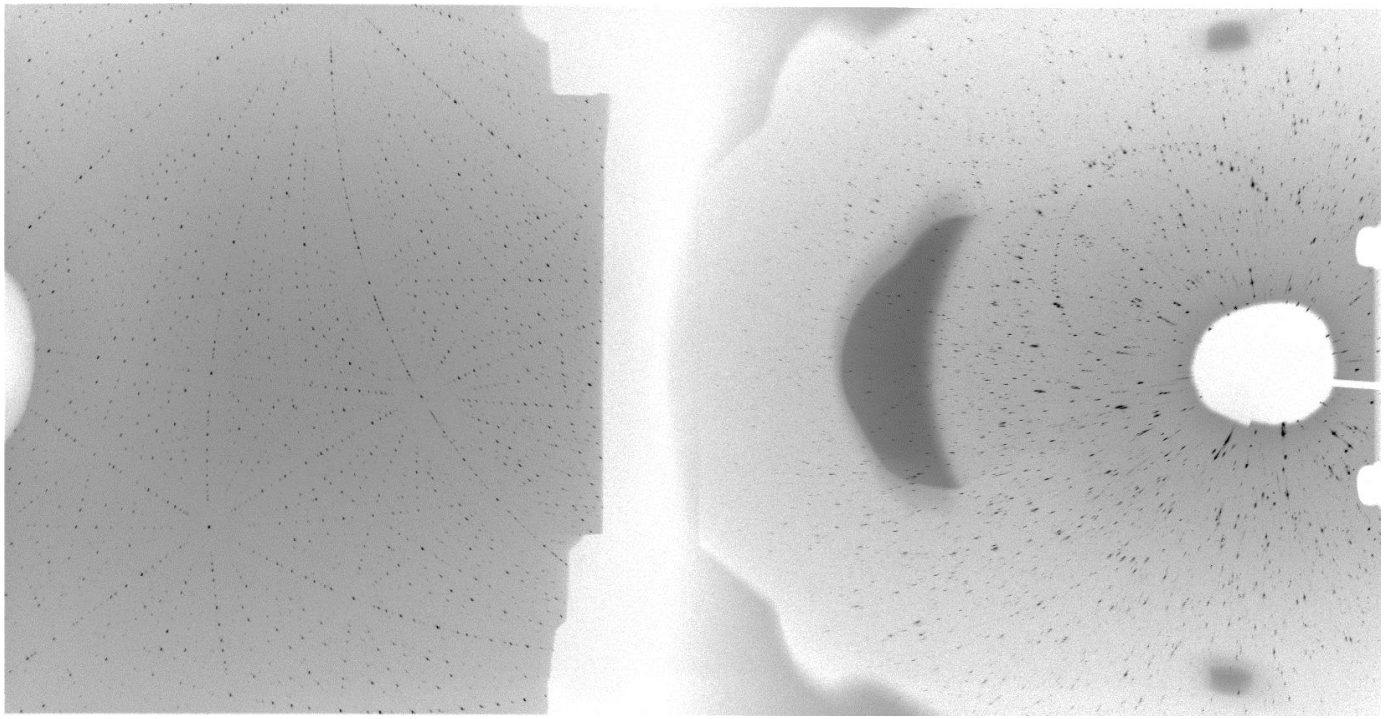
Katayama, I., Parkinson, C.D., Okamoto, K., Nakajima, Y., Maruyama, S., 2000. Supersilicic clinopyroxene and silica exsolution in UHPM eclogite and pelitic gneiss from the Kokchetav massif, Kazakhstan. Am. Miner. 85, 1368–1374.

Kelemen, P.B., Hirth, G., 2007. A periodic shear-heating mechanism for intermediate-depth earthquakes in the mantle. Nature 446, 787–790. doi:10.1038/nature05717
Kim, J.-W., Ree, J.-H., Han, R., Shimamoto, T., 2010. Experimental evidence for the simultaneous formation of pseudotachylyte and mylonite in the brittle regime. Geology 38, 1143–1146.
Kirby, S., Durham, W., Stern, L., 1991. Mantle phase changes and deep earthquake faulting in subducting lithosphere. Science 252, 216 – 225.
Kirby, S., Engdahl, E.R., Denlinger, R.P., 1995. Subduction Top to Bottom. Geophys. Monogr. Am. Geophys. Union 96, 195 – 214.
Kirby, S.H., Stein, S., Okal, E.A., Rubie, D.C., 1996. Metastable mantle phase transformations and deep earthquakes in subducting oceanic lithosphere. Rev. Geophys. 34, 261 – 306.
Konzett, J., Frost, D.J., Proyer, A., Ulmer, P., 2007. The Ca-Eskola component in eclogitic clinopyroxene as a function of pressure, temperature and bulk composition: an experimental study to 15 GPa with possible implications for the formation of oriented SiO2-inclusions in omphacite. Contrib. Miner. Pet. 155, 215–228. doi:10.1007/s00410-007-0238-0
Lin, A., 1994a. Glassy pseudotachylyte veins from Fuyun fault zone, northwest China. J. Struct. Geol. 16, 71 – 83.
Lin, A., 1994b. Microlite morphology and chemistry in pseudotachylite, from the Fuyun fault zone, China. J. Geol. 102, 317 – 329.
Lund, M., Austrheim, H., 2003. High-pressure metamorphism and deep-crustal seismicity: evidence from contemporaneous formation of pseudotachylytes and eclogite facies coronas. Tectonophysics 372, 59 – 83.
Luth, R., W., Boettcher, A.L., 1986. Hydrogen and the melting of silicates. Am. Miner. 71, 264 – 276.
Magloughlin, J., Spray, J., 1992. Frictional melting processes and products in geological timescales: introduction and discussion. Tectonophysics 204, 197 – 206.
Mancktelow, N.S., 2006. How ductile are ductile shear zones? Geology 34, 345. doi:10.1130/G22260.1
Merlet, C., 1994. An accurate computer correction program for quantitative electron microprobe analysis. Mikrochim. Acta 114/115, 363–376.
Mishra, O.P., Zhao, D., 2004. Seismic evidence for dehydration embrittlement of the Pacific slab. Geophys. Res. Lett. 31. doi:10.1029/2004GL019489
Mittempergher, S., Dallai, L., Pennacchioni, G., Renard, F., Di Toro, G., 2014. Origin of hydrous fluids at seismogenic depth: Constraints from natural and experimental fault rocks. Earth Planet. Sci. Lett. 385, 97–109. doi:10.1016/j.epsl.2013.10.027
Moghadam, R., M., Trepmann, C., A., Stockhert, B., Renner, J., 2010. Rheology of synthetic omphacite aggregates at high pressure and high temperature. J. Pet. 51, 921 – 945. doi:10.1093/petrology/egq006
Mohn, G., Manatschal, G., Muntener, O., Beltrando, M., Masini, E., 2009. Unravelling the interaction between tectonic and sedimentary processes during lithospheric thinning in the Alpine Tethys margins. Int. J. Earth Sci. 99, S75 –S101.
Nakajima, J., Tsuji, Y., Hasegawa, A., Kita, S., Okada, T., Matsuzawa, T., 2009a. Tomographic imaging of hydrated crust and mantle in the subducting Pacific slab beneath Hokkaido, Japan: Evidence for dehydration embrittlement as a cause of intraslab earthquakes. Gondwana Res. 16, 470–481. doi:10.1016/j.gr.2008.12.010
Nakajima, J., Tsuji, Y., Hasegawa, A., Kita, S., Okada, T., Matsuzawa, T., 2009b. Tomographic imaging of hydrated crust and mantle in the subducting Pacific slab beneath Hokkaido, Japan: Evidence for dehydration embrittlement as a cause of intraslab earthquakes. Gondwana Res. 16, 470–481. doi:10.1016/j.gr.2008.12.010
Newman, J., Lamb, W., Drury, M.R., Vissers, R.L., 1999. Deformation processes in a peridotite shear zone: reaction-softening by an H2O-deficient, continuous net transfer reaction. Tectonophysics 303, 193 – 222.

Niemeijer, A., Di Toro, G., Griffith, A., W., Bistacchi, A., Smith, S., A.F., 2012. Inferring earthquake physics and chemistry using an integrated field and laboratory approach. J. Struct. Geol. 39, 2 – 36.
O'Hara, K., 1992. Major- and trace-element constraints on the petrogenesis of fault-related pseudotachylyte, western Blue Ridge province, North Carolina. Tectonophysics 204, 279 – 288.
Ogawa, M., 1987. Shear instability in a viscoelastic material as the cause of deep focus earthquakes. J. Geophys. Res. 92, 13801 – 13810.
Orowan, E., 1960. Mechanism of seismic faulting, in: Rock Deformation, Geological Society of America. pp. 323 – 345.
Passchier, C., W., Trouw, J., 2005. Microtectonics. Springer-Verlag, Berlin.
Pec, M., Stünitz, H., Heilbronner, R., Drury, M., de Capitani, C., 2012. Origin of pseudotachylites in slow creep experiments. Earth Planet. Sci. Lett. 355-356, 299–310. doi:10.1016/j.epsl.2012.09.004
Prieto, G.A., Florez, M., Barrett, S.A., Beroza, G.C., Pedraza, P., Blanco, J.F., Poveda, E., 2013. Seismic evidence for thermal runaway during intermediate-depth earthquake rupture: Seismic evidence for thermal runaway. Geophys. Res. Lett. n/a–n/a. doi:10.1002/2013GL058109
Ravna, E.J.K., Andersen, T.B., Jolivet, L., De Capitani, C., 2010. Cold subduction and the formation of lawsonite eclogite - constraints from prograde evolution of eclogitized pillow lava from Corsica. J. Metamorph. Geol. 28, 381 – 395.
Reynard, B., Nakajima, J., Kawakatsu, H., 2010. Earthquakes and plastic deformation of anhydrous slab mantle in double Wadati-Benioff zones. Geophys. Res. Lett. 37, n/a–n/a. doi:10.1029/2010GL045494
Rice, J., R., 2006. Heat and weakening of faults during earthquake slip. J. Geophys. Res. 111, 1 – 29. doi:10.1029/2005
Rondenay, S., Abers, G.A., van Keken, P.E., 2008. Seismic imaging of subduction zone metamorphism. Geology 36, 275 – 278.
Scholz, C.H., 2002. The Mechanics of Earthquakes and Faulting. Cambride University Press.
Shand, S.J., 1916. The pesudotachylyte of Parijs (Orange Free State), and its relation to "trap-shotten gneiss" and "flinty crush-rock". Geolgical Soc. Lond. Q. J. 72, 198 – 217.
Sibson, R., H., 1975. Generation of pseudotachylyte by ancient seismic faulting. Geophys. J. Int. 43, 775–794.
Sibson, R., H., 1977a. Kinetic shear resistance, fluid pressures and radiation efficiency during seismic faulting. Pure Appl. Geophys. 115, 387–400.
Sibson, R., H., 1977b. Fault rocks and fault mechanisms. J. Geol. Soc. 133, 191–213.
Sibson, R.H., 1980a. Transient discontinuities in ductile shear zones. J. Struct. Geol. 2, 165–171.
Sibson, R.H., 1980b. Transient discontinuities in ductile shear zones. J. Struct. Geol. 2, 165–171.
Sibson, R.H., Toy, V., G., 2006. The habitat of fault-generated pseudotachylyte: presence vs. absence of friction-melt. Earthquakes Radiated Energy Phys. Faulting 170, 153 – 156.
Silkoset, P., 2013. Microstructure of ultramafic pseudotachylyte from Alpine Corsica – insights into earthquakes in mantle lithosphere. Unpublished Master thesis: University of Oslo, Norway.
Smyth, J.R., 1980. Cation vacancies and the crystal chemistry of breakdown reactions in kimberlitic omphacites. Am. Miner. 65, 1185–1191.
Spandler, C., Pettke, T., Rubatto, D., 2011. Internal and External Fluid Sources for Eclogite-facies Veins in the Monviso Meta-ophiolite, Western Alps: Implications for Fluid Flow in Subduction Zones. J. Pet. 52, 1207–1236. doi:10.1093/petrology/egr025
Spray, J., 1992. A physical basis for the frictional melting of some rock-forming minerals. Tectonophysics 204, 201 – 221.
Spray, J.G., 2010. Frictional Melting Processes in Planetary Materials: From Hypervelocity Impact to Earthquakes. Annu. Rev. Earth Planet. Sci. 38, 221–254. doi:10.1146/annurev.earth.031208.100045

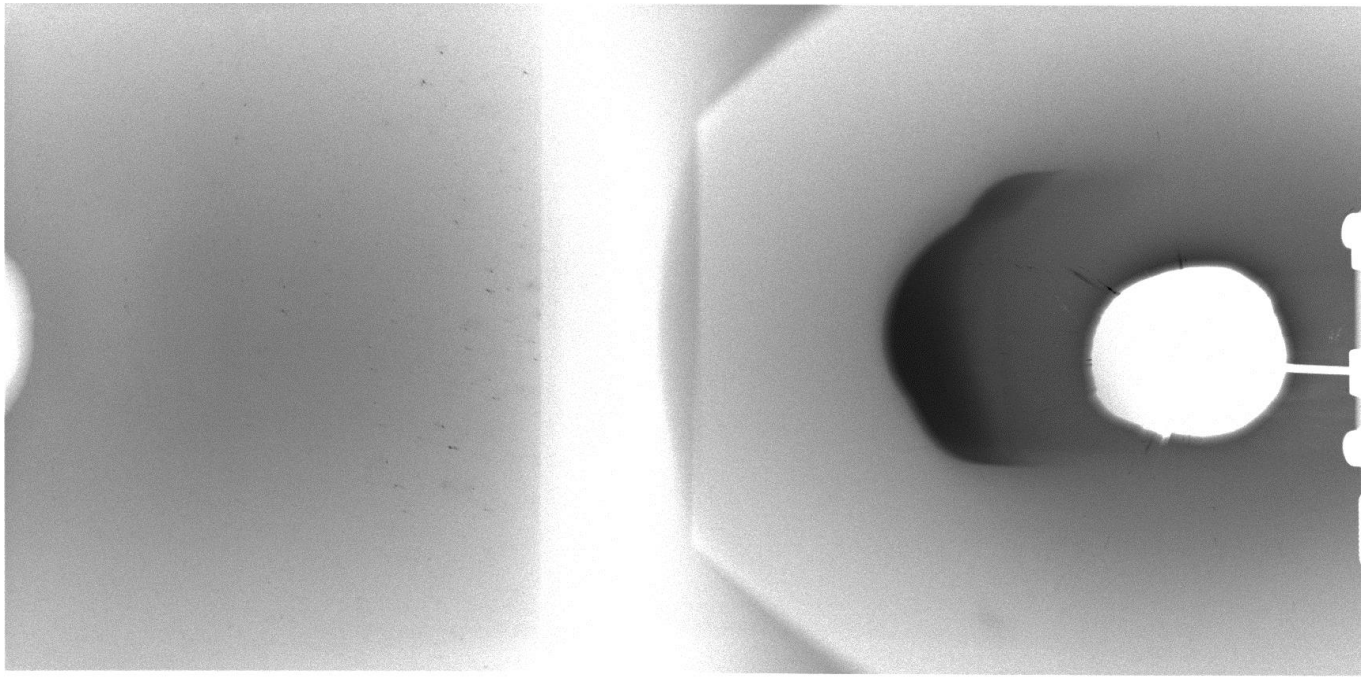
Swanson, M.T., 1992. Fault structure, wear mechanisms and rupture processes in pseudotachylyte generation. Tectonophysics 204, 223 – 242.
Twis, R.J., Moores, E.M., 2007. Structural Geology. W.H. Freeman and Company.
Van Keken, P.E., Hacker, B.R., Syracuse, E.M., Abers, G.A., 2011. Subduction factory: 4. Depth-dependent flux of H_2O from subducting slabs worldwide. J. Geophys. Res. 116. doi:10.1029/2010JB007922
Vitale Brovarone, A., Beyssac, O., Malavieille, J., Molli, G., Beltrando, M., Compagnoni, R., 2013. Stacking metamorphism of continuous segments of subducted lithosphere in a high-pressure wedge: The example of Alpine Corsica (France). Earth-Sci. Rev. 116, 35 – 56.
Vitale Brovarone, A., Herwartz, D., 2013. Timing of HP metamorphism in the Schistes Lustrés of Alpine Corsica: New Lu–Hf garnet and lawsonite ages. Lithos 172-173, 175–191. doi:10.1016/j.lithos.2013.03.009
Vitale Brovarone, Groppo, Hetenyi, Compagnoni, R., Malavieille, 2011. Coexistence of lawsonite-bearing eclogite and blueschist : phase equilibria modelling of Alpine Corsica metabasalts and petrological evolution of subducting slabs. J. Metamorph. Geol. 29, 583 – 600.
Wang, Q., 2010. A review of water contents and ductile deformation mechanisms of olivine: Implications for the lithosphere–asthenosphere boundary of continents. Lithos 120, 30–41. doi:10.1016/j.lithos.2010.05.010
Warren, J.M., Hirth, G., 2006. Grain size sensitive deformation mechanisms in naturally deformed peridotites. Earth Planet. Sci. Lett. 248, 438–450. doi:10.1016/j.epsl.2006.06.006
Wenk, H.R., 1978. Are pseudotachylites products of fracture or fusion? Geology 6, 507 – 511.
Wilson, A.H., 2012. A Chill Sequence to the Bushveld Complex: Insight into the First Stage of Emplacement and Implications for the Parental Magmas. J. Pet. 53, 1123–1168. doi:10.1093/petrology/egs011
Yamasaki, T., Tetsuzo, S., 2003. Double seismic zones and dehydration embrittlement of the subducting slab. J. Geophys. Res. 108.
Zhang, J., Green II, H.W., Bozhilov, K., Jin, Z., 2004. Faulting produced by the precipitation of water at grain boundaries in hot subducting oceanic crust. Nature 428, 633 – 636.
Zhao, S., Nee, P., Green, H.W., Dobrzhinetskaya, L.F., 2011. Ca-Eskola component in clinopyroxene: Experimental studies at high pressures and high temperatures in multianvil apparatus. Earth Planet. Sci. Lett. 307, 517–524. doi:10.1016/j.epsl.2011.05.026

Laue pattern from a very well-crystalline grain (For reference)



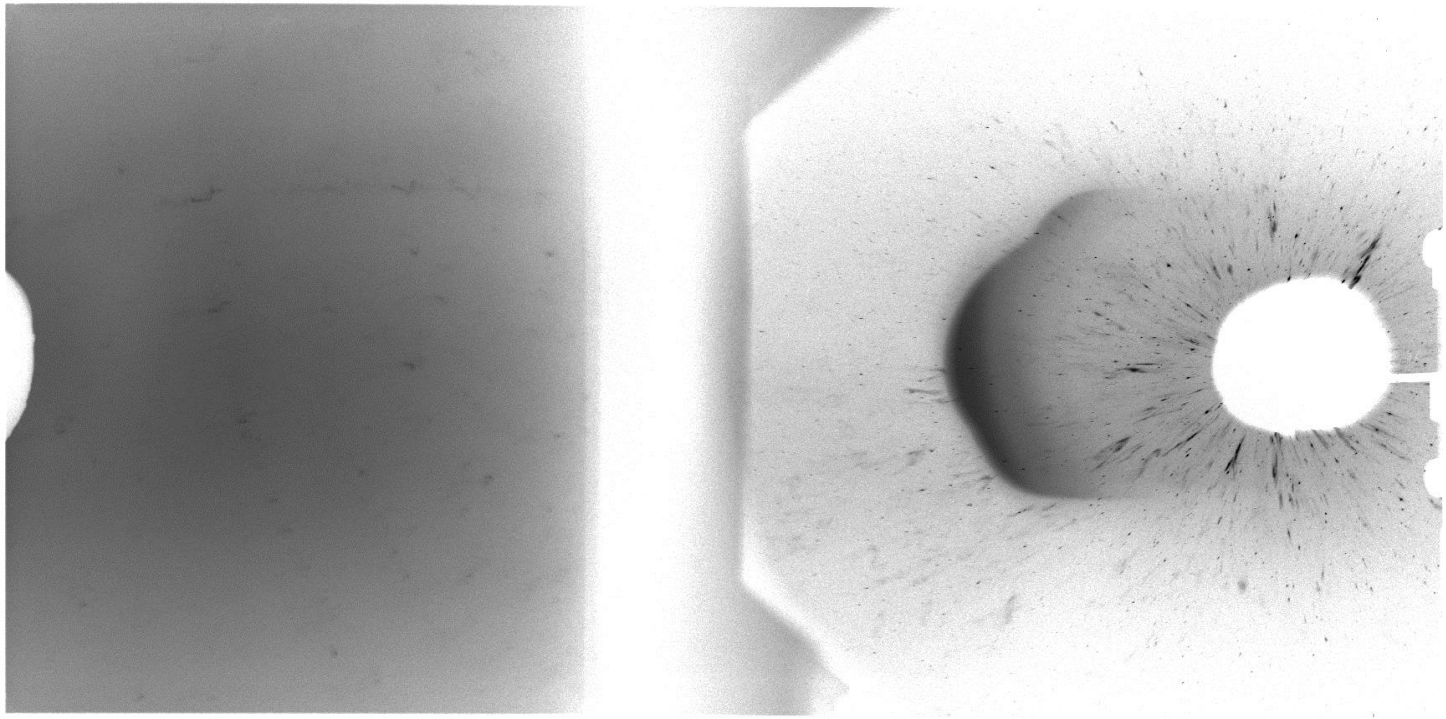
Pyroxene from the ibitira meteorite

Here is what a Laue pattern from poorly-crystalline, polycrystalline grain looks like



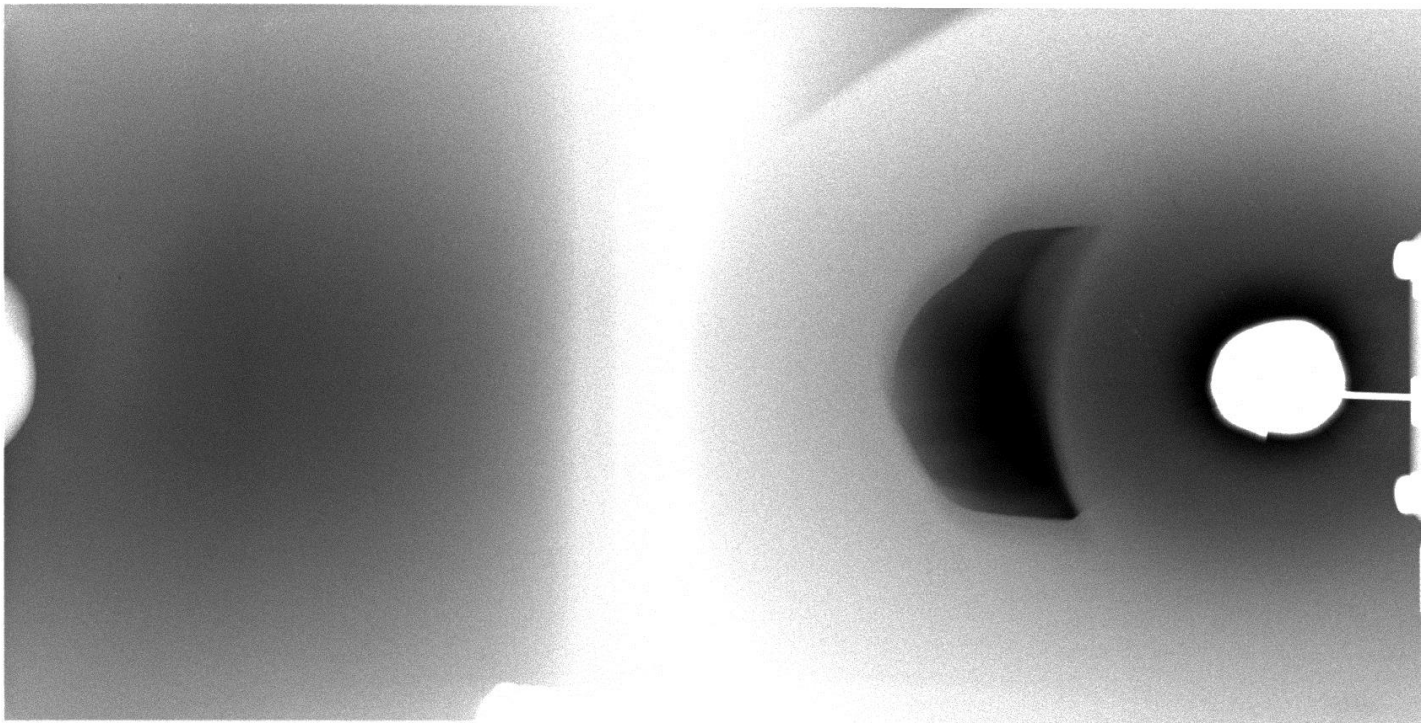
Ca Phosphate from the orgueil meteorite

Here is what a Laue pattern from a strained, barely-crystalline grain looks like

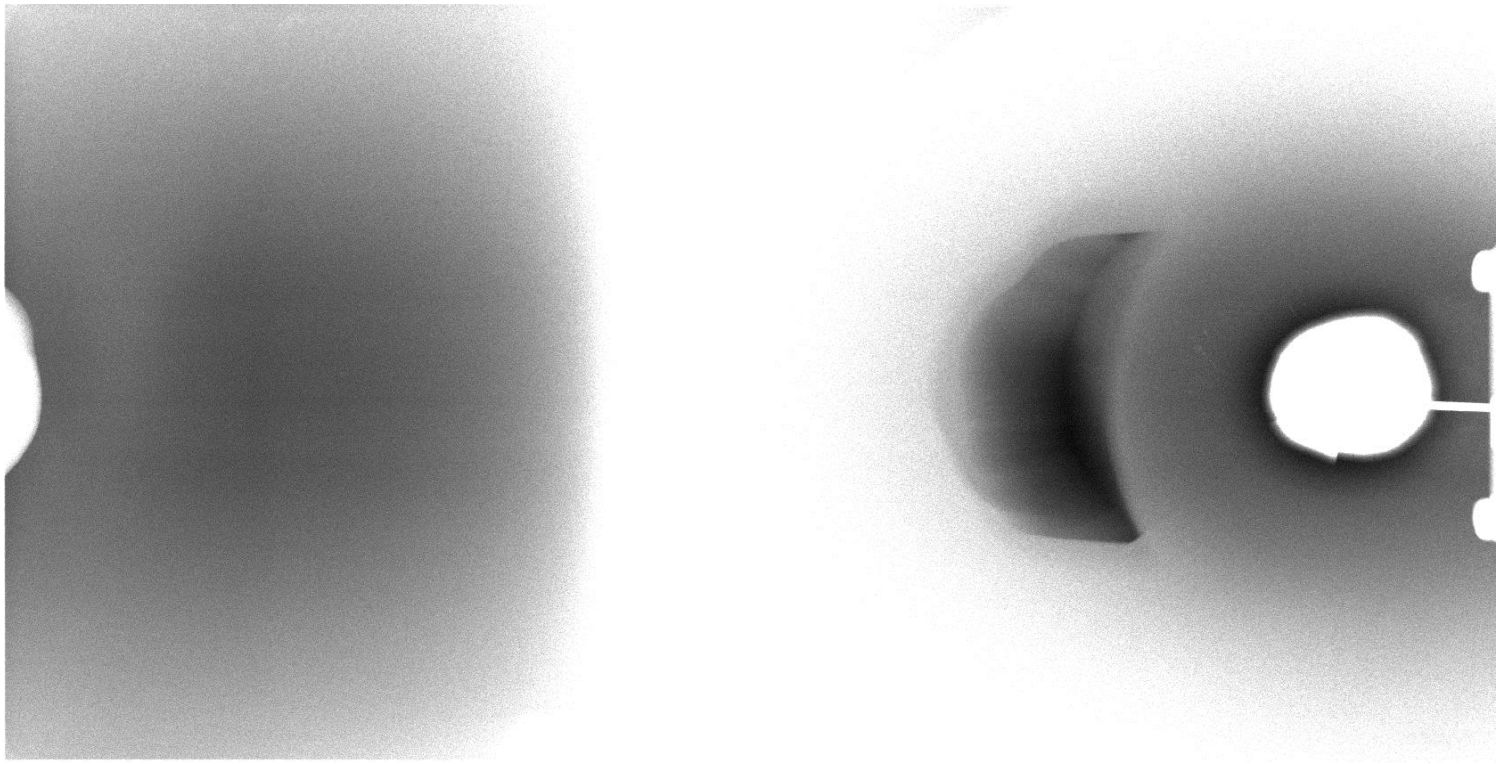


FeS from the orgueil meteorite

Pattern 1 from metagabbro PST glass (PST17B1)



Pattern 2 from metagabbro PST glass (PST17B2)



Sample set of EBSD results courtesy of Petter Silkoset . Sample set is of a peridotite hosted pseudotachylyte fault vein. Data given are for area 3.1

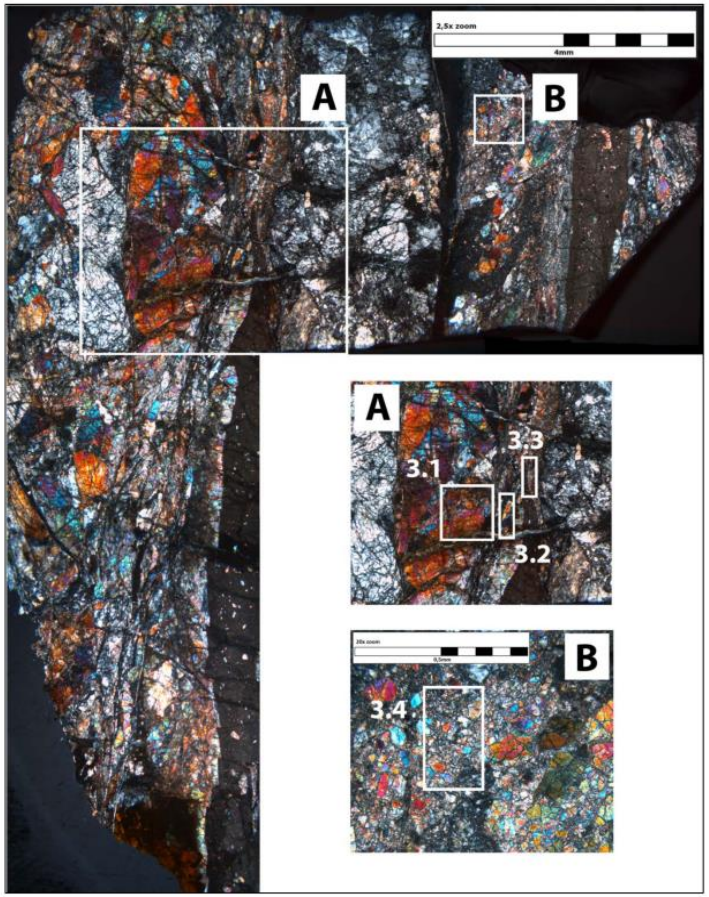


Figure 71: Photomerged section of micrographs in cross-polarised light, portraying a distal, fine grained fault zone margin (left) and the internal damage zone relative to pseudotachylyte fault-veins. The wide, distal fine grained margin is difficult to trace, halted by the size of the sample and by two large ol and opx grains, highlighted in A. Note injection veins ramifying off of the fracture adjacent to area B. Areas selected for EBSD are numbered and indicated with white boxes. These are treated in their respective sections. The large photomerged micrograph is not completely to scale. From sample COR-05-06C.

Software	EDAX/TSL
Step size	1.0µm
Working distance	10.0mm
Wall rock	Cropped map
Avg. angular misfit	1.38°
Avg. image quality	45.05
Indexed fraction	0.291
#Indexed points/clasts	371722/7588
Clasts	Cropped map
Avg. angular misfit	1.27°
Avg. image quality	39.73
Indexed fraction	0.008
#Indexed points/clasts	1995/146
Clasts in fracture	Highlighted map
Avg. angular misfit	1.34°
Avg. image quality	42.82
Indexed fraction	-
#Indexed points/clasts	22058/699
Wall rock margin	Highlighted map
Avg. angular misfit	1.30°
Avg. image quality	41.79
Indexed fraction	-
#Indexed points/clasts	9955/483

Table 7: Acquisitional parameters and properties of datasets in area 3.1.

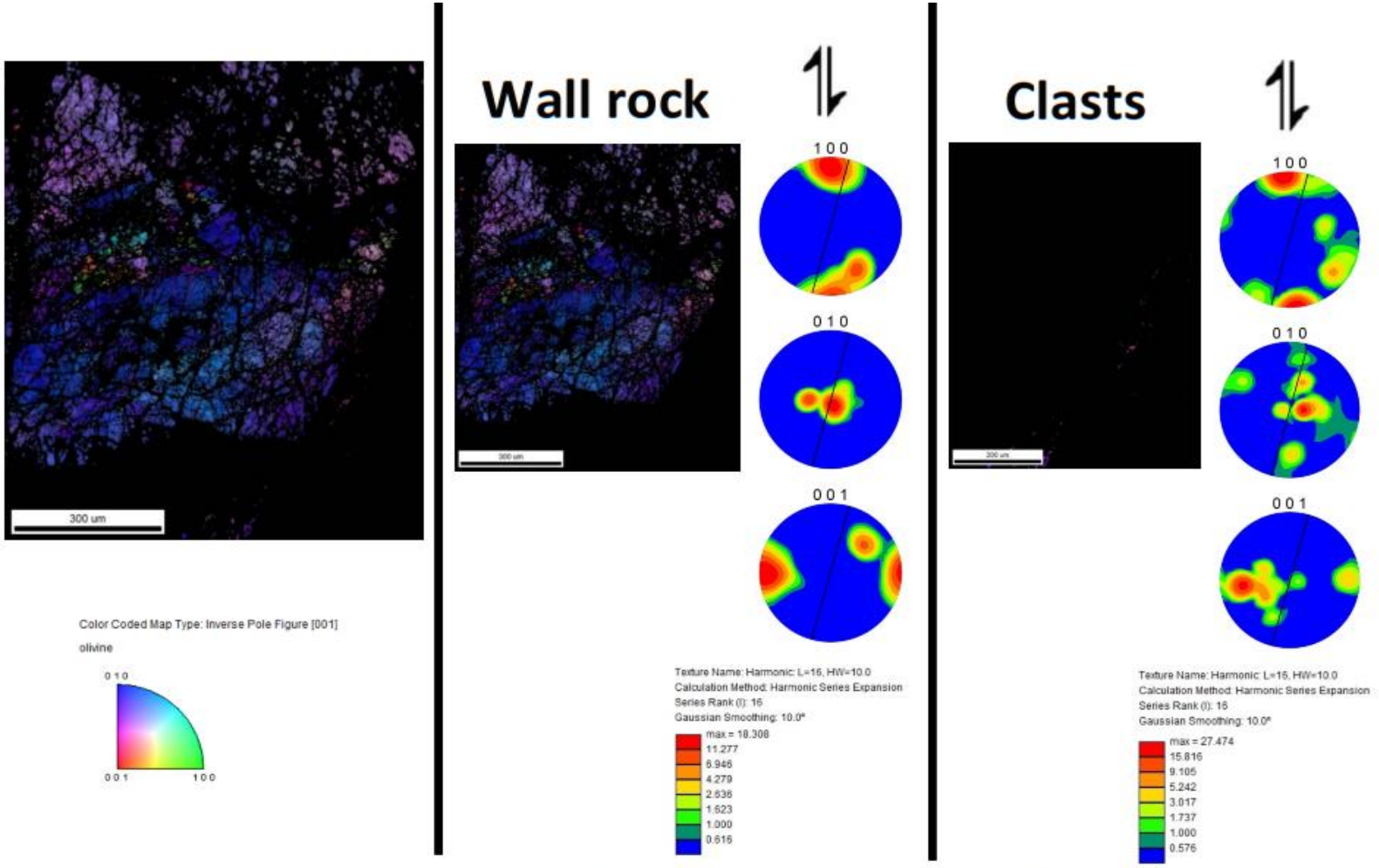


Figure 72: Area 3.1; IQ+IP maps and contoured PF of truncated wall rock ol and peeled-off clasts. The IPF maps are colour-coded according to the unit triangle. The calculation parameters and the intensity of the projections are shown below the respective PF. The solid line on the PF displays the orientation of the fault plane, and the reference direction is marked by shear direction (arrows). See text for discussion.

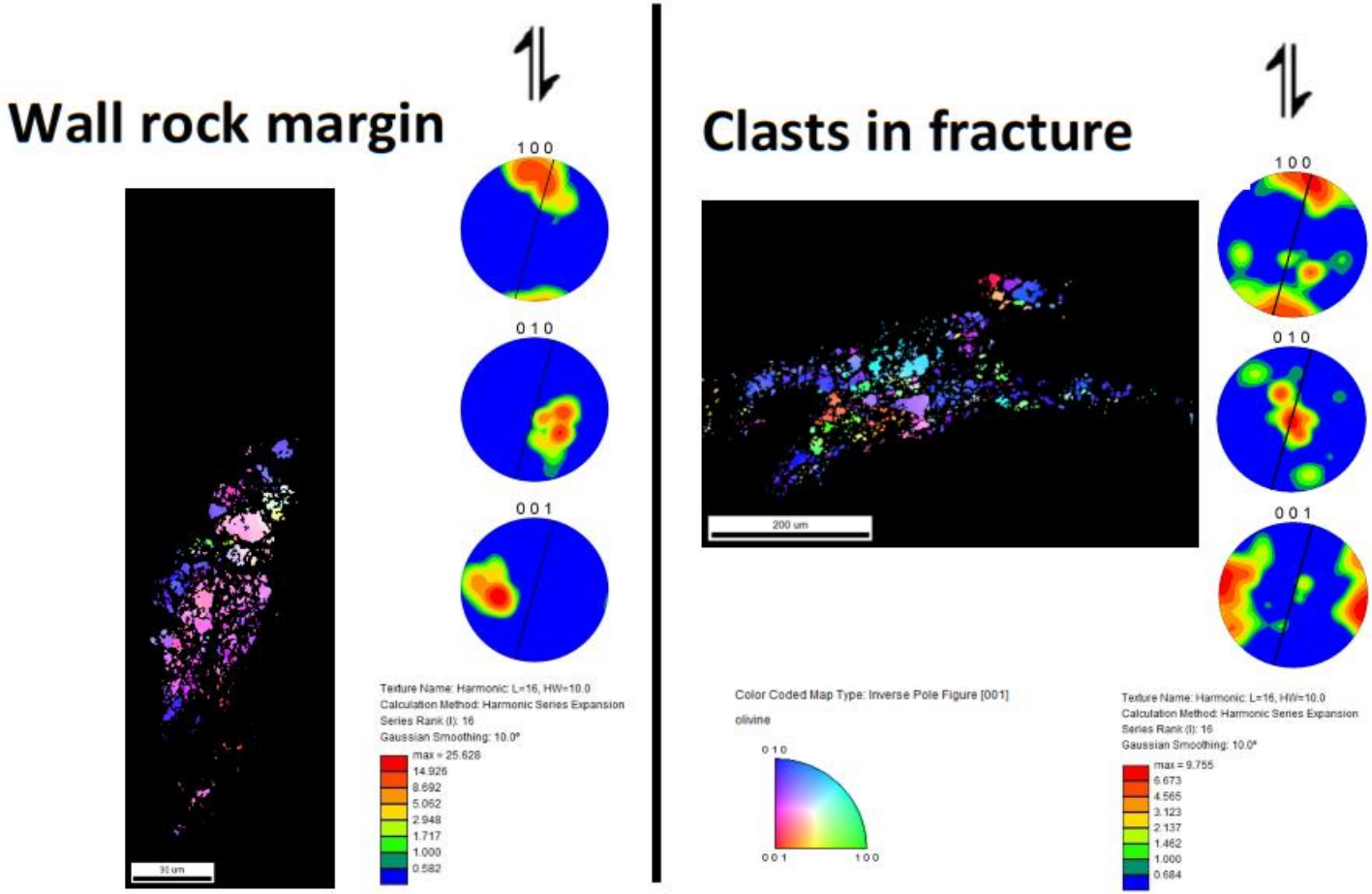


Figure 73: Area 3.1; IPF maps and contoured PF of clasts at the interface between wall rock and fine grained fault zone, and of clasts in a fracture in wall rock. The IPF maps are colour-coded according to the unit triangle. The calculation parameters and the intensity of the projections are shown below the respective PF. The solid line on the PF displays the orientation of the fault plane, and the reference direction is marked by shear direction (arrows). See text for discussion.

1

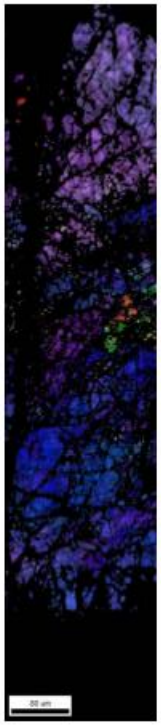


Chart: Grain Size (diameter)

Edge grains excluded from analysis

Diameter [microns]	Number
1.9775	1603
4.25267	265
6.52773	93
8.8028	59
11.0779	24
13.3529	17
15.628	5
17.9031	10
20.1782	9
22.4532	3
24.7283	3
27.0034	4
29.2784	2
31.5535	1
33.8286	2
36.1036	3
38.3787	1
40.6538	1
42.9289	0
45.2039	0
47.479	0
49.7541	0
52.0291	1
54.3042	0
56.5793	0
58.8543	0
61.1294	1
63.4045	0
65.6796	0
67.9546	0
70.2297	2
72.5048	0
74.7798	0
77.0549	0
79.33	0
81.605	0
83.8801	1
86.1552	0
88.4303	0
90.7053	0
92.9804	0
95.2555	0
97.5305	0
99.8056	0
102.081	0
104.356	0
106.631	0
108.906	0
111.181	0
113.456	1

Average	
Number	3.0063
Standard Deviation	5.58287
Area	47.6794

2



Chart: Grain Size (diameter)

Edge grains excluded from analysis

Diameter [microns]	Number
1.8885	1592
3.98538	241
6.08226	101
8.17914	52
10.276	21
12.3729	14
14.4698	13
16.5667	9
18.6635	8
20.7604	4
22.8573	2
24.9542	6
27.0511	0
29.148	3
31.2448	2
33.3417	4
35.4386	1
37.5355	0
39.6324	2
41.7292	1
43.8261	2
45.923	0
48.0199	1
50.1168	1
52.2136	0
54.3105	0
56.4074	2
58.5043	0
60.6012	0
62.698	0
64.7949	0
66.8918	0
68.9887	0
71.0856	0
73.1824	0
75.2793	0
77.3762	0
79.4731	0
81.57	0
83.6669	0
85.7637	0
87.8606	0
89.9575	0
92.0544	0
94.1513	0
96.2481	0
98.345	0
100.442	0
102.539	0
104.636	1

Average	
Number	2.80429
Standard Deviation	5.11336
Area	39.0344

3



Chart: Grain Size (diameter)

Edge grains excluded from analysis

Diameter [microns]	Number
1.5893	1479
3.08778	292
4.58625	140
6.08473	71
7.58321	51
9.08169	22
10.5802	11
12.0786	8
13.5771	9
15.0756	10
16.5741	8
18.0725	7
19.571	9
21.0695	7
22.568	2
24.0665	0
25.5649	6
27.0634	2
28.5619	2
30.0604	0
31.5588	0
33.0573	1
34.5558	0
36.0543	0
37.5528	0
39.0512	0
40.5497	1
42.0482	2
43.5467	1
45.0451	0
46.5436	0
48.0421	0
49.5406	0
51.039	2
52.5375	0
54.036	1
55.5345	1
57.033	0
58.5314	0
60.0299	0
61.5284	0
63.0269	0
64.5253	0
66.0238	1
67.5223	0
69.0208	0
70.5192	1
72.0177	0
73.5162	0
75.0147	1

Average	
Number	2.90512
Standard Deviation	5.15052
Area	34.4197

4



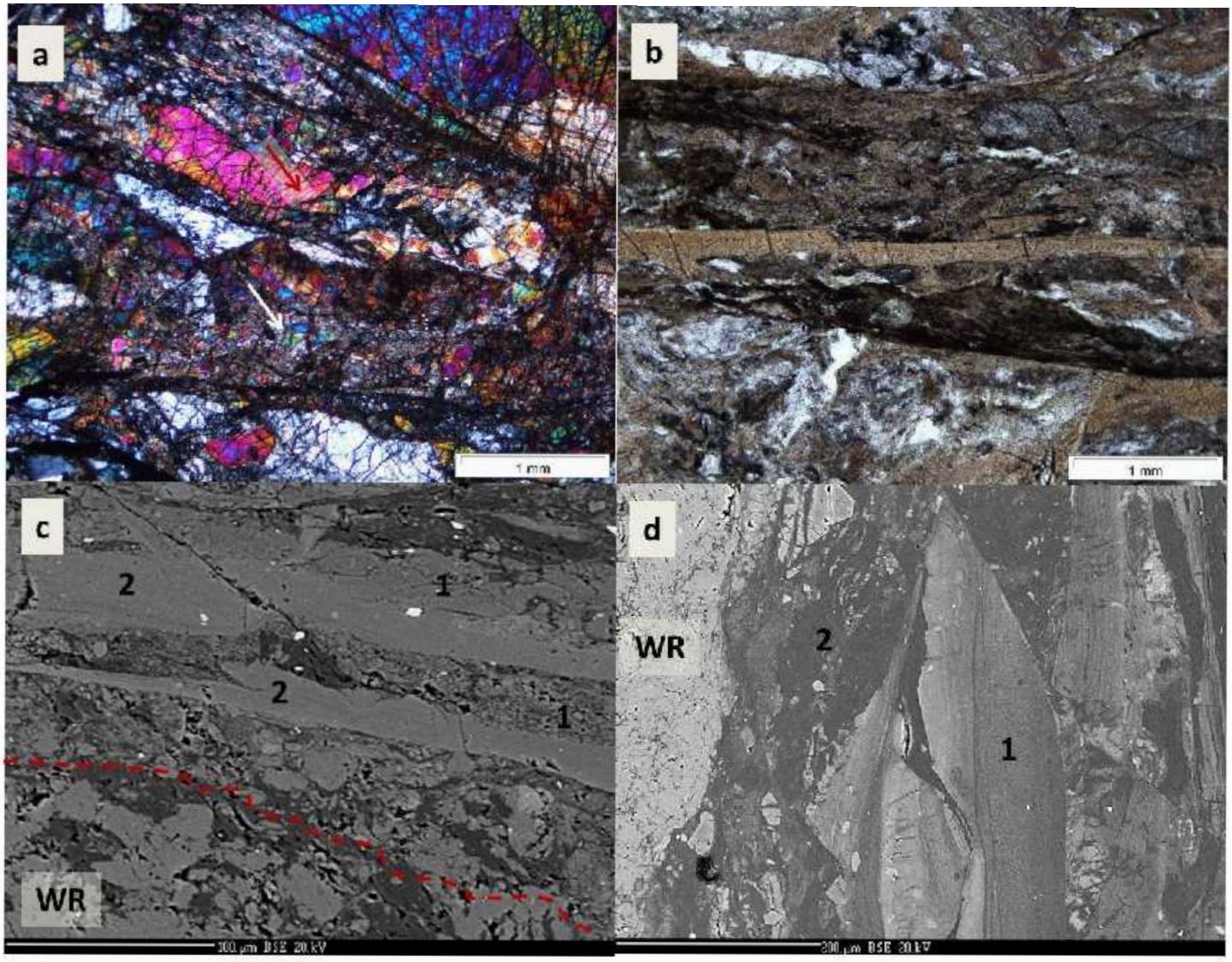
Chart: Grain Size (diameter)

Edge grains excluded from analysis

Diameter [microns]	Number
1.34876	950
2.36615	151
3.38355	92
4.40094	72
5.41833	39
6.43573	22
7.45312	24
8.47052	14
9.48791	8
10.5053	9
11.5227	4
12.5401	7
13.5575	4
14.5749	4
15.5923	3
16.6097	3
17.6271	2
18.6445	3
19.6619	3
20.6792	0
21.6966	1
22.714	3
23.7314	0
24.7488	2
25.7662	2
26.7836	0
27.801	0
28.8184	0
29.8358	2
30.8532	0
31.8706	0
32.888	0
33.9054	1
34.9228	0
35.9402	0
36.9576	0
37.975	0
38.9923	1
40.0097	0
41.0271	0
42.0445	0
43.0619	0
44.0793	0
45.0967	0
46.1141	0
47.1315	0
48.1489	0
49.1663	0
50.1837	0
51.2011	1

Average	
Number	2.52827
Standard Deviation	3.77583
Area	19.5886

Figure 74: Cropped IQ+IPF maps and grain size diameter statistics in wall rock from distal (1) to proximal (4) side relative to the fault zone. Edge grains are excluded from calculations. From the distal area (1) to the proximal area (4), relative to the fault, there are increasing numbers of small grains. The smallest recorded grains are 1.3µm, whereas the step size used was set to 1.0µm (table 7).



Micrographs (a and b) and BSE images (d and c) of thickened PST fault veins hosted in peridotite. a) XPL micrograph shows interlayered slivers of fractures wallrock (red arrow) and altered and b) hydrated PST white arrow). b) Interlayered generations of PST (brown) and wallrock (white, grey) with varying degrees of alteration. c) Interlayered wallrock (WR, delineated by red line), and an early PST (1) and later PST (2). d) Similar to c), alternating layers of WR, altered, deformed PST (1) and later PST (2)

Whole rock XRF results

Rock type	Sample	SiO_2	Al_2O_3	Fe_2O_3	FeO	MnO	MgO	CaO	Na_2O	K2O	TiO_2	P_2O_5	Cr_2O_3	NiO	LOI	TOTAL	FeO+MgO	Mg#	TOTAl-LOI
Peridotite	H1	43.93	2.54	0.89	7.21	0.13	39.26	2.40	0.06	0.00	0.07	0.01	0.38	0.28	2.92	**100.08**	46.47	84.48	97.18
Peridotite	H2	44.75	3.08	0.87	7.04	0.14	38.38	3.34	0.09	0.00	0.09	0.01	0.51	0.28	1.35	**99.93**	45.43	84.50	98.58
Peridotite	H3	43.71	2.13	0.90	7.28	0.14	40.25	2.22	0.12	0.01	0.05	0.01	0.40	0.29	2.41	**99.90**	47.53	84.68	97.50
Peridotite	H4	43.51	2.37	0.93	7.52	0.14	40.46	2.41	0.06	0.00	0.06	0.01	0.39	0.30	1.99	**100.15**	47.98	84.33	98.16
Peridotite	H5	42.94	2.36	0.94	7.58	0.14	40.62	1.97	0.08	0.00	0.06	0.01	0.46	0.30	2.38	**99.83**	48.19	84.28	97.46
Peridotite	H6	43.59	2.68	0.87	7.07	0.13	37.49	2.87	0.08	0.00	0.07	0.01	0.38	0.29	4.66	**100.18**	44.56	84.14	95.53
Gabbro	H7	50.27	18.22	0.55	4.53	0.10	9.74	12.12	2.77	0.04	0.28	0.03	0.08	0.03	1.25	**100.01**	14.27	68.24	98.76
Gabbro	H8	50.29	14.96	0.56	4.47	0.10	11.11	13.18	2.33	0.03	0.29	0.02	0.09	0.02	2.53	**99.98**	15.59	71.29	97.44
Gabbro	H9	44.60	6.82	0.83	6.77	0.13	34.65	2.93	0.48	0.00	0.08	0.01	0.23	0.24	2.11	**99.89**	41.43	83.65	97.78
Gabbro	COR-09-05	48.91	18.47	0.55	4.49	0.10	10.93	11.05	2.64	0.03	0.18	0.02	0.05	0.03	2.68	**100.13**	15.42	70.90	97.44
Gabbro	COR-25-05	50.39	16.78	0.57	4.60	0.10	10.40	12.35	2.85	0.03	0.35	0.03	0.05	0.02	1.32	**99.84**	15.00	69.34	98.53
Gabbro	COR-31-05	43.93	2.67	0.92	7.42	0.15	38.86	2.51	0.09	0.01	0.07	0.02	0.45	0.30	2.53	**99.92**	46.28	83.97	97.40
Gabbro	COR-32-05	43.08	2.42	0.92	7.40	0.14	40.26	2.11	0.12	0.00	0.06	0.01	0.32	0.30	2.61	**99.73**	47.66	84.47	97.13
Gabbro	COR-41-05	43.81	2.09	0.87	7.09	0.13	40.68	2.20	0.10	0.00	0.05	0.01	0.44	0.30	1.97	**99.73**	47.77	85.16	97.76

* Mg # = (MgO/(MgO+FeO)*100)

Gabbro
PST Matrix

Na_2O	3.09	0.37	1.65	2.1	3.19	6.21	0.95	2.42
MgO	8.29	20.41	14.53	9.28	8.97	3.28	15.02	12.4
Al_2O_3	18.34	7.65	10.71	15.83	18.6	20.2	9.86	12.21
SiO_2	50.07	46.47	46.32	48.72	49.56	55.52	46.17	50.72
K_2O	0.05	0.25	0.1	0.07	0.06	0.04	0.07	0.04
CaO	12.93	6.86	9.54	12.93	11.82	8.47	11.45	11.58
TiO_2	0.48	0.07	1.21	0.47	0.36	0.44	1.55	0.45
FeO	4.92	9.63	10.95	6.1	5.13	3.42	10.88	8.08
MnO	0.11	0.12	0.12	0.11	0.1	0.05	0.18	0.13
Cr_2O_3	0.06	0	0.09	0.05	0.05	0.01	0.08	0.08
NiO	0	0.04	0.1	0.02	0.01	0	0.12	0.03
Total	**98.35**	**91.87**	**95.31**	**95.7**	**97.86**	**97.63**	**96.32**	**98.13**

PST Matrix

Na_2O	1.11	1.47	1.32	2.31	3.07	3.4	2.14	2.06
MgO	14.31	14.34	9.66	10.42	8.54	10.41	10.01	9.82
Al_2O_3	10.06	11.02	9.12	11.58	12.75	15.55	15.55	15.94
SiO_2	48.05	46.36	37.56	48.96	43.09	49.53	49.93	49.85
K_2O	0.09	0.09	0.01	0.03	0.04	0.03	0.06	0.09
CaO	14.08	11.35	11.17	13.83	13.32	12.11	12.69	12.83
TiO_2	0.76	1.53	11.15	2.1	5.07	0.53	0.52	0.48
FeO	9.23	10.08	18.39	8.88	9.9	7.46	6.26	5.93
MnO	0.17	0.16	0.38	0.2	0.21	0.13	0.14	0.14
Cr_2O_3	0.12	0.08	0.1	0.06	0.09	0.08	0.09	0.08
NiO	0.06	0.01	0.05	0.02	0.03	0.02	0.03	0.02
Total	**98.05**	**96.48**	**98.92**	**98.39**	**96.11**	**99.26**	**97.42**	**97.24**

PST Matrix

Na_2O	2.26	2.24	4.25	2.33	2.3	2.83	2.71	2.38
MgO	9.54	9.51	8.15	9.31	9	9.96	10.02	10.56
Al_2O_3	16.26	16.08	19.01	16.74	16.88	14.68	16.88	13.31
SiO_2	50.15	50.3	47.62	49.29	49.54	50.86	49.22	50.72
K_2O	0.07	0.08	1.4	0.07	0.09	0.05	0.05	0.05
CaO	12.51	12.45	2.94	12.23	12.46	14.14	11.84	15.27
TiO_2	0.53	0.54	0.26	0.51	0.6	0.54	0.47	0.64
FeO	5.85	5.89	10.48	6.27	6.6	5.32	6.27	5.44
MnO	0.1	0.09	0.06	0.13	0.12	0.12	0.13	0.14
Cr_2O_3	0.08	0.09	0.08	0.07	0.08	0.1	0.08	0.08
NiO	0.03	0.03	0.06	0.05	0.06	0.04	0.02	0.02
Total	**97.37**	**97.3**	**94.31**	**97**	**97.73**	**98.63**	**97.68**	**98.61**

Gabbro

PST Matrix

Na_2O	2.48	3.46	4.29	1.76	3.43	3.52	3.51	2.74
MgO	10.66	8.84	5.02	12.14	9.62	10.17	8.8	10.89
Al_2O_3	14.4	18.05	21.01	9.18	16.7	16.15	16.42	16.07
SiO_2	50.64	50.22	52.93	51.34	50.12	50.49	50.87	48.91
K_2O	0.05	0.05	0.04	0.06	0.03	0.06	0.03	0.07
CaO	14.63	11.68	11.71	17.2	13.3	9.42	12.46	11.67
TiO_2	0.45	0.4	0.28	0.92	0.55	0.4	0.61	0.45
FeO	5.76	5.35	2.98	5.9	4.59	6.54	5.52	6.21
MnO	0.14	0.13	0.05	0.15	0.12	0.12	0.11	0.11
Cr_2O_3	0.1	0.08	0.05	0.11	0.06	0.05	0.05	0.06
NiO	0	0.01	0.01	0	0.02	0	0.01	0
Total	**99.3**	**98.27**	**98.36**	**98.76**	**98.54**	**96.92**	**98.38**	**97.18**

PST Matrix

Na_2O	3.32	2.39	2.6	3.84	3.44	2.79	2.52	1.45
MgO	8.91	11.33	11.65	6.94	9.02	8.86	10.72	10.85
Al_2O_3	18.51	15.67	14.22	19.1	16.65	17.3	15.44	14.56
SiO_2	50.51	50.13	49.38	50.76	50.72	50	49	49
K_2O	0.06	0.05	0.03	0.11	0.05	0.16	0.17	0.06
CaO	11.56	12.98	12.59	11.35	12.62	12.66	12.38	13.7
TiO_2	0.36	0.36	0.57	0.42	0.57	0.39	0.54	0.46
FeO	5.25	5.03	7.57	5.12	5.26	5.47	6.64	7.14
MnO	0.11	0.11	0.15	0.11	0.11	0.12	0.14	0.14
Cr_2O_3	0.02	0.12	0.08	0.05	0.07	0.06	0.07	0.08
NiO	0.02	0.03	0.05	0.02	0.01	0.01	0.01	0.03
Total	**98.63**	**98.2**	**98.9**	**97.81**	**98.53**	**97.82**	**97.62**	**97.47**

PST Matrix

Na_2O	4.26	3.49	1.27	2.81	3.01	0.2	0.26	2.18
MgO	8.2	8.62	14.34	7.13	7.55	2.97	16.22	10.24
Al_2O_3	16.76	17.54	11.8	19.66	18.97	22.89	17.82	16.06
SiO_2	51.2	51.07	49.76	51.67	50.45	44.94	34.02	50.09
K_2O	0.05	0.07	0.04	0.05	0.05	0.01	0.27	0.07
CaO	11.2	11.77	13.97	11.82	11.45	21.43	4.39	12.02
TiO_2	0.8	0.46	0.26	0.23	0.15	0.08	0.86	0.3
FeO	6.58	5.4	5.88	3.73	3.73	4.38	13.61	5.45
MnO	0.14	0.1	0.16	0.06	0.04	0.1	0.19	0.13
Cr_2O_3	0.04	0.05	0.1	0.12	0.02	0.01	0.14	0.09
NiO	0	0.01	0.01	0.03	0	0.02	0.06	0.04
Total	**99.23**	**98.58**	**97.6**	**97.32**	**95.42**	**97.01**	**87.83**	**96.67**

Gabbro

PST Matrix								
Na_2O	2.52	3.42	2.47	2.52	2.8	1.23	1.95	2.46
MgO	9.72	8.34	9.73	10.46	12.32	13.23	10.85	8.88
Al_2O_3	16.23	17.98	16.92	16.98	18.18	12.15	15.39	18.26
SiO_2	48.43	51.42	50.25	49.92	48.78	49.1	48.47	49.72
K_2O	0.06	0.12	0.09	0.09	0.38	0.05	0.17	0.11
CaO	12.95	10.67	12.12	11.55	2.86	14.19	13.84	12.74
TiO_2	0.28	0.26	0.2	0.25	0.26	0.36	0.31	0.26
FeO	5.7	4.38	5.41	5.09	7.94	6.42	5.93	4.67
MnO	0.12	0.08	0.08	0.1	0.1	0.14	0.15	0.12
Cr_2O_3	0.11	0.08	0.11	0.1	0.1	0.1	0.1	0.09
NiO	0.03	0.07	0.03	0.01	0.03	0.03	0.03	0.05
Total	**96.14**	**96.82**	**97.4**	**97.08**	**93.75**	**96.98**	**97.2**	**97.38**

PST Matrix								
Na_2O	1.73	2.83	2.71	1.99	2.07	1.82	3.14	0.74
MgO	10.43	7.57	11	9.7	10.19	12.08	6.88	13.55
Al_2O_3	16.25	17.55	16.87	16.81	16.57	15.12	19.14	8.23
SiO_2	48.46	51.16	48.45	49.96	50.13	50.18	49.93	49.31
K_2O	0.05	0.03	0.23	0.05	0.04	0.03	0.03	0.03
CaO	13.78	13.21	12.2	12.98	12.99	14.37	13.9	17.53
TiO_2	0.25	0.25	0.25	0.24	0.26	0.32	0.29	0.51
FeO	5.33	4.61	4.93	5.33	4.73	5.2	3.35	5.84
MnO	0.09	0.1	0.06	0.14	0.09	0.12	0.09	0.18
Cr_2O_3	0.08	0.06	0.05	0.11	0.12	0.15	0.08	0.21
NiO	0.02	0.02	0.04	0.03	0.03	0.05	0.05	0.05
Total	**96.45**	**97.39**	**96.79**	**97.33**	**97.22**	**99.44**	**96.88**	**96.18**

PST Matrix						**Average**
Na_2O	2.18	1.5	2.92	1.97	2.88	**2.48**
MgO	11.12	13.23	13.04	10.94	10.94	**10.28**
Al_2O_3	14.91	12.32	16.57	12.84	15.01	**15.59**
SiO_2	50.68	47.76	56.04	52.75	51.52	**49.35**
K_2O	0.04	0.12	0.07	0.07	0.11	**0.10**
CaO	14.7	14.1	6.43	12.17	7.97	**12.15**
TiO_2	0.28	0.23	0.24	0.52	0.39	**0.70**
FeO	4.52	7.49	9.09	5.98	7.43	**6.46**
MnO	0.14	0.12	0.15	0.12	0.13	**0.12**
Cr_2O_3	0.14	0.09	0	0.07	0.04	**0.08**
NiO	0.06	0.02	0.01	0.04	0.22	**0.03**
Total	**98.77**	**96.98**	**104.57**	**97.47**	**96.64**	**97.35**

Gabbro

Wallrock Minerals

Diopside

Na_2O	0.36	0.38	0.27	0.42	0.42	0.37	0.37	0.43
MgO	15.15	16.92	17.66	14.25	15.6	16.53	14.43	15.49
Al_2O_3	2.45	2.55	2.08	2.4	2.74	2.41	2.18	2.59
SiO_2	51.46	52.1	51.98	51.87	51.82	52.82	51.65	52.02
K_2O	0.01	0.01	0	0	0	0.01	0	0
CaO	23.01	19.67	17.87	22.27	20.59	20.88	22.48	20.73
TiO_2	0.78	0.43	0.71	0.68	0.74	0.44	0.7	0.96
FeO	5.25	5.24	8.46	6.89	5.95	5.34	6.92	7.22
MnO	0.15	0.15	0.23	0.26	0.15	0.18	0.18	0.21
Cr_2O_3	0.2	0.32	0.17	0.26	0.73	0.22	0.07	0.25
NiO	0.05	0.03	0.01	0	0.04	0.02	0	0
Total	**98.88**	**97.78**	**99.44**	**99.31**	**98.79**	**99.22**	**99**	**99.91**

Diopside

Na_2O	0.44	0.41	0.42	0.59	0.44	0.43	0.36	0.44
MgO	15.05	15.06	15.87	14.43	14.69	14.49	17.66	15.47
Al_2O_3	2.5	2.55	2.31	3.75	2.5	2.59	2.61	3.11
SiO_2	52.01	52.01	52.71	50.11	50.57	50.42	52.65	52.03
K_2O	0	0.01	0	0.03	0.01	0.01	0.01	0.01
CaO	22.67	22.32	21.96	18.89	21.74	22.34	18.23	22.02
TiO_2	0.76	0.99	0.43	0.65	0.72	1.28	0.42	0.52
FeO	5.4	5.61	5.1	8.48	6.92	6.58	5.22	4.48
MnO	0.18	0.2	0.21	0.25	0.73	0.21	0.14	0.14
Cr_2O_3	0.32	0.19	0.36	0.07	0.1	0.12	0.34	0.58
NiO	0	0.02	0.03	0	0	0	0.01	0.03
Total	**99.34**	**99.38**	**99.38**	**97.24**	**98.42**	**98.48**	**97.65**	**98.82**

Diopside

Na_2O	0.5	0.44	0.46	0.64	0.47	0.47	0.33	0.41
MgO	14.7	14.06	14.74	14.73	14.57	15.19	12.8	14.3
Al_2O_3	3.27	2.02	2.58	4.35	2.68	2.75	2.36	0.94
SiO_2	51.61	52.32	51.42	50.64	51.41	50.9	51.06	53.2
K_2O	0.03	0.02	0	0.02	0.01	0	0	0.01
CaO	21.9	21.95	21.65	19.94	22.56	21.38	21.89	22.43
TiO_2	1.14	0.46	0.93	0.92	1.06	0.79	0.45	0.11
FeO	5.91	7.14	6.48	7.1	6.34	6.45	9.46	7.89
MnO	0.19	0.22	0.19	0.21	0.21	0.18	0.46	0.28
Cr_2O_3	0.16	0.04	0.12	0.12	0.14	0.14	0.06	0.05
NiO	0	0	0.01	0.01	0.02	0.01	0	0
Total	**97.04**	**98.66**	**98.57**	**98.7**	**99.47**	**98.27**	**98.87**	**99.63**

Gabbro

Wallrock Minerals

Wallrock Diopside				**Average**
Na_2O	0.4	0.41	0.42	**0.43**
MgO	14.12	14.54	14.46	**15.07**
Al_2O_3	0.84	1.41	1.54	**2.45**
SiO_2	52.77	52.24	52.36	**51.78**
K_2O	0	0	0.01	**0.01**
CaO	22.46	21.62	21.2	**21.36**
TiO_2	0.13	0.42	0.39	**0.67**
FeO	8.08	8.6	8.38	**6.70**
MnO	0.28	0.25	0.24	**0.23**
Cr_2O_3	0.04	0.06	0.05	**0.20**
NiO	0.02	0.01	0.01	**0.01**
Total	**99.15**	**99.55**	**99.08**	**98.82**

Gabbro
Wallrock Minerals

Plagioclase								
Na_2O	5.58	5.31	5.92	5.62	5.37	4.52	4.58	5.11
MgO	0.04	0.05	0.09	0.04	0.02	0.03	0.1	0.09
Al_2O_3	27.72	28.15	26.99	27.87	28.03	29.27	28.87	28.38
SiO_2	54.61	54.07	55.26	57.25	54.3	52.22	52.23	53.46
K_2O	0.07	0.02	0.04	0.05	0.04	0.02	0.05	0.02
CaO	10.82	11.48	10.18	9.97	11.06	12.87	12.36	11.73
TiO_2	0.08	0.06	0.13	0.11	0.06	0.03	0.09	0.05
FeO	0.31	0.26	0.53	0.66	0.2	0.25	0.56	0.22
MnO	0	0	0	0.02	0	0	0	0
Cr_2O_3	0	0	0.01	0	0.02	0	0.01	0.01
NiO	0	0	0	0	0.01	0	0	0
Total	**99.23**	**99.39**	**99.14**	**101.6**	**99.11**	**99.2**	**98.83**	**99.07**

Plagioclase								
Na_2O	5.26	4.41	5.01	4.67	4.59	4.69	4.91	4.6
MgO	0.25	0.54	0.01	0.03	0.24	0.06	0.1	0.25
Al_2O_3	27.45	28.38	28.79	29	28.9	29.05	28.8	29.26
SiO_2	54.04	52.63	52.97	52.37	52.38	52.6	52.64	52.72
K_2O	0.03	0.05	0.03	0.02	0.02	0.04	0.04	0.03
CaO	11.34	12.57	12.1	12.56	12.16	12.44	12.13	12.45
TiO_2	0.11	0.05	0.02	0.05	0.05	0.07	0.07	0.06
FeO	0.73	0.59	0.2	0.28	0.45	0.29	0.26	0.17
MnO	0	0.01	0	0.01	0.01	0.01	0	0
Cr_2O_3	0	0.03	0	0	0.03	0	0	0
NiO	0	0	0.03	0	0.01	0	0	0.02
Total	**99.21**	**99.26**	**99.19**	**98.99**	**98.86**	**99.26**	**98.95**	**99.56**

Plagioclase								
Na_2O	4.63	4.53	4.62	5.14	4.5	4.33	5.1	5.05
MgO	0.04	0.08	0.5	0.03	0.48	0.14	0.14	0.81
Al_2O_3	29.37	29.24	28.07	28.24	29.16	29.54	28.02	27.32
SiO_2	52.13	52.44	53.15	53.49	52.19	51.66	53.86	53.99
K_2O	0.04	0.05	0.08	0.04	0.04	0.03	0.03	0.07
CaO	12.72	12.69	11.54	11.51	12.27	12.96	11.47	10.63
TiO_2	0.06	0.08	0.06	0.1	0.09	0.04	0.05	0.06
FeO	0.36	0.26	0.63	0.3	0.72	0.46	0.36	0.25
MnO	0	0	0	0	0	0.02	0.02	0
Cr_2O_3	0	0.01	0	0	0	0	0.02	0
NiO	0.01	0.01	0.02	0.02	0	0	0.02	0
Total	**99.37**	**99.38**	**98.67**	**98.86**	**99.46**	**99.18**	**99.1**	**98.18**

Gabbro

Wallrock Minerals

Plagioclase

Na_2O	4.71	5	5.19	4.8	4.38	5.4	5.38	5.21
MgO	0.14	0.05	0.09	0.01	2.09	0.03	0.06	0.06
Al_2O_3	28.89	28.51	27.96	28.47	27.09	28.05	27.86	28.1
SiO_2	52.89	53.49	53.83	53.72	50.25	54.43	53.92	53.93
K_2O	0.02	0.02	0.02	0.06	0.73	0.02	0.01	0.05
CaO	12.07	11.86	11.3	11.11	10.26	11.2	11.31	11.6
TiO_2	0.05	0.06	0.11	0.07	0.01	0.05	0.07	0.11
FeO	0.17	0.26	0.38	0.29	2.78	0.2	0.3	0.38
MnO	0	0	0.01	0.01	0.04	0	0.01	0.02
Cr_2O_3	0.02	0	0.02	0	0	0.01	0.02	0.01
NiO	0	0	0	0.02	0.03	0.02	0	0.02
Total	**98.96**	**99.25**	**98.92**	**98.55**	**97.67**	**99.41**	**98.94**	**99.49**

Plagioclase

Na_2O	5.45	5.3	5.18	4.85	6.26	6.93	7.12	5.2
MgO	0.25	0.18	0.03	1.1	0.01	0.45	0.36	0.1
Al_2O_3	27.9	27.86	28.42	27.78	27.19	28.35	27.02	28.26
SiO_2	53.75	54.06	53.81	52.04	55.58	52.94	55.14	53.32
K_2O	0.03	0.03	0.02	0.03	0.04	0.07	0.07	0.02
CaO	11.19	11.26	11.72	10.77	10.1	9.19	7.14	11.64
TiO_2	0.03	0.07	0.07	0.25	0.04	0.08	0.09	0.07
FeO	0.35	0.56	0.21	1.7	0.07	1.14	0.59	0.36
MnO	0	0	0	0.02	0	0.03	0.03	0
Cr_2O_3	0.01	0.02	0	0.01	0.01	0	0.02	0.01
NiO	0.02	0.03	0	0	0	0	0	0
Total	**98.97**	**99.37**	**99.47**	**98.55**	**99.29**	**99.18**	**97.57**	**98.99**

Gabbro

Wallrock Minerals

Mg-Hornblende

Na_2O	0.92	1.08	1.06	1.27	1	2.24	2.51	2.48
MgO	11.45	12.24	12.62	11	13.27	13.43	13.54	13.48
Al_2O_3	8.39	7.51	6.89	8.94	6.16	10.2	10.72	10.89
SiO_2	47.73	48.87	48.54	45.7	49.44	43.86	42.88	42.93
K_2O	0.08	0.09	0.08	0.11	0.06	0.16	0.17	0.16
CaO	12.88	11.96	12.03	11.75	12.06	11.49	11.47	11.52
TiO_2	0.04	0.06	0.06	0.04	0.07	4.16	4.42	4.41
FeO	14.63	15.02	15.81	16.98	14.23	10.8	10.52	10.75
MnO	0.21	0.25	0.34	0.25	0.44	0.15	0.13	0.14
Cr_2O_3	0	0	0	0	0	0.09	0.1	0.1
NiO	0.02	0.02	0.02	0.01	0	0.02	0.03	0.04
Total	**96.34**	**97.09**	**97.46**	**96.05**	**96.73**	**96.6**	**96.48**	**96.89**

Mg-Hornblende

Na_2O	1.68	1.89	1.51	1.64	1.39	0.8	1.64	1.52
MgO	11.9	11.69	11.66	11.44	10.57	13.87	12.32	12.13
Al_2O_3	5.43	6.35	5.54	5.48	8.64	2.59	5.3	5.51
SiO_2	49.93	49.07	49.52	49.3	48.26	52.42	50.23	49.71
K_2O	0.04	0.05	0.06	0.05	0.03	0.01	0.03	0.03
CaO	11.49	11.9	11.88	12.69	14.17	12.86	12.09	12.19
TiO_2	0.37	0.49	0.32	1.66	0.32	0.98	0.33	0.37
FeO	16.01	15.82	16.48	15.09	13.95	13.29	15.78	15.77
MnO	0.23	0.22	0.25	0.19	0.21	0.2	0.22	0.22
Cr_2O_3	0.13	0.14	0.04	0.03	0	0.25	0.03	0.01
NiO	0	0.02	0	0	0.02	0.03	0.02	0.03
Total	**97.21**	**97.64**	**97.26**	**97.56**	**97.55**	**97.29**	**98**	**97.5**

Mg-Hornblende										**Average**
Na_2O	1.6	1.95	1.57	1.71	1.5	1.26	1.02	1.2	1.91	**1.53**
MgO	12.53	12.73	13.09	15.15	14.32	13.13	13.47	12.99	12.7	**12.67**
Al_2O_3	10.25	10.05	10.04	9.04	8.45	7.89	6.73	7.86	10.51	**7.81**
SiO_2	44.34	47.87	43.51	47.33	47.87	48.4	49.09	48.72	43.67	**47.57**
K_2O	0.19	0.2	0.18	0.14	0.13	0.08	0.07	0.11	0.2	**0.10**
CaO	12.01	11.12	11.45	11.47	11.46	11.7	11.45	11.24	11.62	**11.92**
TiO_2	3.39	3.35	2.92	0.77	0.74	0.28	0.3	0.26	2.99	**1.32**
FeO	12.4	11.05	12.42	11.32	11.66	13.56	13.96	14.09	12.05	**13.74**
MnO	0.16	0.14	0.2	0.2	0.21	0.26	0.27	0.28	0.22	**0.22**
Cr_2O_3	0.06	0.07	0.06	0	0	0	0	0.01	0.07	**0.05**
NiO	0.03	0.01	0	0	0	0.04	0.02	0.03	0.02	**0.02**
Total	**96.96**	**98.53**	**95.44**	**97.13**	**96.32**	**96.61**	**96.37**	**96.78**	**95.95**	**96.95**

Gabbro

Wallrock Minerals

Tremolite							**Average**
Na_2O	0.11	0.21	0.1	0.1	0.18	0.25	**0.16**
MgO	19.6	19.1	19.75	19.76	18.97	18.46	**19.27**
Al_2O_3	0.66	1.05	0.51	0.65	0.85	1.61	**0.89**
SiO_2	57.35	55.75	56.75	56.78	56.43	55.74	**56.47**
K_2O	0.01	0.01	0.01	0.02	0.01	0.03	**0.02**
CaO	12.56	12.53	13.06	12.82	13.1	12.8	**12.81**
TiO_2	0	0.01	0	0	0.02	0.11	**0.02**
FeO	6.46	7.24	6.37	6.39	7.35	8.48	**7.05**
MnO	0.31	0.33	0.32	0.2	0.31	0.21	**0.28**
Cr_2O_3	0.01	0	0	0	0	0.01	**0.00**
NiO	0.07	0.05	0.1	0.01	0.08	0.01	**0.05**
Total	**97.16**	**96.29**	**96.97**	**96.73**	**97.31**	**97.73**	**97.03**

Epidote								
Na_2O	0.23	0.06	0.09	0.01	0.01	0.01	0	0.17
MgO	2.73	1.58	1.48	0.11	0.1	0	0.04	2.62
Al_2O_3	24.83	24.59	25.56	26.29	28.64	26.29	27.91	25.35
SiO_2	37.41	40	37.71	38.31	38.68	40.58	38.11	37.62
K_2O	0	0	0.01	0	0	0.01	0	0
CaO	22.98	22.56	22.96	23.83	24.67	23.06	24.28	23.25
TiO_2	0.1	0.1	0.06	0.08	0.05	0.05	0.08	0.1
FeO	3.41	4.51	4.71	7.41	5.08	6.05	6.54	3.62
MnO	0.33	0.14	0.19	0.07	0.07	0.03	0.04	0.34
Cr_2O_3	0.72	0.01	0.01	0	0	0.01	0.01	0.01
NiO	0.01	0.01	0	0	0	0	0	0
Total	**92.75**	**93.56**	**92.76**	**96.11**	**97.3**	**96.09**	**97.01**	**93.09**

Epidote					**Average**
Na_2O	0.21	0.22	0.33	0.2	**0.13**
MgO	2.56	2.87	5.06	2.87	**1.84**
Al_2O_3	22.16	25.23	19.98	25.21	**25.17**
SiO_2	47.94	37.36	41.51	37.56	**39.40**
K_2O	0	0	0.02	0.01	**0.00**
CaO	20.11	22.96	20.88	23.05	**22.88**
TiO_2	0.11	0.11	0.08	0.09	**0.08**
FeO	2.87	3.38	6.22	3.45	**4.77**
MnO	0.31	0.36	0.22	0.34	**0.20**
Cr_2O_3	0	0	0	0	**0.06**
NiO	0.01	0.02	0.02	0	**0.01**
Total	**96.28**	**92.51**	**94.32**	**92.78**	**94.55**

Gabbro PST Glass								
Na_2O	5.54	1.75	2.07	2.8	3.25	1.85	2.39	2.92
MgO	6.7	11.7	10.07	11.16	7.01	9.46	8.52	3.49
Al_2O_3	19.35	14.07	17.13	15.96	20.32	16.34	18.5	25.67
SiO_2	58.66	50.54	51.08	48.83	51.19	50.64	51.71	54.16
K_2O	0.41	0.03	0.01	0.02	0.02	0.05	0.05	0.04
CaO	3.29	12.64	12.65	11.64	11.87	14.69	12.84	11.82
TiO_2	0.41	0.44	0.4	0.45	0.23	0.33	0.29	0.21
FeO	3.52	5.92	4.7	5.66	3.09	4.52	3.91	1.11
MnO	0.06	0.13	0.1	0.11	0.04	0.09	0.1	0
Cr_2O_3	0.07	0.08	0.06	0.05	0.03	0.11	0.05	0.02
NiO	0.04	0.02	0.07	0.02	0.02	0.02	0.01	0.02
Total	**98.04**	**97.32**	**98.34**	**96.68**	**97.07**	**98.1**	**98.37**	**99.47**
Glass								
Na_2O	0.3	0.19	2.24	2.38	3	1.05	1.11	0.93
MgO	11.23	11.86	10.83	11.28	11.05	11.55	11.5	11.39
Al_2O_3	17.85	17.58	16.58	15.3	16.14	16.89	16.85	17.04
SiO_2	53.37	53.34	50.21	49.55	51	52.87	52.84	53.35
K_2O	0.02	0.02	0.05	0.02	0.02	0.02	0.03	0.02
CaO	11.72	11.78	12.74	11.83	11.89	12.31	12.4	12.42
TiO_2	0.35	0.35	0.44	0.44	0.47	0.39	0.41	0.35
FeO	5.1	5.16	5.54	7.36	5.88	4.98	5.03	4.85
MnO	0.12	0.1	0.09	0.13	0.1	0.13	0.08	0.05
Cr_2O_3	0.02	0.04	0.04	0.08	0.04	0.06	0.05	0.05
NiO	0.02	0.01	0.03	0.04	0.03	0.02	0.04	0.04
Total	**100.1**	**100.43**	**98.79**	**98.4**	**99.63**	**100.28**	**100.34**	**100.5**
Glass								
Na_2O	0.57	0.43	0.41	2.16	2.33	2.5	2.45	2.55
MgO	11.55	12.28	12.93	10.22	10.31	11	11.27	10.81
Al_2O_3	17.53	16.89	16.26	17.25	16.75	16.64	16.45	16.77
SiO_2	52.51	53.22	52.04	50.93	50.67	49.91	49.6	49.92
K_2O	0.03	0.02	0.09	0.03	0.03	0.02	0.02	0.03
CaO	11.54	11.96	10.7	12.55	12.66	11.68	11.82	11.82
TiO_2	0.36	0.38	0.36	0.36	0.36	0.4	0.47	0.36
FeO	5.22	5.26	5.78	4.75	4.73	5.11	5.25	5.13
MnO	0.08	0.13	0.08	0.1	0.11	0.11	0.13	0.09
Cr_2O_3	0.07	0.05	0.05	0.07	0.08	0.06	0.07	0.06
NiO	0.07	0.01	0.01	0.03	0.05	0	0	0.03
Total	**99.53**	**100.64**	**98.71**	**98.45**	**98.07**	**97.44**	**97.55**	**97.56**

Gabbro PST Glass				**Average**
Na_2O	2.09	2.26	1.89	**1.98**
MgO	10.82	10.8	11	**10.44**
Al_2O_3	15.8	14.75	15.04	**17.10**
SiO_2	50.41	51.15	50.04	**51.62**
K_2O	0.02	0.03	0.04	**0.04**
CaO	13.09	13.69	12.96	**11.96**
TiO_2	0.4	0.41	0.46	**0.38**
FeO	5.14	4.97	6.03	**4.95**
MnO	0.09	0.11	0.1	**0.09**
Cr_2O_3	0.07	0.1	0.07	**0.06**
NiO	0	0.02	0.02	**0.03**
Total	**97.92**	**98.29**	**97.66**	**98.65**

Gabbro
PST Dendrites

Sphene								**Average**
Na_2O	0.22	0.02	0.09	0.1	0.07	0.04	0	**0.08**
MgO	0.35	0.17	0.26	0.09	0.07	0.07	0.14	**0.16**
Al_2O_3	2.01	1.82	2.47	2.04	1.76	1.75	2.02	**1.98**
SiO_2	32.22	30.62	30.94	30.59	30.5	30.58	30.7	**30.88**
K_2O	0.01	0	0.01	0	0	0.02	0	**0.01**
CaO	25.96	28.31	28.14	28.43	28.38	28.42	28.38	**28.00**
TiO_2	34.78	36.27	34.59	36.03	36.62	36.84	35.91	**35.86**
FeO	1.58	1.27	1.81	1.15	1.2	1.05	1.35	**1.34**
MnO	0.01	0.02	0.02	0.02	0.02	0.01	0.02	**0.02**
Cr_2O_3	0.07	0	0.02	0.02	0.03	0.02	0.01	**0.02**
NiO	0.01	0.01	0	0.02	0	0.02	0	**0.01**
Total	**97.21**	**98.51**	**98.34**	**98.49**	**98.63**	**98.83**	**98.53**	**98.36**

Plagioclase								
Na_2O	0.95	2.53	5.72	4.57	5.25	4.01	5.36	5.18
MgO	0.7	0.74	1.2	2.31	0.95	4.23	0.67	0.15
Al_2O_3	27.15	26.57	25.22	25.67	26.49	23.98	25.83	27.89
SiO_2	46.48	47.84	52.91	53.22	54.07	53.17	53.24	53.78
K_2O	0.02	0.02	0.05	0.03	0.04	0.02	0.05	0.01
CaO	21.07	18.34	10.23	11.18	11.02	11.84	9.88	11.32
TiO_2	0.08	0.05	0.23	0.15	0.12	0.23	0.15	0.07
FeO	1.92	1.69	1.92	1.75	0.8	2.53	1.34	0.45
MnO	0.03	0.02	0.05	0.01	0	0.03	0.03	0
Cr_2O_3	0	0	0.02	0.01	0.01	0.02	0.02	0
NiO	0	0	0.02	0	0	0	0.02	0.01
Total	**98.4**	**97.8**	**97.57**	**98.89**	**98.76**	**100.05**	**96.59**	**98.86**

Plagioclase				**Average**
Na_2O	5.13	5.63	5.23	**4.51**
MgO	0.09	0.13	0.7	**1.08**
Al_2O_3	28.13	27.56	27.12	**26.51**
SiO_2	53.81	55.15	54.16	**52.53**
K_2O	0.03	0.01	0.03	**0.03**
CaO	11.43	10.46	10.91	**12.52**
TiO_2	0.09	0.06	0.11	**0.12**
FeO	0.37	0.39	0.77	**1.27**
MnO	0	0	0	**0.02**
Cr_2O_3	0	0.01	0	**0.01**
NiO	0	0.01	0	**0.01**
Total	**99.09**	**99.41**	**99.03**	**98.59**

Gabbro
PST Dendrites
Omphacite

Na_2O	3.15	2.61	2.78	4.64	2.9	3.07	4.78	3.63
MgO	9.11	9.8	9.82	8.09	9.74	9.39	7.38	7.8
Al_2O_3	17.42	16.98	16.78	17.34	16.72	16.9	17.78	18.44
SiO_2	50.47	50.2	50.29	51.66	50.05	50.35	52.43	51.29
K_2O	0.03	0.03	0.06	0.06	0.03	0.03	0.05	0.02
CaO	12.26	13.36	12.95	10.85	12.8	12.56	10.33	12.34
TiO_2	0.43	0.44	0.45	0.43	0.48	0.41	0.41	0.37
FeO	4.78	4.97	5.11	5.31	5.05	5.15	4.33	4.25
MnO	0.11	0.12	0.09	0.08	0.1	0.13	0.11	0.11
Cr_2O_3	0.1	0.09	0.08	0.08	0.07	0.08	0.07	0.08
NiO	0.03	0.01	0.02	0.03	0.03	0.02	0.05	0.02
Total	**97.87**	**98.63**	**98.44**	**98.57**	**97.97**	**98.09**	**97.71**	**98.36**

Omphacite

Na_2O	4.43	3.96	3	2.65	3.13	0.94	1.71	2.97
MgO	7	9.29	9.48	9.9	8.97	13.92	12.6	9.87
Al_2O_3	20.03	16.71	16.83	16.76	16.98	11.81	13.28	16.78
SiO_2	52.76	50.01	50.26	50.17	50.57	48.81	50.63	49.87
K_2O	0.03	0.05	0.04	0.05	0.03	0.02	0.04	0.05
CaO	9.59	11.86	12.71	12.85	12.87	18.15	16.16	12.9
TiO_2	0.43	0.43	0.43	0.43	0.4	0.68	0.63	0.45
FeO	4.67	5.31	4.8	4.93	4.94	4.94	5.09	5.09
MnO	0.06	0.11	0.09	0.13	0.12	0.12	0.1	0.09
Cr_2O_3	0.08	0.08	0.1	0.06	0.07	0.08	0.07	0.07
NiO	0	0.01	0	0	0.02	0	0	0
Total	**99.08**	**97.84**	**97.74**	**97.92**	**98.09**	**99.47**	**100.29**	**98.15**

Omphacite

Na_2O	2.35	2.45	2.61	2.62	2.86	2.71	2.47	2.7
MgO	12.98	10.17	10.17	9.88	9.81	10.2	10.15	9.81
Al_2O_3	12.49	17.06	17.19	17.26	17.32	17.06	17.11	17.04
SiO_2	48.9	50.69	50.62	50.52	51.29	50.72	50.73	50.66
K_2O	0.07	0.04	0.02	0.01	0.02	0.01	0.03	0.03
CaO	12.81	13.63	13.3	13.52	13.24	13.19	13.3	13.31
TiO_2	0.67	0.42	0.4	0.43	0.39	0.43	0.4	0.44
FeO	7.53	4.79	4.97	4.71	4.83	4.82	4.78	4.95
MnO	0.16	0.1	0.1	0.11	0.11	0.1	0.12	0.11
Cr_2O_3	0.11	0.08	0.1	0.09	0.1	0.07	0.11	0.1
NiO	0.02	0.03	0.01	0.04	0	0.05	0.03	0.05
Total	**98.08**	**99.44**	**99.47**	**99.2**	**99.98**	**99.36**	**99.22**	**99.21**

Gabbro
PST Dendrites
Omphacite

Na_2O	2.88	4.68	3.01	3.25	4	5.88	6.25	4.9
MgO	9.21	7.19	9.15	8.25	8.78	4.74	3.97	2.83
Al_2O_3	17.59	16.48	17.35	17.67	16.55	19.75	19.63	25.59
SiO_2	51.64	54.63	50.55	51.16	49.81	55.26	53.37	52.23
K_2O	0.03	0.03	0.03	0.04	0.05	0.05	0.05	0.05
CaO	12.88	10.75	13.19	13.01	10.92	10.23	11.12	9.87
TiO_2	0.37	0.3	0.42	0.41	0.48	0.31	0.33	0.07
FeO	4.65	4.32	4.71	4.44	6.31	3.12	3.49	2.76
MnO	0.1	0.11	0.09	0.11	0.12	0.09	0.08	0.03
Cr_2O_3	0.04	0.07	0.09	0.06	0.07	0.07	0.06	0.02
NiO	0	0	0.03	0	0	0	0	0
Total	**99.38**	**98.56**	**98.61**	**98.39**	**97.08**	**99.51**	**98.34**	**98.35**

Omphacite

Na_2O	4.44	6.13	2.51	3.6	3.44	3.27	3.2	2.9
MgO	8.85	6.29	9.46	9.42	8.29	8.09	10.24	11.17
Al_2O_3	16.93	19.05	17.84	17.24	18.63	18.91	15.46	14.34
SiO_2	51.76	52.23	50.74	50.86	50.64	50.63	51.01	49.29
K_2O	0.06	0.05	0.02	0.04	0.05	0.05	0.04	0.04
CaO	10.11	8.63	13.23	11.93	12.47	12.64	12.82	11.6
TiO_2	0.46	0.61	0.38	0.33	0.43	0.41	0.62	0.65
FeO	5.86	7.74	3.8	4.44	4.84	4.66	5.26	7.91
MnO	0.11	0.12	0.06	0.06	0.1	0.08	0.13	0.15
Cr_2O_3	0.06	0.04	0.05	0.08	0.07	0.04	0.08	0.05
NiO	0.01	0.01	0.03	0.01	0	0	0.02	0.04
Total	**98.65**	**100.9**	**98.12**	**98**	**98.94**	**98.78**	**98.88**	**98.13**

Omphacite

Na_2O	3.21	5.11	4.92	2.69	2.77	2.71	2.98	4.07
MgO	10.35	5.62	7.46	11.51	10.75	9.8	10.74	8.93
Al_2O_3	15.12	19.86	16.79	14.88	15.55	14.63	14.66	16.01
SiO_2	50.01	52.41	50.89	49.32	49.73	49.4	50.29	51.43
K_2O	0.03	0.04	0.05	0.03	0.02	0.03	0.02	0.03
CaO	12.47	10.67	10.5	12.55	13.06	13.83	13.62	11.5
TiO_2	0.71	0.55	0.65	0.62	0.6	0.73	0.62	0.61
FeO	6.66	4.47	6.57	6.71	5.79	6.41	5.87	6.03
MnO	0.15	0.06	0.11	0.13	0.11	0.13	0.13	0.16
Cr_2O_3	0.06	0.03	0.03	0.08	0.1	0.06	0.05	0.05
NiO	0.05	0.03	0.02	0.03	0.02	0.01	0.03	0
Total	**98.82**	**98.85**	**97.99**	**98.55**	**98.5**	**97.73**	**99.02**	**98.82**

Gabbro

PST Dendrites

Omphacite

Na_2O	3.23	3.49	3.19	3.25	4.81	4.48	4.04	2.01
MgO	9.93	7.79	8.61	10.18	7.27	8.67	8.92	13.31
Al_2O_3	15.35	18.38	16.89	16.27	17.81	16.96	16.54	13.75
SiO_2	50.59	51.96	51.55	50.06	51.39	50.64	49.44	48.01
K_2O	0.02	0.02	0.02	0.03	0.03	0.07	0.06	0.05
CaO	12.57	12.83	13.44	12.16	10.08	8.67	10.08	13.02
TiO_2	0.64	0.5	0.55	0.51	0.56	0.41	0.48	0.47
FeO	5.75	4.67	5.39	5.01	7	6.66	8.48	7.01
MnO	0.13	0.1	0.12	0.11	0.13	0.16	0.14	0.15
Cr_2O_3	0.08	0.04	0.07	0.05	0.05	0.03	0.06	0.05
NiO	0.01	0.01	0.03	0.01	0.05	0.02	0.04	0
Total	**98.29**	**99.79**	**99.87**	**97.64**	**99.17**	**96.75**	**98.27**	**97.82**

Omphacite

Na_2O	5.12	3.76	4.43	1.92	1.21	3.2	2.08	2.85
MgO	6.61	8.97	7.88	12.63	12.73	7.82	11.06	8.74
Al_2O_3	17.22	16.52	17.47	13.4	13.29	18.73	13.64	17.88
SiO_2	51.19	49.94	50.16	49.61	48.47	51.22	48.32	50.99
K_2O	0.05	0.02	0.04	0.04	0.02	0.04	0.08	0.03
CaO	9.21	12.95	9.48	14.08	15.93	13.08	14.35	13.12
TiO_2	0.71	0.67	0.6	0.66	0.63	0.56	0.5	0.57
FeO	7.86	6.26	7.14	6.07	6.15	4.53	7.05	4.91
MnO	0.16	0.15	0.1	0.14	0.13	0.11	0.13	0.11
Cr_2O_3	0.03	0.04	0.03	0.1	0.07	0.08	0.09	0.06
NiO	0.07	0.04	0.02	0.03	0	0	0	0.02
Total	**98.22**	**99.33**	**97.34**	**98.67**	**98.63**	**99.36**	**97.29**	**99.28**

Omphacite									**Average**
Na_2O	1.08	1.47	2.19	1.33	0.63	1.53	2.57	0.78	**3.17**
MgO	14.71	14.15	12.69	13.89	17.68	13.31	10.93	16.14	**9.74**
Al_2O_3	11.35	9.63	12.05	9.7	11.31	12.73	14.72	10.74	**16.23**
SiO_2	49.75	49.79	48.16	49.23	47.95	47.03	48.15	48.73	**50.49**
K_2O	0.03	0.01	0.04	0.04	0.03	0.02	0.03	0.01	**0.04**
CaO	15.91	16.55	13.48	15.68	12.78	13.65	13.94	15.6	**12.60**
TiO_2	0.68	0.75	0.68	0.84	0.39	0.84	0.83	0.57	**0.52**
FeO	4.95	6.18	7.59	7.85	6.96	8.87	7.94	5.31	**5.59**
MnO	0.11	0.13	0.18	0.16	0.14	0.15	0.2	0.13	**0.12**
Cr_2O_3	0.11	0.14	0.1	0.13	0.13	0.09	0.08	0.13	**0.07**
NiO	0.02	0.02	0.02	0.02	0.04	0.02	0.01	0.04	**0.02**
Total	**98.72**	**98.81**	**97.17**	**98.87**	**98.03**	**98.22**	**99.39**	**98.18**	**98.59**

Peridotite

PST Matrix

Na_2O	0.57	0.62	0.33	0.24	0.21	0.09	0.1	0.05	0.04	0.04
MgO	32.9	35.66	39.14	27.99	38.33	37.62	31.37	38.52	39.31	39.8
Al_2O_3	7.22	6.21	5.09	4.38	5.93	4.6	3.17	2.58	2.3	2.99
SiO_2	44.69	44.18	42.89	51.8	41.66	43.45	50.46	43.15	43.48	43.35
K_2O	0	0.02	0.02	0	0	0	0.01	0	0.01	0.01
CaO	4.83	4.18	3.25	8.54	2.64	5.42	7.93	3.91	3.27	2.69
TiO_2	0.09	0.12	0.07	0.06	0.09	0.11	0.07	0.05	0.05	0.11
FeO	6.8	7.05	6.9	3.94	7.69	6.41	4.43	9.03	8.22	7.31
MnO	0.1	0.09	0.08	0.06	0.07	0.08	0.07	0.11	0.1	0.12
Cr_2O_3	0.31	0.35	0.18	0.31	0.38	0.34	0.39	0.32	0.3	0.34
NiO	0.22	0.25	0.25	0.22	0.26	0.28	0.25	0.34	0.27	0.26
Total	**97.73**	**98.72**	**98.2**	**97.73**	**98.72**	**98.2**	**97.73**	**98.72**	**98.2**	**97.73**

PST Matrix

Na_2O	0.14	0.1	0.12	0.38	0.34	0.05	0.06	0.06	0.03	0.04
MgO	36.47	36.25	38.17	34.73	36.31	36.6	35.73	32.19	33.95	38.12
Al_2O_3	4.52	5.26	4.72	11.9	12.49	7.15	7.4	7.39	7.17	6.09
SiO_2	45.62	44.57	43.95	40.04	38.69	44.03	43.3	45.58	42.62	43.03
K_2O	0	0	0	0	0	0	0.01	0	0	0.01
CaO	3.24	2.97	2.65	3.2	2.53	4.11	3.91	6.74	4.27	3.08
TiO_2	0.07	0.09	0.11	0.14	0.15	0.09	0.11	0.1	0.14	0.06
FeO	5.63	6.06	6.1	6.4	6.11	6.83	5.98	5.7	7.9	7.21
MnO	0.08	0.1	0.1	0.07	0.06	0.05	0.07	0.1	0.1	0.09
Cr_2O_3	0.44	0.39	0.32	0.19	0.16	0.28	0.21	0.41	2.36	0.18
NiO	0.25	0.18	0.26	0.14	0.22	0.25	0.27	0.16	0.24	0.25
Total	**98.72**	**98.2**	**97.73**	**98.72**	**98.2**	**99.44**	**97.06**	**98.42**	**98.78**	**98.18**

PST Matrix

Na_2O	0.05	0.05	0.04	0.48	0.11	0.13	0.05	0.25	0.21	0.26
MgO	22.8	32.59	30.46	33.59	33.96	32.99	31.45	32.24	33.13	32.43
Al_2O_3	0.55	17.32	16.75	11.09	12.69	18.41	15.91	9.52	11.42	10.79
SiO_2	56.05	34.39	34.94	41.56	36.33	33.93	33.61	42.35	40.29	41.81
K_2O	0	0.01	0.01	0.01	0.02	0.01	0.01	0.01	0	0.02
CaO	13.15	0.9	0.71	3.16	0.89	1.2	0.15	4.06	3.37	3.57
TiO_2	0.07	0.23	0.07	0.12	0.1	0.12	0.03	0.14	0.16	0.1
FeO	4.9	5.04	3.67	5.49	5.25	5.87	3.78	5.36	5.5	5.54
MnO	0.06	0.05	0.01	0.06	0.04	0.04	0.01	0.04	0.05	0.05
Cr_2O_3	0.21	0.14	0.14	0.16	0.18	0.21	0.55	0.21	0.22	0.23
NiO	0.08	0.24	0.14	0.22	0.21	0.17	0.23	0.19	0.17	0.17
Total	**97.91**	**90.95**	**86.94**	**95.94**	**89.78**	**93.08**	**85.78**	**94.39**	**94.52**	**94.97**

Peridotite

PST Matrix

Na_2O	0.06	0.01	0.06	0.08	0.1	0.03	0.04	0.08	0.37	0.74
MgO	22.59	15.57	34.82	36.2	36.44	38.24	37.18	39.07	32.24	32.71
Al_2O_3	0.59	0.23	5.39	5.57	5.88	4.4	5.45	5.57	8.89	9.5
SiO_2	57.72	53.63	44.44	43.97	44.58	42.98	43.77	40.98	44.59	43.27
K_2O	0	0	0	0.01	0	0.01	0.02	0.03	0	0
CaO	13.41	26.11	3.72	4.3	4.11	3.18	3.65	1.88	5.54	4.65
TiO_2	0.06	0.07	0.11	0.08	0.09	0.09	0.09	0.07	0.12	0.12
FeO	2.28	3.83	6.97	7.19	7	6.97	6.65	6.62	6.01	6.52
MnO	0.03	0.06	0.11	0.1	0.1	0.08	0.08	0.07	0.07	0.04
Cr_2O_3	0.03	0	0.28	0.48	0.47	0.33	0.21	0.2	0.3	0.73
NiO	0.04	0.04	0.25	0.23	0.23	0.28	0.25	0.24	0.2	0.23
Total	**96.82**	**99.55**	**96.15**	**98.22**	**98.99**	**96.58**	**97.41**	**94.81**	**98.34**	**98.5**

PST Matrix

Na_2O	0.04	0.24	0.28	0.69	0.06	0.38	0.27	0.22	0.35	0.45
MgO	38.43	39.31	33.15	31.98	24.35	31.58	31.92	28.97	29.2	28.56
Al_2O_3	5.38	4.88	7.88	9.91	20.89	12.24	12.38	13.89	13.07	13.39
SiO_2	44.46	43.03	43.94	44.59	29.67	42.14	41.45	41.7	41.48	41.57
K_2O	0	0	0.01	0.01	0.04	0	0.02	0.01	0.03	0.03
CaO	2.11	2.87	5.44	4.94	0.27	5.49	5.35	4.62	4.44	5.32
TiO_2	0.12	0.09	0.08	0.08	0.01	0.11	0.16	0.13	0.09	0.12
FeO	7.21	7.37	6.22	5.59	10.86	5.97	6.34	6.21	6.3	6.32
MnO	0.12	0.11	0.07	0.07	0.06	0.08	0.09	0.04	0.06	0.05
Cr_2O_3	0.2	0.18	0.3	0.38	0.02	0.21	0.25	0.21	0.28	0.25
NiO	0.23	0.28	0.19	0.17	0.12	0.18	0.18	0.12	0.15	0.16
Total	**98.3**	**98.36**	**97.56**	**98.42**	**86.35**	**98.39**	**98.39**	**96.13**	**95.44**	**96.21**

PST Matrix

Na_2O	0.09	0.39	0.13	0.08	0.12	0.56	0.47	0.09	0.07	1.14
MgO	22.87	29.88	28.67	28.58	28.28	30.05	32.12	25.86	26.03	14.62
Al_2O_3	0.67	11.18	11.23	7.67	25.26	17.01	14.89	24.27	23.92	19.26
SiO_2	57.73	42.24	40.47	44.25	28.98	36.26	37.37	29.08	30.71	29.35
K_2O	0.02	0.03	0.04	0	0	0.01	0	0.03	0.02	0.03
CaO	13.47	4.52	3.86	5.42	1.89	2.56	2.88	0.26	0.43	6.75
TiO_2	0.04	0.14	0.16	0.06	0.07	0.11	0.1	0.01	0.06	8.64
FeO	2.45	6.05	5.23	5.92	13.05	10.48	10.41	9.83	11.83	17.74
MnO	0.1	0.07	0.06	0.07	0.13	0.12	0.1	0.05	0.06	0.21
Cr_2O_3	0.08	0.38	0.24	0.32	0.31	0.85	0.21	0	0.06	1.61
NiO	0.07	0.16	0.21	0.45	0.12	0.17	0.17	0.14	0.13	0.07
Total	**97.59**	**95.05**	**90.28**	**92.84**	**98.2**	**98.18**	**98.72**	**89.64**	**93.32**	**99.41**

Peridotite

PST Matrix

Na_2O	1.04	0.22	0.22	0.28	0.04	0.03	0.05	0.42	0.25	0.13
MgO	18.37	34.43	37.5	28.67	36.25	27.84	37.97	32.85	36.7	40.27
Al_2O_3	18.67	5.23	3.9	6.55	4.38	4.49	4.36	6.78	5.35	3.13
SiO_2	35.34	47.83	46.15	47.76	46.8	47.61	45.77	46.04	45.29	44.94
K_2O	0.03	0	0	0.01	0	0.01	0	0.01	0	0.02
CaO	5.91	3.88	4.56	7.97	5.01	11.69	3.08	5.73	4.64	3.31
TiO_2	0.08	0.1	0.05	0.12	0.08	0.07	0.09	0.1	0.11	0.01
FeO	15.04	6.12	6.9	5.33	5.98	5.14	6.25	6.08	6.44	6.49
MnO	0.09	0.1	0.1	0.12	0.08	0.07	0.1	0.08	0.09	0.09
Cr_2O_3	0.41	0.34	0.68	0.35	0.38	0.35	0.32	0.61	0.48	0.38
NiO	0.13	0.23	0.24	0.21	0.24	0.27	0.25	0.23	0.26	0.31
Total	**95.1**	**98.49**	**100.31**	**97.36**	**99.24**	**97.56**	**98.25**	**98.94**	**99.58**	**99.08**

PST Matrix

Na_2O	0.19	0.12	0.09	0.04	0.2	0.02	0.04	0.31	0.03	0.05
MgO	39.43	35.85	34.1	37.6	36.52	33.63	34.1	36.01	34.01	31.11
Al_2O_3	3.7	4.76	5.19	4.35	4.76	3.84	4.02	5.66	2.71	3.52
SiO_2	45.7	47.32	47.18	46.91	47.98	45	43.99	45.2	45.51	44.57
K_2O	0	0	0	0	0.01	0	0.01	0	0.01	0.01
CaO	4.26	5.13	6.59	3.93	2.98	4.37	5.45	4.82	9.37	3.82
TiO_2	0.08	0.08	0.08	0.11	0.05	0.07	0.08	0.08	0.08	0.07
FeO	6.77	6.11	5.76	6.72	6.71	7.07	6	6.23	5.78	6.32
MnO	0.08	0.09	0.09	0.11	0.08	0.09	0.12	0.09	0.12	0.09
Cr_2O_3	0.36	0.36	0.37	0.32	0.49	0.7	0.29	0.28	0.25	0.18
NiO	0.26	0.26	0.22	0.28	0.25	0.28	0.25	0.24	0.22	0.25
Total	**100.85**	**100.08**	**99.67**	**100.37**	**100.03**	**95.07**	**94.35**	**98.92**	**98.09**	**90**

PST Matrix

Na_2O	0.11	0.05	0.12	0.22	0.09	0.03	0.23	0.27	0.05	0.11
MgO	42.86	38.03	35.64	33.34	32.79	36.05	36.8	33.46	32.2	39.66
Al_2O_3	3.54	6.88	9.65	10.62	5.08	4.66	4.2	5.2	8.14	1.5
SiO_2	42.26	41.83	44.95	42.76	46.58	44.52	46.89	47.07	42.94	40.57
K_2O	0	0	0.01	0	0.01	0	0.01	0	0	0.15
CaO	2.95	2.74	3.89	4.77	5.49	4.22	4.27	5.84	4.39	2.93
TiO_2	0.1	0.1	0.13	0.15	0.08	0.1	0.08	0.09	0.11	0.02
FeO	7.68	6.25	6.29	5.97	5.67	7.02	5.98	5.79	6.24	8.38
MnO	0.1	0.07	0.08	0.04	0.06	0.08	0.1	0.09	0.08	0.14
Cr_2O_3	0.18	0.19	0.11	0.15	0.24	0.47	0.37	0.38	0.09	0.03
NiO	0.34	0.27	0.22	0.18	0.22	0.26	0.27	0.23	0.22	0.23
Total	**100.11**	**96.42**	**101.09**	**98.18**	**96.31**	**97.41**	**99.17**	**98.42**	**94.47**	**93.73**

Peridotite

PST Matrix

Na_2O	0.07	0.01	0.61	0.64	0.63	0.52	0.34	0.37	0.64	0.05
MgO	24.18	26.73	29.6	29.06	28.47	27.82	35.46	34.58	30.91	38.07
Al_2O_3	23.75	25.16	19.67	18.61	19.7	21.5	8.98	8.98	11.65	6.96
SiO_2	31.15	29.65	36.38	37.3	37.52	35.11	44.01	44.81	43.74	40.13
K_2O	0.01	0.01	0	0.01	0.01	0	0	0	0	0.02
CaO	0.49	0.26	2.56	3.38	3.45	3.05	4.19	4.32	5.88	0.42
TiO_2	0.01	0	0.1	0.06	0.07	0.05	0.12	0.15	0.12	0.12
FeO	14.45	12.48	10.44	9.69	9.74	10.88	6.42	6.27	5.54	7.01
MnO	0.11	0.09	0.07	0.07	0.08	0.09	0.09	0.09	0.09	0.08
Cr_2O_3	0	0.01	0.3	0.35	0.28	0.29	0.26	0.25	0.21	0.92
NiO	0.14	0.1	0.15	0.17	0.19	0.17	0.25	0.22	0.21	0.3
Total	**94.37**	**94.49**	**99.86**	**99.34**	**100.12**	**99.48**	**100.13**	**100.04**	**98.99**	**94.07**

PST Matrix

Na_2O	0.04	0.19	0.06	0.12	0.69	0.62	0.54	0.06	0.08	0.07
MgO	42.59	36.4	39.05	32.73	32.64	32.06	32.05	29.66	34.38	35.96
Al_2O_3	5.33	9.89	6.8	8.71	10.87	14.08	13.55	15.92	10.92	13.68
SiO_2	40.29	39.79	41.54	41.11	42.75	40.93	41.96	35.76	41.17	37.22
K_2O	0.01	0.01	0	0.01	0.01	0.01	0	0.01	0.04	0
CaO	1.03	3.15	2.81	3.2	4.7	3.57	3.84	1.17	0.48	2.15
TiO_2	0.08	0.14	0.09	0.29	0.12	0.14	0.1	0.15	0.14	0.09
FeO	7.78	5.73	7.37	6.08	7.17	7.02	6.57	7.02	6.49	8.86
MnO	0.09	0.09	0.08	0.07	0.07	0.07	0.05	0.05	0.07	0.09
Cr_2O_3	0.19	0.21	0.23	0.62	0.25	0.27	0.26	0.21	0.23	0.08
NiO	0.25	0.23	0.26	0.19	0.18	0.2	0.17	0.12	0.22	0.25
Total	**97.68**	**95.84**	**98.3**	**93.13**	**99.44**	**98.96**	**99.09**	**90.11**	**94.23**	**98.45**

PST Matrix

Na_2O	0.02	0.31	0.12	0.17	0.51	0.21	0.12	0.25	0.21	0.39
MgO	34.73	27.9	32.08	29.9	29.67	29.74	26.95	28.37	26.82	27.5
Al_2O_3	10.42	12.73	15.07	13.05	14.76	14.96	19.53	17.32	17.72	16.18
SiO_2	39.47	41.8	39.67	37.64	39.96	38.11	35.75	37.56	37.21	39.27
K_2O	0.02	0	0.01	0.04	0	0.01	0.03	0.01	0.01	0.01
CaO	0.79	6.2	1.96	2.49	4.79	3.13	0.63	4.46	2.92	4.68
TiO_2	0.13	0.14	0.09	0.12	0.12	0.13	0.11	0.1	0.15	0.13
FeO	7.32	8.06	7.79	9.2	8.44	9.18	5.93	6.98	7.07	6.37
MnO	0.06	0.12	0.07	0.07	0.07	0.08	0.01	0.04	0.04	0.04
Cr_2O_3	0.28	0.11	0.19	0.31	0.37	0.4	0.4	0.33	0.91	0.21
NiO	0.14	0.18	0.15	0.18	0.16	0.19	0.16	0.14	0.15	0.12
Total	**93.37**	**97.55**	**97.2**	**93.15**	**98.85**	**96.13**	**89.63**	**95.56**	**93.21**	**94.9**

Peridotite

PST Matrix

Na_2O	0.35	0.35	0.47	0.21	0.55	0.02	0.05	0.04	0.01	0.05
MgO	34.02	32.8	35.2	39.41	32.77	43.56	44.01	42.19	44.05	43.42
Al_2O_3	8.87	10.11	8.86	5.97	12.99	3.92	2.89	3.05	3.57	2.97
SiO_2	45.17	44.07	43.01	41.46	40.01	41.48	42.64	44.56	42.05	42.98
K_2O	0	0.01	0	0	0	0.01	0.01	0	0	0.01
CaO	4.6	5.08	4.09	2.7	3.52	0.25	0.14	0.16	0.1	0.19
TiO_2	0.1	0.15	0.1	0.07	0.12	0.04	0.03	0.04	0.03	0.05
FeO	6.17	6.46	6.78	8.78	7.81	6.08	6.03	5.99	6.02	6.3
MnO	0.08	0.07	0.07	0.13	0.08	0.07	0.05	0.07	0.06	0.08
Cr_2O_3	0.28	0.74	0.22	0.16	0.26	0.26	0.35	0.41	0.43	0.38
NiO	0.21	0.21	0.21	0.25	0.19	0.27	0.26	0.27	0.27	0.23
Total	**99.85**	**100.06**	**99.02**	**99.14**	**98.32**	**95.96**	**96.45**	**96.79**	**96.61**	**96.65**

PST Matrix								**Average**
Na_2O	0.02	0.09	0.1	0.06	0.06	0.08	0.18	**0.21**
MgO	44.15	34.28	33.92	31.46	33.09	34.94	32.68	**33.36**
Al_2O_3	2.66	4.58	3.95	4.04	1.32	8.97	10.38	**9.15**
SiO_2	40.09	47.36	51.01	50.46	51.82	42.4	43.12	**42.35**
K_2O	0	0.01	0	0	0	0.02	0	**0.01**
CaO	0.1	3.91	3.33	5.31	6.02	2.15	3.91	**4.00**
TiO_2	0.02	0.07	0.06	0.09	0.01	0.04	0.03	**0.16**
FeO	7.02	4.72	4.29	3.52	4.79	5.76	4.9	**6.88**
MnO	0.08	0.09	0.05	0.05	0.06	0.06	0.05	**0.08**
Cr_2O_3	0.21	0.63	0.51	0.47	0.23	0.27	0.24	**0.33**
NiO	0.31	0.21	0.21	0.19	0.21	0.27	0.25	**0.21**
Total	**94.68**	**95.97**	**97.43**	**95.66**	**97.61**	**94.95**	**95.75**	**96.82**

Peridotite

Wallrock Minerals

Olivine

Na_2O	0.01	0	0.06	0.11	0	0.03	0.01	0.02	0.03	0.02
MgO	47.68	47.14	48.06	47.43	48.35	47.7	47.38	48.16	48.36	48.11
Al_2O_3	0	0.14	0.03	0.14	0.01	0.14	0.04	0	0.04	0.1
SiO_2	41.21	41.04	40.97	41.23	41.3	40.93	41.52	41.21	41.12	41.2
K_2O	0	0	0.01	0	0	0	0.01	0	0.01	0.01
CaO	0.04	0.18	0.04	0.23	0.03	0.05	0.03	0.03	0.05	0.08
TiO_2	0	0.01	0.02	0.01	0	0.02	0.02	0.02	0.02	0.01
FeO	10.64	10.43	10.69	10.22	10.05	10.44	10.81	10.31	9.79	9.97
MnO	0.15	0.15	0.16	0.12	0.15	0.14	0.15	0.16	0.14	0.16
Cr_2O_3	0.03	0.03	0.01	0.03	0.02	0.01	0	0	0	0.02
NiO	0.35	0.67	0.35	0.34	0.34	0.23	0.31	0.35	0.28	0.37
Total	**100.12**	**99.8**	**100.4**	**99.86**	**100.25**	**99.69**	**100.28**	**100.26**	**99.83**	**100.07**

Olivine

Na_2O	0.03	0.01	0	0	0.01	0	0	0	0.01	0
MgO	48.19	48.07	48.5	48.2	48.84	46.24	48.47	48.4	48.7	48.34
Al_2O_3	0.01	0.07	0	0.07	0.01	0	0.06	0.06	0	0.01
SiO_2	41.15	41.28	41.34	40.62	41.3	41.08	41.3	41.05	41.36	41.96
K_2O	0	0	0	0	0.01	0.01	0	0	0.01	0
CaO	0.04	0.14	0.02	0.02	0.04	0.01	0.04	0.05	0.08	0.02
TiO_2	0	0.02	0	0	0	0	0.02	0.02	0	0.01
FeO	10.21	9.88	9.74	10.79	9.41	9.99	10.02	9.66	9.48	9.69
MnO	0.13	0.14	0.14	0.13	0.14	0.16	0.12	0.12	0.13	0.12
Cr_2O_3	0.02	0.02	0	0.03	0.01	0.01	0	0.02	0.02	0.02
NiO	0.36	0.33	0.41	0.32	0.36	0.36	0.35	0.36	0.36	0.35
Total	**100.15**	**99.96**	**100.15**	**100.19**	**100.13**	**97.86**	**100.39**	**99.73**	**100.14**	**100.53**

Olivine

Na_2O	0	0	0	0.01	0.01	0	0.01	0	0	0
MgO	48.6	48.62	48.49	49.05	48.96	48.4	48.74	49.06	48.78	47.5
Al_2O_3	0.01	0	0.03	0.05	0.01	0	0	0	0.01	0.13
SiO_2	41.44	41.5	41.32	41.32	41.31	40.95	40.04	41.16	41.04	40.66
K_2O	0	0	0	0	0	0	0	0	0	0
CaO	0.02	0.02	0.38	0.01	0.04	0.01	0.03	0.01	0.11	0.33
TiO_2	0.01	0.01	0.01	0	0	0	0	0	0.01	0.02
FeO	9.72	9.27	9.29	9.36	9.23	10.18	9.75	9.53	9.56	10.82
MnO	0.15	0.11	0.14	0.13	0.12	0.18	0.15	0.17	0.12	0.17
Cr_2O_3	0	0.01	0.01	0.02	0.02	0	0.01	0	0	0
NiO	0.35	0.38	0.38	0.36	0.36	0.35	0.38	0.37	0.3	0.32
Total	**100.3**	**99.92**	**100.05**	**100.31**	**100.07**	**100.08**	**99.1**	**100.31**	**99.93**	**99.95**

Peridotite

Wallrock Minerals

Olivine

Na_2O	0	0.02	0.01	0.03	0.01	0.01	0	0.02	0.01	0.11
MgO	48.64	41.93	46.97	44.5	46.33	41.78	46.85	46.46	48.3	47.94
Al_2O_3	0.06	0.69	0.19	1.43	0.6	0.35	0.02	0.05	0.88	0.24
SiO_2	41.6	43.97	41.37	41.93	42.21	47.64	40.54	42.76	40.11	40.09
K_2O	0.01	0	0	0.02	0	0	0	0	0	0.12
CaO	0.51	3.69	0.96	0.77	1.35	2.77	0.17	0.04	0.09	1.14
TiO_2	0.02	0.01	0.01	0.02	0	0	0	0.03	0.04	0.03
FeO	9.61	8.78	10.41	8.74	9.26	8.54	12	11.46	10.61	10.26
MnO	0.11	0.14	0.16	0.14	0.15	0.14	0.18	0.16	0.14	0.15
Cr_2O_3	0.02	0.03	0.01	0.2	0.06	0.05	0.02	0.01	0	0.02
NiO	0.36	0.31	0.34	0.34	0.36	0.31	0.28	0.38	0.37	1.35
Total	**100.95**	**99.56**	**100.43**	**98.13**	**100.35**	**101.61**	**100.06**	**101.37**	**100.56**	**101.45**

Olivine

Na_2O	0	0	0.02	0	0	0	0	0.02	0.03	0.02
MgO	47.9	47	47.16	47.48	46.93	48.56	48.48	50.3	47.76	45.99
Al_2O_3	0.06	0.01	0.23	0.03	0.13	0	0.02	0.07	0.03	0.01
SiO_2	40.75	40.96	40.67	40.96	41.15	41.21	40.62	39.72	40.72	41.07
K_2O	0	0	0	0	0	0	0	0	0.01	0
CaO	0.1	0.06	0.04	0.08	0.55	0.02	0.12	0.03	0.03	0.03
TiO_2	0.01	0	0	0.01	0.03	0	0.02	0.02	0	0
FeO	10.74	11.13	10.74	10.05	9.9	9.82	11.34	10.73	10.46	10.34
MnO	0.14	0.16	0.19	0.17	0.14	0.14	0.17	0.2	0.16	0.17
Cr_2O_3	0.01	0.02	0	0.02	0.06	0.03	0.01	0	0.04	0.01
NiO	0.39	0.27	0.27	0.26	0.25	0.35	0.3	0.37	0.44	0.25
Total	**100.1**	**99.6**	**99.33**	**99.06**	**99.16**	**100.13**	**101.06**	**101.47**	**99.66**	**97.9**

Olivine					**Average**
Na_2O	0.02	0	0.01	0.03	0.01	**0.01**
MgO	48.29	46.87	47.39	45.78	44.03	**47.57**
Al_2O_3	0.01	0.15	0.34	1.05	0.98	**0.16**
SiO_2	42.2	41.09	40.56	41.24	43.02	**41.33**
K_2O	0.01	0	0	0.01	0.01	**0.00**
CaO	0.02	0.25	0.12	0.95	1.78	**0.32**
TiO_2	0.02	0	0.01	0	0.05	**0.01**
FeO	9.47	10.66	10.52	9.44	9.23	**10.06**
MnO	0.15	0.16	0.16	0.13	0.11	**0.15**
Cr_2O_3	0.01	0.07	0.07	0.09	0.06	**0.02**
NiO	0.38	0.29	0.45	0.32	0.31	**0.36**
Total	100.59	99.54	99.61	99.03	99.58	**100.00**

Peridotite
Wallrock Minerals
Diopside

Na_2O	0.02	0.02	0.05	0.1	0.01	0.02	0.04	0.04	0.03	0.01
MgO	26.07	24.53	25.12	23.58	23.36	23.21	26.37	26.71	16.55	17.44
Al_2O_3	1.72	0.36	1.6	1.85	0.64	0.61	0.73	1.13	0.09	0.12
SiO_2	55.69	56.38	54.96	54.79	56.34	55.98	55.85	55.62	55.6	55.27
K_2O	0	0	0	0	0	0	0	0.01	0	0
CaO	13.83	15.6	13.91	15.51	15.85	16.41	12.7	11.98	26.12	26.16
TiO_2	0.04	0.03	0.04	0.03	0.05	0.02	0.05	0.05	0.02	0.05
FeO	3	2.95	3.15	3.27	2.86	2.85	3.36	3.44	2.89	1.28
MnO	0.07	0.08	0.1	0.11	0.07	0.07	0.08	0.09	0.04	0.01
Cr_2O_3	0.16	0.01	0.07	0.15	0.1	0.04	0.54	0.14	0.01	0
NiO	0.1	0.09	0.1	0.07	0.09	0.12	0.19	0.09	0.02	0.03
Total	**100.7**	**100.05**	**99.11**	**99.47**	**99.38**	**99.34**	**99.9**	**99.31**	**101.37**	**100.38**

Diopside

Na_2O	0.02	0	0	0.02	0.03	0.02	0.02	0.06	0.1	0.03
MgO	15.7	48.78	47.5	20.46	20.8	12.6	13.69	23.86	23.95	24.02
Al_2O_3	0.19	0.01	0.13	0.44	0.46	0.24	0.64	0.67	1.94	0.45
SiO_2	53.95	41.04	40.66	55.92	55.17	53.32	53.33	58.07	57.73	59.86
K_2O	0	0	0	0.01	0.01	0	0	0.01	0.01	0
CaO	25.57	0.11	0.33	21.39	21.52	25.22	25.58	12.74	12	12.18
TiO_2	0.02	0.01	0.02	0.05	0.05	0.02	0.01	0.02	0.05	0.05
FeO	5.19	9.56	10.82	2.03	2.14	9.73	8.3	2.68	2.8	2.85
MnO	0.09	0.12	0.17	0.08	0.08	0.33	0.17	0.08	0.09	0.11
Cr_2O_3	0.01	0	0	0.03	0.02	0.02	0.02	0.01	0.02	0.03
NiO	0.04	0.3	0.32	0.08	0.08	0.02	0.03	0.09	0.08	0.06
Total	**100.78**	**99.93**	**99.95**	**100.51**	**100.36**	**101.52**	**101.8**	**98.29**	**98.75**	**99.66**

Diopside				**Average**
Na_2O	0.03	0.05	0.01	0	**0.03**
MgO	16.71	16.07	17.62	16.77	**22.98**
Al_2O_3	0.15	0.14	0.1	1.14	**0.65**
SiO_2	54.04	52.91	54.73	54.19	**54.23**
K_2O	0.01	0.04	0.01	0	**0.00**
CaO	25.85	25.65	26.27	26.3	**17.87**
TiO_2	0.07	0.01	0	0.01	**0.03**
FeO	3.28	3.05	1.3	2.53	**3.97**
MnO	0.08	0.05	0.02	0.05	**0.09**
Cr_2O_3	0	0	0	0.02	**0.06**
NiO	0.01	0.02	0.02	0	**0.09**
Total	**100.24**	**98**	**100.08**	**101.02**	**100.00**

Peridotite

Wallrock Minerals

Chlorite

Na_2O	0.06	0.04	0.06	0.05	0.04	0.03	0.1	0.05	0.05	0.04
MgO	32.17	26.66	28.02	27.87	26.07	27.09	30.27	30.27	26.07	26.67
Al_2O_3	14.89	18.37	19.82	18.7	22.31	20.28	17.59	19.37	21.44	21.72
SiO_2	35.71	31.16	28.42	32.54	35.19	30	35.13	33.27	30.51	30.56
K_2O	0.01	0.02	0.03	0.02	0.01	0	0.02	0.01	0.02	0.01
CaO	0.15	0.23	0.22	0.38	0.33	0.16	0.32	0.21	0.35	0.27
TiO_2	0.03	0.02	0.03	0.01	0.01	0	0.04	0.07	0.03	0.02
FeO	2.61	7.83	7.55	7.17	9.26	8.96	3.43	2.97	8.07	7.98
MnO	0	0.03	0.03	0.04	0.08	0.04	0.02	0.02	0.03	0.02
Cr_2O_3	1.6	0.08	0.02	0.04	0.01	0.02	0.25	0.03	0	0.03
NiO	0.16	0.12	0.1	0.1	0.1	0.15	0.13	0.16	0.13	0.08
Total	**87.38**	**84.56**	**84.32**	**86.91**	**93.41**	**86.74**	**87.28**	**86.44**	**86.68**	**87.4**

Chlorite

Na_2O	0.04	0.05	0.04	0.05	0.03	0.05	0.05	0.03	0.07	0.03
MgO	26.84	27.73	28.52	30.38	30.44	30.15	29.84	31.82	33.15	33.14
Al_2O_3	22.12	21.58	21.92	17.26	18.5	16.09	17.09	19.16	14.98	15.14
SiO_2	30.15	30.95	30.44	35.16	32.53	36.18	33.71	32.21	35.22	35.06
K_2O	0.01	0.01	0.02	0.01	0.01	0.01	0.01	0.01	0.01	0
CaO	0.27	0.32	0.29	0.65	0.22	1.23	0.32	0.11	0.16	0.04
TiO_2	0.03	0.03	0.05	0.05	0.03	0.03	0.04	0.03	0.04	0.04
FeO	7.12	6.29	5.92	3.21	3.86	3.77	4.25	2.62	2.42	2.36
MnO	0.04	0.02	0.02	0.02	0.01	0.02	0.02	0.02	0.03	0.01
Cr_2O_3	0	0.08	0.13	0.17	0.37	0.01	0.49	0.2	0.33	0.3
NiO	0.12	0.09	0.1	0.12	0.15	0.14	0.18	0.19	0.18	0.16
Total	**86.74**	**87.16**	**87.45**	**87.08**	**86.14**	**87.68**	**86.01**	**86.4**	**86.6**	**86.28**

Chlorite			**Average**
Na_2O	0.01	0.03	**0.05**
MgO	31.51	30.73	**29.34**
Al_2O_3	19.76	19.08	**18.96**
SiO_2	32.08	33.02	**32.69**
K_2O	0.01	0.01	**0.01**
CaO	0.04	0.06	**0.29**
TiO_2	0.04	0.04	**0.03**
FeO	2.94	2.96	**5.16**
MnO	0	0.01	**0.02**
Cr_2O_3	0.13	0.14	**0.20**
NiO	0.19	0.17	**0.14**
Total	**86.71**	**86.25**	**86.89**

Peridotite

Wallrock Minerals

Tremolite

Na_2O	0.04	0.02	0.02	0.02	0.03	0.02	0.03	0.06	0.05	0.04
MgO	24.08	23.18	22.95	23.25	23.52	23.47	23.41	23.56	24.35	22.42
Al_2O_3	0.5	0.22	0.21	0.24	0.19	0.18	0.22	0.59	0.6	0.15
SiO_2	58.14	58.4	58.37	58.55	58.79	58.56	58.47	57.51	57.91	57.51
K_2O	0.01	0.01	0.01	0	0	0	0.01	0	0.01	0
CaO	12.22	13.28	13.37	13.43	14.2	13.37	13.12	12.36	12.51	13.22
TiO_2	0.05	0.05	0.07	0.03	0.05	0.04	0.07	0.04	0.04	0.04
FeO	2.34	2.09	2.42	2.17	2.59	2.04	2.2	2.61	2.24	1.82
MnO	0.08	0.05	0.04	0.06	0.04	0.06	0.05	0.08	0.07	0.03
Cr_2O_3	0.14	0.02	0.01	0.04	0.02	0.01	0.04	0.13	0.06	0.04
NiO	0.04	0.08	0.09	0.12	0.08	0.09	0.08	0.08	0.06	0.06
Total	**97.62**	**97.4**	**97.56**	**97.92**	**99.54**	**97.82**	**97.69**	**97**	**97.89**	**95.32**

Tremolite

Na_2O	0.06	0.02	0.05	0.05	0.02	0.03	0.06	0.05	0.04	0.04
MgO	25.33	22.73	23.6	23.93	23.2	22.37	21.58	23.65	23.85	23.75
Al_2O_3	5.63	0.24	1.7	2.06	0.49	0.41	0.74	0.42	0.28	0.6
SiO_2	52.38	58.63	57.13	56.12	59.24	59.12	56.31	58.88	59.58	59.09
K_2O	0.01	0	0.01	0	0	0.01	0	0	0.01	0
CaO	8.71	13.34	11.97	11.78	12.85	13.74	15.34	13.02	13.21	12.91
TiO_2	0.04	0.01	0.06	0.04	0.02	0.01	0.02	0.05	0.03	0.02
FeO	2.72	3.21	2.74	2.77	2.45	2.53	3.2	2.24	2.17	2.02
MnO	0.06	0.08	0.06	0.05	0.06	0.02	0.06	0.07	0.05	0.06
Cr_2O_3	0.11	0.01	0.28	0.08	0.05	0	0.01	0	0.02	0.09
NiO	0.15	0.16	0.12	0.06	0.11	0.18	0.15	0.09	0.11	0.1
Total	**95.19**	**98.42**	**97.72**	**96.96**	**98.51**	**98.42**	**97.48**	**98.46**	**99.36**	**98.68**

Tremolite					**Average**
Na_2O	0.03	0.05	0.05	0.04	0.07	**0.04**
MgO	27.49	23.58	24.39	25.42	31.82	**24.04**
Al_2O_3	0.34	0.46	1.33	0.84	1.66	**0.81**
SiO_2	54.09	59.07	59.08	52.19	49.8	**57.32**
K_2O	0.01	0.01	0.01	0	0.01	**0.01**
CaO	10.94	13	11.47	10.96	7.02	**12.45**
TiO_2	0.02	0.06	0.05	0.07	0.06	**0.04**
FeO	3.49	2.15	2.27	3.44	5.43	**2.61**
MnO	0.08	0.08	0.1	0.1	0.14	**0.07**
Cr_2O_3	0.06	0.33	0.16	0.53	0.25	**0.10**
NiO	0.1	0.06	0.08	0.06	0.14	**0.10**
Total	**96.65**	**98.84**	**98.99**	**93.64**	**96.41**	**97.58**

Peridotite
PST
Glass

Na_2O	0.02	0.01	0.02	0.02	0.02	0.04	0.02	0.01
MgO	32.7	32.27	31.36	32.14	31.55	31.76	31.53	33.7
Al_2O_3	12.81	11.79	13.77	13.94	13.96	11.45	11.84	13.08
SiO_2	36.86	36.53	35.25	36.11	36.55	42.3	39.77	35.55
K_2O	0.01	0.01	0.01	0.02	0.02	0.03	0.02	0.01
CaO	0.25	0.19	0.09	0.27	0.28	0.62	0.48	0.08
TiO_2	0.08	0.22	0.16	0.34	0.29	0.05	0.09	0.41
FeO	2.67	2.73	2.92	3	3.1	2.91	2.59	3.1
MnO	0	0.01	0.02	0.02	0.02	0.03	0.01	0.03
Cr_2O_3	0.27	0.7	0.33	0.41	0.67	0.31	0.24	0.51
NiO	0.17	0.17	0.16	0.2	0.19	0.14	0.19	0.16
Total	**85.84**	**84.65**	**84.09**	**86.47**	**86.64**	**89.65**	**86.78**	**86.65**

Glass			**Average**
Na_2O	0.01	0.06	**0.02**
MgO	31.8	30.95	**31.98**
Al_2O_3	13.21	9.94	**12.58**
SiO_2	37.12	44.5	**38.05**
K_2O	0.02	0.03	**0.02**
CaO	0.3	1.1	**0.37**
TiO_2	0.2	0.04	**0.19**
FeO	3.08	2.59	**2.87**
MnO	0.03	0.01	**0.02**
Cr_2O_3	0.61	0.31	**0.44**
NiO	0.21	0.12	**0.17**
Total	**86.59**	**89.67**	**86.70**

Peridotite

PST

Olivine								**Average**
Na_2O	0.07	0.03	0	0.01	0.01	0.01	0.01	**0.02**
MgO	49.22	49.14	43.17	48.72	49.53	40.91	48.28	**47.00**
Al_2O_3	0.1	0.12	1.17	0.1	0.04	1.58	0.04	**0.45**
SiO_2	41.58	41.53	45.88	42.02	41.59	49.16	41.51	**43.32**
K_2O	0.01	0	0	0	0.01	0.01	0	**0.00**
CaO	0.13	0.13	0.7	0.24	0.08	1.03	0.07	**0.34**
TiO_2	0.02	0.01	0.02	0	0.01	0	0.01	**0.01**
FeO	8.66	8.71	7.43	8.53	8.56	6	9.56	**8.21**
MnO	0.1	0.1	0.1	0.11	0.1	0.09	0.12	**0.10**
Cr_2O_3	0.05	0.05	0.49	0.02	0.02	1.22	0.04	**0.27**
NiO	0.31	0.34	0.26	0.36	0.32	0.22	0.37	**0.31**
Total	**100.26**	**100.15**	**99.22**	**100.11**	**100.28**	**100.23**	**100.02**	**100.04**

Diopside			**Average**
Na_2O	0.02	0.02	**0.02**
MgO	27.07	27.67	**27.37**
Al_2O_3	4	0.71	**2.36**
SiO_2	53.5	56.82	**55.16**
K_2O	0	0	**0.00**
CaO	11.12	10.95	**11.04**
TiO_2	0.08	0.07	**0.08**
FeO	3.55	3.59	**3.57**
MnO	0.06	0.08	**0.07**
Cr_2O_3	0.17	0.13	**0.15**
NiO	0.11	0.11	**0.11**
Total	**99.67**	**100.16**	**99.92**

Enstatite											**Average**
Na_2O	0.04	0	0	0.02	0.02	0.02	0.09	0.01	0.02	0.17	**0.04**
MgO	28.47	34.98	33.57	34.14	39.83	38.31	36.29	38.84	38.16	33.57	**35.62**
Al_2O_3	2.4	1.16	3.19	2.46	1.84	1.8	2.3	1.84	2	4.64	**2.36**
SiO_2	54.78	58.64	52.57	50.82	48.96	50.05	51.19	50.13	49.41	45.51	**51.21**
K_2O	0	0	0.01	0	0	0.01	0	0.01	0	0.01	**0.00**
CaO	9.89	3.13	2.77	5.5	1.13	2.4	2.72	1.39	2.25	6.34	**3.75**
TiO_2	0.1	0.01	0.05	0.05	0.02	0.03	0.04	0.01	0.04	0.14	**0.05**
FeO	3.62	2	6.26	6.61	7.12	6.7	6.33	6.14	6.52	5.76	**5.71**
MnO	0.09	0.04	0.13	0.11	0.11	0.09	0.1	0.1	0.1	0.08	**0.10**
Cr_2O_3	0.63	0.11	0.97	0.86	0.75	0.8	0.95	0.97	0.6	0.3	**0.69**
NiO	0.11	0.15	0.15	0.21	0.22	0.21	0.17	0.24	0.21	0.23	**0.19**
Total	**100.12**	**100.24**	**99.67**	**100.79**	**99.98**	**100.43**	**100.19**	**99.68**	**99.32**	**96.73**	**99.72**

Supplementary Material

Evidence for Large Subduction Earthquakes along the fossil MOHO in Alpine Corsica

Torgeir B. Andersen[1*], Håkon Austrheim[2], Natalie Deseta[3], Lewis D. Ashwal[3] and Petter Silkoset[1]

[1]Centre of Earth Evolution and Dynamics [2]Physics of Geological Processes, University of Oslo, P.O. Box 1048, Blindern 0316 Oslo Norway

[3]School of Geosciences, University of Witwatersrand, Wits 2050 Johannesburg, South Africa

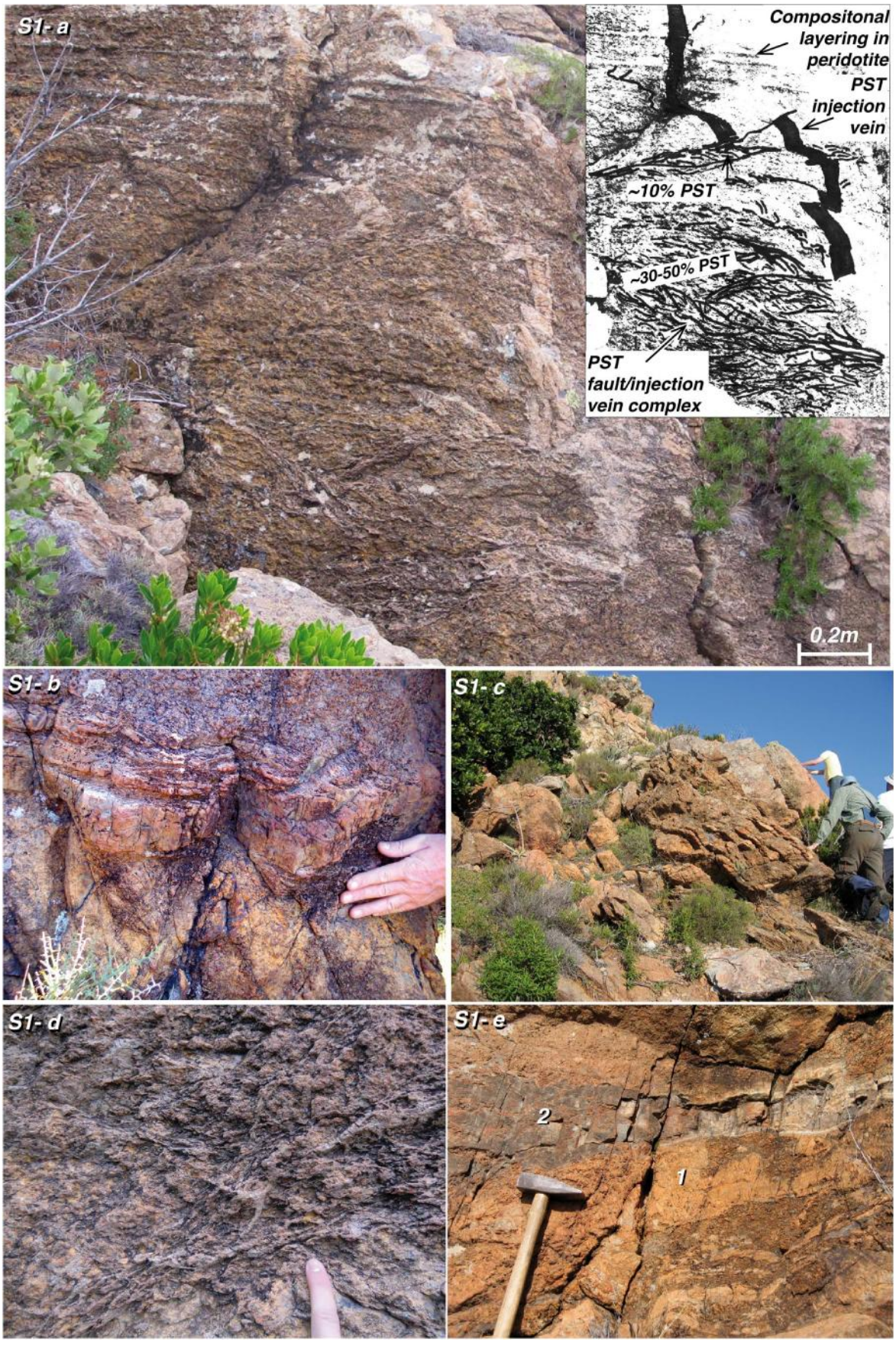
**Correspondence to: t.b.andersen@geo.uio.no*

Supplementary figures:

The supplementary material, figures, S1a-g, S2a-d and S3 a-b are included as backup and documentation for the interpretations presented in the main text. S1 shows evidence for the generation of large volumes of pseudotachylyte in at most a few large rupture events along the main Moho fault zone. All pictures are from the mantle peridotite in the footwall of the fault.

S2 shows detailed pseudotachylyte textures in micrographs and documents that mantle peridotite as well as the crustal gabbro melted and quenched and also supports previously published interpretations that there was ductile deformation as a precursor to faulting (S2d).

S3 provide additional information regarding the post-faulting shearing and shows that the main Moho fault has been partially reactivated as a blueschist facies shear zone.


S1- a
Compositonal layering in peridotite
PST injection vein
~10% PST
~30-50% PST
PST fault/injection vein complex
0,2m
S1- b
S1- c
S1- d
S1- e
2
1

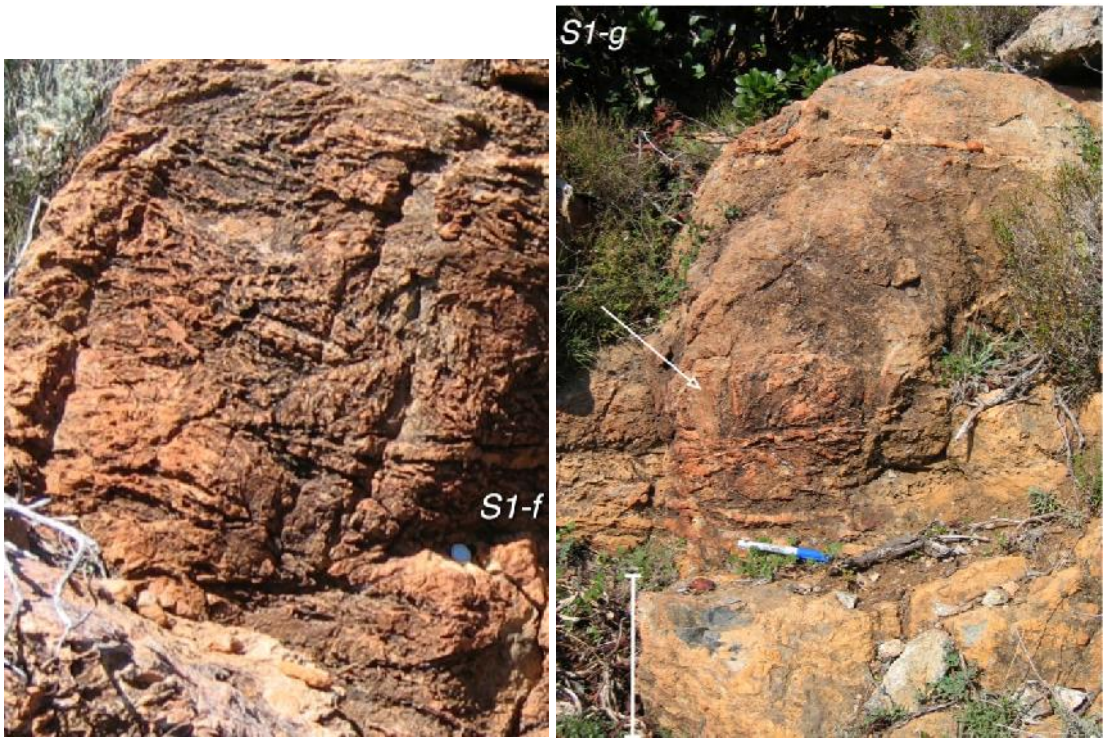


Fig. S1-a: A 1.9 m cliff-face at Locality 2 below Punta di Muzzelli in mantle peridotite with compositional layers (top) penetrated by a dense network of pseudotachylyte fault and injection veins (highlighted in line drawing top right). Notice the near vertical, thick (up to 0.2 m) cross-cutting but rootless ultramafic PST injection vein, which possibly record a secondary major melt-generating event.

Fig. S1-b and c: Major Moho-parallel fault and damage zone below the main Moho fault at Locality 1 (Fig.1) in Fig. 1. The single rupture fault-vein in b is ~0.4m thick and is found in the center of the 2 to 3m wide fault damage zone shown in S1-c.

Fig. S1-d: Intense pseudotachylyte net-vein/breccia in from the main MOHO fault zone at Locality 2. More that 50% of the rock is ultramafic pseudotachylyte formed by 100% melting of the mantle. There is no obvious hierarchy of the PST veins in this outcrop.

Fig. S1-e: Cliff-face, 50 m below the Moho fault at Locality 1, with 2 stages (marked 1 and 2) of thick (up to 42 cm thick) ultramafic pseudotachylyte injection veins. Hammerhead is 0.14 m long

Fig. S1-f: Pseudotachylytes without obvious hierarchy of veins in peridotite at the main Moho fault. We interpret these veins to have formed in one pseudotachylyte-

forming rupture event. Total thickness seen in outcrop is ~0.7 m (2 Euro coin for scale).

Fig. S1-g: Details from a several meter thick fault strand (also shown in S1-c) in the Moho fault damage zone at locality 1 (Fig.1, main text). The star-shaped (arrowed) pattern of radiating melt-veins apparently formed by a single stage explosive expulsion of ultramafic pseudotachylyte into the wall rock. Notice the more than 30 cm (vertical scale bar) massive pseudotachylyte fault vein at the base of the section and the prominent injection vein near the top of the outcrop.

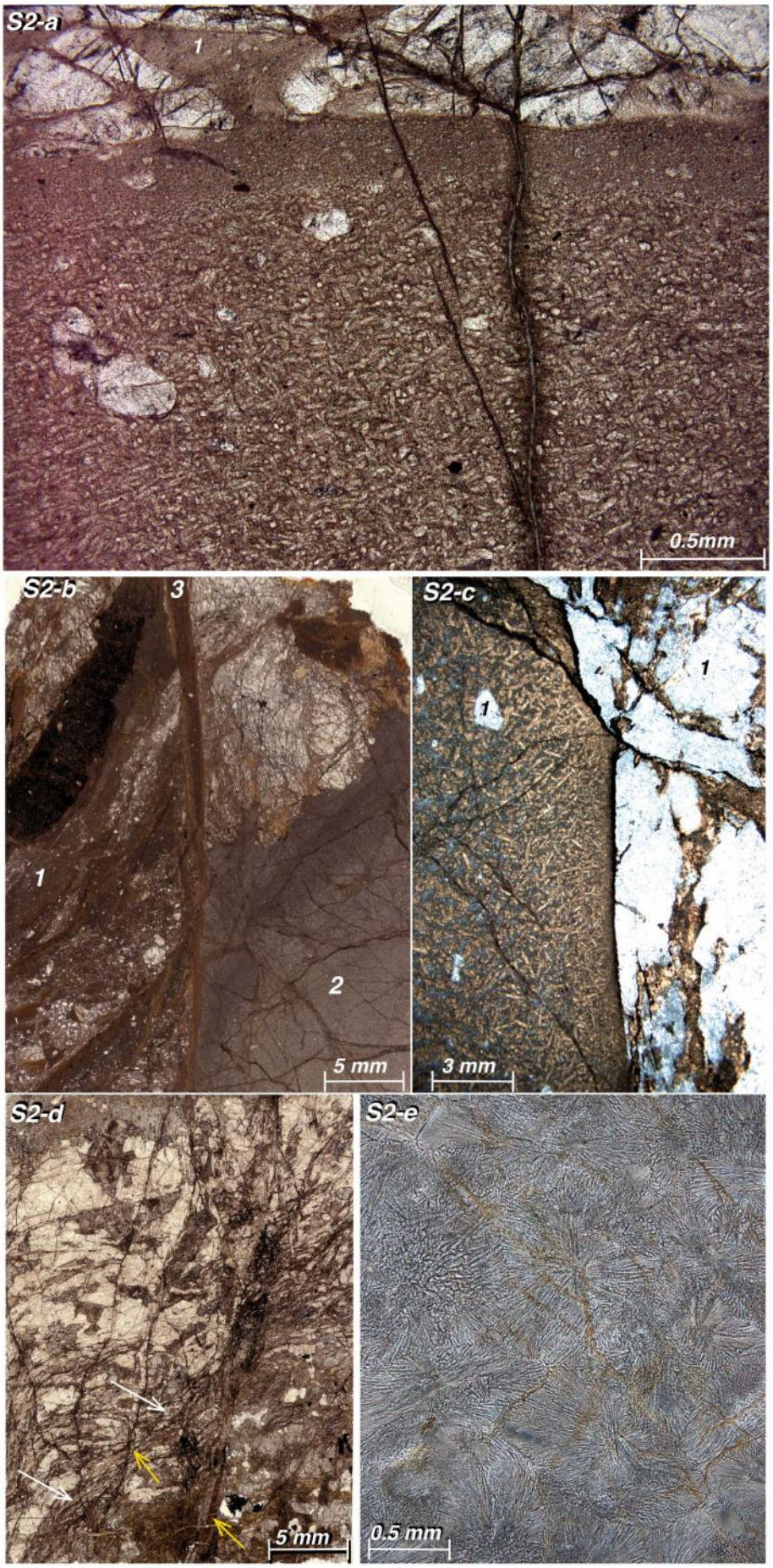

S2-a
1
0.5mm
S2-b
3
1
2
5 mm
S2-c
1
1
3 mm
S2-d
5 mm
S2-e
0.5 mm

Fig. S2-a: Photomicrograph (parallel light) of ultramafic pseudotachylyte showing chilled glassy margin and minor injection veins (top), and thermally rounded olivine wall-rock fragments. Small needle shaped and aligned diopside crystals are defining a vague flow during quenching of the melt.

Fig. S2-b: 3 stages of faulting (1 & 3) and injection (2) of pseudotachylyte near the Moho fault. Notice strong deformation of the peridotite wall rock and the preserved chilled margin (darker) in the injection vein marked 2.

Fig. S2-c: Statically hydrated pseudotachylyte where original olivine in the wall rock and the fragments marked 1 are all altered to serpentine. The needle shaped diopside crystals defining the chilled margin similar to (S2-a) are also altered but the quench texture is preserved through static hydration and recrystallization after faulting.

Fig. S2-c: Small pseudotachylyte veins (yellow arrows) truncating ductile fabric (white arrows) in the peridotite.

Fig. S2-d: Pseudotachylyte quench texture with dendritic spherulites of omphacite formed after 100% melting and quenching of gabbro.



Fig. S3-a: The reworked Moho-fault at locality 1 (Fig. 1) showing large orange weathering fragments of pseudotachylyte veins (below overhang) in a blueschist facies mylonitic matrix.

Fig. S3-b: Detail from the same zone showing 7 x 28 cm lozenge shaped fragment of pseudotachylyte in the mylonitic matrix, which also contains numerous small PST fragments.

Tectonophysics 610 (2014) 138–149

Contents lists available at ScienceDirect

Tectonophysics

journal homepage: www.elsevier.com/locate/tecto

A weakening mechanism for intermediate-depth seismicity? Detailed petrographic and microtextural observations from blueschist facies pseudotachylytes, Cape Corse, Corsica

N. Deseta [a,*], T.B. Andersen [b], L.D. Ashwal [a]

[a] Department of Geosciences, University of the Witwatersrand, Private Bag 3, 2050 Johannesburg, South Africa
[b] Department of Geosciences, CEED, University of Oslo, PO Box 1047, Blindern, 0316 Oslo, Norway

ARTICLE INFO

Article history:
Received 9 July 2013
Received in revised form 16 October 2013
Accepted 3 November 2013
Available online 12 November 2013

Keywords:
Shear localisation
Intermediate-depth earthquakes
Pseudotachylyte
blueschist

ABSTRACT

Gabbro- and peridotite-hosted pseudotachylytes from the Alpine Schistes Lustres Unit in Corsica, previously determined to have formed at blueschist to lawsonite-eclogite facies conditions, have been causally linked to the generation of intermediate-depth earthquakes, which occur at depths of 50–300 km. Detailed petrographic and microtextural analyses of these pseudotachylytes suggest that their initiation may be controlled by a thermally-activated shear runaway process that is controlled by rheology rather than mineralogy. This is documented by sheared out, prolate, kinked and twinned wallrock clasts that have been peeled off and entrained into the pseudotachylyte vein as sigmoid survivor clasts. The presence of metastable high temperature crystallisation products in the pseudotachylyte, such as hoppers and dendrites of olivine, enstatite and diopside (peridotite) and Al-rich omphacite and Fe-rich anorthite in metagabbro, are suggestive of a short-lived high-temperature event resulting from thermal instability. These high temperature mineral assemblages are overprinted by ones indicating a return to ambient conditions of lower temperatures, but still high pressures: glaucophane, albite and epidote in metagabbro and clinochlore; and fine-grained granoblastic olivine, enstatite and diopside in peridotite. The observations from this detailed study of natural samples suggest that intermediate-depth seismicity may be generated by a thermal runaway process.

© 2014 Elsevier B.V. All rights reserved.

1. Introduction

The initiation of intermediate-depth earthquakes has long been a subject of debate. These phenomena occur at depths from 50 km to 350 km, which, due to high confining pressures, preclude traditional brittle failure (Green and Houston, 1995; Hacker, 2003; Jung et al., 2004; Ogawa, 1987). In order to address this problem researchers have put forth several hypotheses, which include dehydration embrittlement, transformational faulting and thermal runaway processes. These hypotheses can be divided into brittle — (solid-state dehydration embrittlement and transformational faulting) and crystal-plastic — (shear-heating and thermal runaway) controlled processes. These models are based on experimental, numerical and geophysical modelling, with no field observations and little work on natural samples (Green and Houston, 1995; Hacker, 2003; John et al., 2009; Kelemen and Hirth, 2007; Ogawa, 1987). In the past two decades however, several discoveries of high pressure pseudotachylytes associated with intermediate-depth earthquakes have been made (Austrheim and Boundy, 1994; Jin et al., 1998; John and Schenk, 2006; Kanamori et al., 1998), providing researchers with natural material with which to evaluate previous models. This paper presents detailed petrographic and microstructural observations of peridotite- and metagabbro-hosted pseudotachylytes associated with subduction zone seismicity, in the Cima di Gratera area of Cap Corse, Corsica. Previous work suggests that faulting and pseudotachylyte generation took place during subduction at blueschist to lawsonite-eclogite facies conditions under pressures of 1.8–2.6 GPa (Austrheim and Andersen, 2004; Andersen and Austrheim, 2006; Ravna et al., 2010; Vitale Brovarone et al., 2011). A detailed discussion on the geochemistry of these rocks and the role that water plays in earthquake generation will be addressed in a separate paper.

2. Geological setting

The study area is located on the SSW side of Cima di Gratera, Cape Corse, northern Corsica (Fig. 1). The pseudotachylytes, first described by Austrheim and Andersen (2004), occur within lenses of gabbro and mantle peridotite enclosed by serpentinite (Fig. 2). These rocks form part of the Schistes Lustres Complex (part of the Alpine age high pressure–low temperature subduction complex), and which has been interpreted as either nappes of exhumed Ligurian oceanic lithosphere, which have slivers of crystalline continental material, or hyper-stretched continental lithosphere interleaved with mantle imbricates (Agard et al., 2002; Beccaluva et al., 1977; Jolivet, 1993; Mohn et al., 2009; Vitale Brovarone et al., 2011). This rock package was thrust onto

* Corresponding author.
E-mail address: suridae@gmail.com (N. Deseta).

0040-1951/$ – see front matter © 2014 Elsevier B.V. All rights reserved.
http://dx.doi.org/10.1016/j.tecto.2013.11.007

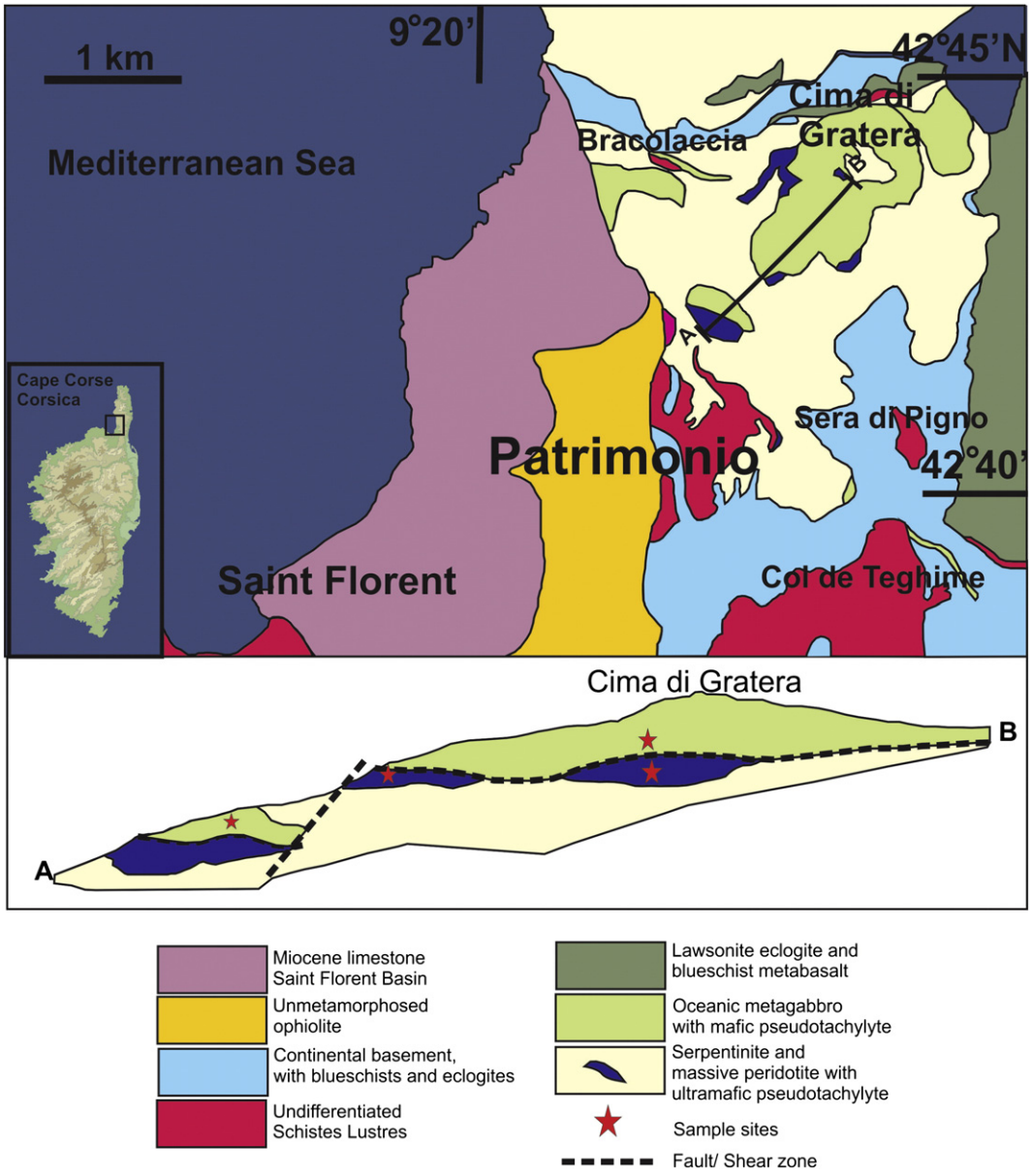


Fig. 1. Simplified geological map of the study area in Cima di Gratera. Modified after Andersen and Austrheim (2006).

the continental margin of Europe during the Late Cretaceous to Tertiary Periods (Fig. 1) (Jolivet, 1993).

The metagabbros are compositionally uniform and encompass a range of igneous textures marked by differences in grain size. Common textures are cumulate layering and the interfingering of irregularly shaped domains of fine- and coarse-grained gabbro. Conversely, the peridotites are relatively uniform in terms of composition, texture and grain size. The pseudotachylyte-bearing fault rocks have been partially metamorphosed to blueschist and greenschist facies only in patches, except within the shear zones where the metamorphic reactions are fully equilibrated. The pseudotachylytes occur within the pristine lenses of gabbro and peridotite that are relatively undeformed and least affected by the regional HP–LT metamorphism (Andersen and Austrheim, 2006).

2.1. Field observations

In outcrop the pseudotachylytes typically have a positive relief with respect to the host rocks. The pseudotachylyte veins weather to a rust-red colour but on fresh surfaces are black-grey and aphanitic (Fig. 2). Comminuted wallrock clasts and flow banding are commonly observed. In the peridotite, the pseudotachylytes occur in two sets that extend for up to 1 km: a sub-vertical set and a sub-horizontal set. Within the vein sets the pseudotachylytes form complex vein networks that over-print and re-inject one another, indicating multiple generations of pseudotachylyte (Fig. 2). In the peridotite, the pseudotachylyte veins occasionally form radial 'explosive' networks. These veins are thicker than other injection or fault veins and contain more re-injections and comminuted wallrock material (Fig. 2b). In contrast with the peridotite-hosted veins, those in the gabbro are thinner and more discrete, commonly (but not always) occurring along the boundary between the very coarse-grained (<15 mm) metagabbro and fine-grained (<2 mm) metagabbro (Fig. 2). The peridotite pseudotachylytes show cross-cutting relationships with serpentinised host rocks, which have been entrained into the veins as sigmoidal lozenges, indicating a brittle–ductile overprint relationship. In the metagabbro fault rock, the pseudotachylytic crystallisation products (glaucophane) have formed CPO (crystallographic preferred orientation) fabrics and contain boudinaged wallrock clasts, indicating a ductile overprint post-dating pseudotachylyte generation (Fig. 12) (Andersen and Austrheim, 2006). Many of the pseudotachylytes are cut by later serpentine veins and show a hydration

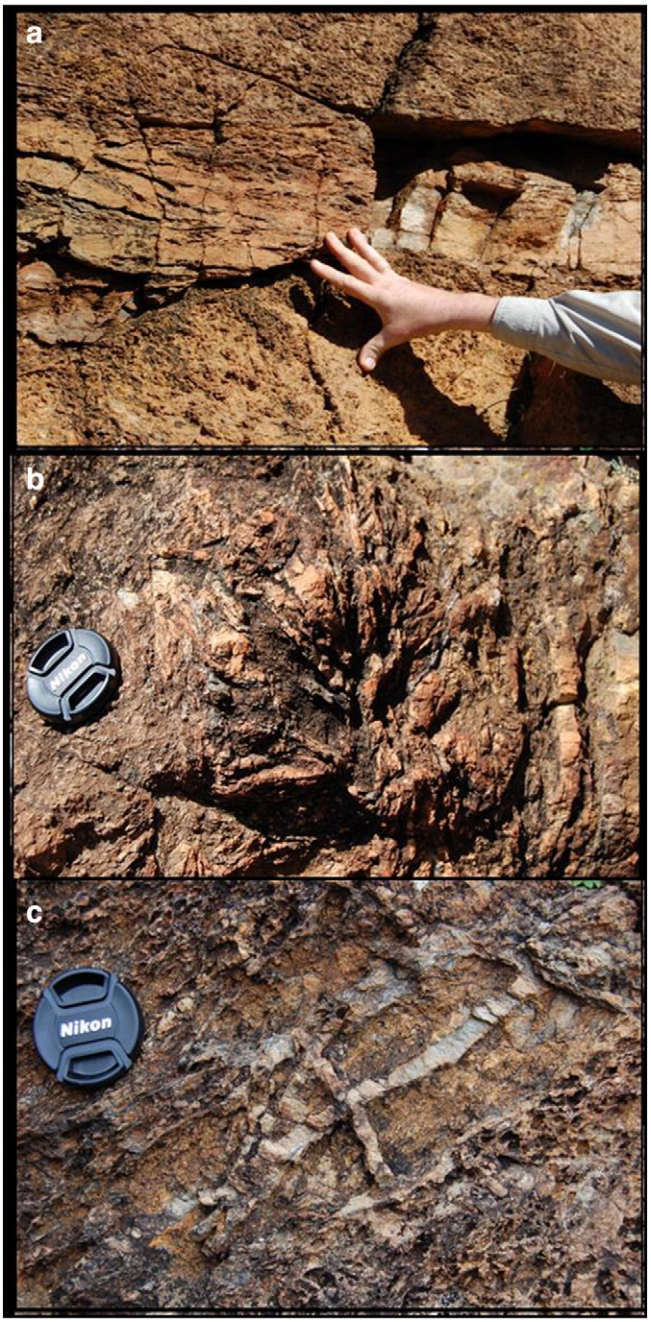


Fig. 2. Photographs of pseudotachylyte hosted by peridotite. Panel a shows one of the thickest (up to 25 cm) pseudotachylyte fault veins observed in the field. The thickness of this vein is principally due to multiple generations of pseudotachylyte that have nucleated along the same plane. (b) Explosive network veining of pseudotachylytes that radiate in all directions away from the centre of the fault plane. (c) Cross-cutting relationships of pseudotachylyte self-injecting.

overprint. Care was taken to analyse only pristine, unaltered pseudotachylytes.

3. Materials and methods

Detailed thin section petrography and back-scatter electron (BSE) imaging for mineral identification and microtextural analysis were done on both gabbro- and peridotite-hosted pseudotachylyte. Electron microprobe analyses were conducted using a Cameca SX-100 instrument at Spectrau Laboratory, University of Johannesburg, South Africa. Analyses of the bulk matrix (wide beam (10 μm) and narrow (1 μm)), wallrock, entrained minerals as well as crystallisation products (glass and crystallites) were done. The beam current was reduced to minimise sodium loss on glass, but tests on higher currents showed loss to be negligible. Analyses were run at 20 kV, 10 nA. The reference standard used was a Ni-bearing glass. Refer to Merlet (1994) for more detailed operating parameters.

4. Petrographic and microtextural observations

Detailed petrographic microtextural analyses were carried out on the pseudotachylyte and the adjacent wallrock in both the metagabbro and peridotite in order to ascertain the rheological behaviour of the rock at the time of fusion. Features of the host rocks and microtextures common to both rock types will be discussed in the first section, followed by those characteristic to only the metagabbro or the peridotite.

4.1. Metagabbro host rock

The metagabbro host rock is heterogeneous in grain size with large, irregular domains (up to approximately a metre in outcrop) of very coarse-grained (up to 15 mm) gabbro occurring in contact and interfingering with a much more fine-grained (~1 mm) gabbro. The margin between the coarse- and fine-grained domains is consistently sharp, less than 5 mm thick. Despite the large grain-size variability in the metagabbro, the constituent mineral assemblage is not significantly variable.

The primary gabbro mineralogy is largely preserved and comprises plagioclase, diopside, olivine and minor ilmenite. In thin section the gabbro adjacent to pseudotachylyte faults retains little of its original igneous texture, most of which has been transformed into an annealed granoblastic texture with poikiloblasts of olivine and diopside. Grain boundary migration and dynamic recrystallisation are common, particularly in diopside. Early greenschist facies metamorphism of the host rock has led to variable replacement and recrystallisation of diopside by actinolite, bastite and Mg-hornblende. Plagioclase alteration to sericite has also taken place, causing the grains to become cloudy and grey. Alteration of the olivine to serpentine, magnetite or iddingsite has also been observed. Post-dating the early greenschist alteration is the development of blueschist facies assemblages, which manifest in the replacement of diopside, actinolite, Mg-hornblende and plagioclase by glaucophane, barroisite, albite and epidote. Late blueschist facies metamorphism that post-dates pseudotachylyte generation at these conditions is associated with ductile deformation and pseudotachylyte recrystallisation (Fig. 12). Late retrograde metamorphism, particularly marked by serpentine veins and the presence of epidote, clinochlore and pumpellyite overprints the blueschist assemblage phase and patches of the pristine material (Fig. 13).

The early greenschist metamorphism of the host rock may be associated with seafloor hydration and/or hydration-associated fracturing in the slab bend, as well as earlier hydration associated with extensional tectonics (Mohn et al., 2009; Vitale Brovarone et al., 2011). The late greenschist metamorphic overprint has been observed in thin section and BSE images and is interpreted to be associated with hydration and faulting upon slab exhumation. This late retrograde metamorphism overprints some of the pseudotachylyte veins and is not cut by later pseudotachylyte generations (Fig. 13).

4.2. Peridotite host rock

The peridotite host rocks show gradational transitions from fine- to coarse-grained (<1 mm–7 mm) textures. The mineralogy corresponds to that of a plagioclase lherzolite with olivine > diopside > enstatite, as well as minor plagioclase and magnetite. The rocks exhibit a granoblastic texture with annealed poikiloblasts and some grain boundary migration. The diopside and enstatite commonly show exsolution lamellae of each other and twinning of the diopside and olivine has been observed.

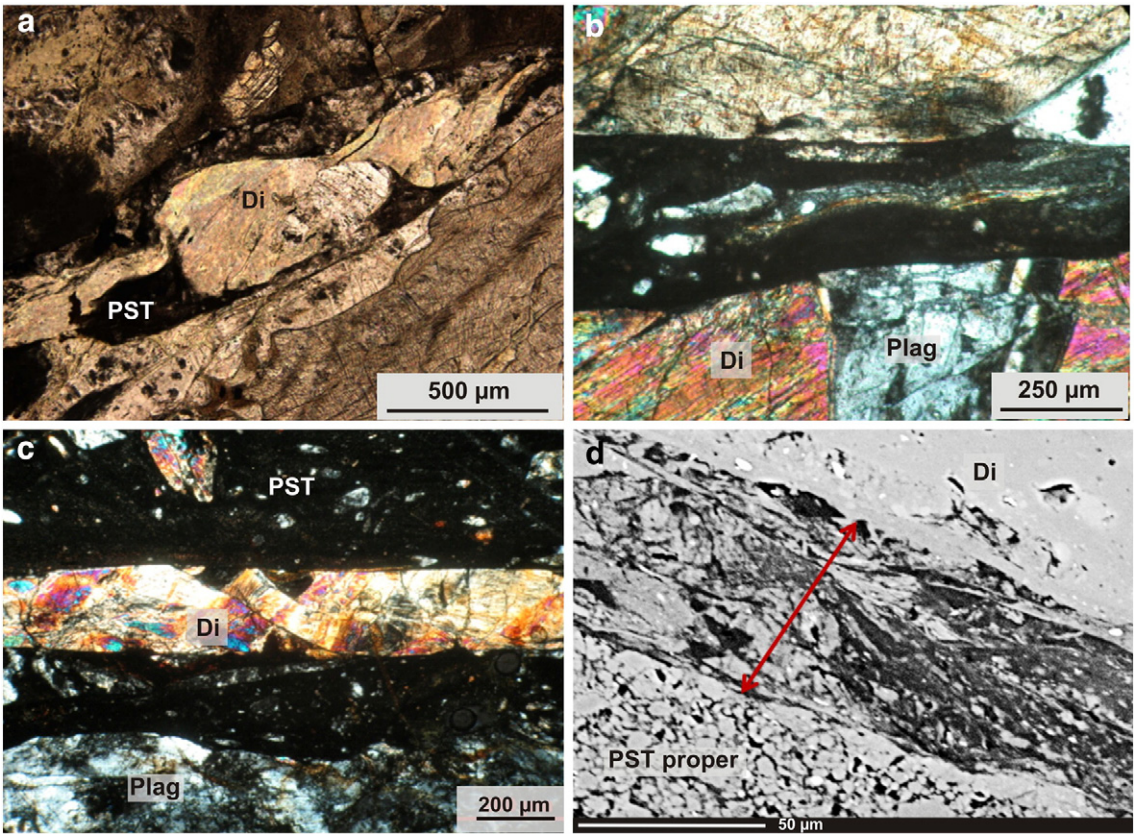


Fig. 3. Images of microstructures at fault vein boundaries in metagabbro. All these images clearly show that wallrock material at these boundaries has been subjected to crystal plastic deformation. Panel a shows a boudinaged, kink-banded diopside enclosed in a dark brown, glassy pseudotachylyte matrix. (b) Pseudotachylyte vein with entrained, boudinaged, wallrock aggregate of plagioclase and diopside. The wallrock diopside and plagioclase clearly show kinking and deformation twinning, respectively.

There is some early greenschist facies metamorphism of diopside and enstatite to fine-grained clinochlore and tremolite by dynamic recrystallisation. The clinochlore has a plumose and feathery texture. Various generations of serpentinisation (including magnetite and Cr-spinel) overprint all pre-existing features and are variably distributed throughout the rock; occasionally associated with late reactivation of pseudotachylyte veins (Fig. 12c). The peridotite shows no blueschist facies mineral assemblages; only multiple stages of early and late greenschist metamorphism are observed prior to and after the period(s) of pseudotachylyte generation. The early greenschist metamorphism has been attributed to events occurring prior to pseudotachylyte generation associated with ocean–continent hyperextension and hydrothermal alteration due to prograde subduction (Vitale Brovarone et al., 2011). The late greenschist facies metamorphism is likely associated with slab exhumation processes.

4.3. Fault vein characteristics

Fault veins form parallel to displacement surfaces in the host rock. Wallrock clasts locally underwent crystal plastic deformation in proximity to vein boundaries or melted along/with the fault plane (Fig. 3). Microscope- and BSE-based observations of the pseudotachylyte vein

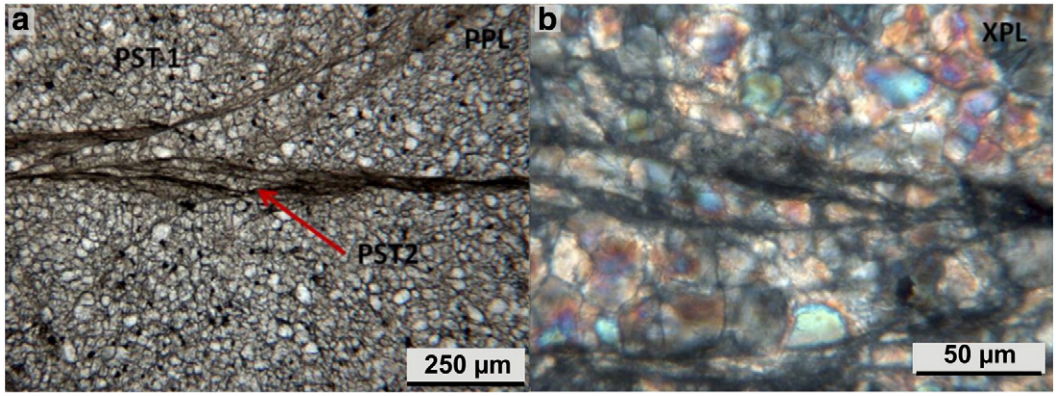


Fig. 4. Micrographs of fine-grained, recrystallized peridotite-hosted pseudotachylyte (PST 1) cut by later pseudotachylyte (PST 2). Panel b is a high magnification view with crossed nicols of where the red arrow is pointing to in panel a. In panel b the grains enclosed by the glassy black melt veins are prolate and lozenge-shaped compared to those grains not in contact with PST 2. Grain boundary migration is suggested by the grain boundary alignment of grains enclosed by fault veins. In contrast to the previous figure (Fig. 5), where coarser-grained wallrock was deformed, these photomicrographs show fine-grained recrystallised peridotite-hosted pseudotachylyte cut by a later generation of pseudotachylyte.

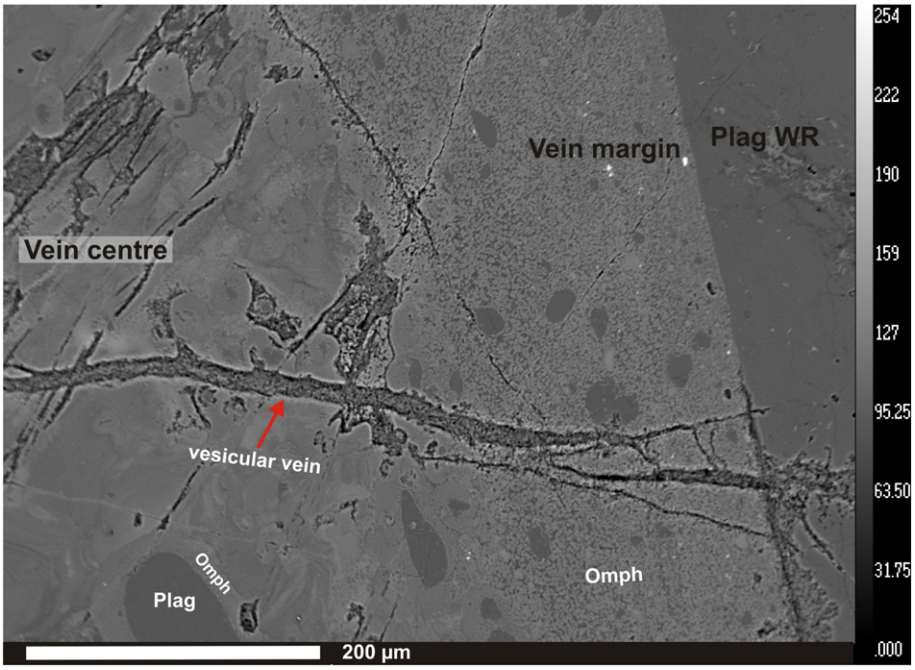


Fig. 5. BSE image of a pseudotachylyte fault vein hosted by metagabbro. The dark grey thermally rounded clasts are plagioclase upon which dendrites of omphacite have crystallised with interstitial glass. The smaller veins cross-cutting the main pseudotachylyte vein in this image, are contemporaneous with the molten pseudotachylyte, as can be seen by the lobate–cuspate boundaries enclosing the dendrites. These cross-cutting veins appear, by their low atomic numbers and low totals (on EPMA analysis) to have contained dissolved hydrous fluids that later vesiculated. Plag: plagioclase, Plag WR: Wallrock plagioclase, Omph: omphacite.

boundaries reveal a syndeformational zone in the associated wallrock that begins several grain widths from the vein 'proper'. This region is dominated by highly strained, sheared, kinked, elongate wallrock grains (Figs. 3, 6). The vein boundary is sharply cut by the pseudotachylyte and has commonly been observed to be dragged or peeled off into the vein and is surrounded by injecting melt (Fig. 3b).

Creep textures associated with the formation of the pseudotachylytes were observed in the full range of grain sizes observed in the wallrock; from 20 mm to 30 μm (Figs. 3 and 4), from shearing and kinking as seen in the coarser-grained material (Fig. 4) to what appears to be grain boundary creep in fine-grained re-crystallised pseudotachylytes that were subsequently reactivated to generate a melt (Fig. 4).

The thickness of fault veins ranges from less than 1 mm to more than 30 cm. Fault veins were typically formed by a single event. However, reactivation and multiple fusion events are exemplified by older pseudotachylyte survivor clasts entrained into younger veins (Fig. 4) and by cross-cutting relations. The lack of offset markers as well as the injection of melt into dilational fractures precludes the determination of the true dimensions of the fault zone during a single pseudotachylyte-forming event. However, due to the pristine nature of the pseudotachylyte matrices studied, we have concluded that no significant post-pseudotachylyte vein deformation occurred.

4.4. Injection vein characteristics

The injection veins are secondary pseudotachylyte veins that emanate from parent fault veins into the adjacent wallrock. Injection veins cannot in all instances be traced to their sourcing fault vein. This is due to chaotic networks of nearby multiple injection veins in proximity and arching self-injections that cross-cut one another. The veins vary widely in thickness, ranging from 200 μm, thinner than the average fault vein, to >20 cm, thicker than the average fault vein. They inject at all angles from their parent veins, from near-parallel to perpendicular. They cut between and through wallrock grains and are not associated with or dependent on precursory wallrock deformation or foliations.

4.5. Microtextures of ultracataclasite

Syndeformational ultracataclasite at the margins of coarse-grained pseudotachylyte fault veins is a common feature in both the metagabbro and peridotite host rocks. The ultracataclasite comprises a mixture of comminuted clasts, melt and plastic ribbons (Fig. 6). The size range in comminuted wallrock material is from 30 μm < 1 μm. The mineral assemblage in the ultracataclasite matches that of the adjacent wallrock. The deformation of different mineral species in the ultracataclasite appears to be determined by fracture toughness, as predicted by Spray (1992). Minerals with greater relative fracture toughness such as diopside, plagioclase, Mg-hornblende and olivine typically form the portion of comminuted grains and mineral ribbons. Softer minerals such as clinochlore, tremolite, serpentine and actinolite comprise the melt and the rest of the ribbon portion in the ultracataclasite (Fig. 6). It is possible that some of the displacement in the fault veins is accommodated by preferential crystal plastic deformation and fusion within the ultracataclasite, explaining the lack of kinematic markers between the fault vein pseudotachylyte and wallrock (Kim et al., 2010; Sibson, 1980; Spray, 1992). The microtextures of this unusual crystal-plastic ultracataclasite may hold information regarding the earliest stages of pseudotachylyte generation. It is important to take note that no ultracataclasite appears to form in pseudotachylyte fault veins hosted by equigranular, fine-grained rock (~20 μm) in both the peridotite and metagabbro.

4.6. Microtextures of the pseudotachylyte matrix

The matrices of the metagabbro and peridotite pseudotachylytes are typically dominated by crystallisation products of the melt, with interstitial crypto-crystalline material or glass and entrained wallrock clasts that vary greatly in size and can constitute up to 20% of the vein, but are normally much less. The presence of interstitial glass was confirmed with XRD synchrotron analysis (Fig. 8). The veins are commonly marked by streaks or colour bands that indicate compositional variation, predominantly due to clusters of spinel, and inefficient mixing of the melt

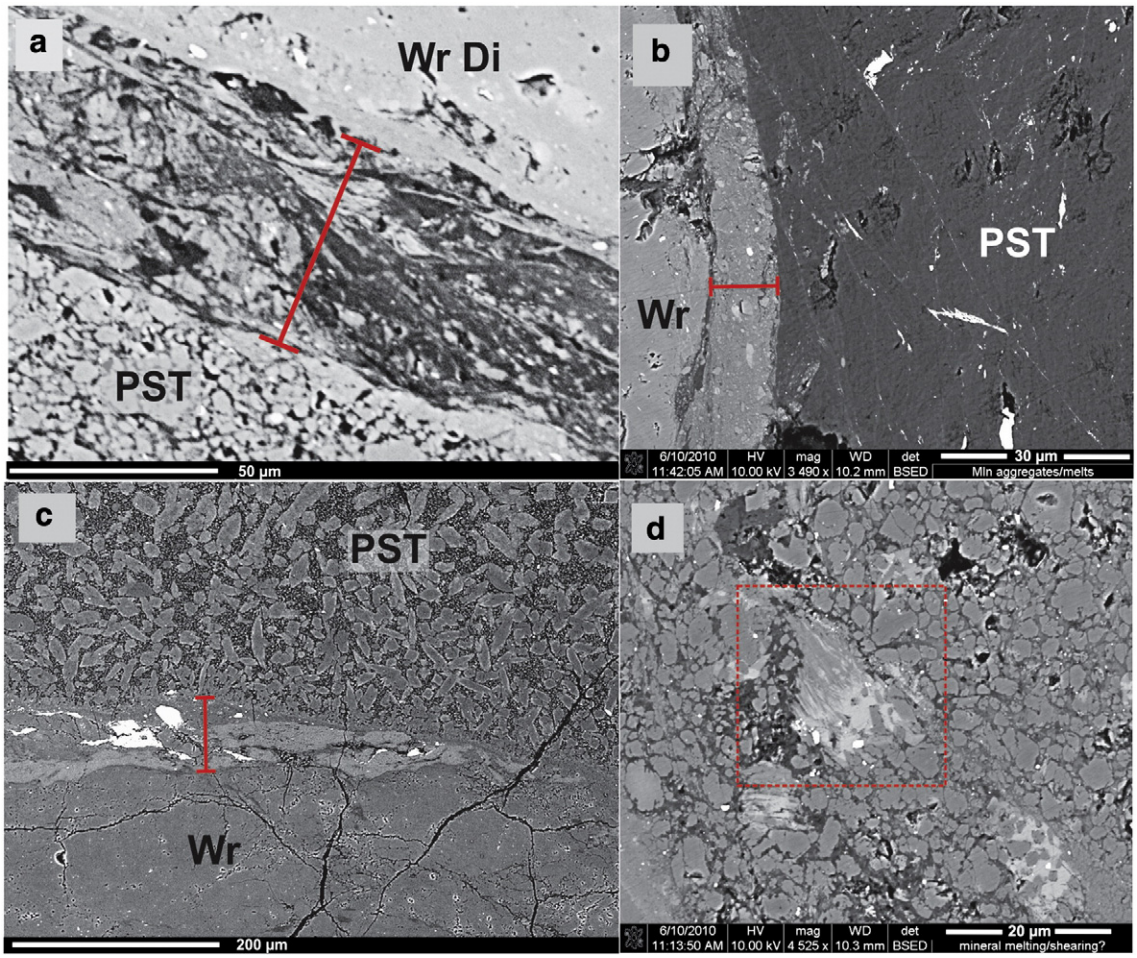


Fig. 6. BSE images a–c of ultracataclasites at fault vein boundaries in peridotite. A range of brittle–ductile textures are present in the ultracataclasite, the width of which is shown by the capped red line. (a) Close-up of the ultracataclasite; the black areas are a hydrous Al-rich melt, the dark grey areas are a sheared out pseudotachylyte matrix, and the lighter grey is a combination of sheared out survivor clasts of wallrock diopside and pseudotachylyte matrix. Image d shows a pseudotachylyte matrix crystallising olivine (grey) and diopside (light grey) in a hydrous matrix (dark grey). The red box encloses an olivine–diopside crystal complex being sheared out prior to total solidification indicating continued displacement along fault veins post melt production and failure. Panel c shows a similar feature; brittle-looking ultracataclasites with a matrix hosting ribbons of stretched out diopside microlites (in white). Wr: Wallrock, Wr Di: Wallrock diopside grain.

(Fig. 7). The crystallisation products have various habits: hopper crystals, simple acicular laths, and feathery plumes, which nucleate on clastic material in the vein forming dendrites or along vein boundaries. A principal control on microlite size is the presence or absence of a nucleation surface and the size of this surface. When the nucleating surface is particularly small it generally forms the core of a larger than average complex dendrite composed of several mineral species. Space may also exert a control on crystallisation; areas that appear to be

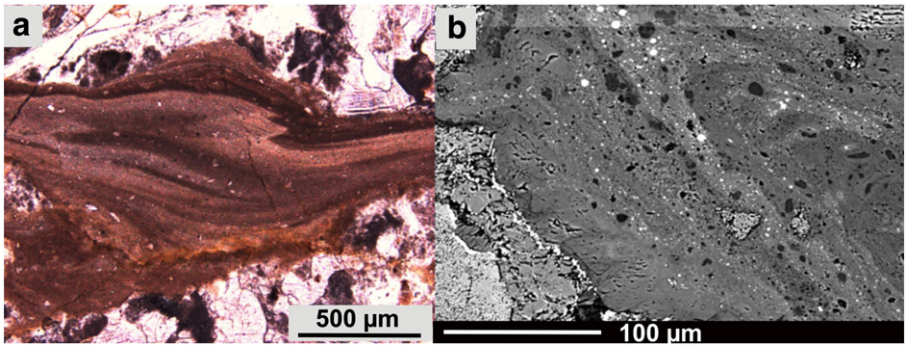


Fig. 7. Micrograph (a) and BSE image (b) of pseudotachylyte matrix in a metagabbro. Colour bands in these veins are evident in both images and are attributed to zones where individual minerals or aggregates have fused and become decrepitated and sheared out. Clusters of microlites and glassy material are also observed to form bands. However, the crystallisation products of the melt are strongly controlled by its composition, and hence the pre-existing minerals that fused will be the dominant control over the formation of these colour bands. Minimal physical sorting or fractionation has been observed in these veins, so this is not considered to be a significant factor.

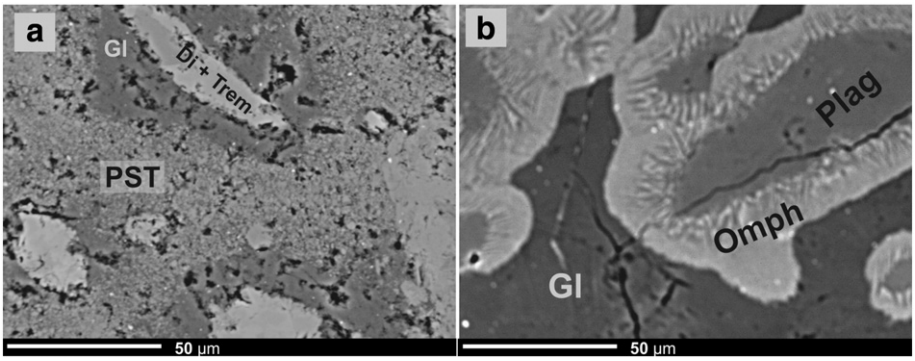


Fig. 8. BSE images of individually fusing clasts enclosed in a pseudotachylyte matrix. (a) The matrix is dominated by microlites and minute relict clasts. However, at the boundary of melting clasts there is a zone of Al-rich, hydrous glass (Gl). Conversely, in panel b the matrix is glass dominated (anhydrous) and the fusing grains are bounded by a crystallisation front of Al-rich omphacite (Omph) nucleating on plagioclase (Plag) derived from wallrock. Di + Trem: aggregate clast of wallrock diopside and tremolite.

absent of any nucleating surface are typically host to some of the largest crystals.

4.7. Microtextures of survivor clasts

Survivor clasts comprise wallrock material that has been dragged into the pseudotachylyte during its formation. These can be monomineralic or composed of aggregates of minerals. They are typically angular or tabular in shape, with thermally rounded margins. The larger tabular forms are aggregates from the deformed wallrock that have been scoured away from the vein boundary by injecting melt (Fig. 3). The composition of the clasts is the same as that of the adjacent wallrock mineralogy, but not in the same proportions. Hydrous minerals such as Mg-hornblende, clinochlore and serpentine occur only in rare aggregates with anhydrous minerals and are thus inferred to have melted preferentially. Monomineralic olivine, diopside, magnetite, ilmenite and plagioclase have all been observed in the matrix of both types of host rock. Diopside and plagioclase are the most common clasts derived from the metagabbro host rock, whilst olivine and diopside are those abundantly found in the peridotite. Survivor clasts commonly exhibit undulose extinction and kink-banding similar to that observed just beyond fault vein boundaries in the wallrock, suggesting that they may be derived from the wallrock and underwent similar crystal plastic deformation. Sieve textures in sheared out wallrock and partially resorbed survivor clasts of older pseudotachylyte have also been observed (Fig. 9).

Further detailed petrographic data have been divided according to the metagabbro and peridotite host rocks. Within those groups the most pristine samples were selected for microtextural and geochemical analysis. The pseudotachylytes are highly heterogeneous in composition down to the micron scale, so this separation is the best way to gain information from these veins and interpret their mechanism of formation meaningfully.

4.7.1. Metagabbro: pseudotachylyte

Compositionally the pseudotachylytes hosted by metagabbro are highly heterogeneous, strongly reflecting local mineral compositions of the adjacent wallrock and survivor clasts. However, despite the compositional variability of the melt, the mineralogy of the crystallisation products in the pseudotachylytes is simple albeit showing great chemical variability. The pseudotachylyte matrix is defined as a combination of glass, crystallisation products and comminuted material that are too small to be resolved by electron microprobe analysis (EPMA) beam (<1 μm). The crystallisation products are divided into two groups: a high temperature quench assemblage with pockets of interstitial glass, and a lower temperature assemblage in which devitrification of the glass and recrystallisation of the pseudotachylyte matrix have taken place.

4.7.1.1. Microlite assemblage in the metagabbro pseudotachylytes. This microlite assemblage is dominated by omphacite and plagioclase, with minor ilmenite (Fig. 10). This is the first reported evidence of natural crystallisation of omphacite directly from a melt. Omphacite has been reclassified from fassaite, as it was termed by Andersen and Austrheim (2006). The composition of the minerals is highly variable and is strongly controlled by melt composition in the matrix or by fusing

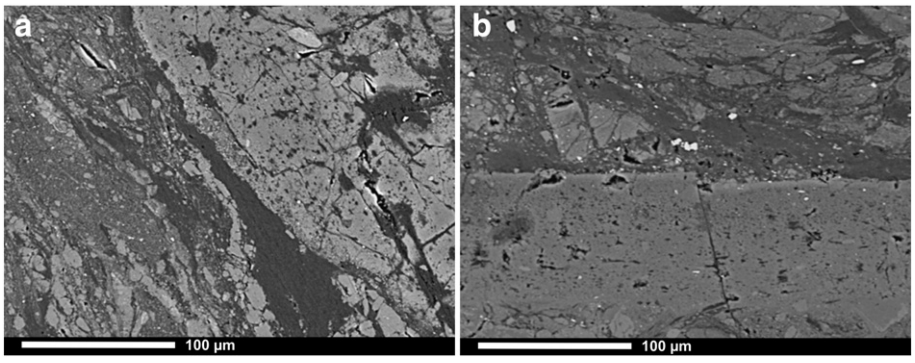


Fig. 9. BSE images of sieve textures in a peridotite-hosted pseudotachylyte matrix. Both panels a and b show at least two generations of pseudotachylyte. The sieve textured material in both images is the oldest generation that has been deformed and partially digested by a younger pseudotachylyte generation into which sheared out clasts of the older pseudotachylyte have been entrained. The oldest generation of pseudotachylyte contains inclusions of relative low atomic number (and low totals when analysed with EPMA; ~86%), suggesting that these are quenched melt inclusions with fluids dissolved in them to varying degrees. Preliminary Raman spectroscopy shows these vesicles to contain glassy material and empty cavities, presumably once filled with fluid.

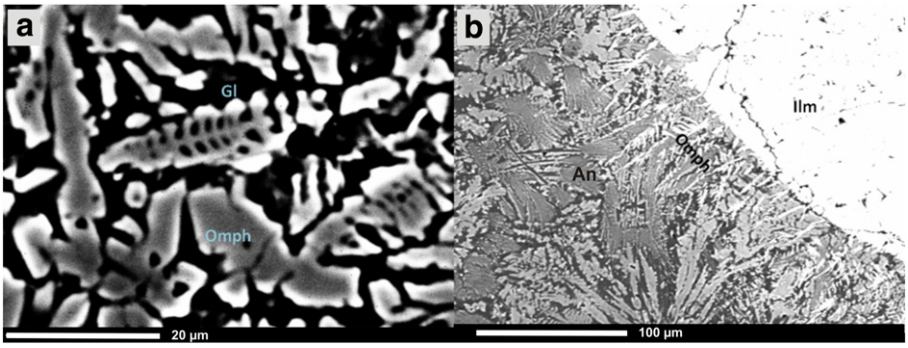


Fig. 10. Omphacite is the principal high temperature mineral crystallising from gabbroic pseudotachylyte, with anorthite and ilmenite to lesser degrees. Panel a shows delicate, zoned hopper crystals of omphacite enclosed by glass; this crystal habit is an indicator of rapid, high temperature quenching. Panel b shows omphacite in white and light grey with feathered and dendritic textures. The dark grey dendrites are anorthite. The variation in the composition of omphacite is controlled by the mineral that it nucleates on, as shown by the change in greyscale; its local melt composition and zoning in the crystals. Omph: omphacite, Ilm: Ilmenite.

clasts on which the microlites have nucleated. The omphacite is characterised by significant Al-enrichment relative to typical omphacite, which could be due to the high temperature and pressure of crystallisation (average Al_2O_3: 17.3 wt.%). The plagioclase is characterised by high FeO_{total} and MgO contents (average FeO_{total} = 1.3 wt.%, MgO = 1.1 wt.%), possibly due to the rapidity or high temperature of crystallisation, or inclusions of unresolvable omphacite or ilmenite. These microlites take the form of laths, dendrites and skeletal hoppers crystallising freely in the pseudotachylyte matrix or nucleating on vein boundaries or on survivor clasts. The omphacite is clearly zoned with Mg-rich cores and Fe-rich rims (Fig. 10).

4.7.1.2. Metagabbro: devitrification and recrystallisation of pseudotachylytes. Devitrification of glass and recrystallisation of the higher temperature minerals that quenched directly from the pseudotachylyte melt produce its own assemblage of blueschist facies minerals: glaucophane, Fe-rich albite, epidote and minor sphene (Fig. 11a, b). The crystals in this assemblage are commonly coarser than those in the higher temperature assemblage (up to 2 mm). They are also more irregular and blocky in form, no longer exhibiting the dendritic habits of the replaced minerals. They occasionally show a deformation fabric expressed as folds and boudins of pseudotachylyte at the thin section scale, indicating a ductile blueschist facies overprint (Fig. 12a).

4.7.2. Peridotite: pseudotachylyte

At the millimetre to micron scale the peridotite pseudotachylytes show great variability in composition and abundance of bulk matrix, glass and crystallisation products. Despite this variability, the microlites consistently comprise diopside, olivine and enstatite. As with the metagabbro, the peridotite fusion products can be divided into a high temperature quench assemblage and a lower temperature devitrification assemblage.

4.7.2.1. Microlite assemblage in peridotite-hosted pseudotachylytes. Olivine, diopside and enstatite occur as clusters of monomineralic blocky microlites (particularly olivine) or as dendritic complexes. Also common are larger, polymineralic laths and dendrites (Fig. 11). The interstitial material of the bulk matrix ranges is a variable mixture of olivine and enstatite and has an H_2O content ranging from 0 to 14.2 wt.% H_2O.

4.7.2.2. Peridotite: devitrification and recrystallisation of pseudotachylytes. Devitrification of glass and recrystallisation of the higher temperature minerals that quenched directly from the pseudotachylyte melt produce distinct assemblages. Typically the devitrified melt is characterised by the formation of microfibrous clinochlore, serpentine and tremolite (Fig. 9). In contrast, pseudotachylyte that has completely recrystallised comprises fine-grained (<50 μm) granoblastic diopside, olivine and enstatite (Fig. 4).

5. Discussion

The microtextures analysed in this study are spatially and temporally associated with pseudotachylyte generation. The observed crystal–plastic phenomena that are considered to be causally linked to fusion and seismic failure include: dislocation creep/glide, deformation twinning, kinking, bending and ultracataclasite/melt formation (Figs. 6 and 13). The ultracataclasite observed in these rocks is unusual in that it contains angular comminuted wallrock minerals as well as ribbons and strings of minerals exhibiting syndeformational ductile features (Fig. 6). The interstitial areas of the ultracataclasite contain glassy pockets of preferentially melted hydrous minerals, e.g. tremolite and clinochlore. Together, these textures suggest that the wallrock minerals may have undergone power law creep-dominated deformation that reached seismic strain rates, to induce the heating and fusion of the wallrock that is characterised by the presence of pseudotachylyte in these rocks (John et al., 2009; Kameyama et al., 1999).

The quench products of the pseudotachylytes indicate initially very high temperatures (~1600 °C), followed by a return to blueschist to lawsonite-eclogite conditions (~430 °C–550 °C, 1.8–2.6 GPa) (Andersen and Austrheim, 2006; Ravna et al., 2010). When the pseudotachylytes devitrify or recrystallise, the resulting mineral assemblages (glaucophane, albite and epidote in the metagabbro and diopside, olivine, enstatite and clinochlore in the peridotite) indicate a high pressure, low temperature environment (Ravna et al., 2010).

5.1. Precursors to pseudotachylyte formation

To date, several mechanisms have been put forward to explain the initiation of intermediate-depth seismicity. They all share the commonality of being fundamentally dependent on precursory conditions (Green and Houston, 1995; John et al., 2009; Kelemen and Hirth, 2007). Therefore, we need to investigate in detail the evidence of any preserved pre-existing elements that may elucidate the sequence of events that culminate in the production of these high pressure pseudotachylytes. A close spatial relationship between pseudotachylyte formation and fabric development is observed in the host rocks. This is not a unique occurrence and has been noted by previous workers in other pseudotachylyte studies (Bestmann et al., 2011; Hobbs et al., 1986; Jin et al., 1998; Kim et al., 2010; Lin, 1994; Lund and Austrheim, 2003). Hobbs et al. (1986) were amongst the first to propose the possibility that in high pressure cases, pseudotachylyte and mylonite formation may be inter-related processes; suggesting that at the highest deformation rates pseudotachylyte would form, followed by cataclasis

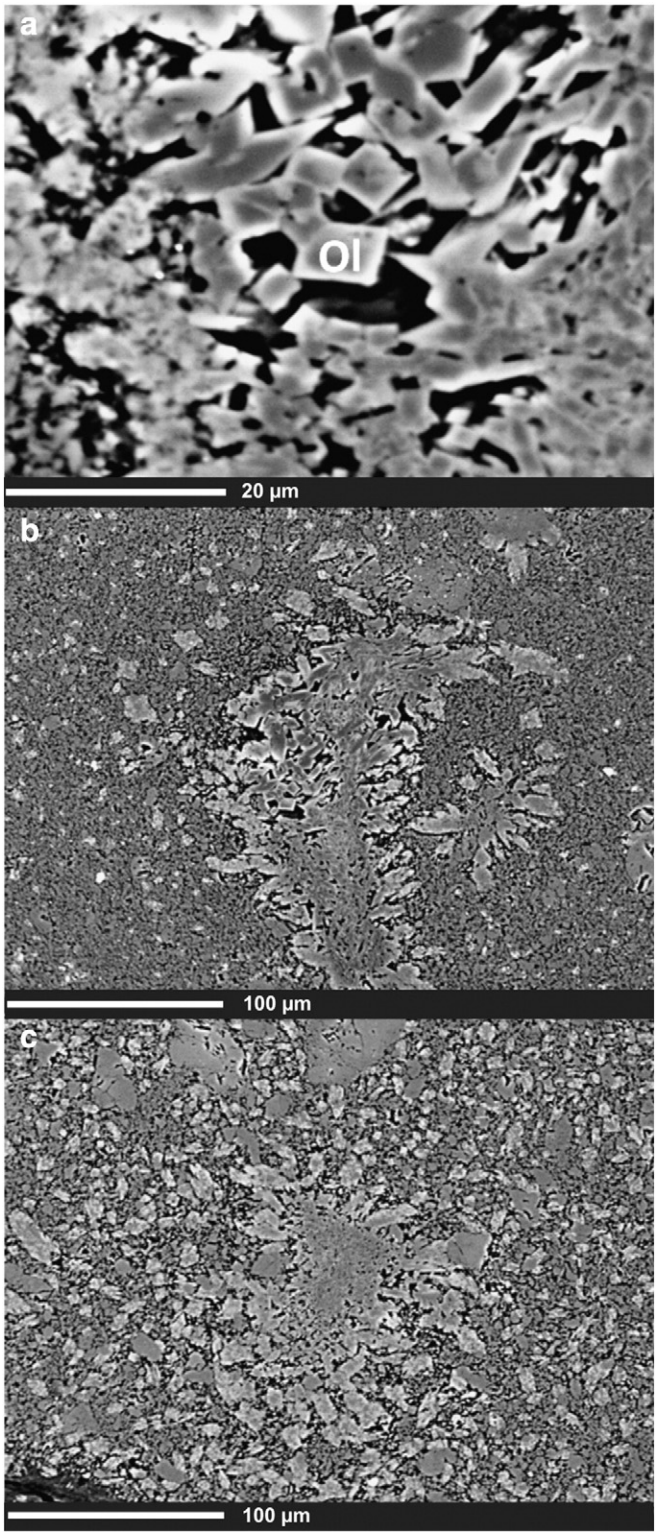


Fig. 11. BSE images showing the three principal types of crystallisation styles in peridotite hosted pseudotachylyte. Panel a shows blocky microlites of olivine surrounded by glass (black in images). The olivine crystals show strong Mg–Fe zoning from core to rim. Panel b shows pure olivine dendrites clustered in an aggregate with interstitial glass in a matrix of blocky olivine crystals and complex laths of diopside (light grey) and olivine (darker grey). (c) This image shows an aggregate of crystallised material in the centre. Close inspection shows that the aggregate is composed of three minerals; enstatite (darkest grey), olivine (mid-grey) and diopside (light grey). The aggregate is dominated by these complex, tri-mineralic dendrites. The black interstitial matrix in all three images was analysed to be a variably Al-, H_2O-enriched glassy material.

and then fabric development, potentially culminating in mylonite at the lowest deformation rates.

Incipient fabric development prior to and after pseudotachylyte formation has been observed (Figs. 6d, 12a, 14). Detailed EBSD analysis of a peridotite fault section from the same field area shows that the wallrock minerals are exposed to increasing strain towards pseudotachylyte fault veins. The wallrock has undergone recrystallisation to form an incipient lattice preferred orientation (LPO) prior to and/or during fault vein development (Silkoset, 2013). Crystal plastic deformation such as folding, boudinaging, annealing and foliation development occurring after fault vein formation has been observed within veins and the associated wallrock (Figs. 6d, 12, 14). The time lapse between pseudotachylyte generation and fabric development (before and after) is unknown. However, the simplest explanation of the observations involves: recrystallisation in the wallrock with increasing strain towards vein boundaries as well as rotation of elongate wallrock clasts into parallelism with developing fault vein boundaries. Continued shearing (Fig. 6) occurs after displacement and fusion have taken place, at which point the fault zone had cooled enough to crystallise glaucophane (in the metagabbro) and clinochlore (in the peridotite). We suggest the following sequence of events to explain our observations:

The majority of wallrock material for both metagabbro and peridotite is coarse-grained and partially deformed due to previous events. As a result the wallrock grains will likely contain numerous crystallographic imperfections that can be exploited when in the right orientation in the stress field to form the loci of fault nucleation and initial fusion due to low temperature creep, followed by power law creep.

1. The fault wallrocks developed a damage zone with synchronous recrystallisation and an increasing strain-gradient towards the future fault plane as also observed by Silkoset (2013).
2. Anisotropic wallrock fragments have rotated so that long axes become parallel with the developing slip surface.
3. Deformed wall-rock fragments become entrained, as survivor clasts in the pseudotachylyte melt and their deformation is associated with the shearing event that produced the melt. Some undergo near complete to complete fusion.
4. In some veins, shearing and displacement continued after fusion, locally attested to by deformed and recrystallised pseudotachylyte.
5. Pseudotachylyte and fault damage zones cooled down sufficiently to devitrify or recrystallise to glaucophane (in metagabbro) and clinochlore (in peridotite).

It is possible that at lower deformation rates foliations may develop in the pseudotachylyte and wallrock between major faulting events.

Based on the observations and sequence of events presented above, we suggest the following model for pseudotachylyte generation:

The metagabbro and peridotite were mostly coarse-grained rocks, but both host rocks had structural and mineralogical heterogeneities inherited from earlier events. During subduction-related deformation, pre-existing zones with numerous crystallographic imperfections at favourable orientation relative to the new stress field become the loci of enhanced deformation (Jessell and Lister, 1991; Kameyama et al., 1999; Sibson, 1980). Low temperature and subsequent power law creep, induced by seismic strain rates eventually gave rise to fusion. It is possible that several loci in the same orientation underwent contemporaneous strain-induced fusion. These individual melt spots may in turn have linked up to form primitive fault planes. Stick-slip action along such plane will be preferentially activated for further slip and facilitate comminution and fusion. As the stress is released by comminution, displacement and fusion, the temperature of the fault and damage zone will remain elevated until the stress has dropped below the strength of the transient melted material of the fault. Thereafter, heat is dissipated by diffusion beyond the cooling vein and damage zone to facilitate crystallisation of the wallrocks. The delicate preservation of quench textures in pseudotachylytes suggests neglible post-quenching

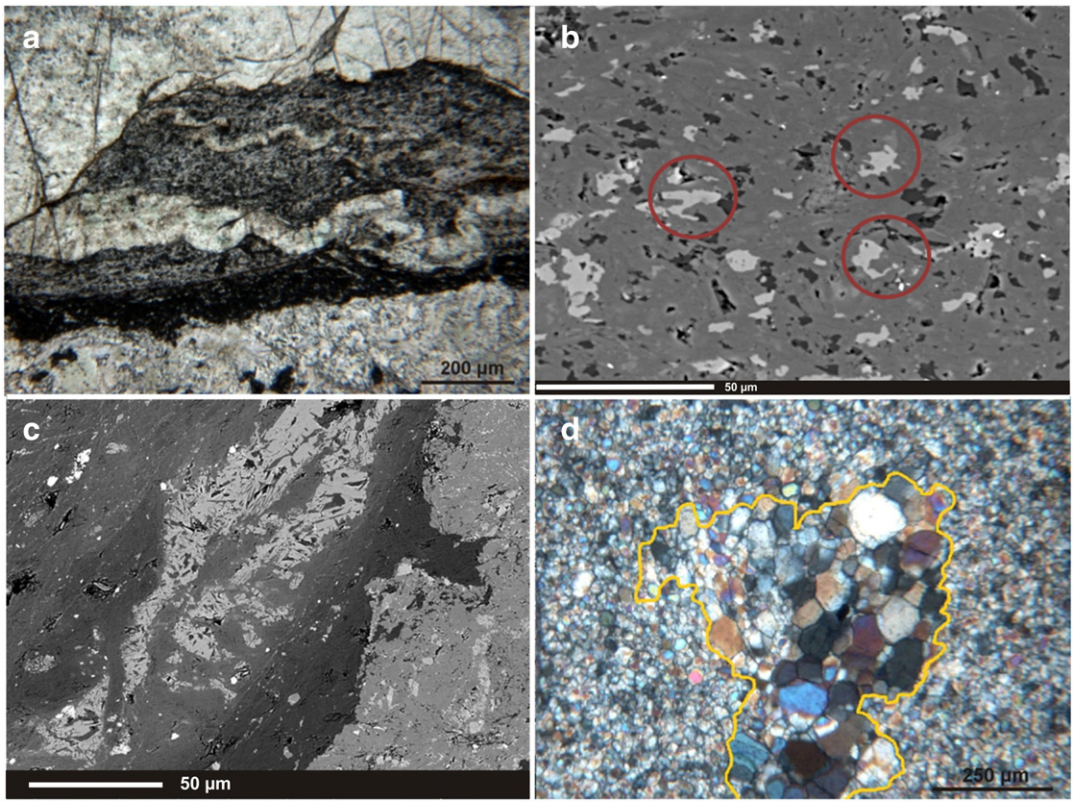


Fig. 12. Micrographs and BSE images showing the various recrystallisation textures in pseudotachylytes from both host rocks. Panels a and b metagabbro pseudotachylyte (a) from the same thin section sample as panel b, only at a lower magnification. (a) Folding of the recrystallised pseudotachylyte. The microlites in panel b are blocky, no longer the dendritic forms shown in previous examples. EPMA analyses show the mineral assemblage to be glaucophane, sphene (light grey crystals), albite (dark grey crystals) and epidote (darkest grey). The crystals are subhedral and deformed and aligned in a subtle fabric due to folding, as shown in panel a. Images c and d: peridotite–pseudotachylyte. (c) A devitrified pseudotachylyte matrix that has an ultrafine (<1 µm) of clinochlore composition. The matrix is not recrystallised as pristine quenched dendrites of diopside are observed (light grey dendrites (c) and stretched out, deformed clasts are evident along with zoning/colour banding in the vein that are preserved. Panel d shows a recrystallised matrix; the yellow line indicates the form of a recrystallised wallrock aggregate that was entrained into the pseudotachylyte. The surrounding fine-grained material comprises olivine and enstatite clasts which have replaced earlier dendrites and upon stage rotation under the microscope, shadows of now replaced dendrites can be observed. The clasts in this photomicrographs are annealed, forming a granoblastic texture and show no evidence of deformation. It is important to note that peridotite pseudotachylyte recrystallises to a harzburgitic composition.

deformation in most of the pseudotachylyte veins except in those areas where later regional deformation and metamorphism are penetrative.

5.1. Possible influence of grain size on pseudotachylyte formation

The grain size of both the metagabbro and the peridotite ranges from approximately 20 µm–260 µm. The principal deformation mechanism of the wallrock material and entrained survivor clasts that have been sheared and kinked but show no evidence of crystallographic recovery prior to pseudotachylytic fusion is interpreted to be dislocation creep/glide. EBSD analysis in a recent study indicates that the wallrock encountered rapidly increasing strain towards the pseudotachylyte boundaries, with weakly developed LPOs (Silkoset, 2013). The incipient LPO development could be due to localised stresses in the rock being accommodated by high dislocation densities in different grains (Branlund et al., 2000; Kameyama et al., 1999; Newman et al., 1999). EBSD analysis by Silkoset (2013) and intracrystalline microtextural observations (Figs. 3) in this study suggest dislocation creep as a possible dominant deformation mechanism associated with pseudotachylyte formation. If this is the case then there would be little grain size reduction through dynamic recrystallisation associated with the instability as diffusion creep would be a secondary deformation mechanism (Kameyama et al., 1999; Kelemen and Hirth, 2007). In finer-grained material (grain-size approximately 20 µm) strain has been accommodated by grain boundary sliding as opposed to intra-grain deformation; grain boundaries associated with the pseudotachylyte are aligned and grains appear squamous in shape as opposed to equant (Fig. 4).

It appears that higher volumes of melt are formed in the coarser-grained host rock. Of course, the current fault and injection vein thicknesses are not expected to be an exact indication of melt volume. However, taking vein dilation, draining and deformation into account the melt volume produced by coarse-grained rock relative to fine-grained rock is orders of magnitude greater; refer to Fig. 2a vs Fig. 4 where an outcrop scale image of an average fault vein is compared to the largest fault vein observed in the finest grained host rock, seen in thin section as it is so small. This may correspond with power law creep as a principal deformation mechanism as coarser-grained material would be easier to deform than finer-grained material. Coarser grains can accumulate more dislocations and higher dislocation densities in local areas of slip than can finer grains suggesting a greater potential for localised heating (Kameyama et al., 1999). Images of pseudotachylyte in the finer-grained host rock (Fig. 4) suggest that grain boundary sliding occurs preferentially over intra-grain deformation to resolve the applied stress.

Furthermore, our geochemical results show that grain size influences melt composition such that the bulk composition of a pseudotachylyte derived from a fine-grained host rock will better approximate fusion akin to that of an equilibrium melt (this is due to melt formation occurring primarily along grain boundaries), whereas in pseudotachylyte derived from a coarser-grained host, the bulk melt composition tends to reflect wholesale fusion of individual minerals such as olivine or diopside.

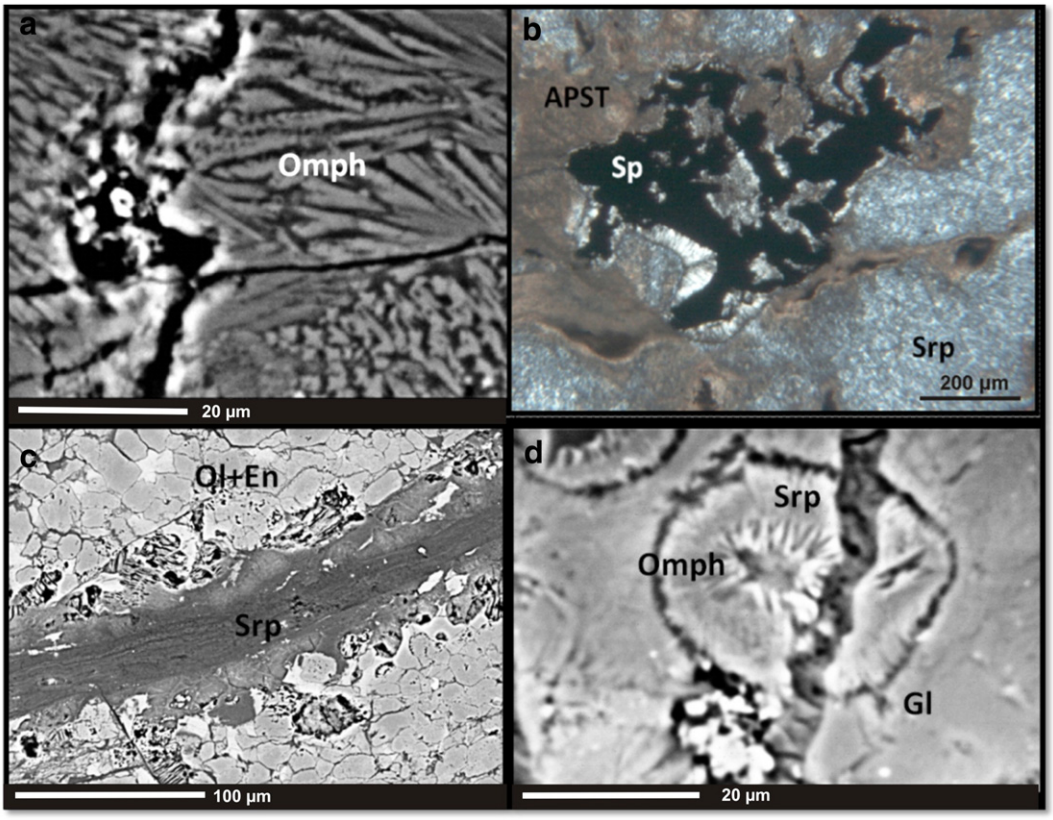


Fig. 13. BSE images and a photomicrograph (b) of hydrated/altered pseudotachylyte. In all images serpentine and associated spinel is the principal late alteration mineral (as is the case in both host rocks), but late epidote and actinolite are also present in the metagabbro. These images show how serpentinisation destroys the delicate textures associated with the pseudotachylyte forming event (dendrites and vein boundaries) and bleaches the pseudotachylyte, removing magnesium. (a) A black vein crosscuts a pristine pseudotachylyte matrix of omphacite in a metagabbro. The boundaries of the vein can be seen on BSE to have bleached the matrix enriching it in Fe. (b) Serpentinised peridotite pseudotachylyte where all microscopic crystallisation textures have been obliterated. (c) A late serpentine vein cuts through a recrystallised peridotite pseudotachylyte. Microfibres of serpentine can be seen eroding the fine-grained granoblastic texture. (d) Serpentine vein crosscutting spherulitic omphacite in an otherwise glassy pseudotachylyte matrix. Ol: olivine, En: enstatite, Srp: serpentine, Omph: omphacite, Gl: glass, Sp: spinel APST: altered pseudotachylyte.

Grain size reduction adjacent to vein boundaries was observed from the outcrop scale to the micron scale. Microtextural relationships suggest that this change in grain size is a feature contemporaneous with pseudotachylyte generation and is due to intense shearing along the fault surface, whereby the heat released by shearing facilitates recrystallisation and the shearing itself induces the reorientation of wallrock clasts and/or their comminution. This is in contrast with the results of Kelemen and Hirth (2007) and John et al. (2009) where a pre-existing fine-grained zone in the host rock was proposed in order to provide a nucleation site for shear instabilities to take place.

5.2. Present model compared to previous mechanisms

The Corsican pseudotachylytes contain up to 15 wt.% H_2O. This coupled with the large melt volumes produced by these events, apparently precludes dehydration embrittlement as a mechanism for the observed paleofaults. There is no evidence that free water or other fluids were available before faulting. Previous work by Green (1973), Jung et al. (2004) and Kirby et al. (1991), indicates that dehydration embrittlement is related to a solid-state monomineralic reaction. Its occurrence in polymineralic materials such as those studied here has to our knowledge not been tested experimentally. Instead we suggest that the high

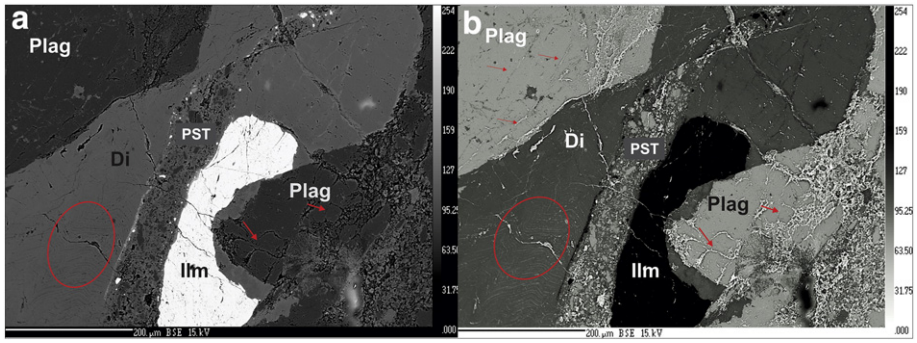


Fig. 14. BSE image of metagabbro with several generations of pseudotachylyte. The image on the left is the original BSE image and the image on the right has been inverted to highlight some features. The red circle highlights kinkbanding in wallrock diopside (Di). A minute fault vein has formed within a kink plane. The arrows indicate preferential fusion in the plagioclase (Plag) along certain planes. The white clast in the centre is ilmenite (Ilm).

temperature deformation related to local shear-heating was more significant for failure than a solid-state dehydration reaction weakening. Previously published shear heating models (John et al., 2009; Kelemen and Hirth, 2007) are not perfect fits either. Both these models prescribe precursory mylonites or fine-grained zones that act as strain concentrators in order to initiate self-localisation. Our observations from the rocks in Corsica however, indicate that, despite various differences in the host rocks, seismic faulting and fusion took place regardless of grain size, rock fabric or composition. The only discernible restriction on mineralogy is fracture toughness; minerals must have a shear yield strength great enough to allow for a sufficiently large stress build-up (Spray, 1992), which explains why no pseudotachylytes occur in the serpentinites surrounding the peridotite and metagabbro blocks. A non-quantified and speculative option may be that the rheological behaviour of rocks traditionally predicted at high pressure may not be simply constrained by visco-elasticity or Von Mises Criterion as suggested by (Mancktelow, 2006).

6. Conclusions

Both shear instabilities and dehydration reactions are thermally activated processes. However, the activation of thermal instability is derived from local rheological heterogeneities that provide a viscosity contrast in the host rock material at sufficiently high stresses that it behaves as a non-linear viscoelastic material (Braeck and Podladchikov, 2007; John et al., 2009; Kameyama et al., 1999; Ogawa, 1987). Conversely, dehydration embrittlement is induced by warming of the previously hydrated slab making it dependent on the presence of pre-existing hydrous mineralogy and an efficiently warmed slab. In addition, there is no evidence in the petrographic data to support the hypothesis of a dehydrated precursor to pseudotachylyte nucleation. This is not to say that dehydration embrittlement does not occur; it may well occur in the serpentinite enclosing the blocks of peridotite and metagabbro. The results from this study suggest that these pseudotachylytes produced at high pressure and seismic strain rates, in different host rocks, with different degrees of hydration, may have been generated by a high temperature crystal-plastic shear process. Detailed petrographic analysis suggests that low temperature and power law creep may play dominant roles in producing thermal instabilities and high pressure pseudotachylytes. Deformation of wallrock grains at the boundary of fault veins results in the formation of subtle LPOs in olivine grains and grain size reduction due to comminution (Silkoset, 2013). These features form at the onset of and during pseudotachylyte generation, not before, and they are not the precursory elements that form the nucleation sites of pseudotachylyte generation in previous models (John et al., 2009; Kelemen and Hirth, 2007). Future work to test this interpretation might involve high pressure fusion experiments, numerical modelling, detailed EBSD on more complex fault veins and geochemical analysis.

Acknowledgements

This work is supported Wits University, the National Research Foundation and the Mellon Foundation as well as the Research Council of Norway through its Centres of Excellence funding scheme, project number 223272 (CEED). Thanks to Prof. M. Zolensky of NASA for assisting with EBSD and XRD synchrotron analysis of some samples.

References

Agard, P., Monié, P., Jolivet, L., Goffé, B., 2002. Exhumation of the Schistes Lustrés complex: in situ laser probe $^{40}Ar/^{39}Ar$ constraints and implications for the Western Alps. J. Metamorph. Geol. 20, 599–618.

Andersen, T., Austrheim, H., 2006. Fossil earthquakes recorded by pseudotachylytes in mantle peridotite from the Alpine subduction complex of Corsica. Earth Planet. Sci. Lett. 242, 58–72.

Austrheim, H., Andersen, T.B., 2004. Pseudotachylytes from Corsica: fossil earthquakes from a subduction complex. Terra Nova 16, 193–197.

Austrheim, H., Boundy, T., 1994. Pseudotachylytes generated by seismic faulting and eclogitization of the deep crust. Science 265, 82–83.

Beccaluva, L., Ohnenstetter, D., Ohnenstetter, M., Venturelli, G., 1977. The trace element geochemistry of Corsican ophiolites. Contrib. Miner. Pet. 64, 11–31.

Bestmann, M., Pennacchioni, G., Frank, G., Göken, M., de Wall, H., 2011. Pseudotachylyte in muscovite-bearing quartzite: coseismic friction-induced melting and plastic deformation of quartz. J. Struct. Geol. 33, 169–186.

Braeck, S., Podladchikov, Y., 2007. Spontaneous thermal runaway as an ultimate failure mechanism of materials. Phys. Rev. Lett. 98.

Branlund, J.M., Kameyama, M.C., Yuen, D.A., Kaneda, Y., 2000. Effects of temperature-dependent thermal diffusivity on shear instability in a viscoelastic zone: implications for faster ductile faulting and earthquakes in the spinel stability field. Earth Planet. Sci. Lett. 182, 171–185.

Green, D.H., 1973. Experimental melting studies on a model upper mantle composition at high pressure under water-saturated and water-undersaturated conditions. Earth Planet. Sci. Lett. 19, 37–53.

Green, H.W., Houston, H., 1995. The mechanics of deep earthquakes. Annu. Rev. Earth Planet. Sci. 23, 169–213.

Hacker, B.R., 2003. Subduction factory 2. Are intermediate-depth earthquakes in subducting slabs linked to metamorphic dehydration reactions? J. Geophys. Res. 108.

Hobbs, B.E., Ord, A., Teyssier, C., 1986. Earthquakes in the ductile regime? Pure Appl. Geophys. J. R. Astron. Soc. 124, 309–336.

Jessell, M.W., Lister, G.S., 1991. Strain localization behaviour in experimental shear zones. Pure Appl. Geophys. 137, 421–438.

Jin, D., Karato, S., Obata, M., 1998. Mechanisms of shear localization in the continental lithosphere: inference from the deformation microstructures of peridotites from the Ivrea zone, northwestern Italy. J. Struct. Geol. 20, 195–209.

John, T., Medvedev, S., Rüpke, L.H., Andersen, T.B., Podladchikov, Y.Y., Austrheim, H., 2009. Generation of intermediate-depth earthquakes by self-localizing thermal runaway. Nat. Geosci. 2, 137–140.

John, T., Schenk, V., 2006. Interrelations between intermediate-depth earthquakes and fluid flow within subducting oceanic plates: constraints from eclogite facies pseudotachylytes. Geology 34, 557.

Jolivet, L., 1993. Extension of thickened continental crust, from brittle to ductile deformation: examples from Alpine Corsica and Aegean Sea. Ann. Geofis. 36, 139–153.

Jung, H., Green, H.W., Dobrzhinetskaya, L., 2004. Intermediate-depth earthquake faulting by dehydration embrittlement with negative volume change. Nature 428, 545–549.

Kameyama, M., Yuen, D.A., Karato, S.-I., 1999. Thermal–mechanical effects of low-temperature plasticity (the Peierls mechanism) on the deformation of a viscoelastic shear zone. Earth Planet. Sci. Lett. 168, 159–172.

Kanamori, H., Anderson, D., Heaton, T., 1998. Frictional melting during the rupture of the 1994 Bolivian earthquake. Science 279, 839–842.

Kelemen, P.B., Hirth, G., 2007. A periodic shear-heating mechanism for intermediate-depth earthquakes in the mantle. Nature 446, 787–790.

Kim, J.-W., Ree, J.-H., Han, R., Shimamoto, T., 2010. Experimental evidence for the simultaneous formation of pseudotachylyte and mylonite in the brittle regime. Geology 38, 1143–1146.

Kirby, S., Durham, W., Stern, L., 1991. Mantle phase changes and deep earthquake faulting in subducting lithosphere. Science 252, 216–225.

Lin, A., 1994. Glassy pseudotachylyte veins from Fuyun fault zone, northwest China. J. Struct. Geol. 16, 71–83.

Lund, M., Austrheim, H., 2003. High-pressure metamorphism and deep-crustal seismicity: evidence from contemporaneous formation of pseudotachylytes and eclogite facies coronas. Tectonophysics 372, 59–83.

Mancktelow, N.S., 2006. How ductile are ductile shear zones? Geology 34, 345.

Merlet, C., 1994. An accurate computer correction program for quantitative electron microprobe analysis. Mikrochim. Acta 114/115, 363–376.

Mohn, G., Manatschal, G., Muntener, O., Beltrando, M., Masini, E., 2009. Unravelling the interaction between tectonic and sedimentary processes during lithospheric thinning in the Alpine Tethys margins. Int. J. Earth Sci. 99, S75–S101.

Newman, J., Lamb, W., Drury, M.R., Vissers, R.L., 1999. Deformation processes in a peridotite shear zone: reaction-softening by an H_2O-deficient, continuous net transfer reaction. Tectonophysics 303, 193–222.

Ogawa, M., 1987. Shear instability in a viscoelastic material as the cause of deep focus earthquakes. J. Geophys. Res. 92, 13801–13810.

Ravna, E.J.K., Andersen, T.B., Jolivet, L., De Capitani, C., 2010. Cold subduction and the formation of lawsonite eclogite — constraints from prograde evolution of eclogitized pillow lava from Corsica. J. Metamorph. Geol. 28, 381–395.

Sibson, R.H., 1980. Transient discontinuities in ductile shear zones. J. Struct. Geol. 2, 165–171.

Silkoset, P., 2013. Microstructure of Ultramafic Pseudotachylyte From Alpine Corsica — Insights Into Earthquakes in Mantle Lithosphere. Unpublished Master thesis: University of Oslo, Norway.

Spray, J., 1992. A physical basis for the frictional melting of some rock-forming minerals. Tectonophysics 204, 201–221.

Vitale Brovarone, Groppo, Hetenyi, Compagnoni, R., Malavieille, 2011. Coexistence of lawsonite-bearing eclogite and blueschist: phase equilibria modelling of Alpine Corsica metabasalts and petrological evolution of subducting slabs. J. Metamorph. Geol. 29, 583–600.

Downloaded from geology.gsapubs.org on May 15, 2014

Geology

Large subduction earthquakes along the fossil Moho in Alpine Corsica

T.B. Andersen, H. Austrheim, N. Deseta, P. Silkoset and L.D. Ashwal

Geology 2014;42;395-398
doi: 10.1130/G35345.1

Email alerting services click www.gsapubs.org/cgi/alerts to receive free e-mail alerts when new articles cite this article

Subscribe click www.gsapubs.org/subscriptions/ to subscribe to Geology

Permission request click http://www.geosociety.org/pubs/copyrt.htm#gsa to contact GSA

Copyright not claimed on content prepared wholly by U.S. government employees within scope of their employment. Individual scientists are hereby granted permission, without fees or further requests to GSA, to use a single figure, a single table, and/or a brief paragraph of text in subsequent works and to make unlimited copies of items in GSA's journals for noncommercial use in classrooms to further education and science. This file may not be posted to any Web site, but authors may post the abstracts only of their articles on their own or their organization's Web site providing the posting includes a reference to the article's full citation. GSA provides this and other forums for the presentation of diverse opinions and positions by scientists worldwide, regardless of their race, citizenship, gender, religion, or political viewpoint. Opinions presented in this publication do not reflect official positions of the Society.

Notes

© 2014 Geological Society of America

THE GEOLOGICAL SOCIETY OF AMERICA

Downloaded from geology.gsapubs.org on May 15, 2014

Large subduction earthquakes along the fossil Moho in Alpine Corsica

T.B. Andersen[1]*, H. Austrheim[1], N. Deseta[2], P. Silkoset[1], and L.D. Ashwal[2]
[1]Centre of Earth Evolution and Dynamics, Department of Geosciences, University of Oslo, P.O. Box 1047, Blindern 0316 Oslo, Norway
[2]School of Geosciences, University of Witwatersrand, Wits 2050 Johannesburg, South Africa

ABSTRACT

Subduction earthquakes release vast amounts of energy to crust and mantle lithosphere. The products of such drastic events are rarely observed in the field because they are mostly lost by subduction. We present new observations of deformation products formed by a few very large and numerous small intermediate-depth Alpine subduction earthquakes that are preserved along the exhumed gabbro–mantle peridotite contact of the Piemont-Liguria oceanic basin in Corsica. The abrupt release of energy resulted in shear heating events that completely melted both gabbro and peridotite. The large volumes of melt that were generated can be studied in the fault and injection vein breccia complex along the fault zone. The energy required for wholesale melting of a large volume of peridotite along the fault combined with previous estimates of stress drops show that very large earthquakes took place along the Moho of the subducting plate. Because these fault rocks formed by intraplate seismicity, we suggest, by analogy with present-day subduction, that they represent a proxy for the lower seismogenic zone.

INTRODUCTION

Pseudotachylytes (PSTs) are melt rocks formed by earthquake faulting or by shock events such as extraterrestrial impacts. Such sudden release of strain energy may generate very high temperatures and may melt rocks regardless of bulk composition (e.g., Spray, 1995). Wadati-Benioff zones are the most seismically active domains on Earth and host the largest known earthquakes. Exhumed high-pressure (HP) and low-temperature (LT) provinces are regions recording low geotherms characteristic of subduction and collision; therefore, ancient HP-LT terrains may provide opportunities to make direct observations of phenomena produced by collision and subduction earthquakes (Austrheim and Boundy, 1994). Field examples of PST produced by intermediate depth earthquakes (~50–300 km; Frohlich, 2006) are rare (Austrheim and Boundy, 1994; John and Schenk, 2006), not because the processes they record are rare, but because the likelihood of exhumation of such fault rocks to the surface, enabling direct observation, is very small. Such rocks will normally be lost permanently by subduction (Bjørnerud et al., 2002) or be restructured and recrystallized during exhumation. Only a few occurrences worldwide are known (Sibson and Toy, 2006).

Previous studies in the HP-LT terrains of Alpine Corsica (Ravna et al., 2010; Vitale Brovarone et al., 2011a) documented coseismic slip evinced by numerous, mostly small PST fault and injection veins (Andersen and Austrheim, 2006; Deseta et al., 2014). These studies demonstrated that complete melting and high-*P* quenching of gabbro and peridotite took place and that large stress drops (>570 MPa) were caused by small (<5 cm) slip events in the peridotite (Andersen et al., 2008). Here we present new observations of PSTs that formed by much larger earthquakes than described previously. The gabbro–mantle peridotite contact exposed at Cima di Gratera (Fig. 1) formed in the slow-spreading Piemont-Liguria Ocean or in distal parts of its hyperextended passive margin. It represents the fossil crust-mantle boundary (Moho) in the vestiges of the oceanic basin that closed during Alpine subduction (Vitale Brovarone et al., 2011b, 2013). In this study, the exposed gabbro–mantle peridotite contact in Cape Corse (Fig. 1) and its evidence for HP-LT coseismic faulting are taken to represent a proxy for an oceanic lithosphere Moho during subduction.

FIELD OBSERVATIONS

Earthquakes along the paleo-Moho in the study area (Corsica; Fig. 1) caused melting of large volumes of spinel- and plagioclase-bearing mantle peridotite (Fig. 2) as well as the gabbro of the lower crust (e.g., Austrheim and Andersen, 2004; Deseta et al., 2014). The exposed crust-mantle interface is a sharp, gently dipping contact between serpentinitized to well-preserved mantle peridotite and the overlying layered to variably textured metagabbro. Evidence for dramatic PST generation events can be studied within both gabbro and mantle peridotite lenses, which are as much as 140 m thick and 850 m long and preserved for ~2.5 km along the exposed crust-mantle contact (Fig. 1). The contact is offset by later normal faults that also truncate the nonmetamorphic Miocene Saint Florent Basin (Fig. 1). The PST faulting

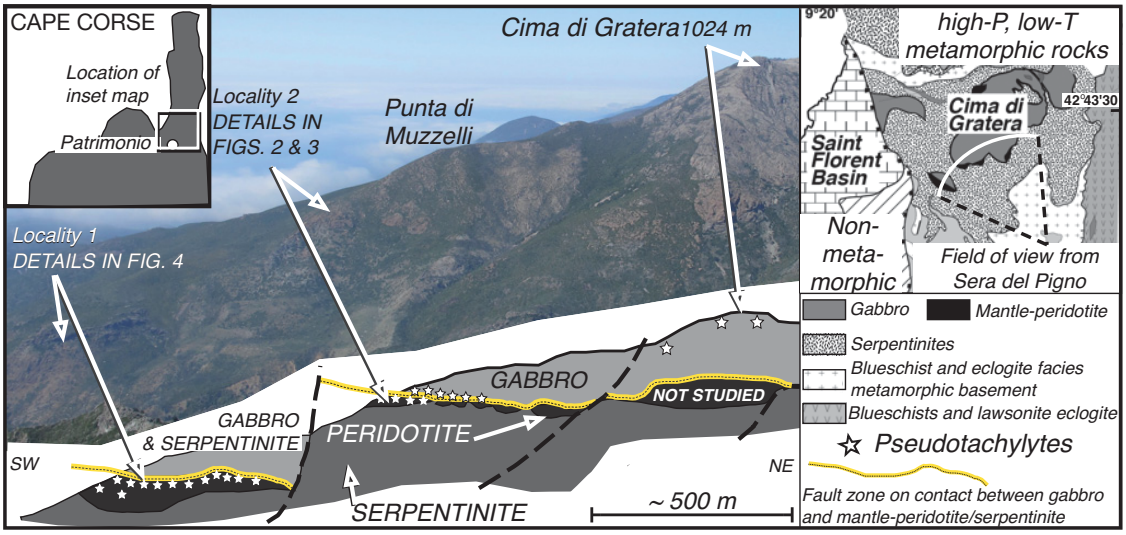


Figure 1. View and sketch of south face of Cima di Gratera, Cape Corse, Corsica. Fossil crust-mantle boundary of Piemont-Liguria ocean basin (yellow line) is preserved along distance of ~2.5 km. Best-preserved pseudotachylytes (PST) in peridotite are found at locality 2; for details see Figures 2 and 3. All visited outcrops have large volumes of ultramafic PST. Inset maps show location (left) and view with local geology (from Ravna et al., 2010). *P*—pressure; *T*—temperature.

*E-mail: t.b.andersen@geo.uio.no.

GEOLOGY, May 2014; v. 42; no. 5; p. 395–398; Data Repository item 2014145 | doi:10.1130/G35345.1 | Published online 17 March 2014
© 2014 Geological Society of America. For permission to copy, contact Copyright Permissions, GSA, or editing@geosociety.org.

Downloaded from geology.gsapubs.org on May 15, 2014

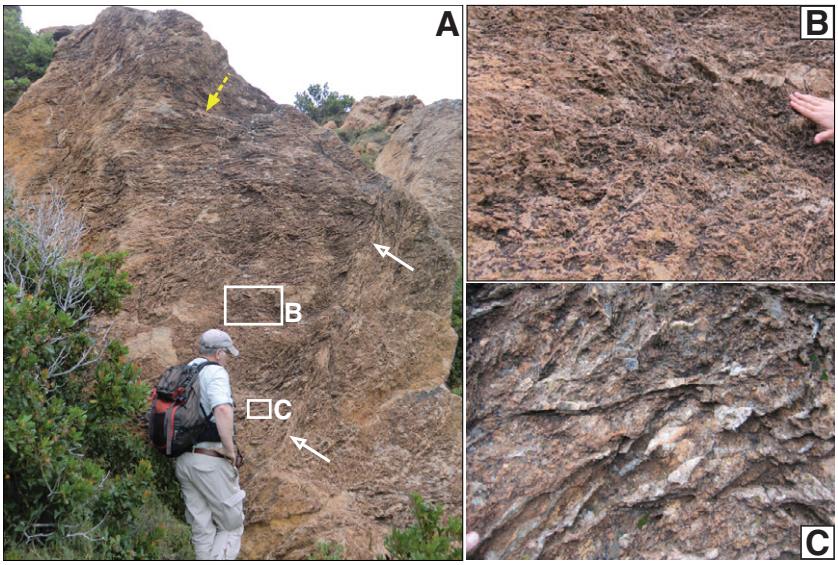


Figure 2. A: View toward northeast of main melt vein complex with >6-m-thick damage zone in peridotite at locality 2 (Fig. 1). Cliff face constitutes net veined, sponge-like breccia with dominantly subparallel, but mutually crosscutting, ultramafic pseudotachylyte (PST) veins dipping gently to left. PST veins and pockets form positive topography on weathered surface. Some veins coalesce into massive injection veins, to 15 cm thick (at dotted arrow). Vein complex is truncated by later steeply (~60°) dipping fault also decorated by PST (2–4-cm-wide fault veins at arrows). Main vein complex is without obvious temporal vein hierarchy. B: Detail showing intensity of sponge-like net veining with >50% melt. Positive surface features are mostly formed by hair-thin to centimeter-wide melt accumulations and PST matrix also without obvious sequence of emplacement. Lichen-covered (darker) negative surface features are disintegrating host-peridotite fragments. Note thicker veins to 8 cm wide above hand and lack of later faults cutting vein complex. This part of vein complex formed by only one event. C: Detail of glassy bifurcating and coalescing net veins making positive topography on weathered surface with ~40% melt (fingertip on extreme lower left for scale). With exception of late steep fault seen in A, there is no suggestion that this vein complex was formed by multiple, distinctly time separated and crosscutting events, as would be the case if fault vein complex was formed by number of individual fault episodes.

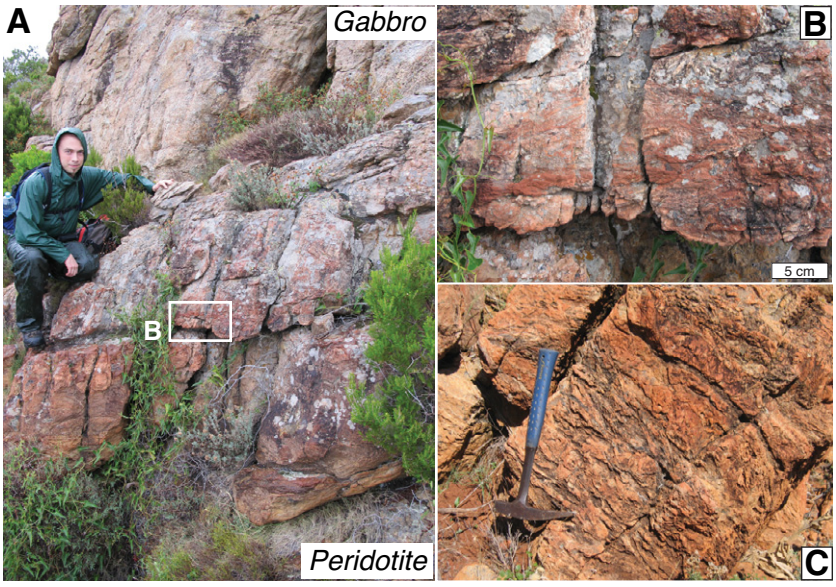


Figure 3. Moho fault. A: Close up of fault at locality 2. Gabbro-peridotite contact is sharp (at person's left hand). Both lithologies have pseudotachylytes (PSTs). Damage zone in peridotite is >2 m wide (limited by outcrop) and consists mostly of PST as intensely net veined material with as much as 80% melt as shown in the detail of A in B. B: Detail of A. C: Detail from Moho fault damage zone at locality 1 showing lack of vein hierarchy. PST thickness (>0.8 m) corresponding to ~2.4 tons of mantle melt per square meter fault surface occurred in single event. Hammer is 32 cm.

occurred along two main fault systems, a steep and a more gently dipping (~30°) set of faults parallel to the Moho fault zone (Andersen and Austrheim, 2006; Silkoset, 2013).

The PSTs are pristine in the least hydrated parts, and occur as relicts in areas with more hydration. Evidence for prograde dehydration of serpentinites near PST faults has not been observed (Deseta et al., 2014). The crust-mantle contact is mostly overprinted by ductile shearing at locality 1 (Fig. 1), but evidence for the former presence of PSTs is found as porphyroclasts in the mylonitic rocks along the contact (Fig. DR3 in the GSA Data Repository[1]). The PST veins increase in abundance at the paleo-Moho at localities 1 and 2. In the best preserved areas (locality 2) the upper ~6 m of the mantle consists of a PST network breccia, which may contain ~50% ultramafic PST (Fig. 2). The largest melt volumes form a dense network of mutually intruding veins (Figs. 2 and 3C; Figs. DR1a, DR1d, and DR1f in the Data Repository). Locally, this produces a breccia with a PST matrix without an obvious temporal hierarchy of individual veins (Figs. 2 and 3C). A number of minor faults with PST postdate the large vein breccia (Fig. 2; Fig. DR1). Other localities along the Moho have massive and thicker fault veins that may be >1 m in cumulative thickness (Fig. 3; Fig. DR1). These were formed by at most a few major ruptures succeeded by several minor events, as shown by reinjection of younger PST (Fig. DR2b). The fault veins and dense vein network constitute a several-meter-wide damage zone along the Moho fault. The distribution of PST along the fault zone varies considerably; there is an apparent maximum in areas where the vein network is thickest (locality 2). From the lateral thickness variation it is obvious that redistribution by flow of ultramafic melt along the fault took place after generation, but before complete solidification. The partial solidification, remobilization, and back veining are interpreted to have produced the sponge-like network where PST occupies space in veins and between fragments (Fig. 2; Fig. DR1). The network breccia in Figure 2 is >6 m thick, and is composed of as much as 50% ultramafic PST. It is truncated by several minor faults with PST, which also remelted older PST (Fig. DR2b). These faults may represent aftershocks succeeding the main earthquakes.

[1]GSA Data Repository item 2014145, Figure DR1 (photo documentation of macroscopic features of the PST along the Moho fault zone), Figure DR2 (microtextures and electron backscattered diffraction data from the Moho fault zone), and Figure DR3 (photo documentation showing remnants of PST veins along the Moho fault zone where it is overprinted by ductile blueschist facies deformation), is available online at www.geosociety.org/pubs/ft2014.htm, or on request from editing@geosociety.org or Documents Secretary, GSA, P.O. Box 9140, Boulder, CO 80301, USA.

Downloaded from geology.gsapubs.org on May 15, 2014

MELT VOLUMES, ENERGY BUDGET, AND EARTHQUAKE MAGNITUDE

Locality 2 provides excellent evidence that rapid release of energy accompanied by melting has intensely fractured the wall rocks. Wall-rock fragments and deformed xenocrysts were incorporated and progressively assimilated in the PST, producing domains of variable composition and banding at a millimeter scale (Deseta et al., 2014). Thin melt channels remained open and the bifurcating and coalescing network could effectively funnel cubic meters of melt from the generation zone in the fault core several meters into the wall rocks (Fig. 2). In order to transport PST melts several meters in thin channels and sheets, the melt must have had a low viscosity (Suzuki et al., 2001), or it would have solidified toward the wall rocks. The melts may have been superheated, even supercritical (Kanamori et al., 1998) during their explosive formation and drainage from the generation zone, in which case additional melt may have been produced within the vein complex during injection. The presence of a melt zone as much as 3 m thick (Fig. 2A) shows that as much as ~9500 kg of the peridotite may have melted per square meter of the fault plane.

Most of the net vein complex is without an obvious crosscutting vein hierarchy, and it is likely that most of it may have formed in just one major event. Even after careful examination it is difficult to ascertain if the thick breccia formed by a single or by a few major events, in addition to the many smaller ones described previously (e.g., Andersen et al., 2008; Deseta et al., 2014). There are some rootless, crosscutting injection veins in the main fault zone, suggesting that more than one major melting event took place (Fig. DR1a). Because veins of different generations have different weathering (Fig. DR1e) and textural characteristics (Fig. DR2), our interpretation is that the main melt zone (Figs. 2 and 3) may have formed by at most a few (2–3) large events and a number of associated aftershocks. In the calculation of earthquake magnitude we assume that most of the melt breccia with a cumulative melt thickness of as much as 3 m formed by a few large melt-generating events. It is not yet possible to quantitatively deduce more specifics about relative importance and magnitude of these large events.

Using standard values for heat capacity and heat of fusion for an olivine-rich peridotite (Weatherley and Katz, 2012), the release of energy must have been $>1.9 \times 10^{10}$ J m^{-2} along the fault plane in order to melt the observed volumes of ultramafic PST (Fig. 2A). Along strike the PST is more concentrated in thicker veins and the cumulative thickness is less, commonly 1–1.5 m (Fig. 3). We also observed smaller branching vein patterns with a three-dimensional star shape (Fig. DR1g); we interpret these to reflect local explosive production and injection of melts on a smaller scale but similar to the thick sponge-like melt breccia described herein. Both structures demonstrate that melt volumes stored on generation surfaces are much smaller than the total volume generated, and that in most cases melt volumes will be underestimated.

In calculating earthquake magnitude we use mantle strength $\Delta\sigma$ = 500 MPa (Andersen et al., 2008; Obata and Karato, 1995), mantle density ρ = 3200 kg m^{-3}, heat capacity C_p = 1200 J kg^{-1} °C^{-1}, temperature change δT = 1250 °C (regional T of 420 °C to melting T of 1670 °C; Katz et al., 2003), and heat of fusion $H = 5 \times 10^5$ J kg^{-1} (C_p and H, Weatherley and Katz, 2012). We assume that >95% of the total energy of the earthquake is dissipated as heat (McGarr, 1999). It is possible to make an estimate of the shear strain ($\gamma - d/h$, where d is displacement and h is thickness of fault core) if we assume that a single earthquake produced the melt. From the equation for 100% melting:

$$\Delta\sigma = \rho(C_p\ \delta T + H)\gamma^{-1}, \quad (1)$$

(e.g., Di Toro et al., 2005), we obtain $\gamma \approx 12.8$. Provided that the movement took place across a 1.5-m-wide slip zone, as indicated by massive PST fault veins, cogenetic fault vein ladder networks, and breccias (Sibson, 1977) (Fig. 3), the displacement along the Moho fault may have been >19 m. If this was a single slip event, the earthquake must have had a moment magnitude (M_w) of ~8. Generation by 2–3 successive large events would reduce the displacement for the individual earthquakes by as much as 1/3, which still suggest displacements of >6 m displacement and magnitude ~7.5 earthquakes.

DISCUSSION

The rupture length associated with the largest magnitude estimates may have been as much as several hundred kilometers (e.g., Bonilla et al., 1984), and so the fossil earthquakes in Corsica may have affected a large part of the early Alpine subduction zone and been effective almost on a basin scale in the relatively small Piemont-Liguria oceanic basin (Handy et al., 2010). Therefore, the subduction earthquakes exposed in Corsica may have been cogenetic with the deeper HP-LT coseismic events described from the western Alps (Angiboust et al., 2012).

A point of contention concerning intermediate-depth earthquakes is the weakening mechanism for the seismic events. The main hypothesis used to explain the weakening (Rice, 2006) involves high pore-fluid pressures (Green and Houston, 1995; Kirby, 1996). Fluid pressure reduces effective stress and may cause failure and a runaway stress drop of the system. High fluid pressures in this model are nourished by prograde metamorphic dehydration of subducted sediments and serpentinized mantle (Hacker et al., 2003). There may also be a close link between metamorphism and seismicity in subduction zones (Rondenay et al., 2008). Our initial work in Corsica was strongly influenced by the dehydration embrittlement hypothesis, but we found no mineralogical or textural evidence suggesting that prerupture dehydration reactions occurred in the fault zones (Austrheim and Andersen, 2004), and formation of secondary anhydrous minerals produced by dehydration of serpentine, talc, clinochlore, or amphiboles in the gabbro and peridotite has not been observed. Secondary anhydrous minerals within the PST veins are very common, but it is the shear heating, melting, and crystallization, and not prograde metamorphism, that formed them.

Consequently, alternative weakening mechanisms have been explored based on textural and mineralogical evidence. Localized ductile precursors to the faulting along smaller faults from Corsica have been described by Deseta et al. (2014). Evidence for viscous precursor deformation has also been documented by dislocation slip systems in olivine (Silkoset, 2013). The deformation studied by electron backscatter diffraction analyses (Fig. DR3d) is characteristic of intermediate to high water contents and high stresses (200–340 MPa in experiments at ~1250 °C, type E, by Jung et al., 2006). We therefore infer shear heating as the most likely weakening mechanism (Kelemen and Hirth, 2007). Viscous dissipation of heat resulted in thermal runaway and earthquake faulting. Theoretical investigations (Braeck and Podladchikov, 2007) and numerical simulations (John et al., 2009) of thermal runaway show that it requires lower differential stresses than frictional faulting at the ambient conditions of intermediate and deep earthquakes in the absence of a free fluid. A recent seismological study of 253 intermediate-depth earthquakes recorded in the Andean subduction zone also support the suggestions that such earthquakes are triggered by a thermal runaway mechanism rather than by brittle faulting (Prieto et al., 2013).

CONCLUSIONS

The observations presented here show that at most a few very large earthquakes produced a thick PST melt zone along the crust-mantle boundary of the Piemont-Liguria basin during the Alpine subduction. The commonly used mechanism for explaining subduction earthquakes is embrittlement by dehydration of seawater-altered rocks (e.g., Green and Houston, 1995). Our current and previous work provides no evidence for prerupture prograde metamorphic dehydration, and we therefore support previous interpretations (John et al., 2009; Kelemen and Hirth, 2007) that shear heating was the most likely weakening mechanism for large subduction earthquakes in the HP-LT metamorphic rocks in Corsica.

Downloaded from geology.gsapubs.org on May 15, 2014

ACKNOWLEDGMENTS

Constructive reviews by A. Vitale Brovarone, M. Steltenpohl, and an anonymous reviewer are greatly acknowledged. We also acknowledge the South African National Research Foundation (NRF) for grants to Ashwal, and the Mellon Foundation for support to Deseta. The Norwegian Research Council Centre of Excellence [grants 223272 to CEED and PGP] funded this work.

REFERENCES CITED

Andersen, T.B., and Austrheim, H., 2006, Fossil earthquakes recorded by pseudotachylytes in mantle peridotite from the Alpine subduction complex of Corsica: Earth and Planetary Science Letters, v. 242, p. 58–72, doi:10.1016/j.epsl.2005.11.058.

Andersen, T.B., Mair, K., Austrheim, H., Podladchikov, Y.Y., and Vrijmoed, J.C., 2008, Stress release in exhumed intermediate and deep earthquakes determined from ultramafic pseudotachylyte: Geology, v. 36, p. 995–998, doi:10.1130/G25230A.1.

Angiboust, S., Agard, P., Yamato, P., and Raimbourg, H., 2012, Eclogite breccias in a subducted ophiolite. A record of intermediate-depth earthquakes?: Geology, v. 40, p. 707–710, doi:10.1130/G32925.1.

Austrheim, H., and Andersen, T.B., 2004, Pseudotachylytes from Corsica: Fossil earthquakes from a subduction complex: Terra Nova, v. 16, p. 193–197, doi:10.1111/j.1365-3121.2004.00551.x.

Austrheim, H., and Boundy, T.M., 1994, Pseudotachylytes generated during seismic faulting and eclogitization of the deep crust: Science, v. 265, p. 82–83, doi:10.1126/science.265.5168.82.

Bjørnerud, M.G., Austrheim, H., and Lund, M.G., 2002, Processes leading to eclogitization (densification) of subducted and tectonically buried crust: Journal of Geophysical Research, v. 107, no. B10, p. 1–18, doi:10.1029/2001JB000527.

Bonilla, M.G., Mark, R.K., and Lienkaemper, J.J., 1984, Statistical relations among earthquake magnitude, surface rupture length and surface fault displacement: U.S. Geological Survey Open-File Report 84–256, 46 p.

Braeck, S., and Podladchikov, Y.Y., 2007, Spontaneous thermal runaway as an ultimate failure mechanism of materials: Physical Review Letters, v. 98, doi:10.1103/PhysRevLett.98.095504.

Deseta, N., Andersen, T.B., and Ashwal, L.D., 2014, A weakening mechanism for intermediate-depth seismicity? Detailed petrographic and microtextural observations from blueschist facies pseudotachylytes, Cape Corse, Corsica: Tectonophysics, v. 610, p. 138–149, doi:10.1016/j.tecto.2013.11.007.

Di Toro, G., Pennacchioni, G., and Teza, G., 2005, Can pseudotachylytes be used to infer earthquake source parameters? An example of limitations on the study of exhumed faults: Tectonophysics, v. 402, p. 3–20, doi:10.1016/j.tecto.2004.10.014.

Frohlich, C., 2006, Deep earthquakes: Cambridge, UK, Cambridge University Press, 573 p.

Green, H.W., and Houston, H., 1995, The mechanics of deep earthquakes: Annual Review of Earth and Planetary Sciences, v. 23, p. 169–213, doi:10.1146/annurev.ea.23.050195.001125.

Hacker, B.R., Peacock, S.M., Abers, G.A., and Holloway, S.D., 2003, Subduction factory: 2. Are intermediate-depth earthquakes in subducting slabs linked to metamorphic dehydration reactions: Journal of Geophysical Research, v. 108, p. 1–8, doi:10.1029/2001JB001129.

Handy, M.R., Schmid, S.M., Bousquet, R., Kissling, E., and Bernoulli, D., 2010, Reconciling plate-tectonic reconstructions of Alpine Tethys with the geological-geophysical record of spreading and subduction in the Alps: Earth-Science Reviews, v. 102, p. 121–158, doi:10.1016/j.earscirev.2010.06.002.

John, T., and Schenk, V., 2006, Interrelations between intermediate-depth earthquakes and fluid flow within subducting oceanic plates: Constraints from eclogite facies pseudotachylytes: Geology, v. 34, p. 557–560, doi:10.1130/G22411.1.

John, T., Medvedev, S., Rüpke, L.H., Andersen, T.B., Podladchikov, Y.Y., and Austrheim, H., 2009, Generation of intermediate-depth earthquakes by self-localizing thermal runaway: Nature Geoscience, v. 2, p. 137–140, doi:10.1038/ngeo419.

Jung, H., Katayama, I., Jiang, Z., Hirago, T., and Karato, S.I., 2006, Effect of water and stress on the lattice-preferred orientation of olivine: Tectonophysics, v. 421, p. 1–22, doi:10.1016/j.tecto.2006.02.011.

Kanamori, H., Anderson, D.L., and Heaton, T.H., 1998, Frictional melting during the rupture of the 1994 Bolivian earthquake: Science, v. 279, p. 839–842, doi:10.1126/science.279.5352.839.

Katz, R.F., Spiegelman, M., and Langmuir, C.H., 2003, A new parameterization of hydrous mantle melting: Geochemistry Geophysics Geosystems, v. 4, p. 1–19, doi:10.1029/2002GC000433.

Kelemen, P.B., and Hirth, G., 2007, A periodic shear-heating mechanism for intermediate-depth earthquakes in the mantle: Nature, v. 446, p. 787–790, doi:10.1038/nature05717.

Kirby, S.H., 1996, Intermediate-depth intraslab earthquakes and arc volcanism as physical expressions of crustal and uppermost mantle metamorphism in subducting slabs, *in* Bebout, G.E., et al., eds., Subduction top to bottom: American Geophysical Union Geophysical Monograph 96, p. 195–213, doi:10.1029/GM096p0195.

McGarr, A., 1999, On relating apparent stress to the stress causing earthquake fault slip: Journal of Geophysical Research, v. 104, p. 3003–3012, doi:10.1029/1998JB900083.

Obata, M., and Karato, S.I., 1995, Ultramafic pseudotachylyte from the Balmuccia peridotite, Ivrea-Verbano zone, northern Italy: Tectonophysics, v. 242, p. 313–328, doi:10.1016/0040-1951(94)00228-2.

Prieto, G.A., Florez, M., Barrett, S.A., Beroza, G.C., Pedraza, P., Blanco, J.F., and Poveda, E., 2013, Seismic evidence for thermal runaway during intermediate-depth earthquake rupture: Geophysical Research Letters, v. 40, p. 1–5, doi:10.1002/2013GL058109.

Ravna, E.J.K., Andersen, T.B., Jolivet, L., and Capitani, C., 2010, Cold subduction and the formation of lawsonite eclogites—Constraints from prograde evolution of eclogitized pillow lava from Corsica: Journal of Metamorphic Geology, v. 28, p. 381–395, doi:10.1111/j.1525-1314.2010.00870.x.

Rice, J.R., 2006, Heating and weakening of faults during earthquake slip: Journal of Geophysical Research, v. 111, B05311, doi:10.1029/2005JB004006.

Rondenay, S., Abers, G.A., and van Keken, P.E., 2008, Seismic imaging of subduction zone metamorphism: Geology, v. 36, p. 275–278, doi:10.1130/G24112A.1.

Sibson, R.H., 1977, Fault rocks and fault mechanisms: Geological Society of London Journal, v. 133, p. 191–213, doi:10.1144/gsjgs.133.3.0191.

Sibson, R.H., and Toy, V.G., 2006, The habitat of fault-generated pseudotachylyte: Presence vs. absence of friction-melts, *in* Abercrombie, R., et al., eds., Earthquakes: Radiated energy and the physics of faulting: American Geophysical Union Geophysical Monograph 170, p. 153–166, doi:10.1029/170GM16.

Silkoset, P., 2013, Microtexture of ultramafic pseudotachylyte fault veins from Corsica, an SEM-EBSD analysis [M.S. thesis]: Oslo, University of Oslo, 196 p.

Spray, J.G., 1995, Pseudotachylyte controversy: Fact or friction?: Geology, v. 23, p. 1119–1122, doi:10.1130/0091-7613(1995)023<1119:PCFOF>2.3.CO;2.

Suzuki, A., Ohtani, E., Urakawa, S., Terasaki, H., and Kato, T., 2001, Viscosity of komatiite magma at high pressure: Bayerisches Forschungsinstitut für Experimentelle Geochemie und Geophysik, Universität Bayreuth Annual Report, v. 2001, p. 105.

Vitale Brovarone, A., Groppo, C., Hetenyi, G., Compagnoni, R., and Malavieille, J., 2011a, Coexistence of lawsonite-eclogite and blueschist: Phase equilibria modeling of Alpine Corsica metabasalts and petrological evolution of subduction slabs: Journal of Metamorphic Geology, v. 29, p. 583–600, doi:10.1111/j.1525-1314.2011.00931.x.

Vitale Brovarone, A., Beltrando, M., Malavieille, J., Giuntoli, F., Tondella, E., Groppo, C., Beyssac, O., and Compagnoni, R., 2011b, Inherited ocean-continent transition zones in deeply subducted terranes: Insights from Alpine Corsica: Lithos, v. 124, p. 273–290, doi:10.1016/j.lithos.2011.02.013.

Vitale Brovarone, A., Beyssac, O., Malavieille, J., Molli, G., Beltrando, M., and Compagnoni, R., 2013, Stacking and metamorphism of continuous segments of subducted lithosphere in a high-pressure wedge: The example of Alpine Corsica (France): Earth-Science Reviews, v. 116, p. 35–56, doi:10.1016/j.earscirev.2012.10.003.

Weatherley, S.M., and Katz, R.F., 2012, Melting and channelized magmatic flow in chemically heterogeneous, upwelling mantle: Geochemistry Geophysics Geosystems, v. 13, p. 1–23, doi:10.1029/2011GC003989.

Manuscript received 29 November 2013
Revised manuscript received 14 January 2014
Manuscript accepted 17 February 2014

Printed in USA